UNIVERSIDAD COMPLUTENSE DE MADRID
FACULTAD DE CIENCIAS QUÍMICAS

TESIS DOCTORAL

Terapias avanzadas basadas en nanopartículas: transporte eficiente de fármacos y edición génica mediada por CRISPR/Cas

Nanoparticle-based advanced therapies: drug delivery and CRISPR/Cas mediated gene editing

MEMORIA PARA OPTAR AL GRADO DE DOCTORA

PRESENTADA POR

Ana Belén Latorre Lozano

DIRECTOR

Álvaro Somoza Calatrava

Madrid

UNIVERSIDAD COMPLUTENSE DE MADRID

FACULTAD DE CIENCIAS QUÍMICAS

TESIS DOCTORAL

TERAPIAS AVANZADAS BASADAS EN NANOPARTÍCULAS: TRANSPORTE EFICIENTE DE FÁRMACOS Y EDICIÓN GÉNICA MEDIADA POR CRISPR/Cas

NANOPARTICLE-BASED ADVANCED THERAPIES: DRUG DELIVERY AND CRISPR/Cas MEDIATED GENE EDITING

MEMORIA PARA OPTAR AL GRADO DE DOCTOR

PRESENTADA POR

Ana Belén Latorre Lozano

DIRECTOR

Álvaro Somoza Calatrava

“Algunos de los héroes más grandes han confesado que

justo antes de entrar en combate les entró un momentáneo temor”

-Peter Pan-

ACKNOWLEDGMENT

Haber llegado hasta aquí no ha sido un camino fácil, pero ahora ya puedo decir que, después de cuatro años de tesis, ¡esto se acaba!

En primer lugar, me gustaría agradecer a mi director de tesis, Álvaro Somoza, por haberme dado la oportunidad de entrar al grupo. Todavía me acuerdo de aquel primer email que le mandé hacia el año 2013 con más vergüenza que otra cosa, por si conocía a alguien con quien pudiese hacer el TFG. Quién nos iba a decir, que no sólo acabaría haciendo el TFG. Gracias por ayudarme y apoyarme durante todos estos años, y por confiar en mí.

En toda esta etapa he podido conocer a mucha gente, con la que he pasado muchos momentos y experiencias. Espero no olvidarme de ninguna.

A los compañeros del grupo "Nanobiotecnología" (L137, L151 y L157), por todos los buenos momentos que hemos pasado, tanto dentro como fuera del labo. Y especialmente a Ciro, Nuria, Carmen, María y Paula por todas las risas, los nervios de los experimentos, las confidencias y por todas las veces que cerrábamos la puerta del laboratorio para contarnos cotilleos. Y no puedo olvidarme de Mila. Gracias por ayudarme tanto durante la recta final y tranquilizarme en los momentos malos.

Y a los que no son del grupo. David, por tu ayuda con los experimentos siempre con una super sonrisa, y a Carlos por esos ratos que animan a todo el mundo.

También me gustaría agradecer a Adri y Zulay, por todo el tiempo compartido en los despachos, las risas, los consejos que me habéis dado y por ayudarme siempre que lo necesitaba.

Gracias también a todos los "Imdeanianos" que ya no están en IMDEA. A Alfonso, mi hermano y compañero de mesa, por enseñarme tantas cosas y ayudarme siempre, siempre, aun no estando ya en IMDEA. A Alberto, mi tutor en la sombra, por explicarme todas las cosas bio con tanta paciencia. A Merce y Enrique, el Equipo desayuno, por todos los cafés y poleos, y por todos los ánimos y consejos que me dais. A Tere, que, aunque no estábamos en el mismo laboratorio, siempre sacábamos un tiempo para vernos y reírnos mucho, y por esos ratos de compras y de viajes. Cómo se echan de menos esos momentos con vosotros…

¡A mis amigos! Gracias Elena y Hernán, por estar conmigo en los momentos buenos y hacer un poquito más llevaderos los malos. Y también a Tony, y esas comiditas en la UAM. Espero que sigamos compartiendo muchos más momentos juntos.

Por último, quiero agradecer a la mejor familia del mundo. Somos muchos, pero me gustaría nombrar a los que habéis estado conmigo todos estos años apoyándome de forma incondicional. A mis tías Loren y Jose, y a mis primos Dori y Manu, Juan, Juanito y Lidia, y Raquel, Manolo y Manu. También a mi tía Merche y mi prima Tere.

A mi hermano Alfonso y Noelia, por escucharme, motivarme y darme fuerzas. A Mario, aunque todavía en muy pequeñito, sólo con dos palabras suyas todo se ve mucho mejor. Y al mejor papi de todos, Alfonso, por estar ahí conmigo siempre.

Pero no podría terminar estos agradecimientos sin hacer una mención especial a mi mami, Eugenia. Todo lo que soy y todo lo que he conseguido ha sido gracias a ella. Muchas gracias, mamá.

Abstract/Resumen

Abstract

Nanotechnology is an area of research that studies and uses materials between approximately 1 and 100 nm in size. At this scale, new properties appear allowing novel applications. In this sense, one of the most studied applications of nanotechnology in recent years is focused on the use of nanoparticles in medicine to diagnose and treat diseases such as cancer.

In this thesis, different nanostructures have been used to transport various therapeutic agents for the treatment of cancer.

In particular, albumin-based nanostructures were selected for the transport of antitumor drugs and CRISPR/Cas gene-editing proteins. Specifically, albumin stabilized gold nanoclusters (BSA-AuNCs) were used for the transportation of the drug AZD8055 for the treatment of uveal melanoma, and doxorubicin and SN38 in the same nanostructure to treat breast cancer. These drugs were covalently conjugated with stimuli-responsive linkers that allow for better control of the release of the drugs into the cancer sites, minimizing the exposure of healthy tissues to cytotoxic agents. The systems developed in this work presented remarkable antitumoral activity in *in vitro* and *in vivo* models.

Besides the delivery of chemotherapeutics, BSA was employed as a carrier of the gene-editing protein Cpf1. In this case, it was covalently conjugated to protect the protein from premature degradation in biological systems and to improve their transport to the tumoral cells. The preliminary results of this study showed the efficient formation of a BSA-Cpf1 nanocomplex that can cut the EGFP gene *in vitro*.

Also, cationic modified carbon nanotubes (SWNT-PEI) were used as a gene delivery system of CRISPR/Cas9 plasmid. In this case, the negative charges of the plasmid allow for strong electrostatic interaction with the modified nanotubes. The resulting nanocomplex was able to internalize in HEK293 cells efficiently. However, the plasmid-mediated gene editing in cells must be improved.

In summary, the results achieved in this thesis highlight the potential of the different nanostructures for their used in cancer treatment.

Resumen

La nanotecnología es una rama de la ciencia que estudia y usa materiales de entre aproximadamente 1 y 100 nm de tamaño. A esta escala, aparecen nuevas propiedades que permiten aplicaciones novedosas. En este sentido, una de las aplicaciones más estudiadas de la nanotecnología en los últimos años se centra en el uso de nanopartículas en medicina para diagnosticar y tratar enfermedades como el cáncer.

En esta tesis, se han utilizado diferentes tipos de nanoestructuras para el transporte de agentes terapéuticos para el tratamiento del cáncer.

Específicamente, se emplearon nanoestructuras basadas en albúmina para el transporte de fármacos antitumorales y proteínas del sistema de edición génica CRISPR/Cas. En concreto, se utilizaron nanoclusters de oro estabilizados con albúmina (BSA-AuNCs) para el transporte del fármaco AZD8055 para el tratamiento del melanoma de úvea, y doxorrubicina y SN38 en la misma nanoestructura para el tratamiento del cáncer de mama. Estos fármacos se conjugaron covalentemente con conectores sensibles a estímulos que liberan los fármacos específicamente en el tumor, minimizando el daño en los tejidos sanos. Los resultados obtenidos en este trabajo revelaron una disminución de la viabilidad celular en modelos *in vitro* e *in vivo* de los tumores seleccionados. Además del trasporte de agentes quimioterapéuticos, la BSA también fue utilizada como vehículo de la proteína de edición de génica Cpf1. En este caso, la BSA fue conjugada covalentemente con la Cpf1 para protegerla de la degradación prematura en los sistemas biológicos y favorecer su transporte a las células tumorales. Los resultados preliminares de este estudio mostraron la formación eficiente de un nanocomplejo de BSA-Cpf1 capaz de realizar el corte *in vitro* del gen EGFP.

Por último, se utilizaron nanotubos de carbono catiónicos (SWNT-PEI) como sistema de transporte de un plásmido CRISPR/Cas. La carga negativa del plásmido permitió la interacción electrostática con los nanotubos modificados. Los complejos resultantes pudieron internalizar en células HEK293 de manera eficiente. Sin embargo, la edición de genes mediada por dicho plásmido en las células aún debe mejorarse.

En resumen, los resultados logrados en esta tesis resaltan el potencial de las diferentes nanoestructuras para su uso en el tratamiento del cáncer.

Table of Content

Abbreviations

A	**ABC**	ATP-binding cassette transporters
	ABN	Albumin-based nanostructures
	AD	Anno Domini
	ADCs	Antibody-drug conjugates
	AFM	Atomic Force Microscope
	ANOVA	Analysis of variance
	Au	Gold
	AuNCs	Gold-nanoclusters
	AZD-PySS	Modified AZD8055
B	**BC**	Before Christ
	bFGF	Basic fibroblast growth factor
	BRAF	B-Raf Proto-Oncogene
	BRCA	Breast Cancer gene
	BSA	Bovine serum albumin
C	**CAR**	Chimeric antigen receptor
	Cas	CRISPR associated protein
	Cav-1	Caveolin-1
	CNTs	Carbon nanotubes
	CPT	Camptothecin
	CRISPR	Clustered Regularly Interspaced Short Palindromic Repeats
	crRNAs	CRISPR RNA
	CSCs	Cancer stem cells
	CT	Computed tomography
	CTLA-4	Cytotoxic T-lymphocyte-associated protein
D	**DAPI**	4 ',6-diamidino-2-fenilindol
	DCC	N,N'-Dicyclohexylcarbodiimide
	DDR	DNA damage response
	DIC	Differential interference contrast
	DIPEA	N,N-Diisopropylethylamine
	DLS	Dynamic Light Scattering
	DMAP	4-Dimethylaminopyridine
	DMF	N,N-Dimethylformamide
	DMSO	Dimethyl sulfoxide
	DNA	Deoxyribonucleic acid
	DOX	Doxorubicin
	DOX-HCl	Doxorubicin hydrochloride
	DOX-iMal	Modified doxorubicin
	DSBs	Double-stranded breaks
	DTT	Dithiothreitol

E	**EDTA**	Ethylenediaminetetraacetic acid
	EGF	Epidermal growth factor
	EGFP	Enhanced green fluorescent protein
	EGFR	Epidermal growth factor receptor
	EMA	European Medicines Agency
	EPR	Enhanced permeability and retention effect
	ER	Estrogen receptor
F	**FBS**	Fetal bovine serum
	FcRn	Neonatal Fc receptor
	FDA	Food and Drug Administration
G	**GLP-1**	Glucagon-like peptide-1
	GNA11	G protein subunit alpha 11
	GNAQ	Guanine nucleotide-binding protein
	gp	Albumin-binding glycoprotein
	gRNA	Guide RNA
	GSH	Glutathione
H	**H&E**	Hematoxylin and eosin
	H2AX	H2A histone family member X
	H_2DCF-DA	2',7'- dichlorodihydrofluorescein diacetate
	$HAuCl_4$	Hydrogen tetrachloroaurate (III) hydrate
	HDR	Homology-directed repair
	HER2	Human epidermal growth factor receptor 2
	HPLC	High-performance liquid chromatography
	HSA	Human serum albumin
I	**i.t.**	Intratumoral
	i.v.	Intravenous
	ICP-MS	Inductively coupled plasma mass spectrometry
	indels	Insertions o deletions
M	**MAPK**	Mitogen-activated protein kinase
	MDR	Multi-drug resistance
	miRNAs	Micro-RNAs
	MRI	Magnetic resonance imaging
	mRNA	Messenger RNA
	mTOR	Mammalian target of Rapamycin
	MTT	Dimethylthiazolyl-diphenyl-tetrazolium bromide
	MWNTs	Multiwalled carbon nanotubes
N	**NHEJ**	Non-homologous end-joining
	NHS	N-Hydroxysuccinimide
	NIR	Near infrared

	nm	Nanometer
	NP	Nanoparticle
	NT	Non-targeting
P	**p53**	Tumor protein p53
	PAA	Poly(acrylic acid)
	PAM	Motif adjacent to the protospacer
	PBS	Phosphate buffered saline
	PD-1	Programmed cell death protein 1
	PDI	Polydispersity index
	PD-L1	Programmed cell death protein ligand 1
	PDT	Photodynamic therapy
	PEG	Polyethyleneglycol
	PEI	Polyethylenimine
	PET	Positron Emission Tomography
	PNK	T4 Polynucleotide kinase
	PR	Progesterone receptor
	PTT	Photothermal therapy
R	**Raf**	*Raf*-1 Proto-Oncogene, Serine/Threonine Kinase
	Ras	Rat sarcoma
	Rb	Retinoblastoma
	Rcf	Relative Centrifugal Force
	Redox	Oxidation-reduction
	RES	Reticuloendothelial system
	RGD	Arginylglycylaspartic acid
	RNA	Ribonucleic acid
	RNAi	RNAs interference
	RNP	Ribonucleoprotein
	ROS	reactive oxygen species
	Rpm	Revolutions per minute
S	**SD**	Standard deviation
	SDS-PAGE	Sodium dodecyl sulfate polyacrylamide gel electrophoresis
	SEM	Scanning electron microscopy
	siRNAs	Small interfering RNAs
	SN38	7-ethyl-10-hydroxy-camptothecin
	SN38-PySS	Modified SN38
	SPARC	Acidic and cysteine rich secreted protein
	STEM	Scanning transmission electron microscope
	SWNTs	Single-walled carbon nanotubes
T	**TAE**	Tris-Acetate-EDTA
	TALEN	Transcriptional activator-type effector nucleases
	TEM	Transmission electron microscopy

	TFA	Trifluoroacetic acid
	TGA	Thermogravimetric analysis
	TLC	Thin layer chromatography
	TOP1	Topoisomerase I
	TOP2A	Topoisomerase II
	tracrRNA	Trans-activating CRISPR RNA
U	**Unmod**	Unmodified
	UV	Ultraviolet
V	**VGFR**	Vascular endothelial growth factor receptor
	Vis	Visible
W	**WHO**	World Health Organization
Z	**ZFN**	Zinc finger nucleases

Introduction

1. INTRODUCTION

1.1. Nanoscience and nanotechnology

Nanoscience is the study of phenomena and manipulation of structures and molecules on the nanometer scale, whereas the practical application of nanoscience to design and develop new materials that could have a great influence in different scientific areas is called nanotechnology. Thus, nanoscience is the study of matter at the nanoscale and nanotechnology use these materials to create something new[1,2].

The fundamental components of this area are the nanomaterials. The definition of nanomaterial is not straightforward, and a variety of definitions are employed. Among all, the most widely accepted defines it as a material produced on a nanometric scale, where one or more external dimensions are between 1 nm - 100 nm[3,4].

The prefix “nano” was taken from the Greek, and means it extremely small. It is a unit of measure, particularly, one thousand millionth of a meter (0.000000001 or 10^{-9} m)[5]. It could be challenging to imagine how small these nanomaterials are; thus, to visualize it better, illustrative examples are described below (**Figure 1**):

- A tennis ball has a diameter of approximately 100000000 nm.
- A human hair is approximately 100000 nm thickness.
- A bacterium is about 1000 nm long.
- A double-stranded DNA molecule has a width of 1 nm.

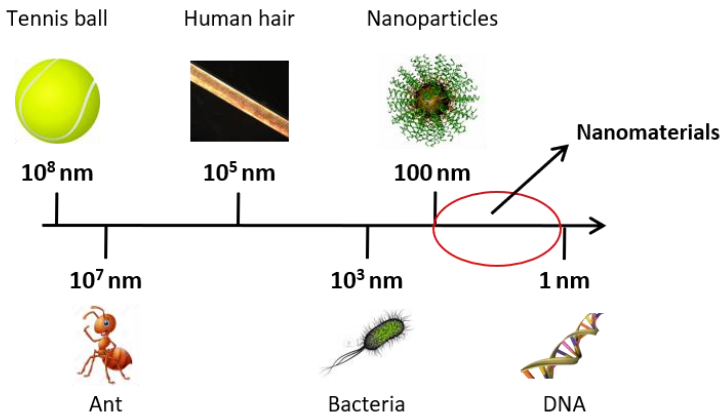

Figure 1. Nanometer-scale showing different examples. The scale ranges from 10^8 to 1 nm, where nanomaterials are defined between 1 a 100 nm (red circle).

The idea of nanoscience and nanotechnology was attributed to the Nobel Prize laureate Richard Feynman in 1959 during his talk entitled "There's Plenty of Room at the Bottom". In that talk, Feynman describes a process on how scientists could manipulate individual atoms and molecules, hypothesizing that in the future, we would be able to write "the entire 24 volumes of the Encyclopedia Britannica on the head of a pin"[6]. However, the term nanotechnology was used and define the first time by Norio Taniguchi in 1974 as "nanotechnology mainly consists of the processing of separation, consolidation, and deformation of materials by one atom or one molecule"[7]. But it was not until 1981 and 1986, with the development of the scanning tunneling microscopy (STM) and atomic force microscopy (AFM), respectively, that scientists were able to see individual atoms, and the nanoscale world was better understood[8].

1.1.1. History of nanotechnology

Although nanoscience and nanotechnology are relatively new fields of research, nanometric materials have been used by humans for centuries.

It is known that nanoparticles (NPs) have existed in nature forever. In ancient times, clay minerals were used on a nanometric scale for the controlled reinforcement of a ceramic matrix with natural asbestos nanofibers more than 4500 years ago. However, the most remarkable effects occur with the use of metallic nanoparticles as color pigments to create glass using metals between the 14^{th} to 13^{th} centuries BC in Egypt and Mesopotamia. Recent studies revealed that the colors of some of that glasses are due to the presence of silver and copper nanoparticles dispersed within its outermost layer[9,10].

The Lycurgus Cup is a 4^{th} century AD Roman glass cup and is one of the most famous discoveries of the ancient glass industry. The most remarkable property is based on its dichroism, which means that the Cup changes its color in certain conditions of light: the glass is green when the light illuminates from outside, while it turns red when it passes inside. In the 90s, many scientists have analyzed the Cup by TEM and X-Ray to explain the dichroism phenomena of the glass and its composition. These studies revealed that the Cup was made using 50-100 nm size nanoparticles of silver-gold alloy with a ratio of about 7:3, containing in addition about 10% of copper disperse in the glass. The red color was attributed to the biggest gold nanoparticles, which absorbed the light at a

wavelength of 520 nm, while the green color was attributed to the light scattering of the colloidal dispersion of silver nanoparticles with a size less than 40 nm[11]. Similar examples were found in the windows of medieval churches, doped by mixtures of different size silver and gold nanoparticles, which reflected light yellow and red, respectively[12].

Later, during the 9th-17th centuries, glazed ceramics for metallic luster decorations were used in the Islamic world and Europe containing different types of nanoparticles, such as silver or copper nanoparticles, among others. For example, Italians create Renaissance pottery in the 16th century, in which nanoparticles were distributed in only one layer[10]. In addition, a recent study of Damascus steel from the 17th-18th showed that this material contains carbon nanotubes and cementite nanowires, providing them with high strength and endurance and an exceptionally sharp edge[13].

Although the colors and new properties would be done intentionally by the artists of that time, they surely did not know that they were working with nanoparticles.

In 1857, Michael Faraday reported the first synthesis of gold nanoparticles in solution. He demonstrated that the optical properties of these nanoparticles differ from their corresponding bulk material, producing different colors when they are exposed under different light conditions[14]. Later, the specific colors of metal nanoparticles were explained by Mie in 1908[15]. These events were probably the first studies in which the effect of the nanoscale on materials was observed.

1.2. Nanoparticles

A nanoparticle can be defined as a nano-object where all its dimensions are within the nanoscale range (1-100 nm)[16]. Remarkably, at that scale, the materials might present new physical and chemical properties different from those of the same materials at larger scales[17]. This phenomenon is because, at this scale, the surface of the nanoparticles is large with respect to their total volume (surface/volume ratio > 1), increasing the chemical reactivity and stability[18]. The new properties offer the possibility to design and build systems based on nanoparticles with a great interest in different scientific fields. For example, gold is a yellow material formed by millions of atoms that can be found in nature. However, when a few gold atoms are stabilized in a

minimal space, gold nanoparticles are obtained. These nanoparticles acquire new properties that are reflected in a color change (**Figure 2**).

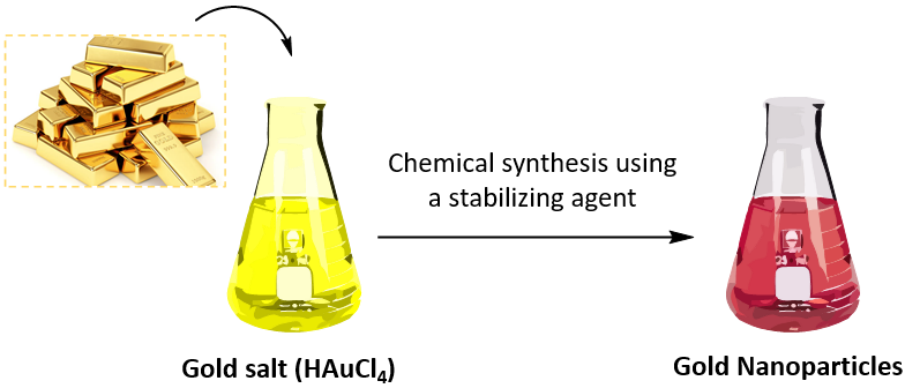

Figure 2. Schematic representation of gold nanoparticles formation. The process starts from a yellow gold salt that, under certain conditions of synthesis and using a stabilizing agent that helps confine the gold atoms in a small space, leads red-wine gold nanoparticles.

In the last years, the development of new synthesis techniques has allowed the obtention of nanoparticles with different characteristics, changing their optical, mechanical, physical and chemical properties[19]. Besides, nanoparticles can be of different sizes and shapes such as spherical, cubes, rod, cubic, among others[20].

1.2.1. Properties of nanoparticles

As describe before, nanoparticles have unique physicochemical properties compare to the corresponding bulk materials, such as extensive surface area, chemical reactivity, and optical activity, among others. Some of the most important properties are the following.

1.2.1.1. Optical and electrical properties

These properties are related to the small size of the nanoparticles that caused electron confinement. Semiconductors and metal nanoparticles exhibit massive changes in these properties, depending on the particle size. For example, in metal nanoparticles, the size-dependent properties are due to the difference in the energy band gap, which influences their plasmon resonance. It is important to mention that surface plasmon resonance band is produced due to the excitation of outer electrons of nanoparticles, and it is only observed if the size of the materials is less than the excitation wavelength. It is well

known that the relationship between the color of the colloidal suspension of metal nanoparticles change with their size[21,22].

1.2.1.2. Magnetic properties

Due to the great variety of applications that magnetic nanoparticles have, different synthesis strategies are being developed. Their magnetic properties are the result of the interaction between the charges of electrons and the magnetic spins of the materials that compose them. Due to their large surface/volume ratio, nanoparticle atoms undergo different magnetic coupling with nearby atoms, leading to magnetic properties. These properties also depend on the nanomaterial synthesis method, since they influence the shape, size distribution, particle size, surface chemistry and, consequently, its magnetic properties[23].

1.2.1.3. Mechanical properties

The basic mechanical properties of nanoparticles are related to different mechanical parameters such as elasticity, hardness, stress, adhesion and friction. Various factors can influence the maintaining or variation of these properties, including the homogeneous dispersion of the nanoparticles or the contacting substrate, which determines if the particles are deformed when the contact pressure is high[24].

1.2.1.4. Catalytic properties

Nanoparticles can catalyze reactions by their reaction with substrates and reagents. Again, this property derives from the large surface to volume ratio, which implies a more significant number of reactive atoms in the surface of the particle with respect to the total number[25]. Compared to their corresponding bulk material, nanoparticles enhance the reactivity and selectivity of the catalytic process. Some of the factors involved in this process are related to the particle size, oxidation state, composition, and physicochemical environment[22].

1.2.2. Synthesis of nanoparticles

The development of fast and reproducible synthesis methods is one of the biggest challenges in nanotechnology. In those processes, controlling the size, morphology and degree of aggregation of the particles is crucial. The methods developed to obtain

nanoparticles can be divided into two different approaches: bottom-up and top-down approaches (**Figure 3**)[26,27].

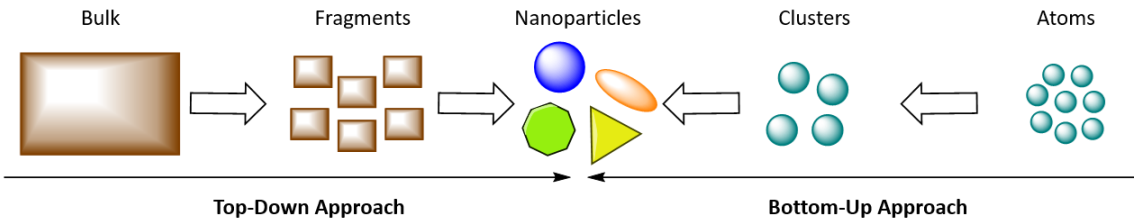

Figure 3. Top-down and bottom-up approaches using for the synthesis of nanoparticles.

1.2.2.1. Top-down approach

This approach is based on destructive methods, where the bulk material is fragmented into the nanoparticles. The process occurs by applying energy, which can be mechanical, chemical, or another form such as laser irradiation[27].

The main advantage of this approach is that nanoparticles can be synthesized in bulk quantities quickly. However, these nanoparticles result in non-homogenous size distribution.

1.2.2.2. Bottom-up approach

Conversely to the previous method, in the bottom-up approach, nanoparticles are formed from the interaction of atom or molecules by physicochemical methods[26].

The main advantage of this method is that the resulting nanoparticles have a homogenous distribution size and chemical composition. In addition, they are quite stable, which is crucial for further applications. However, this process is usually time-consuming, and large-scale production is challenging.

1.2.3. Classification of nanoparticles

As mentioned before, nanoparticles can differ in size, shape, morphology and chemical composite. Most nanoparticles can be classified into three major groups depending on their composition: organic, inorganic and carbon-based[18].

1.2.3.1. Organic-based nanoparticles

Are made from organic materials such as dendrimers, micelles, liposomes and polymers (**Figure 4**). The main advantages of these nanoparticles are their biodegradability and

biocompatibility. The final structures are usually obtained by the self-assembly of the single molecules of which nanoparticles are composed[28].

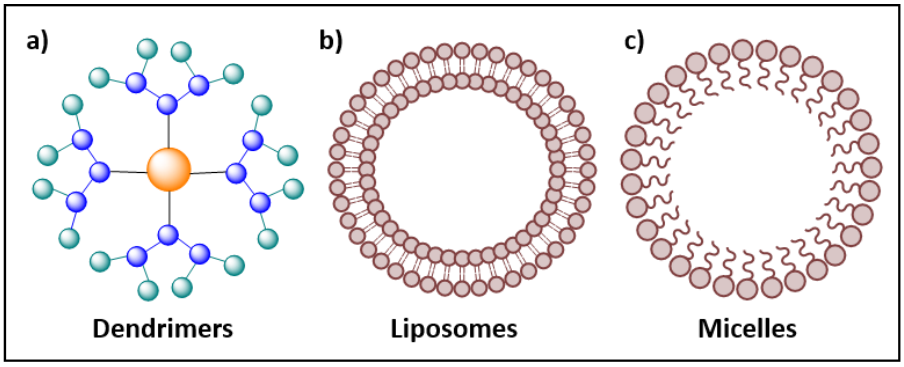

Figure 4. Representation **a)** dendrimers nanoparticles, **b)** liposomes and **c)** micelles included in organic-based nanoparticles.

1.2.3.2. Inorganic-based nanoparticles

Nowadays, inorganic nanoparticles are attracting the attention of many scientists because they can be synthesized with an active chemical group that allows their conjugation with different active molecules such as drugs, targeted agents, ligands, and contrast imaging agents, among other. This means that these nanoparticles can have a wide range of possible applications, making them especially attractive [18,29–31].

Typically, inorganic-based nanoparticles are composed of different layers (**Figure 5**)[32]:

- Core: is the inner material and the central part of the particle. It is normally used to name and classify the particle itself.
- Shell: is formed of a different material than the core. The selection of this material is usually related to the end application of the nanoparticle.

In addition, the surface of the nanoparticles can be functionalized with different small molecules. Ionic surface molecules generate a uniform charge, which plays an essential role in the size and morphology of the nanoparticle.

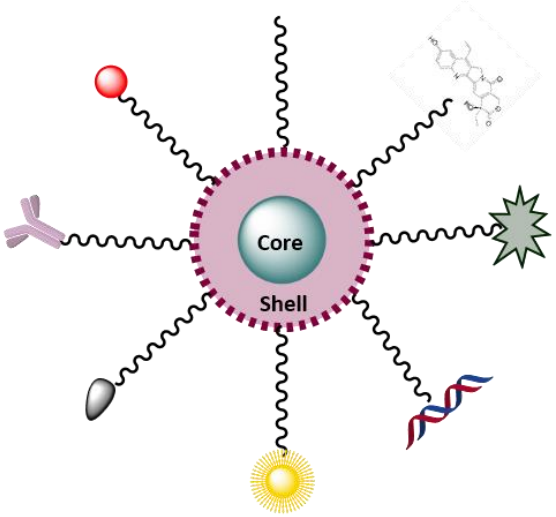

Figure 5. Schematic representation of the three layers of nanoparticles: core, shell and surface functionalized with different small molecules

Inorganic-based nanoparticles include metal and metal oxide nanoparticles (**Figure 6**).

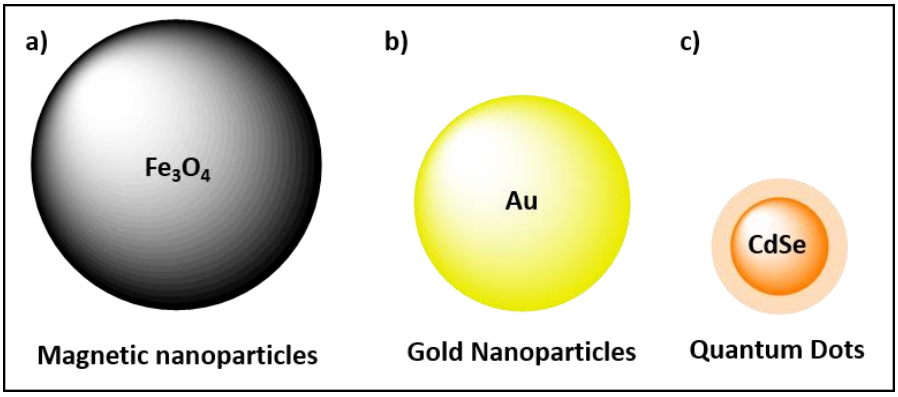

Figure 6. Representation of different types of inorganic nanoparticles such as **a)** magnetic nanoparticles composed by iron oxide, **b)** gold nanoparticles and **c)** quantum dots made of cadmium selenide.

- Metal-based nanoparticles: these nanoparticles are synthesized from metals to nanometric scales, where almost any metals can be employed in their preparation. The most commonly used are aluminum, cadmium, cobalt, copper, gold, iron, lead, silver and zinc. Metal-based nanoparticles present unique physicochemical properties such as small size ranging between 1-100 nm, large surface area to volume ratio, charge surface, stability in aqueous media, high reactivity and sensitivity to environmental factors. In addition, they can be synthesized with different sizes and shapes.

  Currently, they are widely used in biomedical science and engineering.

- Metal oxide nanoparticles: These types of nanoparticles are synthesized to modify the properties of their respective metal nanoparticles, increasing their reactivity and efficiency. They are commonly synthesized of aluminum oxide, cerium oxide, iron oxide, magnetite, silicon dioxide, titanium oxide, zinc oxide.

  Due to their excellent new properties, metal oxide nanoparticles are playing a fundamental role in areas such as electronics, aerospace, medicine, and photocatalysis.

1.2.3.3. Carbon-based nanoparticles

Are entirely made of carbon atoms, which are arranged in different allotropic forms. This type of material is of great interest due to its high electrical conductivity, resistance, electron affinity and versatility. Graphene, carbon nanotubes and fullerenes are included in this category (**Figure 7**)[33].

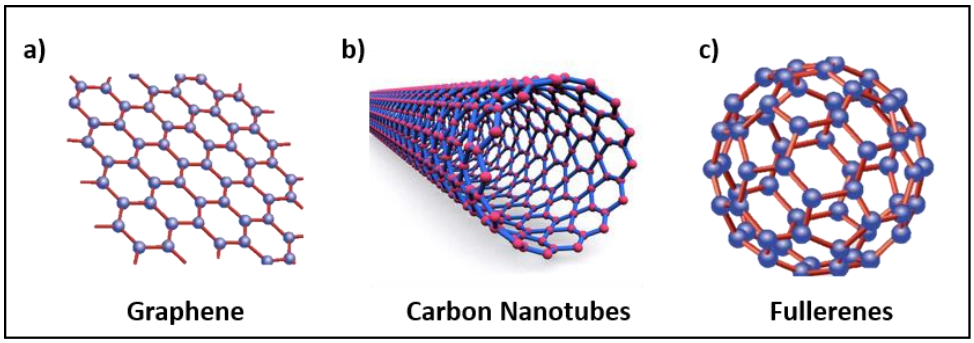

Figure 7. Allotropic forms of carbon **a)** graphene, **b)** carbon nanotubes and **c)** fullerenes forming nanomaterials.

1.3. Applications of nanotechnology

Although it seems surprising, currently, nanomaterials are present in people's daily lives. Due to their unique properties, during the last decades, they are widely investigated in different areas of science and engineering. Thanks to the research in nanoscience and nanotechnology, scientists are achieving to develop new and innovative tools for applying nanomaterials to different types of sectors and industries such as the environment, electronic devices, cosmetics, medicine, among others (**Figure 8**). Some of the most relevant applications are described below.

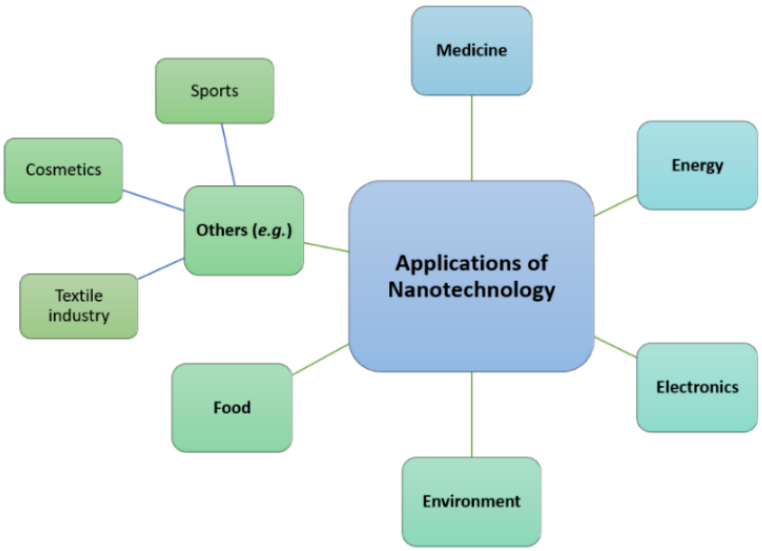

Figure 8. Schematic representation of various applications of nanotechnology.

1.3.1. Medicine

The use of nanoparticles in medicine (nanomedicine) has been used to improve the early detection and treatment of different types of diseases, taking advantage of their unique properties. In this regard, nanotechnology is being used to improve some of the physical and chemical properties of medicines, such as solubility or biodistribution, and even improve the delivery's selectivity, which can lead to reduced side effects[34].

Many tablets, suppositories and creams contain synthetic amorphous silica (SAS), which consists of nano-sized particles, to control the viscosity and uniformity of the active molecules[35]. Furthermore, silver nanoparticles have been used for several years as antibacterial agents for wound healing[36].

The safety of nanomedicine products is regulated by drug regulatory agencies such as the European Medicines Agency (EMA) or the Food and Drug Administration (FDA), exactly like conventional drugs and medical devices. There is a wide variety of nanomaterials currently approved by the EMA for the treatment of different diseases. These nanomedicines must follow a thorough characterization, a toxicity assessment, and, finally, be evaluated in clinical trials. Some examples are summarized in **Table 1**.

Drug	Nanoparticles	Disease
Abraxane	Protein NPs	Breast cancer, pancreatic cancer, non-small cell lung cancer
Caelyx/Doxil	Liposomes	Metastatic breast cancer, ovarian cancer, Kaposi's sarcoma, multiple myeloma
Onyvide	Liposomes	Pancreatic cancer
Vysudine	Liposomes	Eye disease: Age-related macular degeneration, pathological myopia, ocular histoplasmosis.
CosmoFer/INFeD/Ferrisat	Magnetic NPs	Treatment of anemia
Rapamune	Nanocrystals	Prophylaxis of organ rejection in kidney transplant patients
PegIntron	Polimeric NPs	Chronic hepatitis C
Pegasys	Polimeric NPs	Hepatitis B and C
Somavert	Polimeric NPs	Growth hormone analog
Krystexxa	Polimeric NPs	Gout disease
Neulasta	Polimeric NPs	Neutropenia induced by chemotherapy
Taxotere	Micelles	Breast cancer, non-small cell lung cancer, gastric cancer, neck and head cancer

Table 1. Various approved nanomedicines by the European Medicines Agency (EMA).

This topic will be discussed in more detail in the following sections.

1.3.2. Energy

Due to the need to replace the large amount of fossil fuels consumed today and reduce the impact of energy production from nuclear and electrical plants that in some way cause environmental pollution, scientists are investigating new clean and renewable energy sources using nanotechnology. There are different strategies that are being explored to produce more efficient and cost-effective energy due to the unique properties of materials at the nanoscale. In particular, the large surface area ratio that contributes to the development of the new optical, magnetic, electrical and catalytic characteristics of these materials[37]. The most promising applications of nanoparticles in this field are related to the production of electricity by using solar energy[38,39], and in the development of new high-capacity batteries that facilitate the storage of electricity[40].

1.3.3. Electronics

Nanotechnology in the electronic industry (nanoelectronics), is responsible for the characterization, manipulation, and manufacture of electronic devices, chips, and circuits at the nanoscale. Nanoelectronics seeks to increase the portability and capabilities of electronic devices while reducing their weight and energy

consumption[41,42]. Nanoparticles are currently being used to improve screens in electronic devices, reducing their energy consumption, weight and thickness, increasing the storage capacity of the chips, and reducing the size of transistors used in integrated circuits[43,44].

1.3.4. Environment

Nanotechnology for environmental purposes has excellent potential since it provides solutions to a wide range of current problems. This includes direct applications of nanomaterials to detect, prevent, and eliminate contaminants, as well as indirect applications to develop cleaner industrial processes and create environmentally responsible products[45]. Among the different applications, the most used are those related to water treatment, bioremediation, environmental sensors to control the amount of pollutants in water and air, and a profitable alternative clean and renewable energy sources[46].

1.3.5. Food science

Like other sectors previously described, nanotechnology offers new possibilities for innovation in the field of food and other related areas. Applications in this sector can be divided into two groups. On the one hand, nanotechnology is being employed both throughout the processing of food and in their packaging. In this regard, nanomaterials can be used to reduce the amount of food additives and avoid lumps, as antimicrobial agents, to improve the absorption capacity of some nutrients, and to develop the most resistant and durable packaging. On the other hand, nanomaterials are also used as sensors to achieve better food quality and a safety assessment[47–50].

1.3.6. Other applications

Some examples of these products are related to:

- Cosmetics: the use of nanomaterials in this sector is used to enhance colors with better quality, improve the stability of cosmetics, prolong their effect, and leave no residue. In addition, some nanomaterials are capable of scattering light and acting as UV protectors[51].
- Textile industry: different nano-treatments in textiles can confer special properties like breathability, water repellence, soil resistance, wrinkle-free property, flame

retardancy, anti-static property or UV protection, among others[52]. One of the aims of the research in this field is to create clothes with new properties, known as "smart clothes"[53].

- Sports: sports equipment, such as rackets, baseball bats or hockey sticks, contains different nanoparticles that can improve their performance, flexibility and durability, and reduce their weight. Furthermore, they can be used on stadium floors and walls to make them resistant to water and humidity, maintaining their long-term cleanliness and extending their useful life[54].

1.4. Cancer

Cancer is a very broad term used to refer to a range of diseases characterized by the uncontrolled growth of abnormal cells in the body. This process takes place when the control mechanisms of cells stop working. Normally, the cells of the body grow and divide to form new cells. When these cells become old or damaged, programmed cell death mechanisms are triggered, and the cells are replaced by healthy ones. However, if this process does not occur, the abnormal cells begin to grow uncontrollably and can form masses in the tissues called tumors (**Figure 9**). It is worth mentioning that there are other types of cancer related to blood cells, such as leukemias, that do not form solid tumors[55,56].

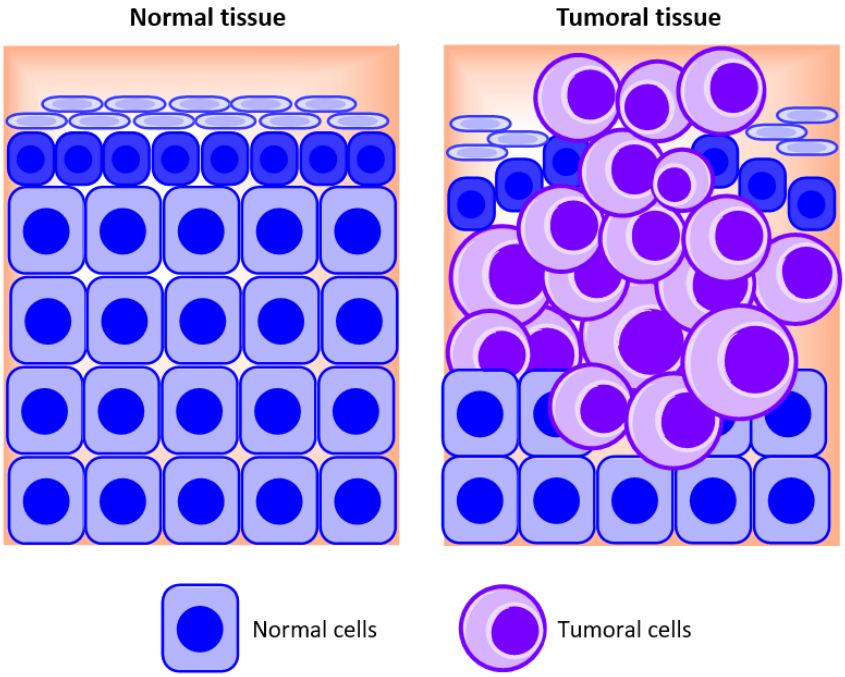

Figure 9. Comparison between normal and carcinogenic tissue. In the tumor, the cells divide uncontrollably and can invade other tissues.

Malignant tumors are characterized by their ability to invade nearby tissues, and even spread to more distant places of the body through the blood or lymphatic system. These circulating cancer cells, may remain in distant tissues and form secondary tumors called metastases. Besides, malignant tumors may cause severe irreversible damage to tissues and normal body functions, produced by themselves or by metastasis, and can sometimes lead to the death of patients[57].

Cancer is one of the world's biggest health problems. According to the World Health Organization (WHO), 17 million people were diagnosed with cancer in 2018 worldwide[58]. It is the second leading cause of death after cardiovascular diseases causing around 9.5 million people per year[59,60]. In particular, in Spain, two hundred thousand new cases were diagnosed in 2018, causing one hundred and thirteen thousand deaths[61].

The reasons why a normal cell becomes carcinogenic is not well known, but it is clear that cancer is a genetic disease that involves one or more changes in the genomic material called mutations. These changes can be inherited from the family or acquired during life as a result of lifestyles and exposure to external environmental factors such

as tobacco, alcohol consumption or UV radiation. Among the different genes involved in cancer development, oncogenes and tumor suppressor genes play a crucial role.

Oncogenes derive from normal cellular genes called proto-oncogenes, which are involved in different cellular growth-controlling pathways. Activation of a proto-oncogene into an oncogene usually involves a gain of function mutation that entails an excessive or uncontrolled growth-promoting signal inducing abnormal cell proliferation and tumor development[62]. This process results from genomic alterations such as point mutations, DNA segment duplications and chromosome translocations[63]. Ras and Raf oncogenes proteins are well-known examples of what its alteration leads to the development of cancer[64].

Conversely, tumor suppressor genes are responsible for inhibiting cell proliferation and tumor growth. The loss or inactivation of these genes leads to eliminating negative regulators and contributes to the abnormal proliferation of cells avoiding the apoptosis mechanism. *Rb* and *p53* genes are some tumor suppressor genes associated with tumor formation[65].

In this regard, genetic mutations are the driving forces that give some cells an advantageous phenotypic characteristic that leads to tumor development. However, cancer is a complex disease, and it requires the accumulation of different abnormalities in the cells, rather than a simple mutation. Therefore, different types of cells can coexist in the same tumor. This heterogenicity, along with the acquisition of new mutations, allows them to survive, proliferate, disseminate and be resistant to drugs, thereby promoting the tumor[66,67].

In 2000, Hanahan and Weinberg published a review article entitled "The Hallmarks of Cancer". They summarized six alterations that occur in the transformation of a normal cell to a tumor. These include self-sufficiency in growth signals, insensitivity to growth-inhibitory signals, evasion of programmed cell death (apoptosis), limitless replicative potential, sustained angiogenesis, and tissue invasion and metastasis[68]. Ten years later, the authors added two new features: reprogramming of energy metabolism and evasion of the immune response[69]. They proposed that these characteristics are common in most, if not all, types of human tumors (**Figure 10**).

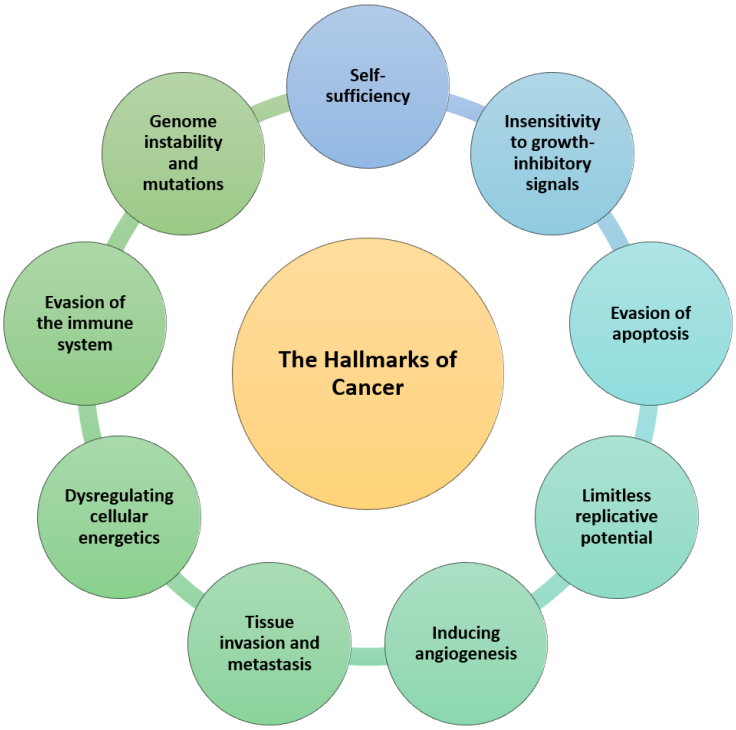

Figure 10. Schematic representation of the "Hallmarks of cancer". Adapted from Hanahan and Weinberg review[69].

The main different characteristics between normal and tumoral cells are summarized in **table 2**.

Hallmarks of cancer	Normal cells	Tumoral cells
Self-sufficiency in growth signals	No type of normal cells can proliferate in the absence of stimulatory signals	Tumoral cells can generate their own growth signals.
Insensitivity of anti-growth signals	In normal tissue, a wide range of anti-growth signals are produced to maintain cellular quiescence and tissue homeostasis	Tumor cells can evade the controls that occur in cell division and proliferate, having their own growth cycle.
Evading apoptosis	In a normal situation, the balance between proliferation rate and apoptosis maintain the homeostasis of healthy tissues	Cancer cells can evade apoptosis by becoming insensitive to apoptotic stimuli inactivating p53 of inhibiting caspase activity. Conversely, apoptosis occurs continuously to eliminate the least fit lineages
Limitless replicative potential	Normal cells have a doubling limit capacity at which they stop growing.	Tumor cells can multiply without limit due to the acquisition of

		mutations in genes such as *p53* or *Rb*.
Inducing angiogenesis	In normal tissues, the generation of new blood vessels is transitory and carefully regulated.	Tumors require a large supply of oxygen and nutrients, and therefore activate the induction of angiogenesis to guarantee their needs.
Tumor invasion and metastasis	Normal cells are held in their proper place by adhesion molecules	Cancer cells develop alterations in their morphology, in their adherence to other cells and to the extracellular matrix, allowing them to invade nearby tissues and travel to distant places.
Dysregulating cellular energetics	Normal cells get most of their energy in a process called the Krebs Cycle, while it is rarely obtained through another process called glycolysis.	The metabolism in many types of cancer is reprogrammed, favoring the activation of the glycolysis pathway to increase the entry of glucose into the cytoplasm of the cells.
Evasion of immune system	The immune system is continually monitoring cells and tissues to remove abnormal or damaged cells.	Cancer cells can evade the immune system through three mechanisms: lack of tumor antigen recognition, resistance to cell death, and secretion of immunosuppressive factors.

Table 2. Major differences between normal and cancer cells[68–70].

Although all these characteristics give us a better idea of what cancer is, it is important to know that cancer is not a single disease, and these principles may vary depending on the type of cancer[70]. All these differences, together with genome instability heterogenicity, make cancer a difficult disease to understand and a challenge for current researchers.

1.4.1. Cancer treatment

Currently, there are several therapies and drugs for the treatment of cancer. The types of treatment depend on the location of cancer, its size, whether or not it has metastasized and the general health of the patient. The main goal of treatments is to kill tumor cells producing the fewest possible side effects for best results. For this reason, treatments are usually administered as a combination of different approaches. However, there are various factors (e.g., lack of selectivity of treatments against cancer

stem cells, drug resistance, tumor heterogenicity, among others) that make most of the current therapies unsatisfactory[71].

1.4.1.1. Surgery

Surgery is one of the main treatments for many types of cancer. It is a procedure that consists of the removal of the tumor from the body of patients, and it can be used to prevent, diagnose, stage, and treat cancer[72,73].

This strategy is the most effective treatment when the cancer is localized in only one part of the body due to the complete removal of the tumors. In this case, this type of surgery is called "curative" and is usually the primary treatment along with chemotherapy or radiotherapy. However, it is possible that some tumors develop unnoticed micrometastasis in places distant from the primary tumor even after surgery. Therefore, the probability of relapse always exists.

Palliative or prophylactic surgery may be performed to improve the life quality of people to treat problems caused by advanced cancer or removing tissues that can become in cancer, respectively. For example, in peoples with mutated *BRCA1* and *BRCA2* genes, prophylactic mastectomy can be considered.

1.4.1.2. Radiation therapy

Radiotherapy is a cancer treatment that used high-energy radiation to destroy or damage cancer cells. Ionizing radiation is able to through tissues damaging the genetic material of the cells, which leads to their death. The main disadvantage of this approach is that radiation can affect both cancer cells and surrounding normal cells, resulting in unwanted side effects[74].

Radiation therapy can be administered through an external source of high-energy directly to the location of the tumor. Approximately 50% of patients have to receive radiotherapy during the development of the disease as the only treatment or in combination with others[75].

1.4.1.3. Chemotherapy

Chemotherapy is a type of cancer treatment that uses drugs to destroy tumor cells. Its main objective is to target cells that grow and divide very quickly, just as it occurs in

tumors. Ideally, anticancer drugs should be effective only in tumor cells. However, unlike surgery or radiotherapy, chemotherapy works throughout the body, and therefore can also affect healthy cells that divide rapidly, such as those of the skin, intestine, bones or hair. This is the leading cause of side effects derived from the treatment[76].

Since chemotherapy is used to stop or slow the growth of tumor cells, it can be administered for different purposes. As a treatment, it is used with the intention of "curing" cancer by completely removing the tumor, to prevent it from regrowing or to slow it down. In addition, it can be used to relieve cancer symptoms by trying to reduce its size[76].

Nowadays, chemotherapy is the most promising cancer treatment. However, on many occasions therapy can fail and most patients can develop metastases. This is related to the development of resistance to drugs by tumor cells. There are two different types of drug resistance: cells may be inherently resistant, possibly due to some genetic characteristics, or they may acquire resistance after exposure to the drug[77].

On the one hand, intrinsic factors involved in drug resistance include:

- Tumor heterogenicity within the tumor or between tumors that are in different places in the same patient. The existence of several subpopulations of tumor cells that contain various genetic aberrations explains the lack of response of these cells to drugs and leads to a poor prognosis[77].
- Tumor microenvironment, which favors cell proliferation and survival. Have an essential role in drug resistance through different mechanisms such as hypoxia, extracellular acidity, vascular abnormalities, changes in immune populations, extracellular matrix, and other soluble factors, including cytokines and growth factors[78].
- Cancer stem cell populations have been identified in many tumors. These cells have unique properties that make them resistant to chemotherapy and allow tumor re-growth. These properties include: relative quiescence, drug resistance through the high expression of ABC (ATP-binding cassette) transporters, an active DNA repair capacity, and resistance to apoptosis[79].

On the other hand, cancer cells can become resistant to drugs during the administration of treatments by reducing the drugs' activity. The different defense mechanism by which tumor cells acquire drugs resistance is known as multi-drug resistance (MDR). Various mechanisms have been attributed to MDR (**Figure 11**), including[80,81]:

- The overexpression of ABC family transporters that enhance the drug efflux outside the cells. Overexpression of these transporters is thought to be caused by their exposure to therapeutic agents, and different endogenous tumor stimuli such as hypoxia, acidosis, free radical formation or glucose deprivation.
- Reduction of the absorption of drugs due to the decreased number of transporters.
- Inhibiting apoptosis mechanisms by deregulating genes that are involved in this pathway.
- Changes in metabolism of drugs due to alterations in enzymes involved in the processing of pro-drugs or their inactivation.
- Improvement of DNA repair mechanisms, since many chemotherapeutic agents cause DNA damage in cancer cells.
- Drug compartmentalization into lysosome, golgi, and secretory compartments for their subsequent expulsion from the cells.

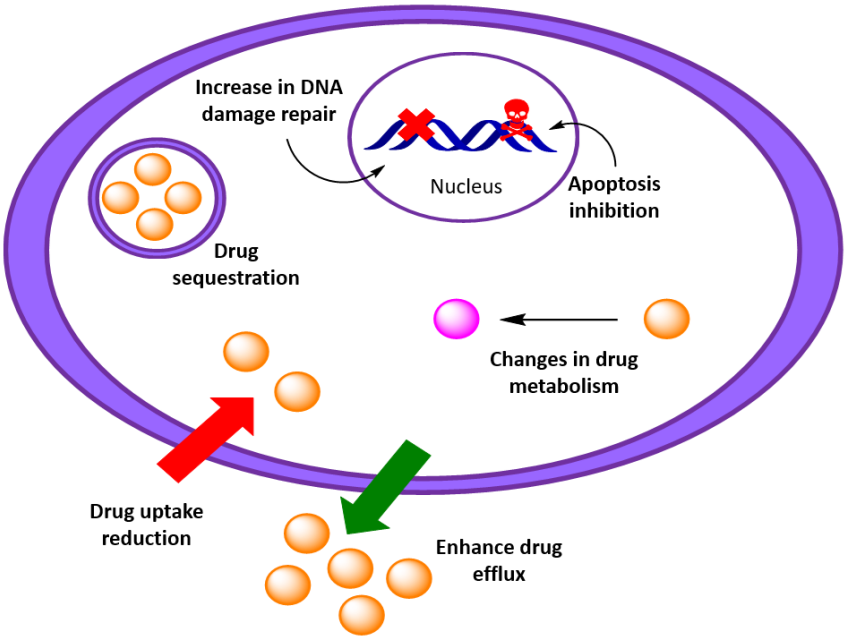

Figure 11. Schematic representation of MDR mechanisms in cancer cells after the exposure of the drugs by increasing drug efflux outside the cells, reducing the drug uptake, changing the drug metabolism, increasing the DNA damage repair systems and sequestering the drugs in different compartments.

MDR is one of the most significant challenges in cancer treatment research. Currently, the standard approach employed to overcome resistance is the use of high doses of drugs. However, it is generally ineffective, producing substantial toxic effects and even, the resistance is further stimulated[82]. Therefore, cancer therapies have been modified to overcome this phenomenon by studying novel drug combinations with various mechanisms of action (combination therapy) to treat the same tumor. The main objective of combined therapy is to achieve therapeutic synergy between drugs, increasing the options of eliminating tumor cells by different pathways[83].

There are many chemotherapeutic drugs that are currently being used for cancer treatment. They can be classified into different groups depending on their mechanism of action:

- Antimetabolites: are employed to replace natural substances involved in critical processes. For instance, they block nucleic acid synthesis by interfering metabolic routes or substituting the natural metabolite, leading to cell death. Examples of antimetabolites are folic acid antagonists (methotrexate), purine antimetabolites (6-mercaptopurine or pentostatin), and the pyrimidine antimetabolites (5-fluorouracil and gemcitabine)[84].
- Genotoxic agents: they can damage DNA or interfere with enzymes involved in its synthesis, leading to cell death by apoptosis. This group may be subdivided into three more groups. These include (i) alkaline agents like cyclophosphamide that modifies the bases of DNA interfering with replication and transcription process, (ii) intercalating DNA agents like doxorubicin, and (iii) enzyme inhibitors like irinotecan, which block replication[77].
- Mitotic spindle inhibitors (e.g., paclitaxel), which prevent the microtubule formation and, therefore, the cell division process[85].

1.4.1.4. Targeted therapy

It is a type of cancer treatment that “target” particular genes or proteins that control how cancer cells grow, divide, and spread. As previously describe, most cancer treatments are not selective and affect both normal and tumor cells. The main objective of this type of therapy is to act more precisely on tumor cells, avoiding normal ones to minimize side effects[86].

However, not all cancers are the same. Some types of cancers have proteins or enzymes that can be exploited to develop new drugs that specifically target changes or substances in cancer cells. These drugs usually block signals to stop cancer cells from dividing and eventually send them signals to activate death mechanisms. For this reason, targeted therapy can be called “personalized medicine”. Even among people with the same type of cancer, tumor cells can have different genetic characteristics, so they are usually analyzed to find the best type of drug target to make the therapy more effective[87].

Targeted therapy is classified into two groups, including small molecules inhibitors or monoclonal antibodies.

- Small molecules inhibitors can translocate the cell membrane and reach the cytoplasm of cells. These molecules are generally designed to inhibit or block enzyme activity by targeting a specific substance within the cell that is mutated or overexpressed in tumors[88].
- Monoclonal antibodies are proteins produced in the lab. Their use is related to the fact that many tumors overexpress certain receptors compared to normal cells. These antibodies can recognize a specific target in a cancer cell, bind to it, block its activation and eventually generate cytotoxicity. One of the most studied examples is the HER family of receptor proteins, associated with tumorigenesis and poor prognosis. The successful development of a humanized monoclonal antibody in the treatment of breast cancer that overexpresses the HER2 receptor suggested that the identification of different targets may be a key point for optimal achievement of effective drugs[89].

  Monoclonal antibodies can also be conjugated with drugs (ADCs) to deliver toxic molecules to target tumor cells in a highly selective manner, and with high cytotoxicity[90].

Despite advances in targeted therapy, the complexity of cancer biology can cause cells to become resistant, making these therapies not entirely successful.

1.4.1.5. Gene therapy

It is a type of treatment whose main objective is to deliver genes in damaged cells to produce a therapeutic effect, such as the correction of abnormalities or the activation of the immune response against cancer cells. This includes the replacement of missing or defective genes such as tumor suppressor genes, inactivation of oncogenes or reprogramming of cancer cells[91]. Among the different strategies most studied in recent years include RNAs interference (RNAi) and the gene-editing CRISPR/Cas system. On the one hand, RNAi is capable of gene silencing in a specific sequence by cleavage the messenger RNA from cells, allowing a precise modulation of the gene expression[92]. On the other hand, the experimental genetic editing technique CRISPR/Cas system allows the modification of the genomic sequence of cells and organisms and the introduction of epigenetic and transcriptional modifications[93].

One of the big challenges in gene therapy is to deliver an adequate amount of genetic material into target cells and to maintain their expression for a desired period of time. There are different genetic carriers (vectors), that can be used, and finding the correct one is crucial for successful gene transfer. Among the various possibilities are physical methods such as electroporation or ultrasound, viral vectors such as lentivirus or adenovirus, non-viral methods such as nanoparticles, and bacterial methods such as bactofection. These vectors must reach as many target cells as possible and express the introduced genes efficiently for the appropriate time. For this reason, they must be stable and have a successful targeting. In addition, the vector's safety is a primary issue to be considered for the success of the treatment [91,94].

Viral vectors are the most studied carriers in gene therapy because of their natural ability to deliver genes. These viruses can be modified in the laboratory to make them not infectious in people[95]. However, there have serious safety concerns related to immunogenicity and mutagenesis. In addition, the low packaging capacity and high production cost have also limited its clinical applications. For these reasons, non-viral vectors using different types of nanomaterials are increasingly attracting attention as a safe alternative to viruses[96].

1.4.1.6. Immunotherapy

Immunotherapy is a type of treatment that uses a person's immune system (e.g., by stimulating it), to increase its defenses and fight cancer[90]. There are different types of immunotherapy to treat cancer.

- Checkpoint inhibitors: they are drugs that work by blocking immune checkpoints, which ensure that the immune system is not continuously activated, leading to autoimmune damage to healthy tissues. By blocking them, these drugs allow immune cells to respond more strongly to cancer[97,98].
- T-cell therapy: is a treatment that improves your own cells of the immune system to attack the tumor. T cells are collected from the patient, and modified in the laboratory to better recognize tumor cells. Once cultivated, they are injected back into the patient's body to fight cancer[99,100].
- Monoclonal antibodies: They are immune system proteins made in the laboratory to bind to specific targets on cancer cells. They work by marking tumor cells so that the immune system can recognize and destroy them[101,102].

Since the immune system can remember and attack tumor variants, immunotherapy is an advantage over other therapies. However, this type of treatment does not work in all types of tumors and patients. In addition, the search for new combinations of drugs to overcome resistance to immunotherapy is necessary[97,103].

1.5. Cancer and nanomedicine

The application of nanotechnology in medicine is called nanomedicine (see above, section **1.3.1**). It used the unique properties of the materials at nanometric scale to develop new tools with huge potential for the detection, diagnosis, and treatment of diseases such as cancer.

As we have seen in the previous section, current chemotherapy treatments often produce side effects because of their lack of selectivity. However, nanoparticles can be employed to differentiate between tumoral and normal cells, thus reducing the toxicity of drugs. This can be accomplished by encapsulating drugs within nanoparticles, or conjugating them on their surface. Since most nanoparticles are synthesized in the

laboratory, they can be modified to have the desired properties depending on the desired application.

Besides the selective delivery of drugs, nanoparticles, can also be used to diagnose tumors as imaging agents. Current diagnostic methods are poorly able to detect tumors at an early stage, so nanoparticles as contrast agents can help to significantly improve existing cancer diagnosis and treatment methods. Among the different imaging mechanisms, magnetic resonance imaging (MRI) is the most commonly studied technique, and magnetic nanoparticles, as contrast agents, are the most widely used. The use of these nanoparticles can increase biocompatibility, selective accumulation in tumor cells, and reduce toxicity[104].

Multifunctional nanoparticles are one of the innovations with the most significant potential in this field of research. Because nanoparticles are larger than most conventional drugs, they can incorporate several active molecules into the nanostructure at the same time. An example of this, is its use for simultaneous diagnosis and therapy. This dual-purpose targeted research is called theranostics, which means that an anticancer drug and an imaging agent are combined simultaneously into the same nanoparticle to treat the tumor[105].

Nanoparticles may also be used to deliver of biological materials to cancer cells, like nucleic acids, which are highly unstable in the systemic circulation and sensitive to degradation. These include plasmid DNA and RNA-based gene therapies, such as small interfering RNAs (siRNAs) and microRNAs (miRNAs). They are often used to provide a copy of a defective gene to patients, or to block proteins involved in tumor development, respectively. These therapies can be administered encapsulated or conjugated to the surfaces of the nanoparticles, and significantly prolong their half-life[106,107].

1.5.1. Advantages of drug delivery systems for cancer treatment

Several properties of the nanoparticles make them suitable for administering chemotherapeutic drugs to the target tumor tissue. Like most chemotherapies, small molecule drugs are broken down or eliminated from the body in a short time, so higher doses of these drugs are necessary. Interestingly, nanoparticles modified with the drugs

can circulate longer, thus improving the drugs' bioavailability and the efficacy of treatments[108]. Furthermore, they make it possible to control the release of the payload once its target tissue has been reached. These properties can improve the effectiveness of treatments while reducing side effects[109].

1.5.1.1. Improved internalization in tumors

The size, shape and surface are key parameters of the nanoparticles that have to be considered to develop therapeutic systems for the different types of tumors. For these reasons, different techniques can be used to evaluate these parameters:

- Scanning electron microscopy (SEM): this technique is based on collecting electrons and photons of the surface of the materials to create an image. SEM provides an image of the morphology of the samples analyzing their surface. Particles of around 20 nm can be observed using this technique[110].
- Transmission electron microscopy (TEM): unlike the previous case, transmission electron microscopy is based on the collection of transmitted electrons through the sample, although some of this microscope can also detect the signal that SEM generates (scanning transmission electron microscope (STEM)). TEM provides information about nanoparticles size and size distribution of the samples. Particles of around 1-2 nm can be observed using this microscope[111,112].
- Atomic force microscopy (AFM): in this technique, a tiny tip is moved up and down over a surface following an x-y pattern. Individual particles and groups can be observed in three dimensions providing an image of the size, distribution and geometrics of the materials. The main advantage compared with SEM and TEM is that no additional pretreatment is required to visualize the samples. Besides, electron microscopy techniques need a vacuum environment, while AFM can be used in ambient conditions[113,114].
- Dynamic light scattering (DLS): it is a widely used method to characterize the behavior of nanoparticles in solution which are moving randomly in all directions (Brownian motion). Smaller nanoparticles are moving at a higher speed than larger nanoparticles. A light laser from the instrument is sent directly to the sample containing the nanoparticles. This light is scattered in all directions, depending on their size and shape. The fluctuations intensity of the scattered light is measured by

a detector to determine the diffusion coefficient (Dτ), which is related to the hydrodynamic size of the nanoparticles by the Stokes–Einstein equation[115].

In addition, another widely used technique to determine the surface charge of the nanoparticles is the zeta-potential. These values provide an indirect measurement of the net charge of the nanoparticles dispersed in a liquid and can be used to determine the tendency of the particle to aggregate in the aqueous medium.

Knowing these parameters is crucial to understand better the cellular uptake and toxicity of nanoparticles in biological systems.

The size of the nanoparticles has a significant impact on the biodistribution and, particularly, in the accumulation in the tumor tissue. The optimum size should be approximately 100 nm, and their optimization can help improve specific absorption in tumor tissue. Nanoparticles smaller than 200 nm can extravasate and accumulate easier than larger nanoparticles in solid tumors[116,117]. This is because the vasculature in solid tumors is hyperpermeable, immature, irregular, and leaky. Also, in normal tissues the intracellular openings between endothelial cells in the blood vessel wall are less than 10 nm. However, in tumor tissues, they can be hundreds of nanometers in size. In addition, venous return is reduced and functional lymphatic vessels decrease, allowing nanoparticles to stay longer in the tumors. Together, these particularities allow nanoparticles with sizes greater than 10 nm to be extravasated and accumulate in the tumor, but not to healthy tissues, making treatments more selective and effective while reducing side effects (**Figure 12**). This phenomenon is known as the enhanced permeability and retention (EPR) effect[118,119].

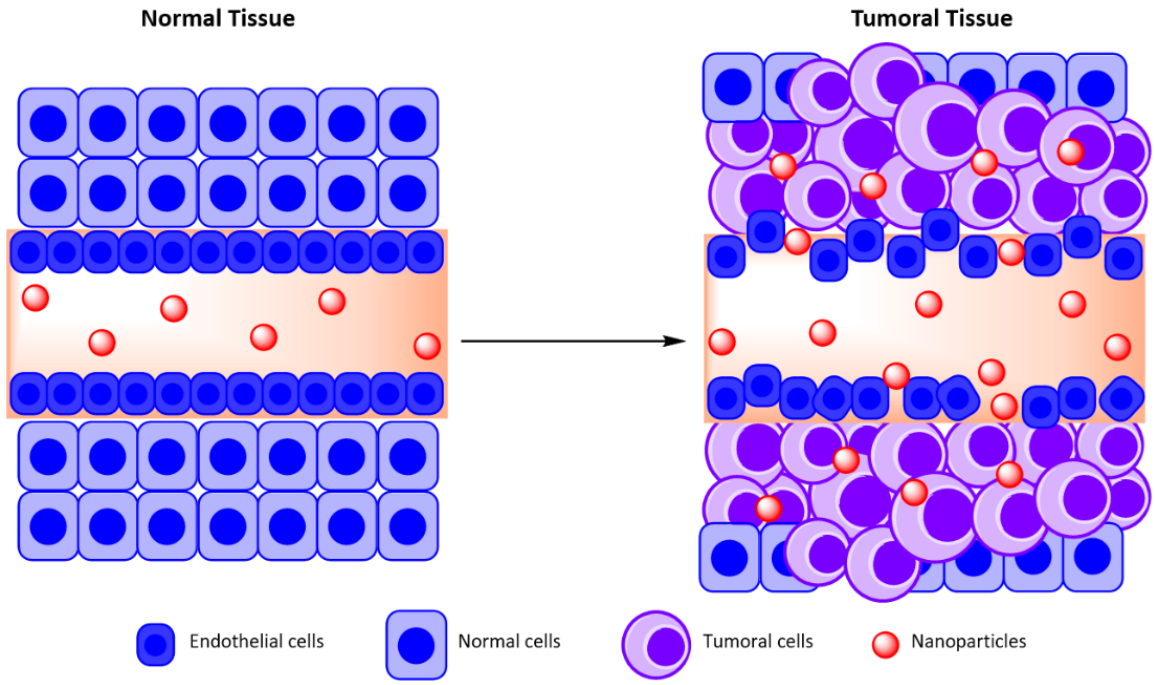

Figure 12. Schematic representation of the enhanced permeability and retention (EPR) effect of nanoparticles in solid tumors. The new tumor vessels have an abnormal space between endothelial cells and lack adequate lymphatic drainage compared to normal tissues, allowing nanoparticles of a size greater than 10 nm to be accumulated in the tumor.

The shape plays an essential role in the toxicity of nanoparticles. Spherical ones generate less toxicity in the endocytosis process than non-spherical ones due to the internalization mechanisms of the cell membrane. Furthermore, the shape of nanomaterials can affect their circulation time, biodistribution, and cellular uptake[120,121].

Finally, the surface charge and hydrophobicity affect the colloidal stability, cellular uptake mechanism and toxicity of the nanoparticles. On the one hand, positively charged nanoparticles internalize better into cells than negatively charged and neutral nanoparticles, but they are more toxic[120]. On the other hand, while positively charged nanoparticles are internalized mainly by a mechanism of micropinocytosis, negatively charged ones are usually internalized by caveolae/clathrin-dependent mechanisms. Remarkably, the surface of nanoparticles can be modified in laboratories with molecules that can make them more stable in blood circulation and targeted at tumor tissues[20,122].

1.5.1.2. Improved solubility and protection from degradation

Drugs with poor water solubility and permeability can be eliminated from the bloodstream before reaching tumor tissue. In this regard, the use of nanoparticles to encapsulate or conjugate drugs can increase the solubility of these drugs and improve their bioavailability[123]. In the case of solubility, small drug-loaded nanostructures have better interaction with the solvent, increasing its solubility[124].

The reticuloendothelial system (RES) recognizes hydrophobic nanoparticles as foreign and removes them from the bloodstream through the liver or spleen. Furthermore, these nanoparticles can be coated with serum proteins (opsonization) and recognized by cells of the immune system, which can trigger an inflammatory response and reduce the number of nanoparticles that can reach the tumor[125]. The most common strategies to avoid this immune recognition and nanoparticle removal include surface modifications, self-peptides, and cell coatings. These modifications increase the half-life of the nanoparticle and improve its bioavailability by allowing the drug to circulate in the blood for a longer time, avoiding degradation before reaching the tissue of interest[126]. For example, modifications into the surface of the nanoparticles with different polymers such polyethyleneglycol (PEG) and polyzwitterions increase their circulation time, or with the CD47 peptide preventing their recognition by the immune system[127].

1.5.1.3. Enhanced selectivity

Nanoparticles should be designed to specifically target, recognize, bind, and deliver drugs to the tumor to minimize damage from treatments to healthy tissue. In this regard, nanoparticles can be modified to use passive and active targeting mechanisms to increase the concentration of drug in the tumors. The enhanced permeability and retention effect (EPR), described above, is considered a passive mechanism, where nanoparticles accumulate in the tumor based on their size and without any surface modification[128]. However, active targeting requires the modification of nanoparticles with specific surface ligands that target the tumor microenvironment, such as folic acid[129], engineered antibodies[130], aptamers[131], proteins[132] or carbohydrates[133]. These ligands have high specificity for molecules (e.g., receptors) that are overexpressed on the surface of tumor cells (**Figure 13**). This interaction induces the accumulation of

nanoparticles mainly at the tumor site, increasing the internalization of the nanoparticles by ligand-mediated endocytosis. In addition, this process can also bypass drug flow pumps (e.g., MDR1), thereby overcoming drug resistance mechanisms (MDR)[104,134].

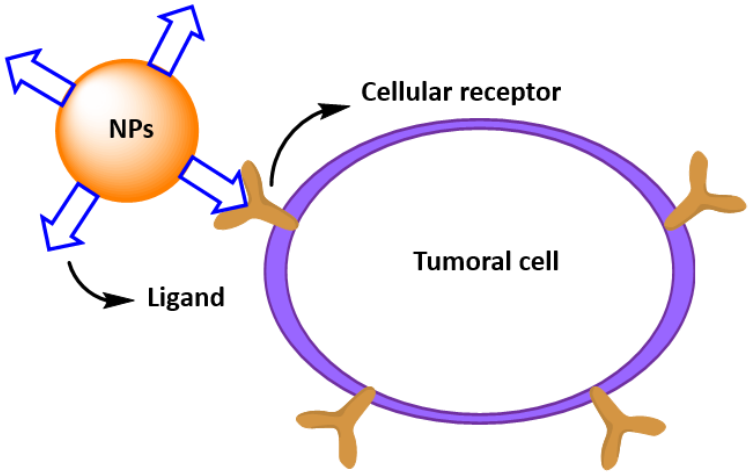

Figure 13. Schematic representation of targeting nanoparticles (NPs) delivery to tumoral cells. The surface of the nanoparticles is modified with a ligand that can recognize receptors overexpressed in cancer cells.

1.5.1.4. Controlled drug release systems

Another approach to increase the efficiency of the therapies is by controlling the release of the drugs from the nanoparticles at the tumor site[135]. These approaches can reduce the exposure of healthy tissues to chemotherapeutics, since the drugs are mainly released in the presence of specific stimuli at the tumor.

There are internal and external stimuli that can be used as triggers. In the case of internal stimuli, they depend on the different characteristics between normal and tumoral cells to trigger the release of drugs, such as different pH, glutathione concentration and enzyme levels. On the other hand, external stimuli are usually physical triggers, such as magnetic fields, light and ultrasound. Interestingly, the duration and strength of external stimuli can be controlled compared to the internal ones, which is advantageous in several cases.

1.5.2. Types of nanoparticles for drug delivery

A wide variety of nanoparticles have been developed in medicine for cancer treatment. Some examples are briefly described below.

1.5.2.1. Lipid-based nanoparticles

Lipid-based nanoparticles are those whose matrix is formed by lipids, which can be of natural or synthetic origin. Based on the organization of lipids in the nanoparticles, a wide variety of structural models have been described (e.g., liposomes, nanostructure lipid carriers and solid lipid nanoparticles)[136].

These nanostructures are being widely used to treat cancer, since they have great advantages such as high stability, high loading capacity and ease of preparation. Moreover, they are capable of releasing drugs that can be hydrophilic or hydrophobic in a controlled way. In this sense, they are used to improve the solubility and bioavailability of molecules that are not very soluble in water[137].

1.5.2.2. Dendrimers nanoparticles

Dendrimers are branched synthesized macromolecules with a tree-like structure and specific shape and size. They usually consist of a centric core, repeated building units attached to the core, and functional groups on the surface. They are monodispersed and have well-defined chemical structures. Dendrimers nanoparticles have great potential as a drug delivery system, mainly due to their unique molecular architectures that confer them flexibility, multifunctional capabilities, and ease of surface modification with multiple active agents, either covalently or by electrostatic adsorption[138].

1.5.2.3. Metallic nanoparticles

Metallic nanoparticles (e.g., gold or iron) offer numerous opportunities in the treatment of cancer, including drug delivery, tumor diagnostic, improved radiation therapy, and thermal ablation. This is due to their unique properties such as a strong electromagnetic field on its surface, wide optical properties depending on its size, shape and composition. Furthermore, these nanoparticles can be obtained easily and modified conveniently with a variety of molecules like small drugs, antibodies or nucleic acids[139]. Despite of that, this type of nanoparticles can be used unmodified for therapeutic or imaging purposes due to their inherent properties.

1.5.2.4. Carbon nanotubes

Carbon nanotubes are cylindrical tubes made of carbon atoms. They are widely studied as biomolecule transporters, such as genes, proteins and small drugs for the treatment

of cancer[140]. Their most significant advantage is that they can directly enter the cytoplasm of cells by different internalization mechanisms and are not only dependent on the endocytosis pathway[141]. They are also being investigated as mediators for photothermal therapy (PTT) and photodynamic therapy (PDT) to destroy cancer cells[142]. However, they have low solubility in water and for this reason, they need to be electrostatically or covalently modified with polymers, proteins or nucleic acids to improve their solubility in water[143].

1.5.2.5. Protein nanoparticles

Protein nanoparticles are non-toxic, biodegradable, easily metabolizable, and have good biocompatibility. These nanostructures can interact with hydrophilic and hydrophobic drugs and even solvents[144], due to their amphiphilic nature. Interestingly, the presence of available reactive groups on its surface makes proteins susceptible to chemical modification. Therefore, protein nanoparticles can be covalently or non-covalently linked with one or different molecules[145].

They can be synthesized from different types of proteins, but one of the most common is albumin. It is an essential soluble protein in the circulating system and is involved in maintaining osmotic pressure and the binding and transport of nutrients to cells. It is stable in the pH range of 4 to 9, and many endogenous molecules and drugs are known to bind to albumin and can be transported. These albumin nanocarriers are biodegradable, easy to prepare, have homogeneous sizes and reactive functional groups on their surface (e.g., -SH, NH_2 and CO_2H) that can be used for the covalently binding of different active molecules[144,146].

1.5.3. Smart nanoparticles as drug delivery systems

As described before, the systematic administration of antitumor agents might affect both normal and tumor cells, which leads to unwanted side effects. The development of efficient treatments that allow the reduction of these adverse effects is a critical point in current research to improve the quality of life of patients.

In this regard, the design of multifunctional nanoparticles for cancer treatment, also known as smart nanoparticles, has potential advantages over conventional treatments. Smart drug delivery systems are composed of nanoparticles containing antitumor

agents, ligands that target the drugs mainly to the tumor site and stimuli-responsive techniques that release the drug in the cancer cells. These properties can allow a decrease in the amount of the drug that must be administered, and therefore potentially reduce the side effects of the treatments[147].

An illustration of an ideal smart drug delivery system is represented in **Figure 14**. These nanoparticles are versatile systems that can be modified with different molecules and carry out distinct functions simultaneously. For example, nanoparticles can bear various drugs, for combination therapies, imaging agents, to localize the tumor, targeting moieties, to increase the selectivity, and stealth agents like PEG to prevent their clearance.

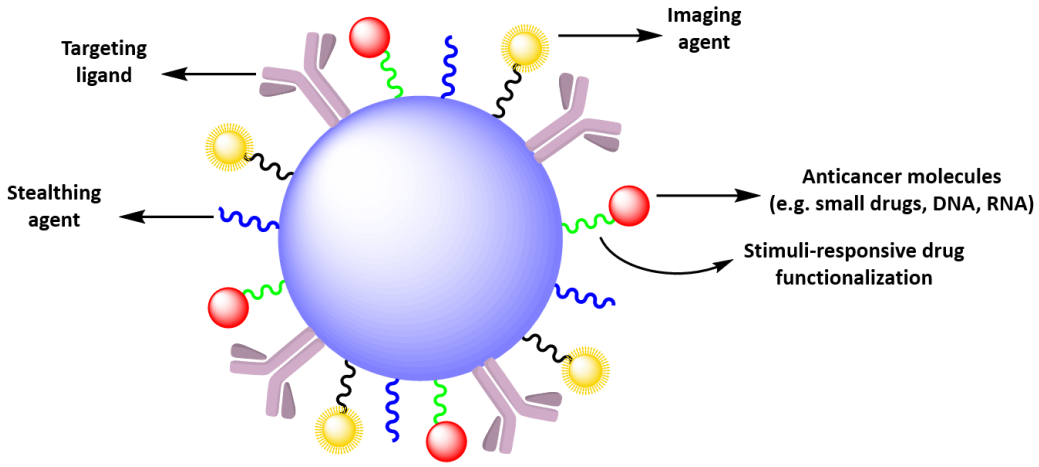

Figure 14. Schematic representation of an ideal smart drug delivery system containing different active molecules.

1.5.4. Current challenges of nanoparticles for drug delivery

Despite all the advantages of using nanoparticles as drug delivery systems, designing effective nanomedicines remains a major challenge. Many thousands of nanoformulations have been evaluated over the years, and only about 50 have reached the market[148].

One of the biggest challenges in using nanoparticles is their toxicity. In this sense, a new branch of nanomedicine, "nanotoxicology", has emerge to evaluate all the parameters related to nanoparticles' toxicity[149]. The biocompatibility and toxicity of nanoparticles in biological systems are strongly related to their physicochemical properties. Therefore, the synthesis and characterization of nanomaterials are vital factors to avoid the

possible unwanted toxicity of nanoparticles to healthy tissues. In this regard, particle size distribution and shape, state of aggregation, purity, solubility, surface reactivity, among other parameters, should be considered in the toxicological profile of nanoparticles[150].

Besides, evaluation in cell cultures is crucial to identifying biocompatible candidates before testing on animals. However, cultured cells growing in monolayers are simplified models that lack the complexity of biological systems, making the *in vitro*/*in vivo* correlation of drug release profiles a significant challenge. In this regard, it is worth mentioning that in the blood circulation, there are a large number of biomolecules and proteins that can interact with nanomedicines, making them ineffective for treating the tumor[151].

Another critical limitation in the use of nanoparticles in biomedicine is their production on a large scale. In addition to the scalability of the process, the batch-to-batch variability is another essential factor to consider. Furthermore, production processes can be long and complicated and require high-cost materials, so the clinical benefit of using these nanoparticles has to justify the costly manufacturing process[152]. The storage and stability of nanoparticles over time are also crucial factors that can influence their pharmacological performance[153].

Hypothesis and Objectives

2. HYPOTHESIS AND OBJECTIVES

Conventional chemotherapy treatments have been found to have several limitations, such as the development of multidrug resistance, high cytotoxicity, and a non-selective biodistribution of drugs. On the other hand, the current methods used for CRISPR/Cas system-based gene editing do not allow effective systemic administration, which may limit their therapeutic application.

In this sense, the use of nanoparticles in medicine (nanomedicine) is increasingly used to treat different diseases such as cancer, since it offers significant advantages over conventional therapies, such as improving the solubility and biodistribution of drugs, among others. Therefore, the effectiveness of the treatments increases while reducing their undesirable side effects.

Hence, we hypothesize that the development and use of new biodegradable and non-toxic vehicles based on albumin nanostructures and modified carbon nanotubes with a controlled release mechanism can be used to deliver drugs, nucleic acids and proteins.

In particular, these nanostructures can be functionalized with drugs to treat breast cancer, such as doxorubicin (DOX) and 7-ethyl-10-hydroxycampothecin (SN38), inhibitors of topoisomerase II and I, respectively. Also, with AZD8055, an inhibitor of mTOR complex used in the treatment of uveal melanoma. Furthermore, these nanostructures can be used to efficiently transport the CRISPR/Cas system to cells for gene-editing.

Specifically, during my doctoral thesis, two lines of research were initiated with the following objectives:

I. **Objective 1**: Development of albumin-based nanostructures for the transport of anticancer drugs for breast cancer and uveal melanoma. The cytotoxic potential of these nanoparticles will be evaluated in established cell lines *in vitro* and in *in vivo* models.
II. **Objective 2**: Development of modified carbon nanotubes and new albumin nanocomplexes for the transport to cells of a functional CRISPR/Cas9 plasmid and the CRISPR-Cpf1 protein, and its subsequent evaluation as a gene-editing system.

Materials and Methods

3. MATERIALS AND METHODS

3.1. General methods

3.1.1. Particle size and zeta potential measurements

The size and zeta potential of nanostructures were determined using a Zetasizer Nano (Malvern). The measurements were performed at 25 °C at a 173° scattering angle using disposable microcuvettes. The Z-Average hydrodynamic diameter, polydispersity index (PDI), and zeta potential were obtained by three cumulative analyses.

3.1.2. Cell Culture

3.1.2.1. Cell lines

The cell lines used in this work and its culture methods are described below.

All the cells were tested periodically for mycoplasma contamination, after growing them in antibiotic-free media for at least two weeks[154].

3.1.2.2. Maintenance and amplification

The cell lines MCF-7, MDA-MB-231, Panc-1, Sp6.5, HaCaT keratinocytes and HEK293 were grown as monolayer cultures in Dulbecco's modified Eagle's medium (DMEM, Biowest) supplemented with 10% (*v/v*) fetal bovine serum (FBS, Biowest), 1% L-Glutamine (Biowest), 1% Penicillin/Streptomycin (Biowest). However, Mel202 and OMM1.3 cells were cultured in RPMI1640 medium (Biowest) supplemented with 10% (v/v) fetal bovine serum (FBS), 2mM L-Glutamine and 1% Penicillin/Streptomycin. All the cells were incubated at standard conditions 37 °C in an atmosphere of 5% CO_2.

Cells were observed every two-three days using an inverted optical microscope. Cells were sub-cultures once 80-90 % confluency was reached. To sub-culture the cells, the cell media was removed and cells were washed with 5 mL of PBS 1X (Biowest). Then, Trypsin-EDTA 1X solution (2 mL) was added and incubated at 37 °C for 2-5 minutes to detach the cells from the culture plates. After that, the cells were resuspended in the appropriate amount of complete growth and a proportion of the suspension of cells were added to a new culture pate to achieve a 1:5 – 1:15 dilution depending on the growth rate of the cell line. More medium was added to the culture plate to reach a volume of 10 mL. The culture plate, was then incubated at standard conditions (37 °C in an atmosphere of 5% CO_2).

3.1.2.3. Freeze/Thaw cells

To preserve the cells, they were stored in liquid nitrogen, once they were prepared as follows. Trypsinized cells were counted in a hemocytometer and resuspended in the appropriated amount of fetal bovine serum (FBS) containing 10 % dimethyl sulfoxide (DMSO, Sigma-Aldrich), which is a cryoprotective agent to get 2 x 10^6 cells per milliliter. Then cells were aliquoted and frozen in cryovials (Thermo Fisher). These vials were placed into an isopropanol chamber to freeze them down in a -80 °C slowly (1 °C/min).

On the contrary, thawing frozen cells had to be a quick process (less than 1 minute) using a 37 °C water bath swirling the cryovial. Then, cells were added dropwise into a 15 mL falcon tube containing 5 mL of pre-warm complete medium (10% FBS) and centrifuge 5 minutes at 1000 rpm. The supernatant was carefully discarded, and the pellet was resuspended in 10 mL of complete medium, providing the cells without the DMSO used in the freezing process. Finally, the thawed cells were plated at high density to ensure recovery into T75 culture flask. This flask was incubated at standard conditions 37 °C in an atmosphere of 5% CO_2.

3.1.2.4. Preparing cells for the experiments

Cells were trypsinized (see method **3.1.2.3**) and counted using a hemocytometer as indicated by the manufacturer. The appropriate volume of medium containing the desired number of cells was seeded into new culture well-plates. Seeding density depended on the surface area of the wells and cell lines.

3.1.2.5. Cytotoxicity Assays

Cells were seeded 24 hours before treatment in 24 well-plates under standard conditions (37 °C, 5% CO_2). Each nanostructure-treated sample was seeded and assayed at least in triplicates).

3.1.2.5.1. MTT tetrazolium reduction assay[155]

Cells were incubated with the corresponding nanostructures in complete growth media for 24 hours at standard conditions (37 °C, 5% CO_2).

After incubation, the culture medium was removed, and cells were washed twice with PBS 1X and cells were incubated 48 hours more after treatment. Then, toxicity was

evaluated using the MTT (dimethylthiazolyl-diphenyl-tetrazolium bromide, Sigma-Aldrich) colorimetric assay as follows. The culture growth medium was replaced with fresh medium containing MTT (5 mg/mL). Five hundred microliters of this MTT solution (50 µg/mL MTT in culture medium) was added to each well, and cells were incubated for 4 hours at 37 °C, 5% CO_2. Then, MTT was removed by aspiration and the reduced formazan crystals obtained during the incubation were dissolved in 500 µL of DMSO and the absorbance measured at 540 nm using a microplate reader (Synergy H4, Biotek). The surviving fraction was expressed as the percentage of absorption of treated cells in comparison with control cells. Data corresponded to mean values ± standard deviation from at least five different experiments.

3.1.2.5.2. Resazurin reduction assay[155]

As described above, cells were incubated with the corresponding nanostructures in complete growth media for 24 hours at standard conditions (37 °C, 5% CO_2).

After incubation, the culture medium was removed, and cells were washed twice with PBS (pH = 7.4). The cell culture medium was replaced with fresh medium containing 1% of resazurin (Sigma-Aldrich) solution (1 mg/mL in PBS 1X), and cells were incubated for 3 hours more at 37 °C, 5% CO_2. Then, 100 µL of the culture media with the reduced resazurin was placed into fluorescence 96 well-plates, and the fluorescence was measured using a microplate reader (λ_{exc} = 550 nm, λ_{em} = 590 nm). The fluorescence was measured 24, 48, and 72 hours after treatment. Cell viability was expressed as a percentage of fluorescence of treated cells and compared with the control. The data obtained correspond to mean values ± standard deviation from at least three different experiments.

3.1.2.6. Statistical analysis

Results were presented as the mean ± standard deviation (SD).

For statistical calculation, data were analyzed by one-way analysis of variance (ANOVA) in R Commander Software. When statistical differences are observed (p-values < 0.05 (*), <0.01 (**) and < 0.001 (***)), Tukey's Test was performed to compare the mean values by pairs.

3.2. Albumin-stabilized gold nanoclusters functionalized with AZD8055 (BSA-AuNCs-AZD) for uveal melanoma treatment

3.2.1. Synthesis of intermediates and pro-drugs

The products described in this section were prepared by postdoctoral researchers from the group.

^{1}H and ^{13}C NMR spectra of intermediates were recorded on a Bruker instrument (MHz indicated in brackets) in $CDCl_3$ at 300 and 75 MHz, respectively. All reactions were monitored by thin-layer chromatography (TLC) using precoated sheets of silica gel 60 F_{254}. The isolating process was done by flash column chromatography using silica gel 60 Å (230-400 mesh, Merck). Eluting solvents are indicated in the text.

3.2.1.1. AZD8055 modified with a redox-sensitive linker (AZD-PySS)

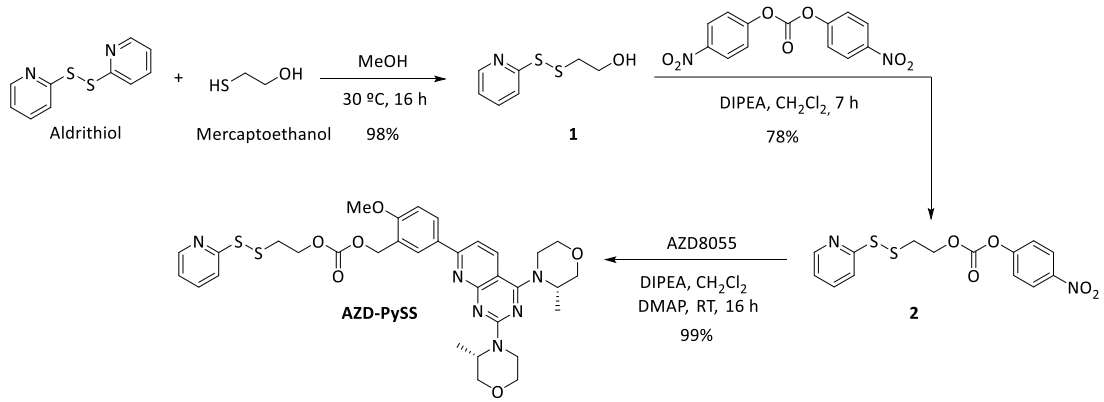

3.2.1.1.1. Synthesis of 2-(pyridin-2-yldisulfanyl)ethanol (1)[156]

To a solution of aldrithiol (500 mg, 2.3 mmol, Sigma-Aldrich) in MeOH (2.5 mL, Scharlab) under Ar, 2-mercaptoethanol (89 µL, 1.27 mmol, Sigma-Aldrich) was added slowly and stirred for 16 hours. Then, the solvent was evaporated in vacuum and the residue purified by flash chromatography (Hexane/AcOEt 1:1) to obtain compound **1** as a colorless oil in 98% yield. **^{1}H NMR (300 MHz, $CDCl_3$)**: δ = 8.51 (d, J = 4.3 Hz, 1H), 7.58 (td, J = 8.0, 1.7 Hz, 1H), 7.40 (d, J = 8.0 Hz, 1H), 7.17-7.13 (m, 1H), 5.72 (bs, 1H), 3.80 (dd, J = 10.4, 6.5 Hz, 2H), 2.97-2.94 (m, 2H).

3.2.1.1.2. Synthesis of 4-nitrophenyl 2-(pyridin-2-yldisulfanyl)ethyl carbonate (2)[156]

To a solution of compound **1** (234 mg, 1.25 mmol), and bis(4-nitrophenyl) carbonate (571 mg, 1.89 mmol, Sigma-Aldrich) in CH_2Cl_2 (4.8 mL, Sigma-Aldrich) under Ar, N,N-Diisopropylethylamine (DIPEA) (329 µL, 1.89 mmol, Sigma-Aldrich) was added and stirred for 7 hours at room temperature. The mixture was washed with water, and the organic phase dried with $MgSO_4$. After solvent evaporation, the residue was purified by flash chromatography (Hexane/AcOEt 3:1) to obtain compound **2** as a colorless oil 78% yield. **^{1}H NMR (300 MHz, $CDCl_3$)**: δ = 8.50 (d, J = 4.8 Hz, 1H), 8.28 (d, = 9.1 Hz, 2H), 7.72-7.59 (m, 2H), 7.38 (d, J = 9.1 Hz, 2H), 7.15-7.10 (m, 1H), 4.57 (t, J = 6.4 Hz, 2H), 3.16 (t, J = 6.4 Hz, 2H).

3.2.1.1.3. Synthesis of modified AZD8055 (AZD-PySS)

To a solution of compound **2** (81.1 mg, 0.23 mmol) and AZD8055 (70 mg, 0.15 mmol, MCF MedChem) in CH_2Cl_2 (2.5 mL) under Ar, DIPEA (40 µL, 0.23 mmol) and 4-Dimethylaminopyridine (DMAP) (5mg, 0.04 mmol, Sigma-Aldrich) were added at room temperature and stirred for 16 hours. Then, the solvent was evaporated and the residue was purified by flash chromatography (Hexane/AcOEt 1:8) to obtain compound **AZD-PySS** as yellow oil in 99% yield. **^{1}H NMR (400 MHz, $CDCl_3$)**: δ = 8.46 – 8.41 (m, 1H), 8.19 (dd, J = 8.6, 2.3 Hz, 1H), 8.13 (d, J = 2.3 Hz, 1H), 8.10 – 8.04 (m, 1H), 7.98 (d, J = 8.5 Hz, 1H), 7.67 (d, J = 8.1 Hz, 1H), 7.62 – 7.56 (m, 1H), 7.41 (d, J = 8.5 Hz, 1H), 7.06 (ddd, J = 7.3, 4.8, 1.0 Hz, 1H), 7.01 – 6.98 (m, 1H), 6.96 (d, J = 8.7 Hz, 1H), 4.40 (t, J = 6.5 Hz, 2H), 4.37 – 4.29 (m, 1H), 4.01 – 3.93 (m, 2H), 3.90 (s, 3H), 3.85 (dd, J = 11.4, 2.9 Hz, 2H), 3.80 – 3.62 (m, 5H), 3.54 (td, J = 11.9, 2.8 Hz, 1H), 3.40 – 3.29 (m, 1H), 3.08 (t, J = 6.5 Hz, 2H), 1.46 (d, J = 6.8 Hz, 3H), 1.33 (d, J = 6.8 Hz, 3H). **^{13}C NMR (101 MHz, $CDCl_3$)**: δ = 165.27, 162.72, 161.52, 159.83, 159.53, 159.35, 154.87, 149.67, 137.12, 134.69, 130.83, 130.02, 129.82, 125.94, 123.43, 120.91, 119.89, 116.10, 112.90, 110.56, 104.47, 71.25, 70.88, 67.21, 66.90, 65.36, 55.70, 52.79, 46.91, 44.33, 39.29, 37.18, 29.68, 14.70, 14.29. **MS (ESI) m/z (%)**: 679.2364 (100) $[M+H]^+$. **EMAR calculated for** $C_{33}H_{39}N_6O_6S_2$ 679.2367, **found** 679.2328 $[M+H]^+$.

3.2.2. BSA-stabilized gold nanoclusters (BSA-AuNCs)

3.2.2.1. Synthesis of BSA-AuNCs

To a solution of BSA (1 mL, 50 mg/mL) (Sigma-Aldrich) at 37 °C with constant stirring, hydrogen tetrachloroaurate (III) hydrate ($HAuCl_4$, Alfa Aesar) (1 mL, 10 mM) was added and stirred for 2 minutes maintaining the temperature at 37 °C. Then, 100 µL of NaOH (Scharlab) solution (1M) was added, and the mixture was stirred for 16 hours more at 37 °C. BSA-AuNCs were purified in PBS (Sigma-Aldrich, pH = 7.4) using an exclusion column NAP-10 of Sephadex-G25 according to the specifications of the distributor (VWR, http://www.gelifesciences.com) and stored at 4 °C.

3.2.2.2. Sulfhydryl activation of BSA-AuNCs

25 equivalents of 2-iminothiolane hydrochloride (Sigma-Aldrich) were added to a solution of 20 µM BSA-AuNCs (1 mL) in PBS (pH = 7.4) and incubated at room temperature for 16 hours. The product was purified using an exclusion column NAP-10 of Sephadex-G25 according to the distributor's specifications (http://www.gelifesciences.com).

3.2.2.3. BSA-AuNCs functionalized with AZD8055 (BSA-AuNCs-AZD)

A solution of modified AZD8055 (**AZD-PySS**) (1 mM, 5 equivalents) in DMSO was added to 1 mL of a solution of purified BSA-AuNCs (20 µM) in PBS (pH = 7.4), and stirred at room temperature for 16 hours. Finally, after purifying the BSA-AuNCs-AZD using a NAP-10 column of Sephadex-G25, the concentration of BSA-AuNCs was adjusted to 20 µM. BSA-AuNCs-AZD were stored at 4°C until use.

3.2.3. Characterization of BSA-AuNCs-AZD

3.2.3.1. Quantification of drug functionalization into BSA-AuNCs by UV-Vis spectra

The loading of the AZD8055 was determined using UV-Vis spectroscopy. The absorbance of 100 µL BSA-AuNCs-AZD (20 µM) in PBS was measured at 380 nm in a microplate reader (Synergy H4). Then, the concentration was quantified by interpolation from a calibration curve using free AZD8055 in DMSO (10, 30, 50 and 70 µM).

3.2.3.2. Quantification of functionalized AZD8055 from BSA-AuNCs by HPLC

Complementarily, the amount of AZD8055 was quantified by HPLC. For the measurement of the BSA-AuNCs-AZD, the release of the drug and the precipitation of the BSA-AuNC were required to not block the HPLC column.

100 µL of BSA-AuNCs-AZD (20 µM) in PBS at pH 7.4 was incubated with 5 mM of GSH at room temperature for 72 hours. Then, this solution was treated with 100 µL 2% $Zn(NO_3)_2$ (Scharlab) solution in H_2O/DMSO (1:1) and centrifuge at 16.1 rcf for 15 minutes. The supernatant was carefully removed and stored at 4 °C until use.

A calibration curve was obtained incubating 100 µL BSA-AuNCs (20 µM) in PBS at pH 7.4 with free AZD8055 at different concentrations (0, 25, 50, 75 and 100 µM) and 5 mM of glutathione (GSH, Sigma-Aldrich). Then, this solution was precipitated with 100 µL 2% $Zn(NO_3)_2$ (Scharlab) solution in H_2O/DMSO (1:1). The supernatant was carefully removed and measured by HPLC.

An Aligent Technologies HPLC, 1260 Infinity, and Column ZORBAX 300SB-C18, 5 µm, 9.4 × 250 mm was employed for the chromatographic separation. 20 µL of the samples were injected into the system in initial conditions of water/acetonitrile 5/95 containing 0.1 % formic acid, followed by a gradual change (flow rate of 1 mL/min) for 15 minutes to water/acetonitrile 95/5 containing 0.1% formic acid. The absorbance at 380 nm was recorded.

3.2.3.3. Transmission electron microscopy (TEM) of BSA-AuNCs

Samples were prepared by placing one drop of a dilute suspension onto a carbon-coated copper grid and leaving it to air-dry at room temperature. Then, particle size was examined by transmission electron microscopy (TEM; 100 kV) using a JEOL JEM 1010 microscope at Instituto de Investigaciones Biomédicas “Alberto Sols”. The size distributions were determined through manual analysis using ImageJ processing.

3.2.3.4. Particle size measurements of BSA-AuNCs-AZD

It was carried out following the general procedure **3.1.1** using 100 µL of the BSA-AuNCs-AZD at 20 µM of concentration.

3.2.3.5. Scanning electron microscopy (SEM) of BSA-AuNCs-AZD

One drop of a solution of functionalized BSA-AuNCs-AZD was deposited over a silicon wafer and air-dried for 16 hours. Then, the samples were observed using a Carl Zeiss AURIGA scanning electron microscope (Zeiss, Jana) at IMDEA Nanociencia.

3.2.3.6. Atomic force microscopy (AFM) of BSA-AuNCs-AZD

A drop of the BSA-AuNCs-AZD solution (20 µl) was spread on freshly cleaved muscovite mica. The sample was left incubating on the substrate for 10 minutes, rinse with ultrapure water 5 times and dry with compressed air. Then, the samples were observed using an AFM JPK (Nanowizard II) at IMDEA Nanociencia and measured in different areas using HQXSC11 D/No Al (Mikromash) tips, with nominal spring constant around 42 N/m and resonance frequency around 350 kHz. The images have been flattened using JPK Data Processing software and the histograms with the height are obtained using WSxM software and represented using Origin software. The histograms show the number of particles which height corresponds to the maximum value of the difference between the cutoff height and the point's height.

3.2.3.7. *In vitro* AZD8055 release from BSA-AuNCs

The release profile of AZD8055 was evaluated using fluorescence spectrophotometry. Thus, 1 mL of a solution of BSA-AuNCs-AZD was incubated in PBS containing GSH (1 µM or 1 mM). At different time intervals, 100 µL of this solution were taken and treated with 100 µL of a 2% $Zn(NO_3)_2$ solution in H_2O/DMSO (1:1). After vigorous stirring, the mixture was centrifuged at 16.1 rcf for 10 min and the fluorescence of the released AZD8055 (supernatant) was analyzed using a microplate reader (λ_{exc} = 380 nm, λ_{em} = 550 nm).

3.2.4. Cell culture experiments

3.2.4.1. Cell lines

Human Uveal Melanoma (Mel202 and OMM 1.3) cells were a donation from Dr. Susana Ortiz-Urda (University of California, San Francisco) and HaCaT keratinocytes and Uveal Melanoma Sp6.5 cells were provided by Dr. Pilar Martín-Duque (Universidad Francisco de Vitoria, Madrid).

3.2.4.2. Subcellular localization of BSA-AuNCs 3–4 hours after treatment

Uveal Melanoma (Mel202) cells grown in 24 well plates with glass coverslips were treated with 50 µM BSA-AuNCs for 3–4 hours and fixed afterward with 4% paraformaldehyde for 15 minutes at room temperature. Fixed cells were subsequently permeabilized and labeled for 20 minutes at room temperature in darkness with a mix containing Saponin 0.25%, DAPI (diluted 1:300 from a 1 mg/mL stock solution), Phalloidin (diluted 1:250 from a 1 mg/mL stock solution), and FBS 5% in PBS buffer (pH = 7.4). All these reagents were obtained from confocal service at Centro Nacional de Biotecnología (CNB). After washing 3 times with PBS, coverslips were mounted onto slides using Fluoroshield™ (Sigma-Aldrich) mounting medium and visualized by confocal microscopy (Confocal multispectral Leica TCS SP8 system).

Data acquisition was performed with Leica software LAS X and images were prepared with ImageJ (https://imagej.nih.gov/ij/). To avoid possible artifacts due to the crosstalk between the red and the blue channels, the blue signal was subtracted from the red 2D images using ImageJ processing.

3.2.4.3. Cellular uptake of BSA-AuNCs-AZD in uveal melanoma (Mel202) cells

Uveal Melanoma (Mel202) cells were seeded in 6 well plates in complete culture medium overnight. Cells were washed with PBS, and the medium was replaced with fresh medium containing free AZD8055 and BSA-AuNCs-AZD at a concentration of 1 µM of drug and incubated for 24 hours. Then, the cells were washed twice with PBS and trypsinized using Trypsin/EDTA 1X. The cell suspensions were centrifuged at 177 rcf for 5 minutes. The supernatant was removed carefully, and the cells were suspended in 500 µL of PBS 1X.

The fluorescence of AZD8055 was measured by flow cytometry at Centro Nacional de Biotecnología (CNB) using a Beckman Coulter GALLIOS equipment (laser 405 nm).

3.2.4.4. Cytotoxicity assay

It was carried out by resazurin assay following the general procedure **3.1.2.5.2** incubating the cells with free AZD8055 and BSA-AuNCs-AZD at a concentration of 1 µM of the drug.

3.2.4.5. Cell viability of uveal melanoma (Mel202) cells in the presence of endocytosis inhibitors

Uveal Melanoma (Mel202) cells were seeded in 24-well plates and incubated at standard conditions (37 °C, 5% CO_2) for 24 hours. Then, the Mel202 cells were pre-incubated for 1 hour with medium containing the following endocytosis inhibitors: 10 µg/ mL Chlorpromazine (MeOH, Sigma-Aldrich), 5 µg/mL Filipin III (DMSO, Sigma-Aldrich). After this pre-incubation time, cells were washed with PBS 1X and incubated with 6 µM of BSA-AuNCs-AZD and free AZD8055 for 4 hours. For negative controls, cells without inhibitor and cells without drugs were used. After this incubation time, the culture medium was removed and the cells were washed twice with PBS 1X. The cell viability was measured 24 hours later by resazurin assay according to the general procedure described before. Data corresponded to the normalized mean values respect its control ± standard deviation from at least three different experiments.

3.2.4.6. Reactive oxygen species (ROS) generation in uveal melanoma (Mel202) cells

Mel202 cells were grown in 24 well plates with and without coverslips and co-incubated with BSA-AuNCs, BSA-AuNCs-AZD, free AZD8055 or H_2O_2 as a positive control and 5 µM of 2',7'-Dichlorofluorescin diacetate (H_2DCFDA, Sigma-Aldrich) for 4 hours at standard conditions (37 °C, 5% CO_2).

On the one hand, cells grown without glass coverslip were washed twice with PBS (pH = 7.4), and trypsinized using Tryosin/EDTA 1X. Then, the cell suspensions were placed into a fluorescence 96 well-plate, and the fluorescence was measured using a microplate reader (λ_{Exc}= 485nm, λ_{Em}= 528 nm).

On the other hand, cells grown onto glass coverslips were washed with PBS, air-dried, mounted with Fluoroshield™ mounting medium and examined by fluorescence microscopy using a fluorescence microscope Leica DMI3000 B (λ_{Exc} = 460-500nm, λ_{Em} = 515-545).

3.2.4.7. *In vivo* study in uveal melanoma (Mel202) tumor models treated with BSA-AuNCs-AZD

Athymic nude mice were purchased from ENVIGO (Research Models and Service) for the evaluation of toxicity of functionalized BSA-AuNCs-AZD.

Fifteen immuno-depressed female mice (nu/nu) weighing around 23 grams were used and divided randomly into four groups. The uveal melanoma tumor model was established by subcutaneously injecting 7 x 10^6 Mel202 cells with Matrigel (Corning, VWR) until the tumors have 0.8 cm^2 size.

Mice were divided into four groups (n = 4) including control, treated with 200 µL of free AZD8055 intratumoral, BSA-AuNCs-AZD (200mg/kg BSA; 6 mg/Kg AZD) intratumoral and intravenously through the lacrimal vein. Mice in the control group were injected with 200 µL of PBS 1X buffer (pH = 7.4) without calcium and magnesium. The treatments were administrated once a week for two weeks and the sizes of the tumors were monitored measuring the tumor size (width and length) twice a week using a caliber.

Finally, the mice were sacrificed 10 days after the second injection, and the tumors, liver, and spleen were extracted for histopathology by hematoxylin/eosin staining (H&E).

3.2.5. Statistical analysis

Statistical analysis of the data was performed following the general procedure **3.1.2.6.**

In addition, for the *in vivo* experiments, the data were analyzed by Levene's and Saphiro-Wilk tests to assess the equality of variance and the normality of the data, respectively. Then, one-way ANOVA Student-Newman-Keuls multiple comparisons test in the GraphPad Prism software was performed (p-values < 0.05 (*), <0.01 (**) and < 0.001 (***)).

3.3. Albumin-stabilized gold nanoclusters functionalized with DOX and SN38 (BSA-AuNCs-DS) for breast cancer treatment

3.3.1. Synthesis of intermediates and pro-drugs

It was carried out following the procedure described in section **3.2.1**.

3.3.1.1. Doxorubicin modified with a pH-sensitive linker (DOX-iMal)

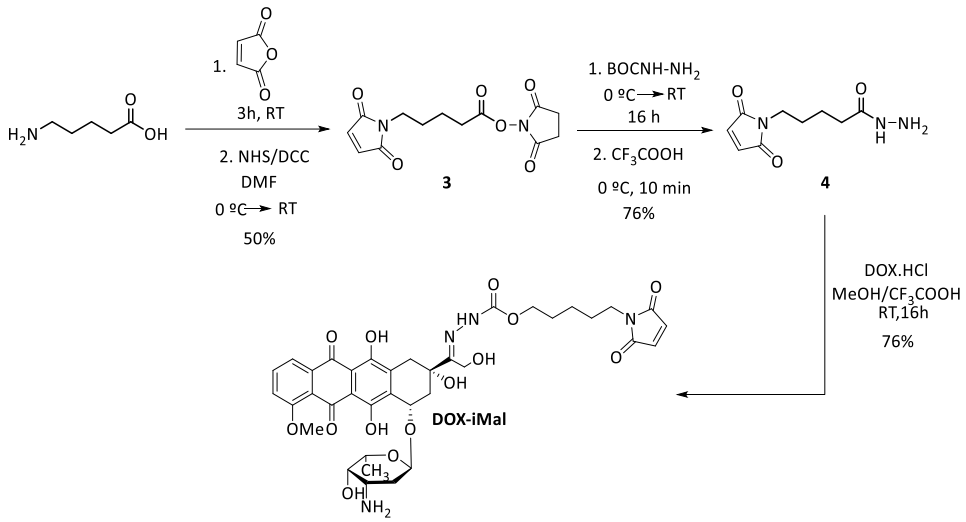

3.3.1.1.1. Succinimido 5-maleimidopentanoate (3)[157]

To a solution of maleic anhydride (167 mg, 1.7 mmol, Sigma-Aldrich) in N,N-Dimethylformamide (DMF) (2 mL, Sigma-Aldrich) under argon, aminovaleric acid (167 mg, 1.7 mmol, Sigma-Aldrich) was added, and the mixture stirred at room temperature for 3 hours. Then, NHS (234 mg, 2 mmol) and DCC (700 mg, 3.4 mmol) were added at 0 °C. After 20 minutes, the mixture was warmed up to room temperature and stirred for 16 hours. The resulting precipitate was filtered off, and the solvent concentrated in vacuo. The residue was purified by flash chromatography (eluent CH_2Cl_2/Isopropanol 97:3) to give the compound 1 in 50% yield as white solid; **^{1}H NMR (300 MHz, $CDCl_3$)** δ 6.69 (bs, 2H), 3.55 (bs, 2H), 2.82 (bs, 4H), 2.64 (bs, 2H), 1.72 (bs, 4H).

3.3.1.1.2. 5-Maleimidovalerohydrazide trifluoroacetic acid salt (4)[158]

To a solution of **1** (30 mg, 0.1 mmol) in CH_2Cl_2 (1 mL), tert-butyl carbazate (15 mg, 0.1 mmol, Sigma-Aldrich) was added at 0 °C. Then, the solution was let to reach room temperature slowly and stirred for 16 hours. The solution was concentrated in vacuo, and the residue purified by flash chromatography (eluent CH_2Cl_2/MeOH 100:1 first and gradually changed to 30:1) to obtain the Boc-protected compound **2** as colorless oil; **^{1}H NMR** (300 MHz, $CDCl_3$) δ 6.68 (bs, 2H), 3.52 (bs, 2H), 2.25 (bs, 2H), 1.63 (bs, 4H), 1.44 (s, 9H).

This intermediate was dissolved in 0.5 mL trifluoroacetic acid previously cooled at 0 °C, and stirred for 10 minutes. The solution was concentrated in vacuo and the resultant

solid purified by washing with Et_2O to obtain compound **2** as dark white solid in 76% yield.

3.3.1.1.3. (5-Maleimidovaleroyl) hydrazine of Doxorubicin (DOX-iMal)[158]

To a solution of compound **2** (15 mg, 0.071 mmol) and Doxorubicin (13 mg, 0.023 mmol, Fluorochem) in MeOH (4.5 mL), two drops of trifluoroacetic acid were added and stirred at room temperature for 16 hours. Then, the solution was concentrated in vacuo, and the residue dissolved in the minimal amount of MeOH. To this solution, CH_3CN (Scharlab) was added, and the mixture cooled to 4 °C during 16 hours. The solvent was decanted and the solid washed with CH_2Cl_2 to obtain compound **DOX-iMal** as red solid in 76 % yield; **^{1}H NMR (300 MHz, MeOD)** δ 7.87-7.80 (m, 2H), 7.54 (d, 1H), 6.76 (s, 2H), 5.48 (s, 1H), 5.07 (s, 1H), 4.74-4.64 (m, 2H), 4.26-4.21 (m, 1H), 4.02 (s, 3H), 3.70-3.54(m, 3H), 3.41 (s, 2) 2.59-2.29 (m, 3H), 2.11-1.88 (m, 2H), 1.67-1.53 (m, 5H), 1.32 (t, 3H). **MS (ESI) m/z (%)**: 737 (M++H, 100), 759 (M^{++}Na, 2); **HRMS (ESI)** calculated for $C_{36}H_{41}N_4O_{13}$ (M^{++}H) 737.2638, **found** 737.2664.

3.3.1.2. SN38 modified with a redox-sensitive linker (SN38-PySS)

Starting from compound **2** described in section **3.2.1.1.2.**

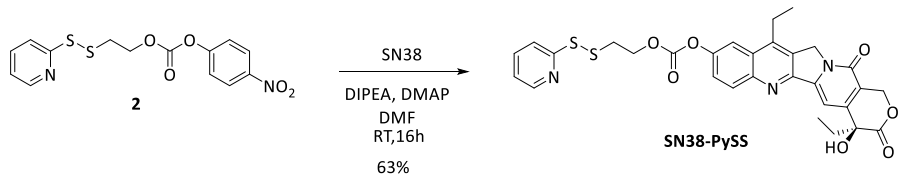

3.3.1.2.1. 4-Nitrophenyl 2-(pyridin-2-yldisulfanyl)ethyl carbonate of SN38 (SN38-PySS)

To a solution of **2** and SN38 (Fluorochem) in DMF under argon, DIPEA and catalytic amount of DMAP were added and stirred during 16 hours. Then, the mixture was concentrated in vacuo and the residue purified by flash chromatography (eluent CH_2Cl_2/MeOH 30:1) to obtain compound **SN38-PySS** as colorless oil in 63 % yield; **^{1}H NMR (500 MHz, $CDCl_3$)** δ 8.42 (d, J= 4.8, 1.3 Hz, 1 H), 8.07 (d, J= 9.1 Hz, 1H), 7.66 (dd, J= 4.6, 1.3 Hz, 1H), 7.45 (dd, J= 9.1, 2.6 Hz, 1H), 7.36 (d, J= 2.6 HZ, 1H), 7.26 (s, 1H), 7.06 (h, J= 4.6 Hz, 1H), 5.71 and 5.40 (AB system, J= 17 Hz, 2H), 5.09 (bs, 2H), 4.39-4.29 (m, 2H), 3.05 (t, J= 6.6 Hz, 3H), 3.01-2.98 (m, 2H), 2.26 (dq, J= 14.8, 7.4 Hz, 1H), 2.14 (dq, J= 14.8,

7.4 Hz, 1H), 1.30 (t, J= 7.7 Hz, 3H), 0.99 (t, J= 7.5 Hz, 3H); **^{13}C NMR (500 MHz, $CDCl_3$)** δ 167.4, 159.3, 157.2, 156.1, 153.5, 149.6, 149.0, 147.4, 145.9, 144.7, 143.6, 137.5, 132.0, 128.5, 126.9, 122.7, 121.1, 120.0, 119.3, 105.5, 95.5, 78.2, 67.1, 66.4, 49.4, 36.9, 31.2, 23.1, 13.6, 7.6; **MS (ESI) m/z (%)**: 303 (20), 606 ($M^{++}H$, 100), 628 ($M^{++}Na$, 1); **HRMS (ESI)** calculated for $C_{30}H_{28}N_3O_7S_2$ ($M^{++}H$) 606.1377, **found** 606.1363.

3.3.2. BSA-stabilized gold nanoclusters (BSA-AuNCs)

The synthesis of BSA-AuNCs and their subsequent sulfhydryl activation were carried out as described in section **3.2.2**.

3.3.2.1. BSA-AuNCs functionalized with doxorubicin and SN38 (BSA-AuNCs-DS)

On the one hand, to synthesize functionalized BSA-AuNCs with doxorubicin (BSA-AuNCs-D), 100 µL of a solution of modified DOX (**DOX-iMal**) (1 mM) in DMF was added to 1 mL of a solution of sulfhydryl-activated BSA-AuNCs (20 µM) in PBS (pH = 7.4) and stirred at room temperature for 16 h. Then, BSA-AuNCs-D were purified using a NAP-10 Sephadex G-25 column. On the other hand, BSA-AuNCs modified with SN38 (BSA-AuNCs-S) were prepared as above by using 150 µL of a solution of modified SN38 (**SN38-PySS**) (1 mM) in DMSO.

Finally, the synthesis of BSA-AuNCs-DS was carried out using the same procedure by adding 100 µL of a solution of modified DOX (**DOX-iMal**) (1 mM) in DMF, immediately followed by the addition of 100 µL of a solution of modified SN38 (**SN38-PySS**) (1 mM) in DMSO.

3.3.3. Characterization of BSA-AuNCs-DS

3.3.3.1. Quantification of drug functionalization into BSA-AuNCs by UV-Vis spectra

The loading of the DOX and SN38 was determined using UV-Vis spectroscopy. The absorption of doxorubicin (490 nm) and SN38 (370 nm) were measured, and the concentration quantified by interpolation from a calibration curve.

3.3.3.2. Particle size and zeta potential measurements

It was carried out following the general procedure **3.1.1** using 100 µL of the corresponding BSA-AuNCs functionalized with DOX, SN38, or both at 20 µM of

concentration.

3.3.3.3. Scanning electron microscopy (SEM) of BSA-AuNCs-DS

It was carried out as described in section **3.2.3.5** using BSA-AuNCs-D, BSA-AuNCs-S and BSA-AuNCs-DS.

3.3.3.4. *In Vitro* DOX/SN38 release from BSA-AuNCs

The doxorubicin release profile was evaluated using fluorescence spectrophotometry. Briefly, 1 mL of a solution of BSA-AuNCs-D in saline citrate buffer at pH = 7.4 or 5 was incubated at 37 °C. At different time intervals, 100 µL of this solution were withdrawn and treated with 100 µL of a 2% $ZnSO_4$ solution in H_20/MeOH (1:1). After vigorous stirring, this mixture was centrifuged at 16.1 rcf for 10 min, and the fluorescence of the DOX released was analysed by fluorescence from the supernatant (λ_{exc} = 495 nm, λ_{em} = 590 nm).

The SN38 release profile was evaluated using a similar protocol. In this case, 1 mL of a solution of BSA-AuNCs-S in PBS at pH = 7.4 containing dithiothreitol (DTT, Sigma-Aldrich) at 1 µM or 1 mM was incubated, and the SN38 released analyzed by fluorescence from the supernatant using a microplate reader (λ_{exc} = 370 nm, λ_{em} = 550 nm).

3.3.4. Cell culture experiments

3.3.4.1. Cell lines

Human breast adenocarcinoma (MCF-7 and MDA-MB-231) and human pancreatic adenocarcinoma (Panc-1) were obtained from American Type Culture Collection (ATCC®: HTB-22™, HTB-26™ and CRL-1469™, respectively).

3.3.4.2. Cytotoxicity assay

This study was performed in breast cancer MCF-7 and MDA-MB-231 and pancreatic cancer Panc-1 cell lines using a constant concentration of BSA-AuNCs (2.6 µM) of the corresponding formulation, BSA-AuNCs-D, BSA-AuNCs-S and BSA-AuNCs-DS.

Toxicity was measured at 24, 48 and 72 hours after treatment following the general procedure **3.1.2.5.**

3.3.4.3. Neutral red staining in breast cancer (MCF-7) cells

MCF-7 cells grown on coverslips in 24-well plates and incubated for 24 hours with the functionalized BSA-AuNCs, using a constant concentration of 2.6 µM, were fixed in cold methanol for 5 minutes and then stained with 0.5% neutral red (Sigma-Aldrich) for 2 minutes. Coverslips were washed with distilled water, air-dried, mounted in DePeX (Sigma-Aldrich) and examined by light microscopy.

3.3.4.4. Live cell imaging in breast cancer (MCF-7) cells

Cells were incubated with the corresponding BSA-AuNCs-D, BSA-AuNCs-S and BSA-AuNCs-DS for 24 hours. Then, the cells were washed twice with PBS 1X and maintained in culture medium for 9 days changing the culture medium every 2–3 days. Untreated cells as well as cells incubated with unmodified BSA-AuNCs, were also visualized. Cells were imaged daily under a differential interference contrast (DIC) inverted microscope (Leica DMI 6000B) equipped with a Leica DFC420 C digital camera (Leica Microsystems, Heerbrugg, Switzerland).

3.3.4.5. Inductively coupled plasma mass spectrometry (ICP-MS) in breast cancer (MCF7) cells

MCF-7 cells treated with 2.6 µM of BSA-AuNCs for 24 hours were harvested and quantified, prior digestion overnight in aqua regia (HCl:HNO_3 3:1) and subsequent dilution in pure water. After that, the quantity of Au^+ in the sample was determined by ICP-MS and relativized per cell unit.

3.3.4.6. Subcellular localization of BSA-AuNCs 3–4 hours after treatment

Subcellular localization of BSA-AuNCs (50 µM) in breast cancer (MCF-7) cells was carried out following the same procedure described in section **3.2.4.2.**

3.3.4.7. BSA-AuNCs-DS internalization at 24 hours after treatment

The internalization of bifunctionalized BSA-AuNCs-DS into MCF-7 cells were visualized by confocal microscopy. Cells grown on coverslips were incubated for 24 hours with 2.6 µM of BSA-AuNCs-DS, washed three times with culture medium without FBS, and visualized under differential interference contrast (DIC) microscopy and confocal

fluorescence microscopy using a multispectral Leica TCS SP5 confocal microscope, operating with 405 Diode (UV) and DPSS (561, visible) laser lines.

3.3.4.8. Microscopic detection of DNA damage in breast cancer (MCF-7) cells after BSA-AuNCs-DS treatment

MCF-7 cells were grown on glass coverslips and incubated with the different BSA-AuNCs for 24 hours. Then, they were immunostained for histone phosphorylated H2AX (γ-H2AX) 48 hours after treatments. Cells were fixed with formaldehyde in PBS (1:10 *v/v*) for 20 minutes, washed three times with PBS 1X, and then permeabilized with 0.5% Triton X-100 in PBS for 5 minutes. Then, cells were incubated with a blocking solution containing 5% bovine serum albumin, 5% FBS, 0.02% Triton X-100 in PBS at room temperature for 30 minutes. After incubation, cells were washed three times with PBS 1X and incubated with primary monoclonal mouse anti-γ-H2AX antibody (Merk Millipore) diluted 1:100 at 37 °C in a wet chamber for 1 hour. After three washes with PBS, incubation with secondary antibody (Alexa Fluor® 488 goat anti-mouse, Life Technologies (Waltham) was identical to that of the first one and so were final washings. Finally, DNA was counterstained by the addition of Hoechst-33258 (0.05 mg/mL in distilled water, Thermo Fisher) for 5 minutes, and the sample was mounted with ProLong Gold antifade reagent (Invitrogen).

Immunofluorescence images were captured using a laser scanning confocal microscope using a multispectral Leica TCS SP5 confocal microscope (Leica, Wetzlar, Germany), operating with 405 nm (argon–UV) and 488 nm (argon) laser lines.

3.3.4.9. Breast cancer (MCF-7) mammosphere culture

Single-cell suspensions of MCF-7 cell line were plated in 96-well plates at 10 cells per well in DMEM/F-12 medium supplemented with GlutaMAX, B27 (Gibco, Thermo Fisher), 10 ng/mL epidermal growth factor (EGF, Invitrogen) and 10 ng/mL basic fibroblast growth factor (bFGF, Millipore) and they were maintained at 37 °C in 5% CO_2.

On day 10, the number of wells with mammospheres was counted, and then nanostructures were added. The final proportion of living spheres were quantified on day 17.

3.3.5. Statistical analysis

Statistical analysis of the data was performed following the general procedure **3.1.2.6.**

3.4. New vehicles based on nanostructures CRISPR/Cas gene-editing system transport

3.4.1. Functionalized carbon nanotubes as gene delivery system

3.4.1.1. Design of a functional CRISPR/Cas9 plasmid

The design of the sequences required to edit the EGFP gene was prepared following standard protocols (http://www.addgene.org/crispr/zhang/). As a control, a non-targeting sequence was also designed.

Briefly, the selected sequences (**Table 3**) were inserted in the plasmid pSpCas9 (Addgene pX330, #42230) using DNA duplexes with four nucleotides overhangs compatible for cloning into the vector: 5'- CACCG in the sense strand and 5'- AAAC in the antisense strand. The resulting DNA was 25 base-pairs length and was obtained from "Integrated DNA Technologies (IDT)".

Gene	sgRNA	Sequence (5' to 3')	Reference
-	Non-targeting (Cas9-NT)	5' CACCGGTACGACCGCACGGTTACCC 3'	(Sun *et al.*)
eGFP	EGFP (Cas9-EGFP)	5' CACCGCCGGCAAGCTGCCCGTGCCC 3'	

Table 3. sgRNA sequences targeting genes used to the pSpCas9 plasmid cloning.

Upon arrival, the lyophilized oligonucleotides were resuspended in ultrapure water to a final concentration of 1 mM and stored at -20 °C until used.

3.4.1.1.1. Dúplex annealing

The duplex formation was carried out just by mixing 1 µL of each complementary strand at a concentration of 100 µM, 0.5 µL of T4 Polynucleotide kinase (PNK, NEB), used for the phosphorylation of 5' ends of the oligonucleotides, 1 µL of T4 ligation buffer 10X (NEB) and 6.5 µL of ultrapure water.

Reactions were performed in a thermocycler (Eppendorf) where the samples were at 37 °C for 30 minutes, heated at 95 °C for 5 minutes and then cooled to 25 °C (5°C/minute).

3.4.1.1.2. Digestion – Ligation

The digestion of the plasmid and the ligation with the duplex took place in a one-step reaction using the restriction enzyme Fast-Digest *BbsI* (Thermo Fisher), and the DNA ligation enzyme T7 ligase (NEB).

For that, 100 ng of pSpCas9 and 400 ng of the synthesized duplex above to a final volume of 20 µL. The reaction was performed in a thermocycler using the protocol indicated by the manufacturer: 5 minutes at 37 °C and 5 minutes at 23 °C for 6 cycles. Then, the mixed solution was stored at 4 °C until used.

3.4.1.1.3. Freeze/thaw of bacteria

For long-term storage of bacteria, 900 µL of a culture grown in LB supplemented with the corresponding antibiotic was mixed with 100 µL of glycerol in 1.5 mL microcentrifuge tubes. Bacteria stocks were then frozen and stored -80 °C until used.

To thaw bacteria from glycerol stocks, a small amount of the frozen stock was collected with a sterile pipet tip and added to the desired amount of LB medium supplemented with antibiotic. Then, bacteria were grown at 37 °C for 16 hours under constant stirring.

3.4.1.1.4. Transformation of competent cells

2 µL of plasmid pSpCas9 with the insert was added to 50 µL of ice-thaw competent bacteria (*E. coli* JM109, Promega) and incubated on ice for 30 minutes. Then, bacteria were heat-shocked in a water bath at 42 °C for 20 seconds and immediately put on ice again for 2 minutes more. After that, 450 µL of LB medium was added and incubated for 1 hour at 37 °C under constant stirring.

Finally, for each transformation reaction 100 µL of competent cells were added into agar plates supplemented with the corresponding antibiotic resistance marker. Bacteria were then incubated at 37 °C for 16 hours, and a resulting colony was pick up and then grown in LB medium supplemented with antibiotic.

Transformed bacteria were stored in glycerol at -80 °C.

3.4.1.1.5. Plasmid DNA extraction from bacteria

The DNA extraction from bacteria was done using the PureYield™ Plasmid Miniprep System (Promega) or the NucleoBond PC 100 Midi column (Machinery-Nagel, Cultek) following the manufacturer's protocol.

3.4.1.1.6. Sequencing

The purified plasmids were sequenced by STABVIDA using 10 µL of plasmid and 5 µL (10 ng/µL) of this primer (5' GGACTATCATATGCTTACCGTAACT 3').

3.4.1.2. Evaluation of a CRISPR/Cas9 plasmid

3.4.1.2.1. Cell lines

Human embryonic kidney (HEK293) cells were obtained of Dr. Antonio Rodríguez from Universidad Autónoma de Madrid.

3.4.1.2.2. Transfection of CRISPR/Cas9 plasmids into HEK293 cells using Lipofectamine 2000

HEK293 cells were seeded in a 6-well plate at the appropriate density and incubated at standard conditions (37 °C, 5% CO2) for 24 hours before transfection in complete medium (10% FBS).

HEK293 cells were transiently transfected using Lipofectamine 2000 and 5.1 µg of DNA per 6-well plate. For CRISPR/Cas9 plasmids (pCas9-NT and pCas9-EGFP), each well was transfected with 3 or 4.93 µg of the corresponding pCas9, 0.17 µg of the reporter EGFP plasmid and DNA carrier pBlueScript plasmid up to 5.1 µg. As a control, cells were transfected with reporter EGFP plasmid. The amounts of each plasmid used for transfection are summarized in **table 4.**

	pEGFP	pBlueScript	pCas9-EGFP	pCas9-NT
EGFP	0.17 µg	4,93 µg	-	-
Cas9-EGFP (3 µg)	0.17 µg	1.93 µg	3 µg	-
Cas9-EGFP (5.1 µg)	0.17 µg	-	4,93 µg	-
Cas9-NT (5.1 µg)	0.17 µg	-	-	4,93 µg

Table 4. Amounts of DNA used in transfection for each CRISPR/Cas9 construct using Lipofectamine 2000.

The transfection procedure of the plasmids using Lipofectamine 2000 took place according to the manufacturer's protocol. 5 µL of Lipofectamine 2000 was added to 100 µL of pre-warmed serum-reduced medium (Opti-MEM, Gibco) and incubated for at least 5 minutes in one microcentrifuge tube. On the other hand, a total amount of 5.1 µg of DNA mixing plasmids (EGFP, Cas9, BlueScript) was incubated with 100 µL of pre-warmed Opti-MEM in a second microcentrifuge tube. Then, the DNA solution was added to the medium containing the transfection reagent and incubated for 15 minutes at room temperature to allow the formation of DNA/Lipofectamine 2000 complexes. After the incubation time, 200 µL of the complexes were added to the wells drop by drop and incubated overnight at standard conditions. Then, the medium was carefully removed and replaced with fresh medium. Cells were visualized daily under optical and fluorescence microscope.

The gene editing capacity of the pSpCas9 plasmid was studied in cells by fluorescence microscopy and flow cytometry. After the transfection of the plasmids, representative fluorescence images of the EGFP expression were taken under a fluorescence microscope (IX81 Olympus) at 72 hours after treatment. At the same time, transfected cells were washed twice with PBS 1X and trypsinized using Trypsin-EDTA 1X. Cell suspensions were centrifuged at 177 rcf for 5 minutes. The supernatants were removed carefully, and the cells were suspended in 500 µL of PBS 1X. The fluorescence of EGFP plasmid was measured by flow cytometry at Centro Nacional de Biotecnología (CNB) using a Beckman Coulter GALLIOS cytometer (laser 405 nm).

3.4.1.3. Functionalization of PEI-modified carbon nanotubes with plasmid DNA

Single-walled carbon nanotubes (SWNT) were modified by Dr. Teresa Naranjo and Dr. Julia Villalva from the group of Prof. Emilio Pérez from IMDEA Nanoscience. The covalent functionalization took place with the positively charged polymer polyethyleneimine (PEI) (branched, 2kDa, Sigma-Aldrich). As a result, PEI-modified SWNT were obtained. The characterization of the reaction by Raman spectroscopy and thermogravimetric analysis was also carried out by Dr. Teresa Naranjo and Dr. Julia Villalva from group of Prof. Emilio Pérez.

1mg of PEI-SWNT were resuspended in 1 mL of complete cell culture medium (10% FBS) and sonicated for 1 hour at 15-minute intervals. Subsequently, the tube dispersion was centrifuged to remove the largest non-resuspended aggregates.

Binding with the DNA plasmid (pDNA, 1 µg) took place by incubating different amounts of PEI-SWNT (1, 10, 20 and 40 µL) at room temperature for 45 minutes under constant stirring leading to PEI-SWNT-pDNA.

3.4.1.3.1. Zeta potential measurements

Zeta potential measurements of the functionalized PEI-SWNTs were carried out following the general procedure **3.1.1**. As a control, non-functionalized SWNTs were also used.

3.4.1.3.2. Retardation assay

PEI-SWNT-pDNA complexes using different ratios were prepared, as previously described. In particular, 1 µg of EGFP plasmid was mixed with 1, 10, 20 and 40 µL of PEI-SWNT at room temperature for 45 minutes. As a control, the EGFP plasmid was used.

Samples were mixed with 6X DNA EZ-Vision loading buffer (VWR) and then analyzed by agarose gel electrophoresis (1% w/v in TAE buffer 1X). Electrophoresis was usually run at 90 V for 45 minutes or when the DNA fragments were clearly spaced. The results were revealed under UV light in a gel documentation system (Syngene, ChemiBox).

3.4.1.3.3. Cell culture experiments

3.4.1.3.3.1. Cell viability assay

It was carried out by resazurin assay following the general procedure **3.1.2.5.2** incubating the cells with PEI-SWNT-EGFP complexes at different ratios.

3.4.1.3.3.2. EGFP plasmid uptake using PEI-modified SWNT

HEK293 cells were seeded in 24-well plates under standard conditions (37 °C, 5% CO_2) and incubated for 24h before transfection. 1 µg of EGFP plasmid was incubated with 20 and 40 µL of PEI-SWNTs at room temperature for 45 minutes under constant stirring. After incubation, the mixtures' volumes were equalized using culture medium, added dropwise to the cells and incubated for 24 hours. The cells were then washed twice with

culture medium and incubated for 48 more. Gene editing capacity of the pSpCas9 plasmid was studied in cells by fluorescence microscopy (Leica DMI 3000B).

The same procedure was carried out on uveal melanoma (Mel202) and pancreatic cancer (Panc1) cells.

3.4.1.3.3.3. Gene editing CRISPR/Cas9 plasmid (pSpCas9) in HEK293 using PEI-SWNT

First, 0.07 µg of EGFP reporter plasmid were transfected using Lipofectamine 2000 as described before. After 6 hours of incubation, the cells were washed twice with PBS 1X and the medium was replaced with complete growth medium.

Second, 1 µg of CRISPR/Cas9 construct (pSpCas9) was incubated with 20 and 40 µL of PEI-SWNTs at room temperature for at least 45 minutes under constant stirring. After incubation, the mixtures' volumes were equalized using culture medium, added dropwise to the cells and incubated, for 24 hours. The cells were then washed twice with culture medium and incubated for 48 more.

As described before, the gene editing capacity of the pSpCas9 plasmid was studied in cells by fluorescence microscopy (Leica DMI 3000B)

3.4.2. Albumin-based nanocomplexes for CRISPR-Cpf1 ribonucleoprotein delivery

3.4.2.1. Covalent modification of native BSA with CRISPR-Cpf1 protein (BSA-Cpf1)

3.4.2.1.1. BSA modification

20 equivalents of 2-iminothiolane (0.32 µmol) were added to a solution of 400 µM of BSA (500 µL) in PBS (pH = 7.4) and incubated at room temperature for 4 hours. The product was purified using an exclusion column NAP-10 of Sephadex-G25, and modified with aldrithiol. Thus, a solution of the product (1 mL, 200 µM) was treated with aldrithiol (20 equivalents, 0.16 µmol) and incubated at room temperature for 16 hours. The resulting activated BSA was purified using an exclusion column NAP-10.

3.4.2.1.2. Covalent conjugation of activated BSA and CRISPR-Cpf1 protein

The Cpf1 protein (40 µL, 10 µM) in PBS at pH = 7.4 was added to 40 µL of activated BSA solution at different concentrations (20, 50 and 100 µM). The mixtures at different ratios

(2:1, 5:1 and 10:1) were incubated 1 hour at room temperature, and then stirred at 4 °C for 16 hours. The resulting products were labeled as BSA-Cpf1 complexes.

3.4.2.1.3. UV-Vis spectrum of pyridinethione

The release of pyridinethione during the preparation of activated BSA and BSA-Cpf1 complexes was evaluated by UV-Vis spectroscopy. The absorption of this compound at 343 nm was measured, and the concentration quantified using the Beer-Lambert equation using the extinction coefficient of pyridinethione 8080 L mol^{-1} cm^{-1}. BSA modified only with aldrithiol and incubated with the Cpf1 was also studied as a control.

3.4.2.1.4. Size measurements (DLS)

It was carried out following the general procedure **3.1.1** using 100 µL of the BSA-Cpf1 nanocomplex (0.8 µM of Cpf1) at different ratios (2:1, 5:1 and 10:1).

3.4.2.1.5. Protein Separation SDS-PAGE

The samples were diluted 1:10, and 5 µl of loading buffer with and without DTT (400 mM) were added. The samples were heated at 95 °C for 5 minutes in a heating block and stored at -20 °C until use.

15 µl of each sample was loaded onto denaturing SDS-PAGE (10%) and allowed to run at 165 V until the marker fragments were separated. Finally, the gel was stained using Coomassie Blue for (0.25 % (p/v)) 30 minutes at room temperature.

3.4.2.1.6. *In vitro* cleavage of EGFP gene using CRISPR-Cpf1 protein

Ribonucleoprotein (Cpf1/sgRNA) and target DNA (EGFP amplicon) were prepared by Carmen Escalona from the group of Dr. Begoña Sot.

The BSA-Cpf1 complexes were incubated with DTT (10 mM) for 1 hour at room temperature. Then, the in vitro cleavage reaction took place by incubating the BSA-Cpf1 samples and the target DNA at 37 °C for 1 hour and then 10 minutes at 65 °C, as follows (**Table 5**).

Component	BSA-Cpf1	Control
DNA target (31 ng/µL)	8 µL	8 µL
Cpf1(RNP) (5 µM)	2.4 µL	-
CutSmart Buffer	1.5 µL	1.5 µL
PBS	Up to 15 µL	Up to 15 µL

Table 5. Reagents used in In vitro cleavage reaction performed by BSA-Cpf1(RNP).

The reaction products were digested with Proteinase K at 65 °C for 10 minutes and analyzed by agarose gel electrophoresis as previously describe (**3.4.1.2.2**).

3.4.3. Statistical analysis

Statistical analysis of the data was performed following the general procedure **3.1.2.6.**

Results

4. RESULTS

4.1. Albumin-stabilized gold nanoclusters functionalized with AZD8055 (BSA-AuNCs-AZD) for uveal melanoma treatment

4.1.1. Uveal melanoma

Uveal melanoma, although rare (3-5% of all melanomas)[159], it is the most common primary malignancy of the eye in adults. It is thought that the factors that predispose to the appearance of this type of cancer may be the light color of the skin and eyes. In this regard, the incidence rates calculated in the US is approximately of 5 cases per million per year, meanwhile in Europe varies between 1.6-8.3 cases per million per year depending on the latitude (from 2 cases per million per year in Spain and Italy to 8 cases per million per year in Norway and Denmark). The incidence in Africa and Asia is much lower, with 0.2-0.3 cases per million per year [160,161].

Uveal melanoma arises from the melanocytes in the uveal tract that involves the choroid, ciliary body and iris (**Figure 15**)[162]. Thus, uveal melanoma can be divided into three categories depending on the location. On the one hand, the most commonly arise from choroidal melanocytes with an 85-90% incidence. On the other hand, less frequently, it can occur at the melanocytes of the iris (3-5%) and the ciliary body (5-8%)[159,160].

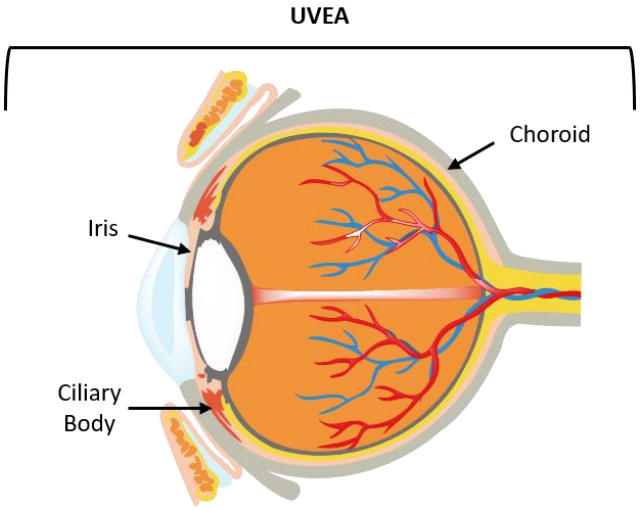

Figure 15. Scheme of the internal anatomy of the eye where the uvea formed by iris, ciliary body and choroid is represented.

In general, the melanomas of the choroid and ciliary body, metastasize faster and more frequently than those that occur from the iris because they are more aggressive and difficult to detect tumors. Although at the time of diagnosis, there is no evidence of metastasis in the majority of patients, approximately 50% of them finally develop metastasis following the initial diagnosis, and 90% of them affect the liver[163]. Once the first metastasis is detected, the average survival of the patient is less than one year[164].

The development of uveal melanoma has been associated with chromosomal alterations and oncogenic mutations[163]. The most studied aberration is the partial or complete loss of chromosome 3, which is associated with worse prognosis and metastatic progression[159]. The *BAP1* (BRCA1-associated protein 1) gene is located on this chromosome and is related to tumor suppressor activity in uveal melanoma. Mutations on this gene are related to metastatic potential[165].

There are other types of mutations in uveal melanoma, and among the most studied are those that affect GNAQ/GNA11 genes, members of the guanine nucleotide-binding G protein family. Mutations on these genes constitutively activate G-protein alpha-subunit that produces an overexpression of mitogen-activated protein kinase (MAPK) and PI3K/AKT/mTOR pathways, which are crucial to regulate cell proliferation and survival[166,167] (**Figure 16**). In addition, a previous report suggests that half of the tumors that do not present mutations in GNAQ, have it in GNA11[168]. Remarkably, several studies support that these mutations occur in up to 90% of uveal melanoma tumors [169].

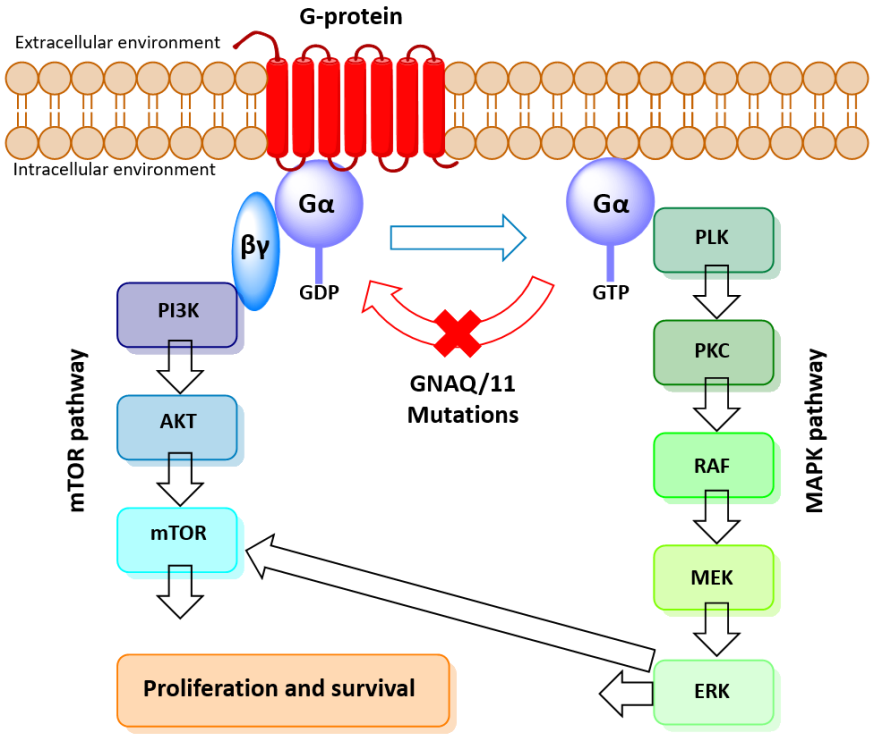

Figure 16. Schematic representation of MAPK and mTOR pathways involved in the development of uveal melanoma tumors. Mutations in GNAQ/GNA11 genes can constitutively activate the G-protein alpha-subunit and produce the overexpression of the signaling cascade in the mentioned routes triggering in the uveal melanoma tumor progression.

4.1.1.1. AZD8055 for uveal melanoma treatment

There are different treatments for local uveal melanoma tumors such as radiotherapy, laser therapy, clinical resection, or even enucleation. However, an effective treatment for metastatic uveal melanoma is not available for patients at the moment. Various chemotherapeutic drugs, immunotherapy, targeted agents against MAPK pathways have been studied without much success[170]. Thus, some patients have to take part in clinical trials to explore new treatments.

As mentioned before, mutations in GNAQ/GNA11 activate the MAPK and mTOR pathways in uveal melanoma tumors and, therefore, drugs that inhibit these pathways could be good candidates to treat metastatic uveal melanoma. In this regard, AZD8055 is a potent ATP-competitive mTOR (mTORC1-mTORC2) inhibitor that prevents kinase activity[171]. It is known that this protein is involved in many essential functions in cells, such as cell growth and autophagy. In this sense, it has been demonstrated in different studies that the use of AZD8055 can induce cell death by autophagy and decreases the

proliferation rates and cell cycle progression in many cells[172,173]. For these reasons, this drug is being investigated as a treatment for uveal melanoma models with promising results[174].

4.1.2. Albumin-stabilized gold nanoclusters (BSA-AuNCs)

One of the most used strategies to treat cancer is chemotherapy, in which different antitumoral agents are used to eliminate tumoral cells. However, these treatments have many side effects due to their high toxicity and non-selective biodistribution of drugs, which act in both healthy and tumoral cells. In the case of AZD8055, the toxicity is related to an increase of transaminases and fatigue[172]. In addition, tumoral cells can develop drug resistance due to the overexpression of membrane transporters that promote an outflow of chemotherapeutic agents to the extracellular environment[175], drug inactivation, and evasion of cells death, among others[176].

To solve some of the drawbacks associated to chemotherapy, the use of nanostructures as drug delivery system is being investigated during the last years. Among the different nanostructures, in this work, we employ gold nanoclusters (AuNCs) due to their excellent properties for biomedical applications such as sensing and imaging[177]. However, these nanostructures need to be modified to obtain stable, water dispersible, highly fluorescent, and biocompatible gold nanoclusters. In this sense, bovine serum albumin (BSA) is one of the most commonly used biomolecule employed for the stabilization of gold nanoclusters[178]. The cysteine and histidine residues present in the BSA can bind the Au^{3+}, and the tyrosine residues reduce the Au^{3+} to Au^{+} (at pH > 10) leading to BSA-stabilized gold nanoclusters (BSA-AuNCs)[179]. These BSA-AuNCs present extraordinary properties as drug delivery systems, such as chemical stability (in a range of pH from 4 to 9), large drug load capacity and biocompatibility[180].

The internalization process of BSA-AuNCs takes place by endocytosis, avoiding the passive transport of drugs into the cells and the development of chemoresistance. In addition, these nanomaterials can accumulate in the tumor site due to the enhanced permeability and retention (EPR) effect[181,182]. Thus, the concentration of drugs in these tissues can be increased, improving treatment's efficiency and reducing the side effects.

Furthermore, BSA-AuNCs show near-infrared fluorescence properties, making these nanostructures excellent agents for the imaging of tumors *in vivo*, which is favored by the EPR effect[183].

4.1.3. BSA-AuNCs-AZD for uveal melanoma treatment

In this work, we proposed the use of BSA-stabilized gold nanoclusters (BSA-AuNCs) as a platform to deliver AZD8055 for the treatment of uveal melanoma. The drug was covalently conjugated to the BSA-AuNCs to avoid their premature release of the nanostructure. The best of our knowledge, we describe here the first therapeutic approach for uveal melanoma based on the combination of nanostructures and the AZD8055.

4.1.3.1. Synthesis and characterization of BSA-AuNCs functionalized with AZD8055

4.1.3.1.1. Synthesis of BSA-AuNCs-AZD

Albumin-stabilized gold nanoclusters were prepared by the incubation of a solution of BSA with a gold salt ($HAuCl_4$) in the presence of NaOH to control the pH, and incubated at 37 °C for 16 hours. This process leads to the formation of the corresponding AuNCs stabilized by BSA (BSA-AuNCs). After the incubation, a reddish-brown solution containing BSA-AuNCs was obtained. These nanostructures lack a plasmon resonance absorption band[184,185], present in larger gold-based nanostructures such as nanoparticles and nanorods, but show a strong fluorescence emission spectrum from visible to the near-infrared (NIR) region (λ_{Ex} 380/480 nm; λ_{Em} 680 nm) (**Figure 17**).

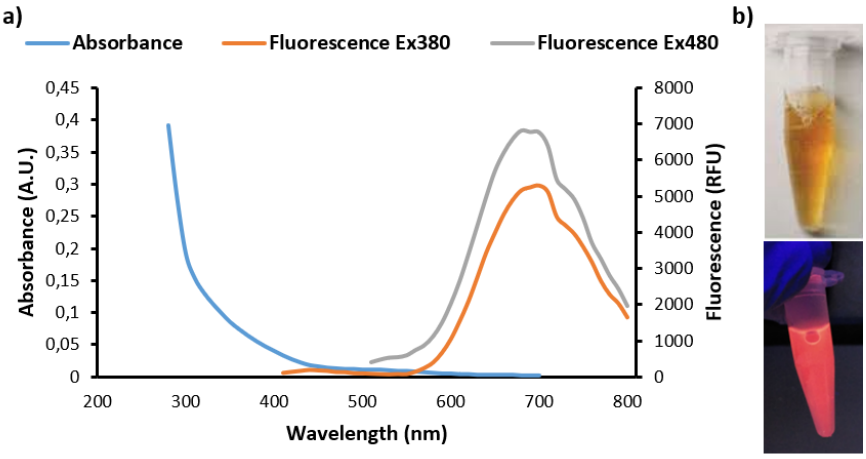

Figure 17. a) UV-Vis and fluorescence spectra of BSA-AuNCs. The fluorescence peaks at the near-infrared region (680 nm) correspond to the excitation of BSA-AuNCs with λ_{Ex} = 380 nm (orange) and λ_{Ex} = 480 nm (grey). **b**) Images of BSA-AuNCs before (top) and after (bottom) the exposure under UV light.

The resulting BSA-AuNCs were studied by transmission electron microscopy (TEM), where 50 and 80 nm albumin aggregates with a gold core of 2-5 nm were visualized (**Figure 18**).

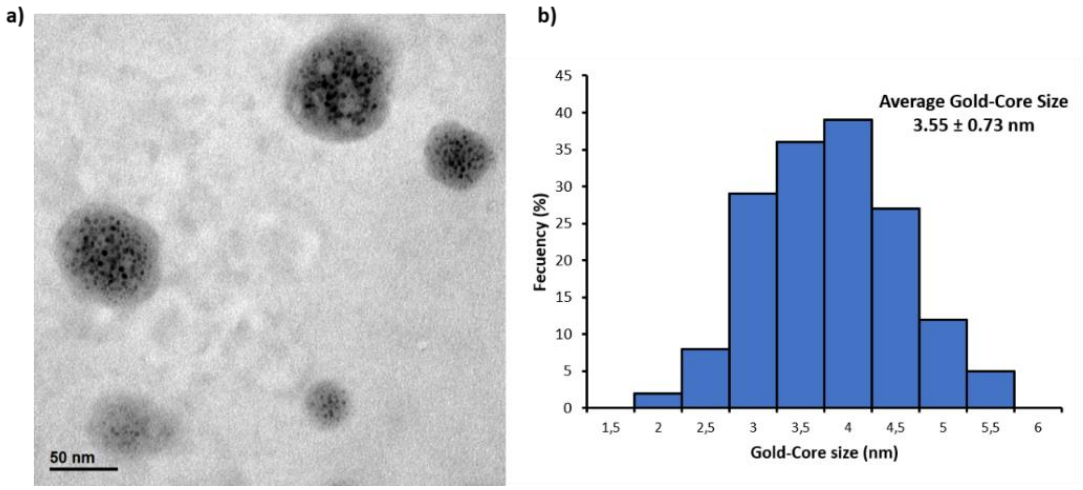

Figure 18. a) TEM image of BSA-AuNCs showing albumin aggregates of 50 and 80 nm size with a gold-core of 2-5 nm. **b)** Frequency counts of the gold core of BSA-AuNCs measure by TEM showed an average size and standard deviation of 3.55 ± 0.73 nm (n = 160).

The modified AZD8055 (**AZD-PySS**) required for the conjugation with the BSA-AuNCs was obtained from the reaction of carbonate **2** with AZD8055. Carbonate **2** was prepared in two steps by combining aldrithiol and mercaptoethanol, followed by the treatment of the resulting alcohol with bis(4-nitrophenyl) carbonate (**Figure 19**).

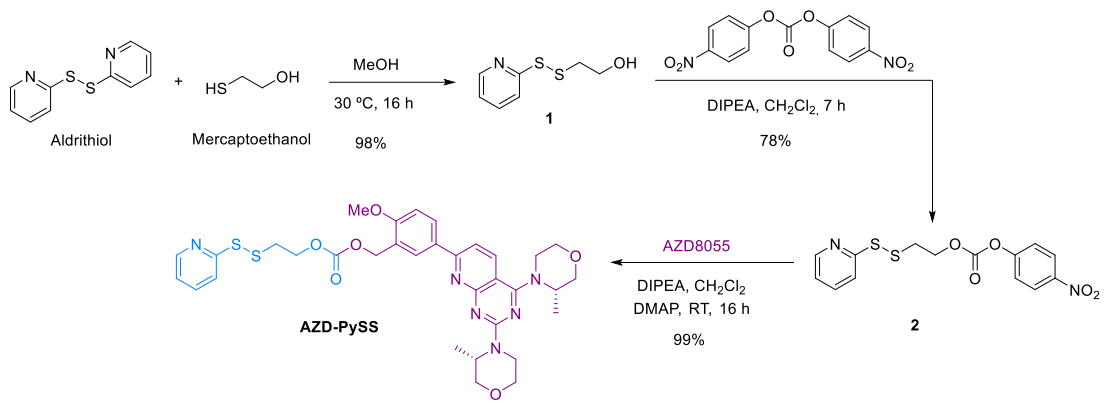

Figure 19. Modified AZD8055 (**AZD-PySS**) synthesis reaction. Representation of AZD8055 (purple) with a redox-sensitive linker (blue).

The functionalization of BSA-AuNCs with AZD-PySS required the introduction of thiol groups in the BSA-AuNCs by the addition of 20 equivalents of 2-iminothiolane. After that, the mixture was incubated at room temperature for 16 hours. Then, 100 µM of the modified drug (**Figure 19**) was added to the sulfhydryl-activated nanostructures leading to the final product (**Figure 20**).

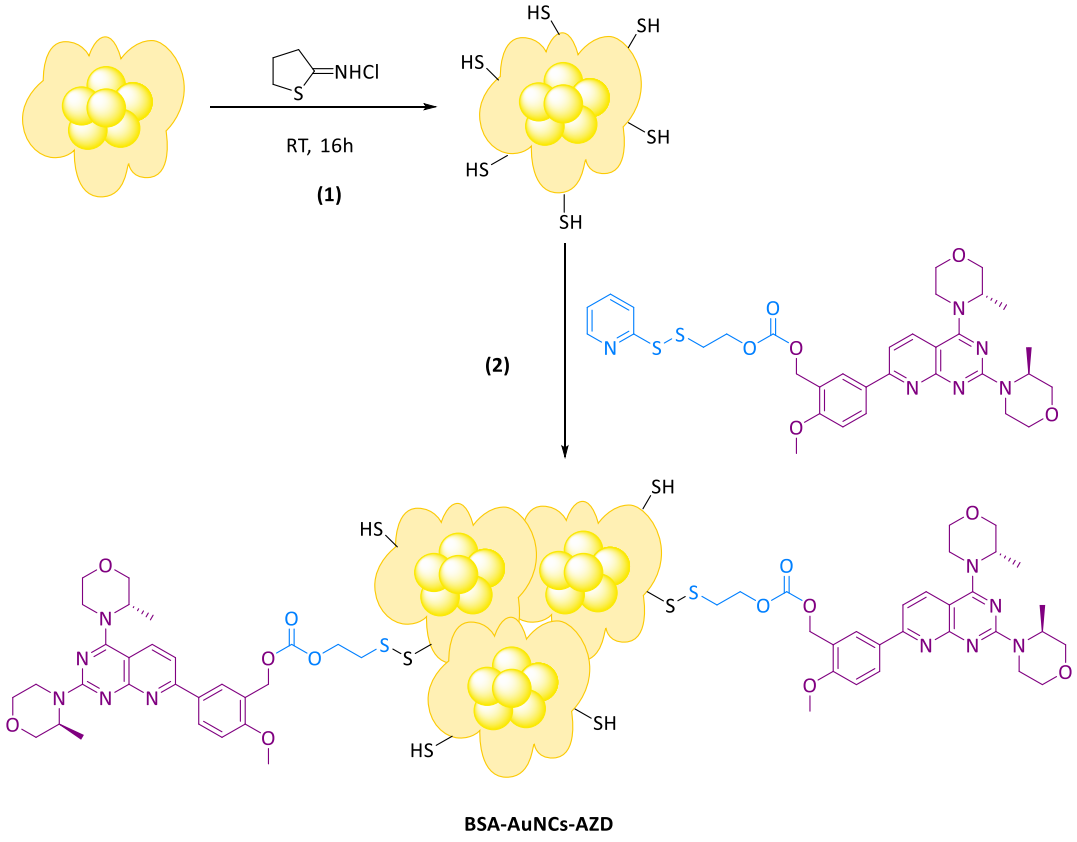

Figure 20. Schematic representation of the synthesis of BSA-AuNCs functionalized with AZD8055 modified with a tailored linker that releases the drug in a reductive environment.

4.1.3.1.2. Characterization of Functionalized BSA-AuNCs

Conjugation of the AZD8055 was studied by UV-Vis and HPLC from samples purified by exclusion chromatography to remove the unbound material. The final product presented a yellow-brown color and the UV-Vis spectra revealed the characteristic profile of AZD8055 at 380 nm (**Figure 21a**). The concentration of this derivative, was calculated interpolating the absorbance measured at 380 nm in the corresponding calibration curve (**Figure 21b**). In addition, these nanostructures showed two fluorescence peaks (λ_{Ex} = 380 nm) at 450 nm and 680 nm corresponding to AZD8055 and BSA-AuNCs-AZD, respectively (**Figure 21a**).

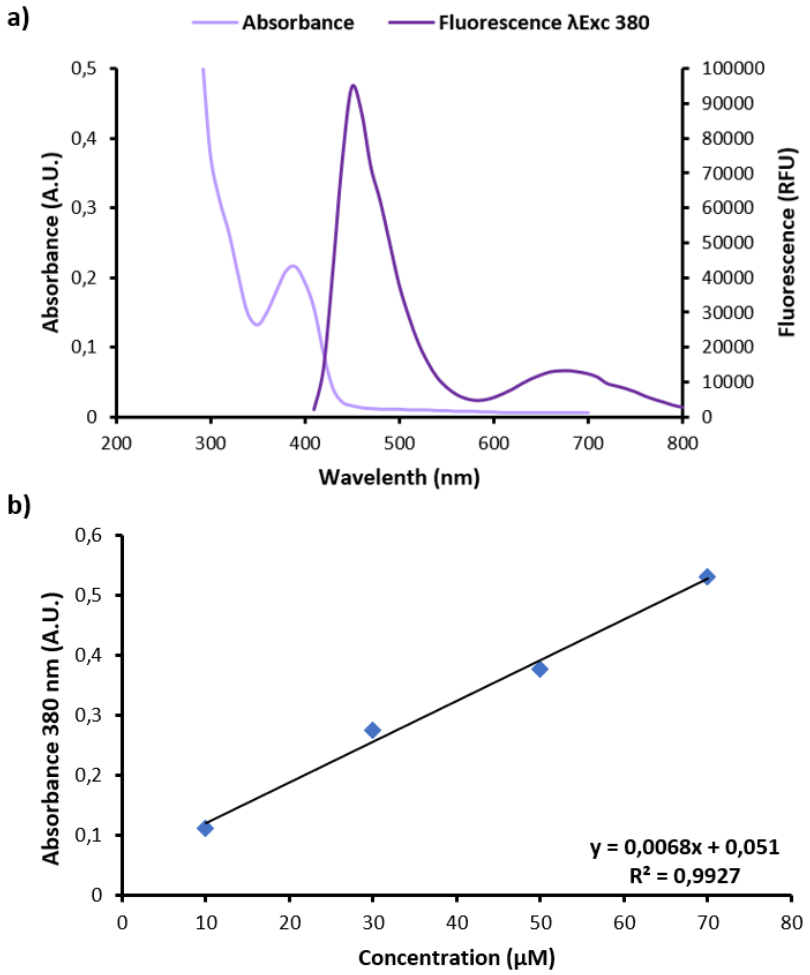

Figure 21. a) UV-Vis and fluorescence spectra of BSA-AuNCs-AZD, where the fluorescence peaks (λ_{Ex} = 380 nm) at 450 and 680 nm are attributed to ADZ8055 and BSA-AuNCs, respectively. **b)** Calibration curve of AZD8055 used to quantify the concentration of the drugs into the BSA-AuNCs.

Alternatively, the total amount of AZD8055 released from BSA-AuNCs was measured at 380 nm by HPLC. The sample was prepared by the incubation of the nanostructure with

5 mM of GSH for 72 hours to force the release of all conjugated drug. A calibration curve using the free AZD8055 at different concentrations (0, 25, 50, 75 and 100 µM), BSA-AuNCs without the sulfhydryl activation and 5 mM of GSH to resemble the conditions of the sample were used. Then, the solutions were treated with 2% $Zn(NO_3)_2$ and centrifuged to pull down the BSA-AuNCs at 16.1 rcf for 15 minutes. The supernatant was carefully removed, and 20 µL were injected into the HPLC equipment. As a control, 100 µM of free AZD8055 in DMSO was also tested. The resulting areas for the measurements were interpolating in the calibration curve to measure the concentration of AZD8055 conjugate to the BSA-AuNCs (**Figure 22**). Remarkably, the maximum peak area of the free AZD8055 showed the same retention time comparing with the drug released from the BSA-AuNCs, indicating that it is being kept its most active form without any modification.

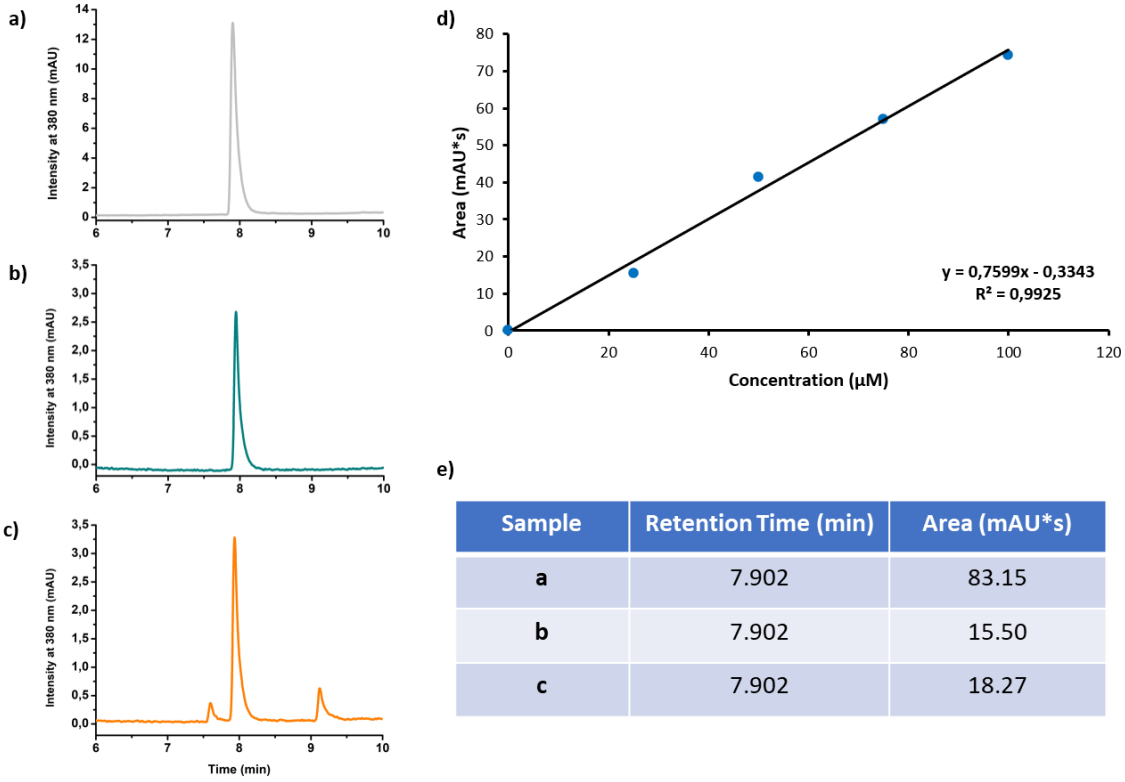

e)

Sample	Retention Time (min)	Area (mAU*s)
a	7.902	83.15
b	7.902	15.50
c	7.902	18.27

Figure 22. Representative HPLC chromatograms of **a)** 100 µM of AZD8055, **b)** calibration point using the AZD8055 at 25 µM, and **c)** AZD8055 released from BSA-AuNCs after the incubation for 72 h with 5 mM of GSH. **d)** Calibration curve of AZD8055 used to quantify the drug's concentration into the BSA-AuNCs by HPLC. **e)** Retention times and areas of the measured samples.

The agreement between the two methods also indicates that there is no evidence for unspecific attachment of the drug to the BSA-AuNCs.

To confirm the formation of the albumin-based nanoparticles after the functionalization

with the AZD8055, the size of the modified nanoparticles was studied by dynamic light scattering (DLS) in PBS. The results showed the formation of a homogeneous material with only one population with an average size of 141.2 nm (PDI: 0.180). Remarkably, the size of the nanostructure was measure after one-week storage in PBS at 4 °C showing the same size (140.5 nm, PDI: 0.199). This result indicates the excellent stability of the BSA-AuNCs-AZD, which were able to keep their colloidal stability over time (**Figure 23**).

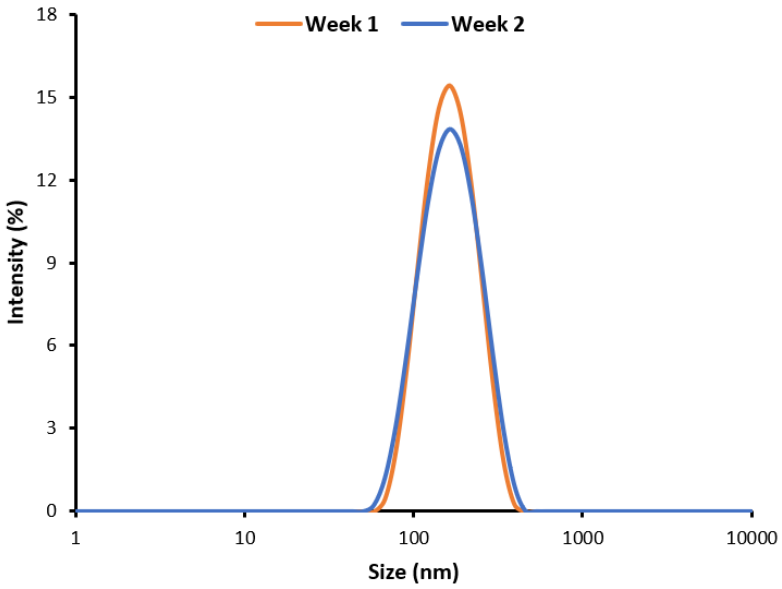

Figure 23. Size of BSA-AuNCs-AZD measured by intensity by DLS for two weeks storage at 4 °C in PBS (pH = 7.4).

Interestingly, the differences in size before and after functionalization evidence a rapid formation of albumin-based nanoparticles through self-assembly of the hydrophobic BSA domains after the conjugation of the hydrophobic drug AZD8055 (**Figure 24**)[186,187].

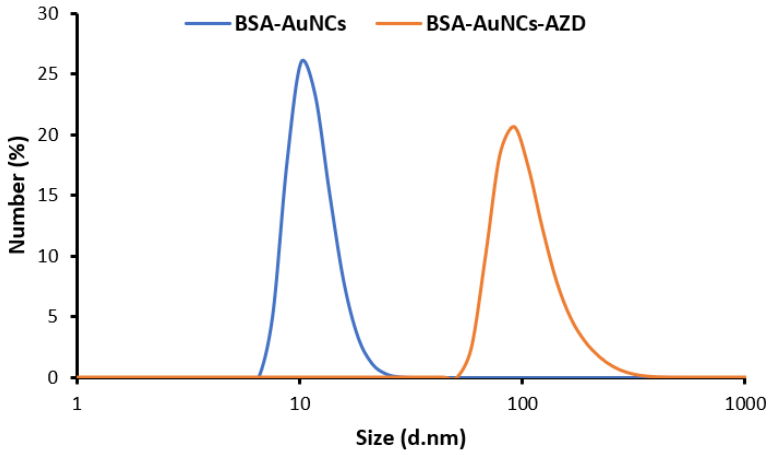

Figure 24. Size of BSA-AuNCs-AZD by number measured by DLS before (**blue**) and after (**orange**) drug functionalization.

Besides, the morphology of these nanostructures was further characterized by scanning electron microscopy (SEM) (**Figure 25a**) and atomic force microscopy (AFM) (**Figure 25b**), revealing a globular morphology with an average size of 73.29 ± 15.1 and 128.6 ± 10.6 nm, respectively. The difference in the size of the BSA-AuNCs-AZD obtained by the two techniques could be due to the different ways of preparing the samples and how each equipment works.

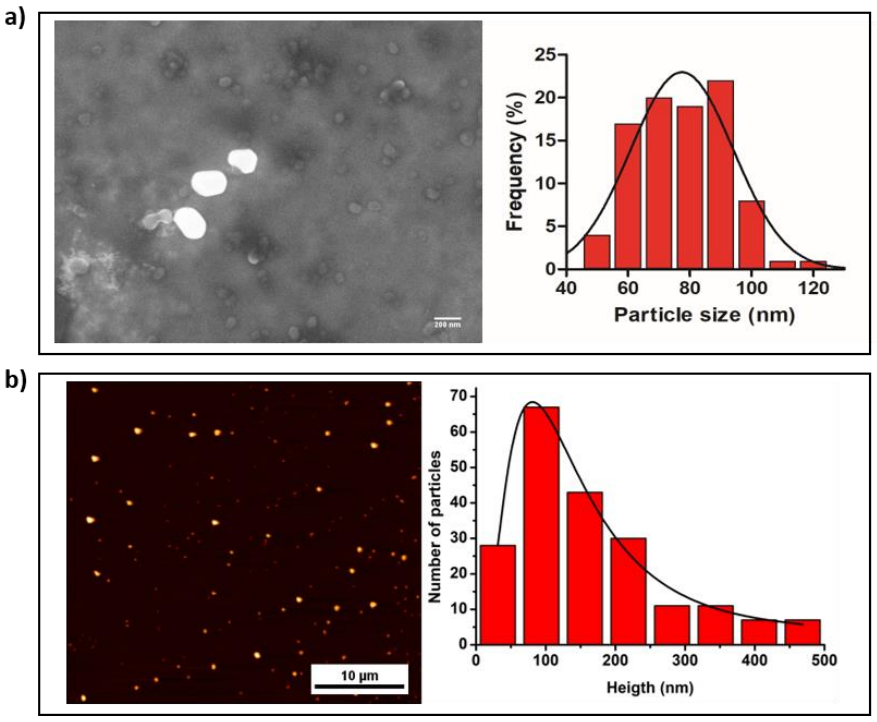

Figure 25. Size of BSA-AuNCs-AZD determined by different techniques. **a**) SEM image showed a globular morphology of BSA-AuNCs-AZD. The white-bright crystals correspond to the PBS salts. Frequency counts of BSA-AuNCs-AZD by SEM result in an average size of 73.29 ± 15.1 nm (n = 100). **b)** AFM image of BSA-AuNCs-AZD showed an average size of 128.6 ± 10.6 nm (n = 204).

4.1.3.1.3. *In vitro* controlled release of AZD8055 from BSA-AuNCs

As previously described, AZD8055 was modified with a tailored linker that contains a disulfide moiety sensitive to the reducing environment due to the GSH present inside the tumoral cells. To determine the *in vitro* release of AZD8055 from BSA-AuNCs, the nanostructures were exposed to different concentrations of GSH, 1 µM and 1mM, and the samples were evaluated after various times. Thus, BSA-AuNCs were precipitated using a zinc salt ($Zn(NO_3)_2$), and the fluorescence of the drug was measured over time (λ_{Ex} = 380 nm, λ_{Em} = 450).

In this sense, the release profile of AZD8055 from BSA-AuNCs-AZD was studied in PBS containing 1 µM and 1mM of GSH, resembling the extracellular and intracellular environment, respectively[188]. The result showed that when 1 mM of GSH was employed, 70% AZD8055 was release for BSA-AuNCs after 96 hours (**Figure 26**, orange line). Remarkably, most of the AZD8055 was released (60%) in the first 24 hours. On the other hand, when GSH 1 µM was employed, just 12% of the drug was released after 96 hours (**Figure 26**, blue line).

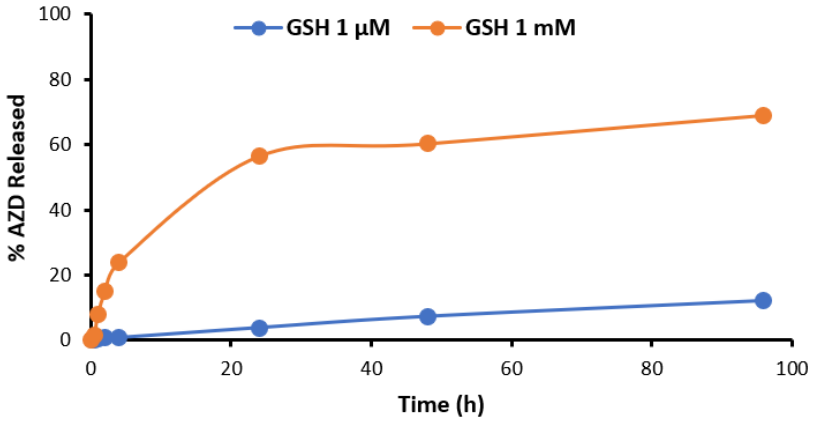

Figure 26. AZD8055 release profile from BSA-AuNCs based nanoparticles in PBS containing 1 mM (orange) or 1 µM (blue) of GSH.

4.1.3.1.4. Chemotherapeutic activity of functionalized BSA-AuNCs in uveal melanoma (Mel202) cells

To check the uptake of the nanostructures into uveal melanoma Mel202 cells, confocal microscopy was performed, taking advantage of the inherent red fluorescent properties of the BSA-AuNCs. Thus, Mel202 cells were incubated for 4 hours and washed with PBS. Cells were fixed using paraformaldehyde 4% and counterstained with DAPI (blue) and Phalloidin (green). A red fluorescence corresponding to BSA-AuNCs was observed in the cytoplasm of the Mel202 cells, confirming the internalization of the nanostructures 4 hours after treatment (**Figure 27**).

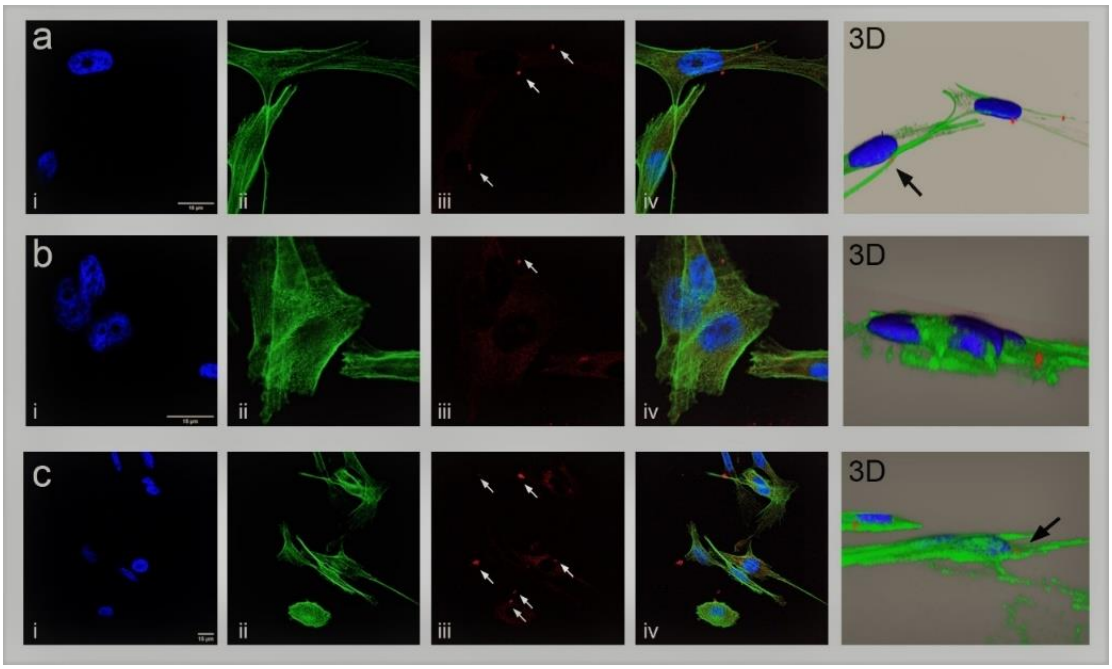

Figure 27. Confocal laser scanning microscopy images of BSA-AuNCs localization in Mel202 cells after 4 hours of incubation. The image shows 3 representative examples (**a-c**). The left side of the panels corresponds to 2D images (one section or focal plane) for (**i**) the nucleus with DAPI in blue (λ_{Ex} = 358, λ_{Em} = 461), (**ii**) actin filaments labeled with Phalloidin in green (λ_{Ex} = 495, λ_{Em} = 519 nm), (**iii**) BSA-AuNCs in red (λEx = 405, λEm = 680 nm) and (**iv**) the merge. The right side of the panels shows the 3D reconstructions of those cells. White arrows show a positive signal for BSA-AuNCs above the cellular autofluorescence. Black arrows show two examples were the BSA-AuNCs are inside the cells. Scale bar: 15µm.

Besides, as mentioned before, the maximum amount of the drug was released at 24 hours in the presence of a reducing environment. For this reason, the fluorescence signal from AZD8055 was analyzed by flow cytometry 24 hours after treatment (λ_{Ex} = 380 nm), to confirm that BSA-AuNCs-AZD were internalized into the Mel202 cells. The free drug was also studied. The results showed that both the free AZD8055 and BSA-AuNCs-AZD were internalized into the cells in a similar percentage, 99.3% and 99.9%, respectively (**Figure 28**).

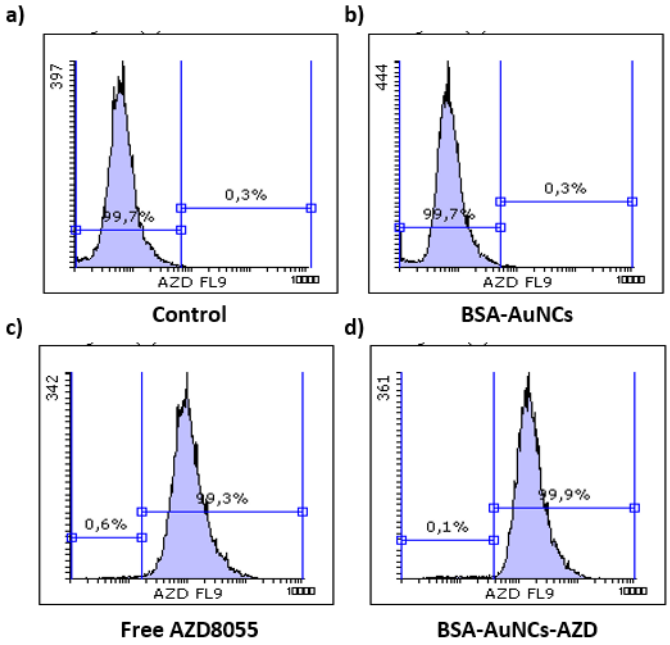

Figure 28. Flow cytometry analyses of uveal melanoma Mel202 cells at 24 hours after treatment with **a)** Control; **b)** BSA-AuNCs 0.5 µM; **c)** Free AZD8055 1.5 µM; **d)** BSA-AuNCs-AZD 0.5-1.5 µM

Then, the cytotoxic activity of BSA-AuNCs-AZD *in vitro* using the resazurin dye assay was studied. This compound is a redox indicator that provides an easy method to analyze the percentage of the viable cells with an active metabolism, which can reduce the resazurin into resofurin, a fluorescent derivative[155]. The *in vitro* assay was performed in three uveal melanoma cell lines, Mel202, OMM1.3 and Sp6.5 cells, and non-tumoral HaCaT keratinocytes, where the free AZD8055 (1.5 µM) and BSA-AuNCs-AZD (BSA-AuNCs: 1 µM; AZD8055: 1.5 µM) were incubated for 24 hours. Then, the cells were washed with PBS to remove the structures that had not been internalized and incubated 48 hours more. The viability assay showed that the uveal melanoma cells OMM1.3 and Sp6.5 were sensitive to the modified nanostructure with an effect similar to the free AZD8055 (52 and 68% cell viability, respectively). However, the antitumoral activity was higher in Mel202 cells, where BSA-AuNCs-AZD and free AZD8055 decreased the cell viability to 45% and 25%, respectively (**Figure 29**). Remarkably, in the case of the non-tumoral cell line (HaCaT keratinocytes), the nanostructure did not affect the cell viability compared to the free AZD8055, which induced a decrease of 50% (**Figure 29**).

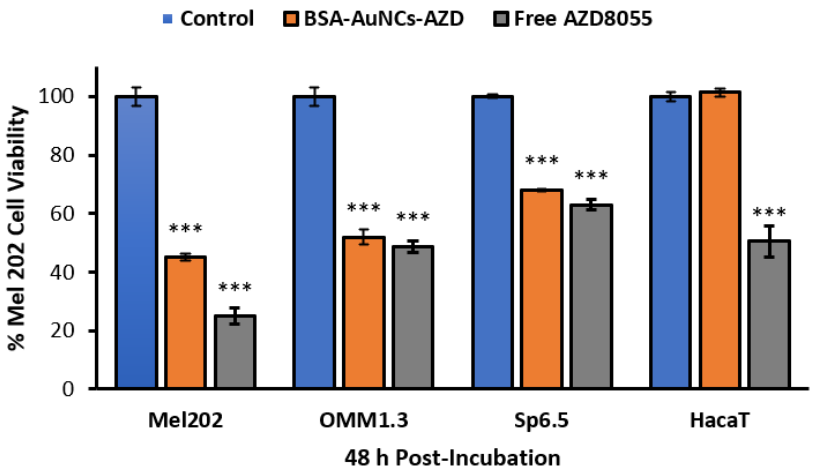

Figure 29. Cell viability of uveal melanoma Mel202, OMM1.3 and Sp6.5 cells and non-tumoral cells HaCaT keratinocytes at 48 hours post-incubation with BSA-AuNCs-AZD and free AZD8055 studied by resazurin assay. Statistical analysis was performed using one-way ANOVA Tukey's test (each group vs. control). ***p-value < 0.001.

In addition, to confirm the biocompatibility of the nanostructure, Mel202 cells were treated with non-functionalized 1 µM BSA-AuNCs for 24 hours. The result evidenced the lack of toxicity of these nanostructures, compared to untreated cells (**Figure 30**). This was expected based on complementary experiments performed in the group in other cell lines (see results, **chapter 4.2**)[189,190].

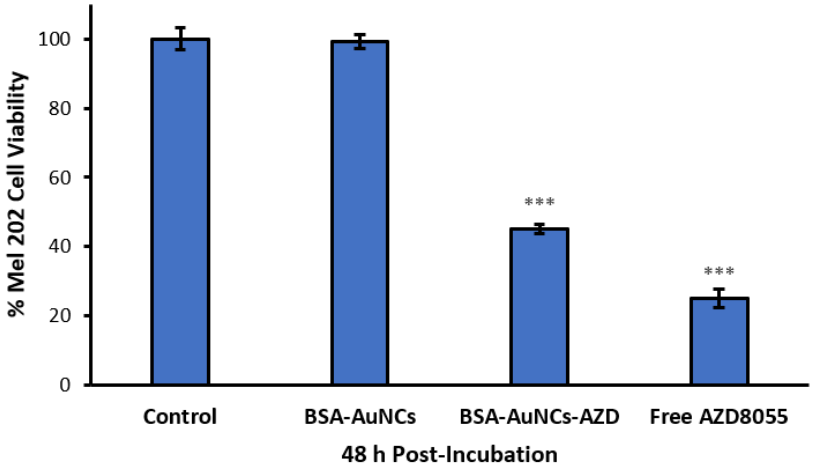

Figure 30. Cell viability of uveal melanoma Mel202 cells at 48 hours post-incubation with BSA-AuNCs (1 µM), BSA-AuNCs-AZD (1 µM – 1.5 µM) and free AZD8055 (1.5 µM) evaluated by resazurin assay. Statistical analysis was performed using one-way ANOVA Tukey's test (each group vs. control). ***p-value < 0.001.

To check the endocytosis pathways related to the uptake of BSA-AuNCs-AZD, we tested in Mel202 cells two different endocytosis inhibitors such as chlorpromazine and filipin III to block clathrin-mediated and caveolae-mediated uptake process, respectively[191,192].

In this regard, cells were pre-treated with the inhibitors for 1 hour before the incubation with the nanostructures (6 µM) for 4 hours. Then, the cells were washed to remove the BSA-AuNCs-AZD that were non-internalized. The higher concentration used in this experiment was due to an attempt to force the cytotoxic activity of the drug at 24 hours after treatment. The viability assay in the presence of the inhibitors showed that filipin III, along with the BSA-AuNCs-AZD, was able to reduce cell viability by 32% compare to the cells pre-treated with the inhibitor. However, employing chlorpromazine, a clathrin-transport inhibitor, cell viability was almost not affected. These results indicate that the main internalization pathway for BSA-AuNCs-AZD could be clathrin-mediated endocytosis (**Figure 31**).

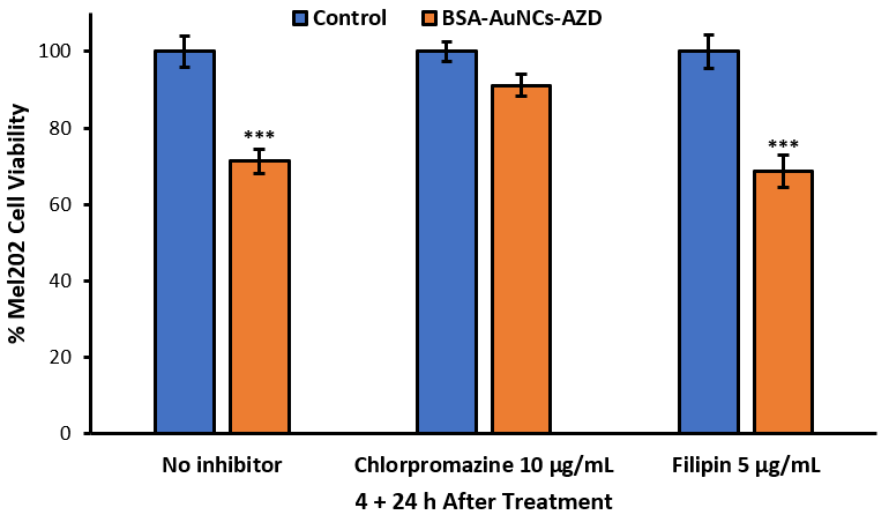

Figure 31. Effects of endocytosis inhibitors in uveal melanoma Mel202 cell viability treated with BSA-AuNCs-AZD. Cells were pre-treated for 1 hour with chlorpromazine and filipin III and then incubated BSA-AuNCs-AZD for 4 hours more. After this incubation time, cells were washed with PBS and cell viability assay was performed 24 hours later by resazurin assay. Statistical analysis was performed using one-way ANOVA Tukey's test (each group vs. control). ***p-value < 0.001.

Finally, it is known that the internalization process, the size, and charge of the nanoparticle, as well as the metallic components of structures, can promote the production of reactive oxygen species (ROS)[193]. For this reason, the potential of the BSA-AuNCs-AZD as generators of ROS was measured. In this regard, the widely used probe 2',7'- dichlorodihydrofluorescein diacetate (H_2DCF-DA) were employed for this experiment. This dye has a low fluorescence signal in its reduced state, but when oxidized by the presence of ROS, it becomes very fluorescence[194]. In this case, cells were

co-incubated with the nanostructures and the probe for 4 hours. The fluorescence signal of the H_2DCF-DA was immediately measured after the treatment (λ_{Ex} = 485, λ_{Em} = 528). The results showed that BSA-AuNCs did not produce a significant difference in ROS generation compared to the control. However, BSA-AuNCs-AZD generates an increase in almost three times the levels of ROS (**Figure 32a**). This result was confirmed by fluorescence microscopy (**Figure 32b**).

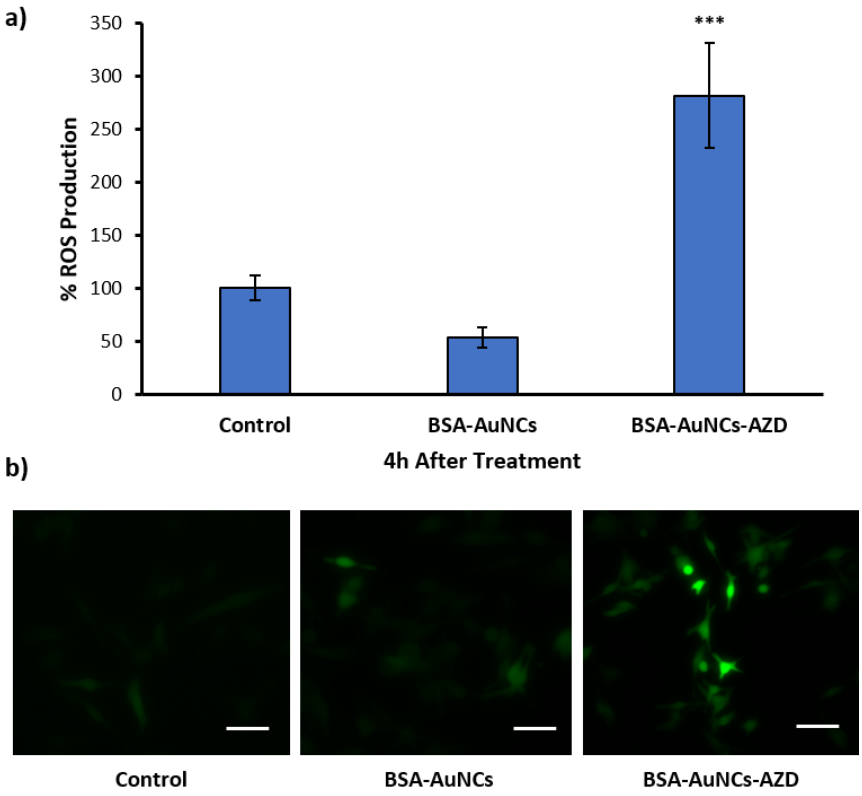

Figure 32. a) ROS production in Mel202 cells measured by H_2DCF-DA after 4 hours of treatment. Data corresponded to mean ± S.D. values and were normalized with respect to the control. Statistical analysis was performed using one-way ANOVA Tukey's test (each group vs. control). ***p-value < 0.001. **b)** Fluorescence microscopy images of ROS production in Mel202 cells at 4 hours after treatment with the nanostructures and the probe. The green color represents the generation of ROS. Scale Bar: 50 µM.

4.1.3.1.5. Chemotherapeutic activity of BSA-AuNCs-AZD in *In Vivo* models of uveal melanoma

The final step in this work was the evaluation of the therapeutic potential of this system in *in vivo* models. To carried out this experiment, the scaled-up of the BSA-AuNCs-AZD preparation was necessary. In this case, the final solution had a concentration of 376.5 µM of BSA-AuNCs (instead of the previous 20 µM) and 1.5 mM of AZD8055.

In this regard, we established a xenograft model in 15 immuno-depressed mice injecting the uveal melanoma Mel202 cell line subcutaneously using Matrigel. Once the tumors reach the appropriate size of around 0.8 cm^2, the animals were treated with PBS, AZD8055, BSA-AuNCs-AZD (intratumoral (i.t.) and intravenously (i.v.)) once a week for two weeks.

The first injection was administrated on day 15 after the inoculation of the tumoral cells (**Figure 33a**, red arrow). The effect of these compounds was evaluated every 3 days for 15 days. While with the intratumoral injection of free AZD8055 the tumor continued to grow, treatment with BSA-AuNCs-AZD intratumoral and intravenously stabilized or even decreased the tumor surface, respectively, compared with the control of PBS. The second injection took place on day 22 (**Figure 33a**, red arrow). The sizes of tumors of the control mice (PBS) increased steadily until they reach more than 1 cm^2. Conversely, after the second intratumoral injection of AZD8055, the size of the tumors was reduced, but less than when BSA-AuNCs-AZD were employed intratumorally and intravenously (**Figure 33a, b and c**).

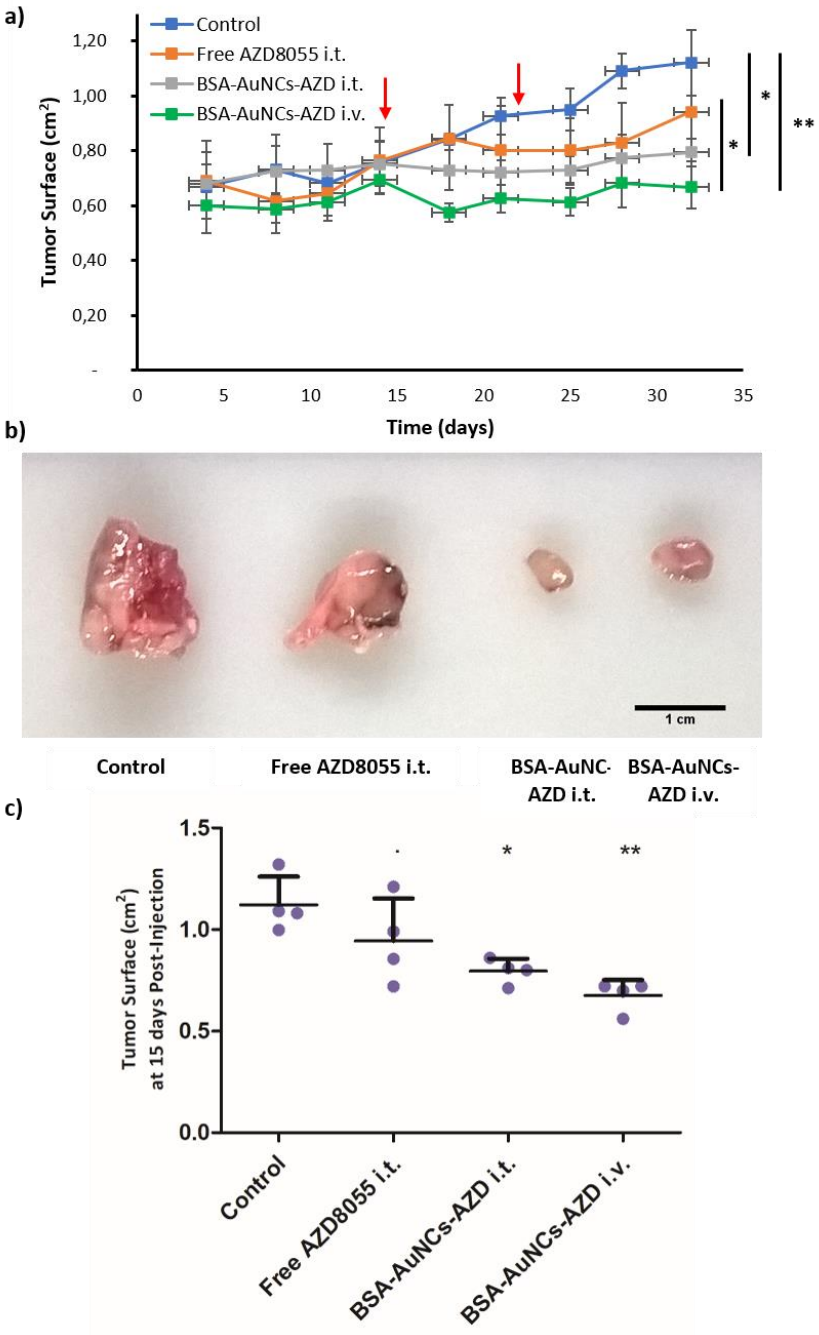

Figure 33. a) Tumor growth curves of different groups of mice after two doses of treatment with PBS, Free AZD8055 intratumoral, BSA-AuNCs-AZD intratumoral (i.t.), BSA-AuNCs-AZD intravenously (i.v). **b)** Representative image of tumor volume at the end of the treatments. **c)** Tumor surface of the different groups of mice on day 32 after the mentioned treatment. In all cases, data correspond to mean ± S.D. values (n = 4) and statistical analysis was performed using one-way ANOVA, Student-Newman-Keuls test. ·p-value < 0.1, *p-value <0.05 and **p-value <0.01.

Finally, the hematoxylin/eosin staining (H&E) at 20 days post-injection did not show significant damage in the liver and spleen (**Figure 34**), indicating the low toxicity of the BSA-AuNCs-AZD in other organs of the body.

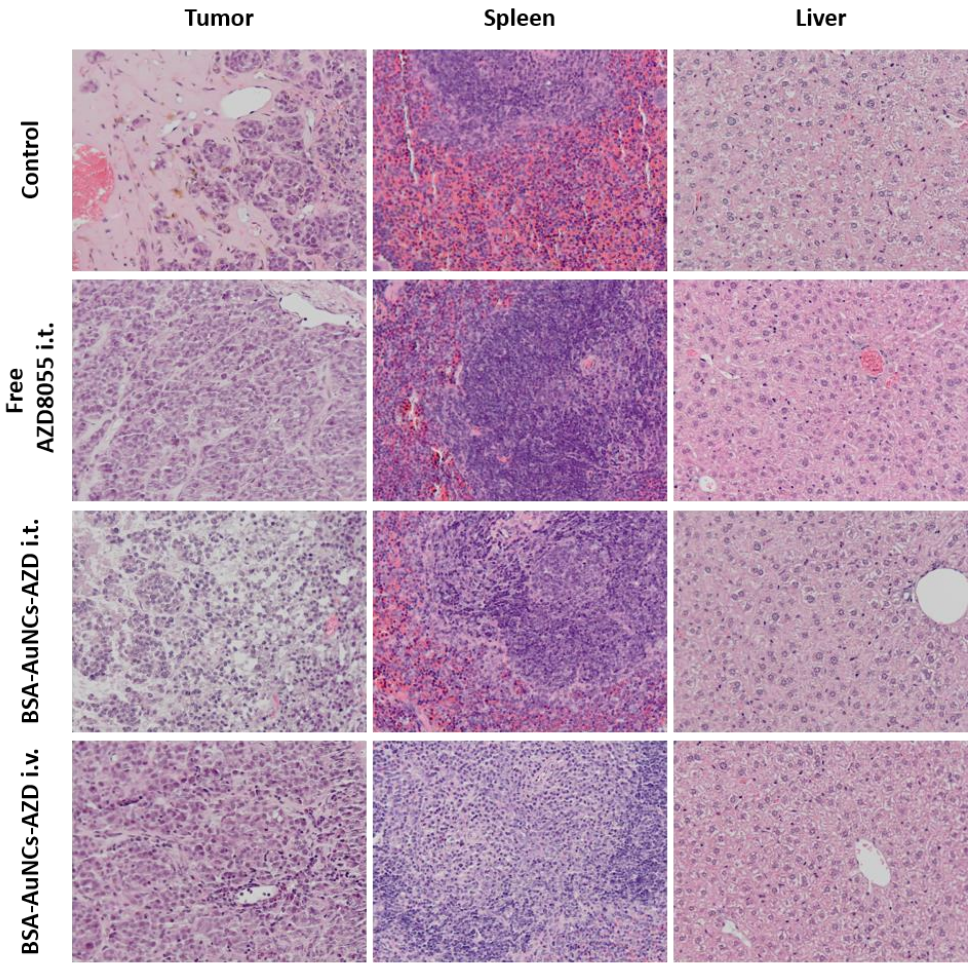

Figure 34. Representative images of tissue pathology (hematoxylin-eosin staining; magnification 20X) of tumor section, spleen and liver from mice treated with Free AZD8055 and BSA-AuNCs-AZD intratumoral and intravenously at 15 days after treatment.

It is important to note that the dose employed in these experiments (6 mg/Kg weekly) is 23 times lower than the one used in previous reports (20 mg/Kg daily)[171,173]. In addition, AZD8055 is a very hydrophobic drug and their conjugation into BSA-AuNCs allows their intravenous injection of AZD. For this reason, this system provides an excellent strategy for the systemic drug delivery of hydrophobic drugs.

4.2. Albumin-stabilized gold nanoclusters functionalized with DOX and SN38 (BSA-AuNCs-DS) for breast cancer treatment

4.2.1. Breast cancer

Breast cancer is the most common cancer in women and the second cause of death. The global incidence of this cancer represents approximately 15% of all cancer among women[195]. This tumor arises from the breast tissues, where the cells grow uncontrollably, leading to the formation of a mass. Breast is formed mainly by two types of tissues, the glandular and stromal tissues. Most breast cancer begins in the glandular tissue, which houses the lobules (milk gland) and the ducts[196].

Depending on the tumor's location, they can be classified as *in situ* or invasive by the histological type, size, and if it is metastatic. Through the gene expression analyses of different biomarkers such as estrogen (ER) and progesterone (PR) receptors and human epidermal growth factor receptor 2 (HER2), breast cancer could be sub-classified into four molecular subtypes according to **table 6**[197,198].

	ER	PR	HER2
Luminal A	+	+	-
Luminal B	+	+	+
HER2-type	-	-	+
Basal-like or triple-negative	-	-	-

Table 6. Classification of breast cancer determined through gene expression analysis. ER, estrogen receptor; PR, progesterone receptor; HER2, human epidermal growth factor receptor 2.

The response to treatments and prognosis is very much related to the molecular subtypes of breast cancer. Therefore, these parameters are usually evaluated in patients[199–201].

- Luminal A patients (58.5 % incidence) have the best prognosis. These cancers present a low proliferative grade, good differentiation, and lowest risk to relapses.
- Luminal B patients (14% incidence) have a slightly worse prognosis. These cancers are more aggressive than luminal A, with a higher proliferative grade.

- HER2-type cancer (11.5% incidence) is a more aggressive tumor with a low grade of differentiation. In addition, p53 mutations are detected in many cases. Despite this, HER2 type tumor is generally successfully treated with HER2 monoclonal antibody (trastuzumab) in combination with conventional chemotherapy.
- Basal-like or triple-negative cancer (16% incidence) is the more aggressive type and has the worst prognosis. It is characterized by forming the largest tumors with poor differentiation, high division rates, necrotic zones, pushing borders and lymphocytic infiltrate. Metastasis in other organs and BRCA1 gene mutations are very common in this type of cancer.

Currently, the most common therapies involve local treatments such as surgery and radiotherapy, and systemic treatments that can reach any part of the organism. Depending on the type of breast cancer, the treatment can vary in different options[202,203]. On the one hand, if the tumor expresses hormone receptors (ER+ and PR+), treatment consists of hormone therapy with drugs that reduce hormone to prevent the interaction with breast cancer cells. On the other hand, tumors that overexpress specific molecules on their surface (e.g., HER2) can be treated with targeted therapies, such as small molecules and monoclonal antibodies, which block cell growth and prevent metastases from damaging healthy tissues. Finally, different chemotherapeutic drugs with cytotoxic activity may be given before and after surgery to shrink the tumor or prevent new ones from forming elsewhere in the body.

These treatments have demonstrated high effectiveness; however, they present a lot of drawbacks that must be improved, such as optimal biodistribution of drugs, high toxicity leading to side effects, and the multidrug resistance developed by tumoral cells[204]. To solve this disadvantage, chemotherapy is usually administrated as a combination of drugs with different mechanisms of action to achieve a synergistic effect[205]. However, the different solubility and pharmacokinetics of the drugs, could reduce the efficacy of the combined treatments due to the different temporally concentrations of the drugs in the target tissues.

In this regard, the development of new treatments for breast cancer based on nanoparticles for drug delivery could solve some of this disadvantage.

4.2.2. Albumin-stabilized gold nanoclusters functionalized with DOX and SN38 (BSA-AuNCs-DS) for breast cancer treatment

As mentioned before (see results, chapter **4.1**), the albumin stabilized gold nanoclusters (BSA-AuNCs), are not toxic materials that have been used as vehicles to deliver drugs, enhancing their blood circulation time and allowing their accumulation at the target tissues (EPR effect). As a consequence, this strategy reduces the toxicity and side effect of conventional chemotherapy and improve the efficiency of the treatments by avoiding the multidrug resistance mechanism developed by the tumor cells.

In particular, for the modification of BSA-AuNCs, doxorubicin (DOX) and SN38 were selected. On the one hand, DOX is an anthracycline chemotherapy drug used to treat different kinds of cancer, including leukemia, lymphomas, multiple myeloma, breast cancer, sarcoma, lung, gastric, ovarian, thyroid and pediatric cancers. However, their use is limited because it is a cardiotoxic drug, and cumulative doses can induce significant damage[12]. Particularly, anthracyclines produce cell damage by two primary mechanisms, such as the intercalation in the DNA and the disruption of topoisomerase II (TOP2A) mediated DNA repair, and the generation of free radical leading to damage in cell membranes, DNA and proteins. DOX is metabolized in cells in a process that releases reactive oxygen species (ROS), which are responsible for the cell damage that leads to apoptosis pathways[206–208] (**Figure 35a**). On the other hand, SN38 (7-ethyl-10-hydroxy-camptothecin) is an analog of camptothecin (CPT) that shows enhanced anti-cancer activity (up to 1000-fold more cytotoxic). However, this drug's use is limited by its low aqueous solubility and stability at pH > 6. This drug inhibits topoisomerase I (TOP1), resulting in DNA breaks and apoptosis[209,210] (**Figure 35b**).

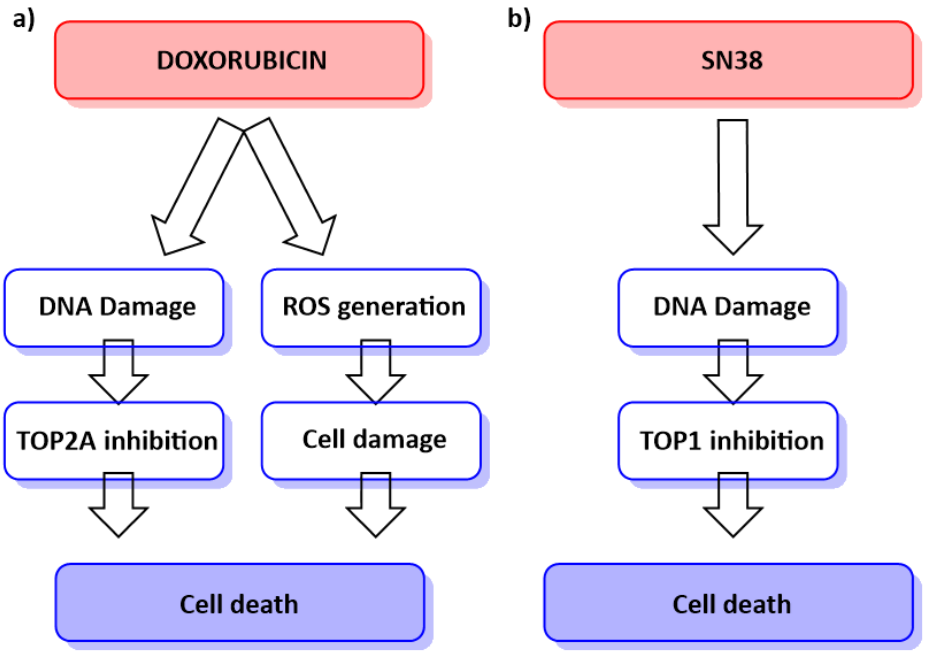

Figure 35. Schematic representation of **a)** doxorubicin and **b)** SN38 mechanism of action.

Recent studies revealed that the combination of DOX and SN38 conjugated into nanostructures showed a synergistic effect, enhancing the cytotoxic activity of these drugs and reducing the side effects of the treatments[211,212].

In this work, we proposed the use of BSA-stabilized gold nanoclusters as a platform to deliver DOX and SN38 in the same nanostructure for combined therapy of breast cancer. This system overcomes the solubility problem and improves the pharmacokinetics of the drugs, increasing the treatment's efficacy. Thus, DOX and SN38 were covalently conjugated to the BSA-AuNCs using two different tailored linkers that control their release through internal stimuli of cancer cells (pH and reducing environment), preventing the premature release of the drugs.

4.2.3. Synthesis and Characterization of BSA-AuNCs Functionalized with DOX and SN38

4.2.3.1. Synthesis of BSA-AuNCs-DS

The synthesis of albumin-stabilized gold nanoclusters (BSA-AuNCs) was performed as previously described (see sections **3.2.2** and **4.1.3.1**).

Doxorubicin drug linker (**DOX-iMal**) was synthesized from amino valeric acid in a few steps. Initially, the amino moiety was transformed in the corresponding maleimide by

the reaction with maleic anhydride, and the carboxylic acid activated as succinimide ester (**3**) in one pot. Then, from the reaction of compound **3** with *tert*-butyl carbazate and its subsequent treatment with trifluoroacetic acid (TFA), the nucleophilic hydrazine ester **4** was obtained. Finally, the reaction of **4** with DOX in the presence of a catalytic amount of TFA yielded the corresponding **DOX-iMal** (**Figure 36**).

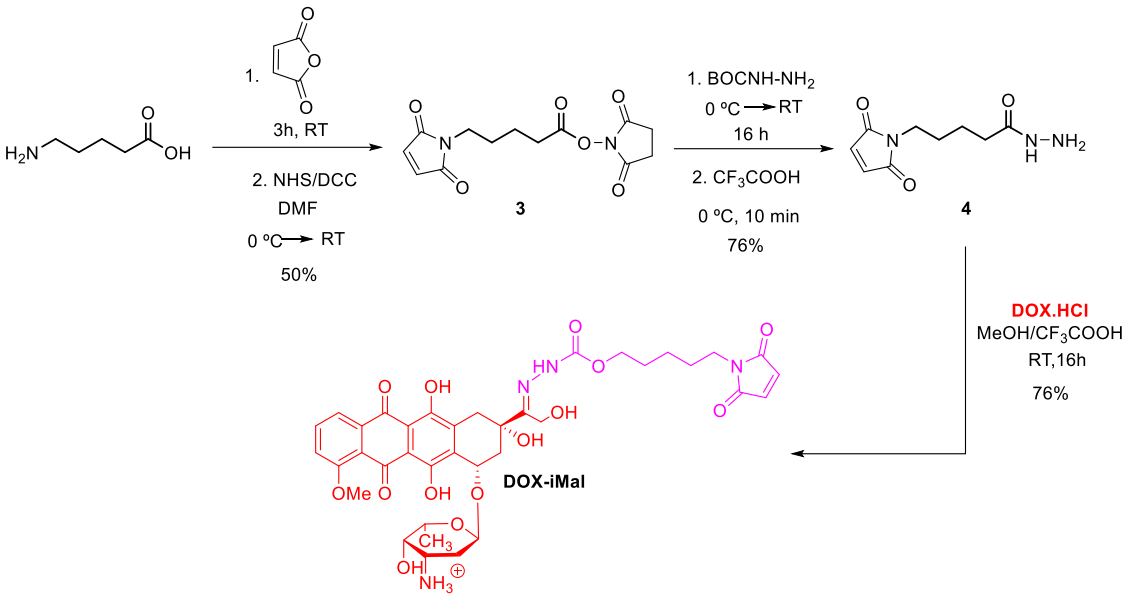

Figure 36. Modified DOX (**DOX-iMal**) synthesis reaction. Representation of DOX (red) with a redox-sensitive linker (pink).

Modified SN38 (**Figure 37**) for conjugation with BSA-AuNCs was obtained from compound **2** following the procedure described with AZD8055 (see Method, **3.2.1.1**).

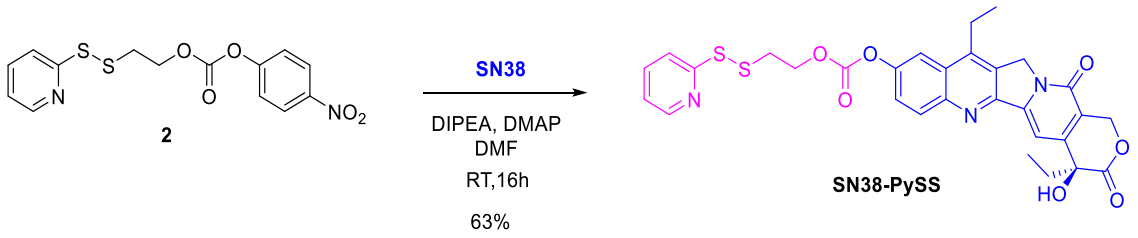

Figure 37. Modified SN38 (**SN38-PySS**) synthesis reaction. Representation of SN38 (blue) with a redox-sensitive linker (pink).

To prepare BSA-AuNCs with DOX-iMal and SN38-PySS, thiols groups were introduced onto the surface of the BSA-AuNCs using 20 equivalents of 2-iminothiolane. Then, the modified drugs were added in their corresponding concentration to the sulfhydryl-activated BSA-AuNCs leading to the formation of BSA-AuNCs based nanoparticles (**Figure 38a**). Particularly, the designed linker for DOX[213] contains a pH-sensitive imine

moiety to control the drug's release in acidic conditions and a maleimide group to ease its conjugation with the previously sulfhydryl-activated BSA-AuNCs (**Figure 38b**). Conversely, the linker employed in the case of SN38 contains a disulfide-based self-immolative moiety and a 2-mercaptopyridyl leaving group to ease the conjugation with the sulfhydryl-activated BSA-AuNCs[214] (**Figure 38c**).

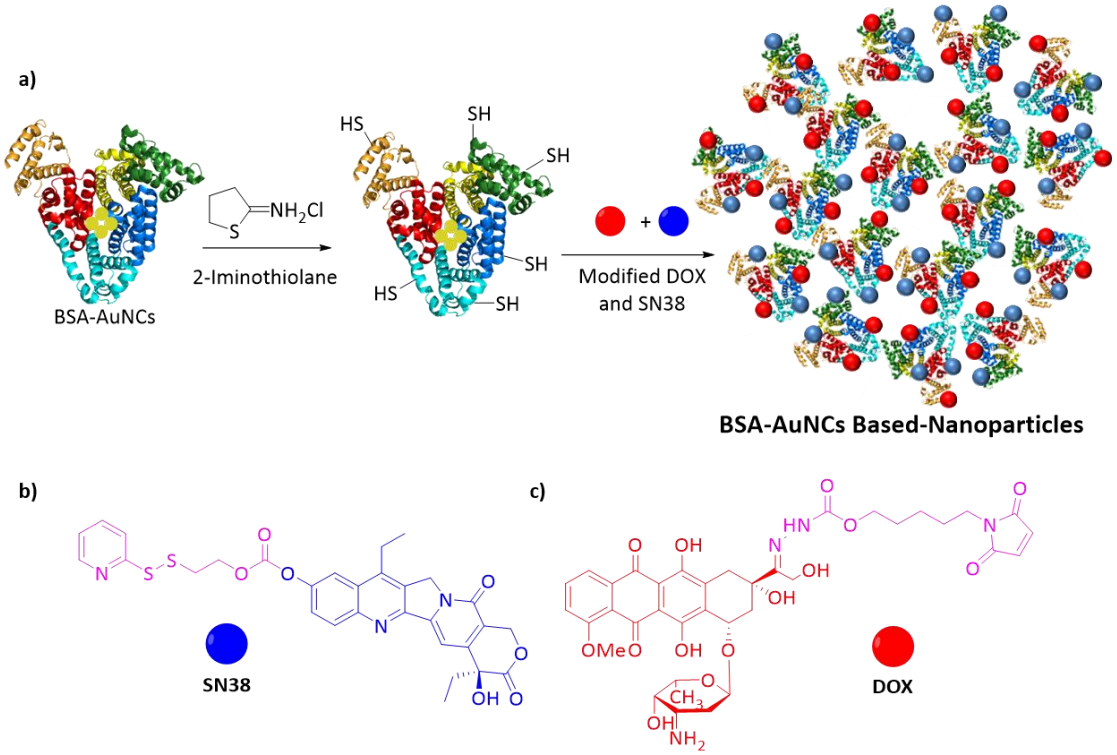

Figure 38. Synthesis of nanoparticles based on BSA-AuNCs modified with Doxorubicin (DOX-iMal) and SN38 (SN38-PySSO). **a)** Schematic representation of the synthesis of BSA-AuNCs-DS based nanoparticles for combined chemotherapy; **b)** Representation of DOX (red) modified with a pH-sensitive linker (pink); and **c)** SN38 (blue) modified with a redox-sensitive linker (pink).

Using these derivatives, the BSA-AuNCs were modified with **DOX-iMal** (BSA-AuNCs-D), SN38-PySS (BSA-AuNCs-S), or both (BSA-AuNCs-DS). The conjugation of one or two drugs onto BSA-AuNCs was performed just by mixing the elements. Therefore, this procedure provides an easy and efficient way of synthesizing vehicles for drug delivery. It is worth highlighting that the linkers employed allowed the release of the drugs with no modification, ensuring their biological activity.

4.2.3.2. Characterization of functionalized BSA-AuNCs

The incorporation of DOX and SN38 on the BSA-AuNCs was studied by UV-VIS (**Figure 39**) after removing unbound material using a Sephadex NAP-10 column. First, the UV-

Vis spectra of modified BSA-AuNCs showed the standard absorption profile of BSA-AuNCs. Second, the characteristic bands of DOX and SN38 (495 nm and 380 nm, respectively), were identified in the samples corresponding to BSA-AuNCs-D and BSA-AuNCs-S. Finally, UV-VIS spectra of the bifunctionalized BSA-AuNCs-DS exposed the bands corresponding to the three different components, revealing that both drugs (DOX and SN38) were covalently attached in a very efficient way to the surface of BSA-AuNCs.

The concentration of the drugs was obtained by interpolating the absorbance measured in the corresponding calibration curve, obtaining 37 µM and 80 µM, respectively (**Figure 39b and 39c**). In the case of bi-functionalized nanoclusters BSA-AuNCs-DS, the concentrations of DOX and SN38 were 37 µM and 70 µM, respectively.

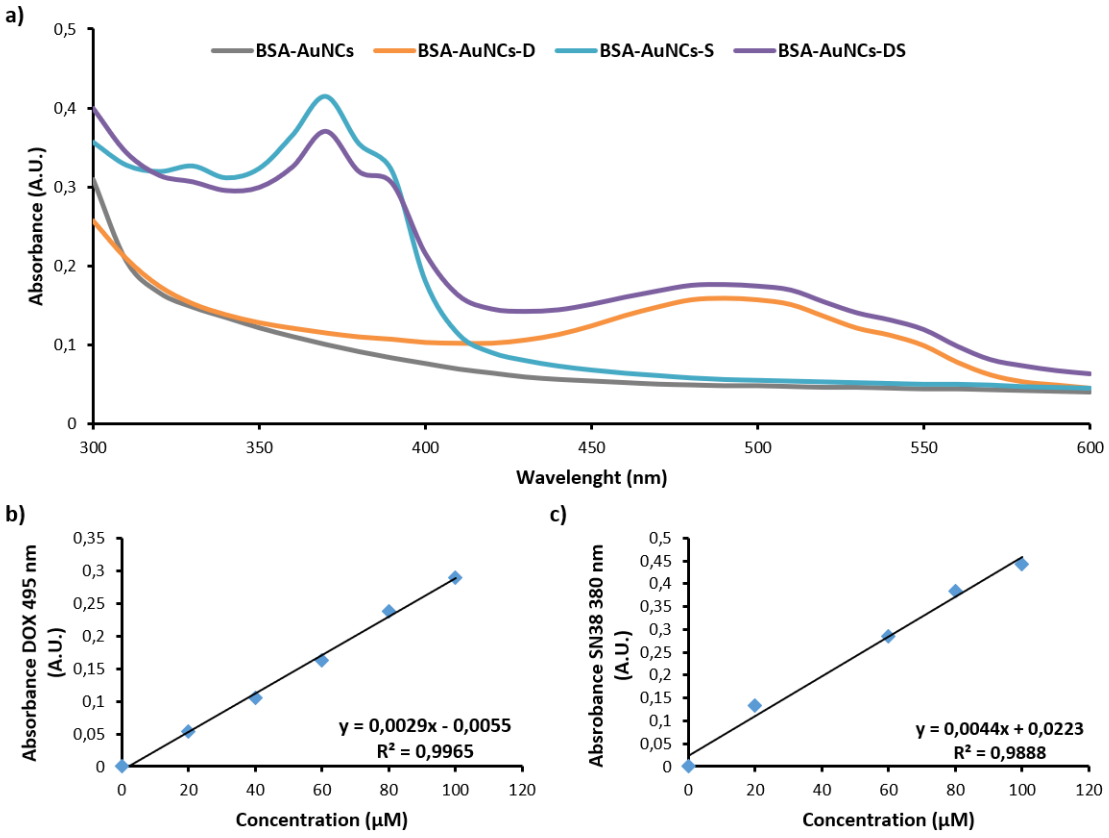

Figure 39. a) UV-Vis spectra of BSA-AuNCs (grey), and BSA-AuNCs modified with DOX (BSA-AuNCs-D) (orange), SN38 (BSA-AuNCs-S) (blue) and both DOX and SN38 (BSA-AuNCs-DS) (purple). **b, c)** Calibration curves of DOX and SN38, respectively used to quantify the concentrations of these drugs into the BSA-AuNCs.

To check the formation of the nanoparticles after the modification of BSA-AuNCs with the drugs, the sizes of the functionalized nanostructures were studied by dynamic light

scattering (DLS) at the end of the synthesis in PBS. On the one hand, measurements of the BSA-AuNCs-D showed the formation of a non-homogeneous material with two nanoparticle size distributions (**Figure 40**, orange line). This result indicates that DOX was a hydrophilic drug that was not able to induce the self-assembly of the BSA-AuNCs to form a stable population of nanoparticles. On the contrary, when the hydrophobic SN38 was employed, only one population of nanostructures was obtained with an average size of 117.5 nm and a polydispersity index of 0.277 (**Figure 40**, blue line). Finally, the combined use of DOX and SN38 in the same nanostructure does not disrupt the formation of a monodispersed population of nanoparticles with an average size of 190.8 nm and a PDI of 0.263 (**Figure 40**, grey line).

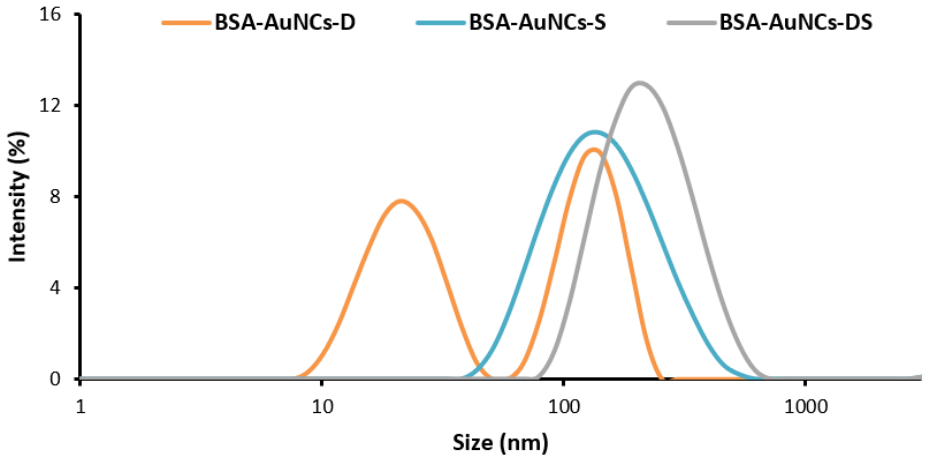

Figure 40. Size of Doxorubicin BSA-AuNCs-D (orange), BSA-AuNCs-S (blue) and BSA-AuNCs-DS (grey) measured by dynamic light scattering (DLS).

In addition to that, modified nanostructures bearing both drugs (BSA-AuNCs-DS) were stored in PBS at room temperature for fifteen days, and their stability and size were measured by DLS. The results obtained from nanoparticles size and PDI showed that BSA-AuNCs-DS were able to keep their size and colloidal stability during these days with minimum variation (**Figure 41**).

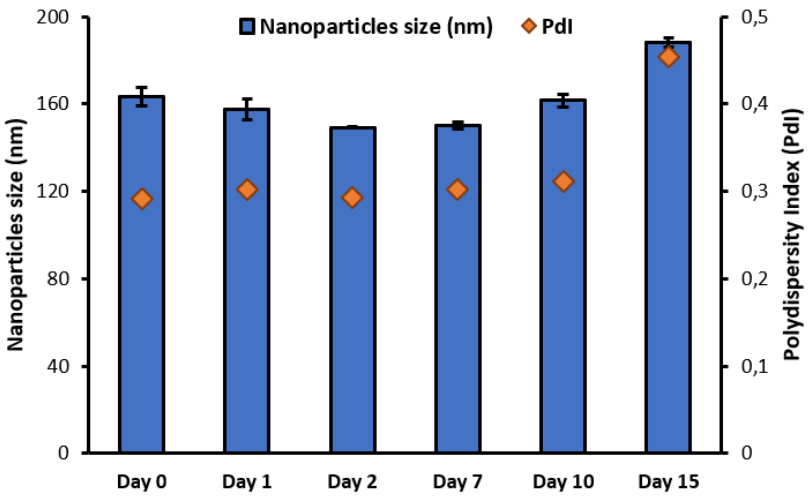

Figure 41. Stability study in PBS (pH = 7.4) of BSA-AuNCs-DS over time stored at room temperature. Mean ± SD, n = 3[190].

Besides, all the nanostructures obtained were characterized by scanning electron microscopy (SEM). In all cases, functionalized BSA-AuNCs showed a globular morphology when they were analyzed (**Figure 42**).

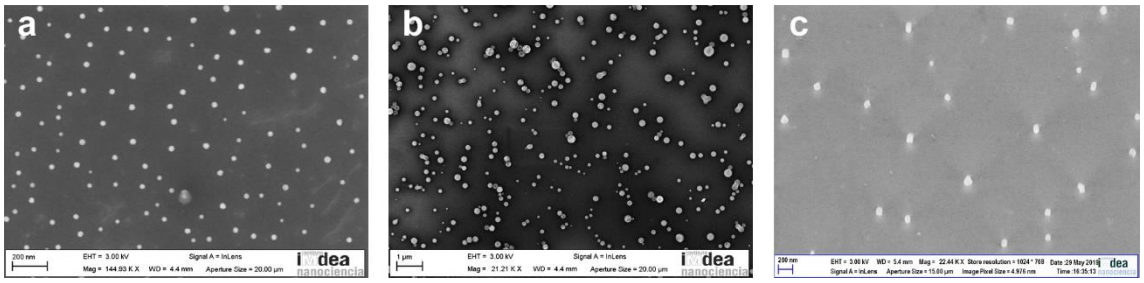

Figure 42. SEM pictures of modified BSA-AuNCs. **a)** BSA-AuNCs-D, **b)** BSA-AuNCs-S and **c)** BSA-AuNCs-DS[190].

4.2.3.3. *In vitro* controlled release of DOX and SN38 from BSA-AuNCs

DOX and SN38 were modified with tailored linkers sensitive to acidic pH and reducing environment, respectively. To determine the *in vitro* release of both drugs from BSA-AuNCs, the nanostructures were exposed to the selected triggering conditions. Aliquots were incubated at different times under the mentioned conditions, then BSA-AuNCs were precipitated using a zinc salt ($Zn(NO_3)_2$), and the fluorescence of the drugs was recorded.

On the one hand, the DOX release from BSA-AuNCs-D was evaluated in phosphate citrate buffer at pH = 5. Under these acidic conditions, we observed that approximately 85% of the total DOX conjugated was released within the first 5 hours (**Figure 43a**,

orange line). However, when the BSA-AuNCs-D are maintained at pH = 7.4, the DOX release was not superior to 20% (**Figure 43a**, blue line). On the other hand, SN38 release was studied in PBS containing DTT at a concentration of 1 µM or 1 mM, which are the concentrations of the normal and tumoral cells, respectively. The results showed that when we employed 1 µM of DTT the release of SN38 was less than 30% after 48 hours, indicating a slow release of the drug from de BSA-AuNCs (**Figure 43b**, green line). However, when we increased the concentration of DTT until 1 mM, 80% of SN38 was released after 48 hours (**Figure 43a**, red line).

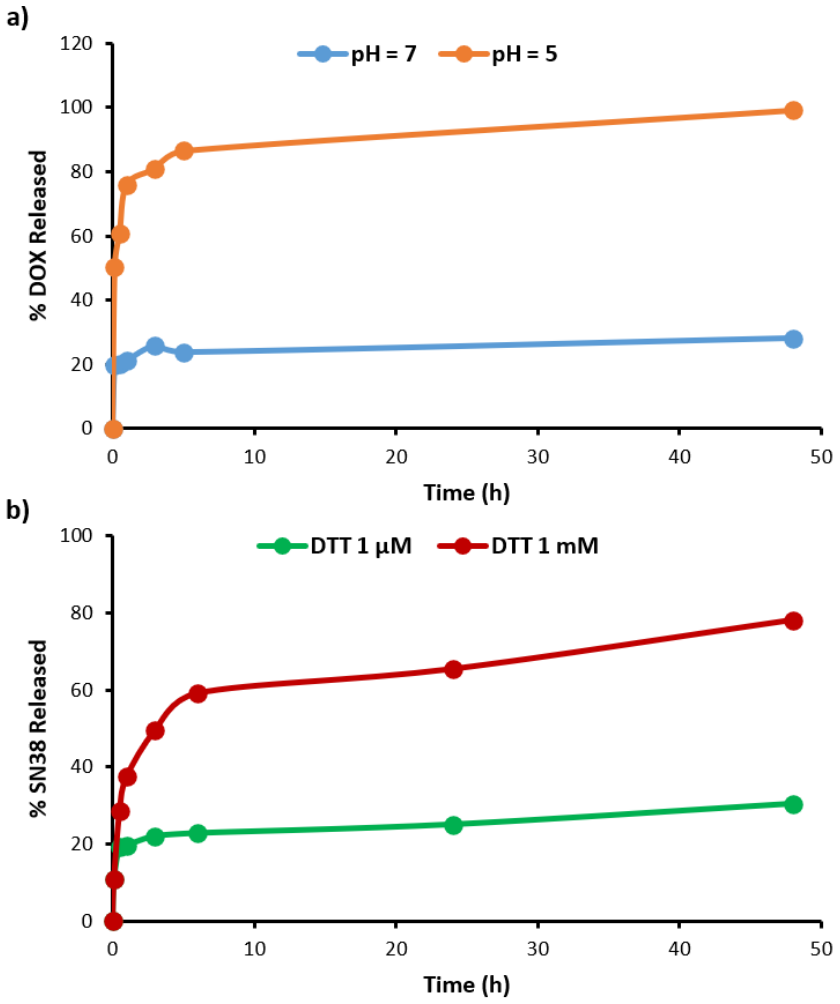

Figure 43. Release profile of Doxorubicin (DOX) and SN38 from BSA-AuNCs. **a**) DOX release profile from BSA-AuNCs based nanoparticles in a phosphate-citrate buffer at pH = 5 (orange line) or 7 (blue line), **b**) SN38 release profile from BSA-AuNCs based nanoparticles in PBS containing 1 mM (red line) or 1 µM (green line) of DTT[190].

4.2.4. Chemotherapeutic activity of functionalized BSA-AuNCs in breast cancer (MCF-7) cells

To determine the toxicity of BSA-AuNCs functionalized with one or two drugs, MCF-7 cells were treated with the different nanostructures at 2.6 µM for 24 hours, and the cell viability was determined after additional 48 hours.

In the case of non-functionalized BSA-AuNCs, no significant differences in cell viability were detected compared to untreated samples. This result highlights the excellent biocompatibility of this nanomaterial in cells. Conversely, functionalized BSA-AuNCs with one drug induced a significant reduction in cell viability. In the case of BSA-AuNCs-D, 70% of cells were dead after treatment. However, only 42% of the cells were dead in the case of BSA-AuNCs-S. Interestingly, BSA-AuNCs functionalized with both drugs (BSA-AuNCs-DS) presented enhanced cytotoxicity, inducing 80% of cell death (**Figure 44**). However, this effect was not as high as expected for the combination of the two drugs. Probably, the excellent activity observed in the case of BSA-AuNCs-D, could be limiting the optimum assessment of the combined therapy.

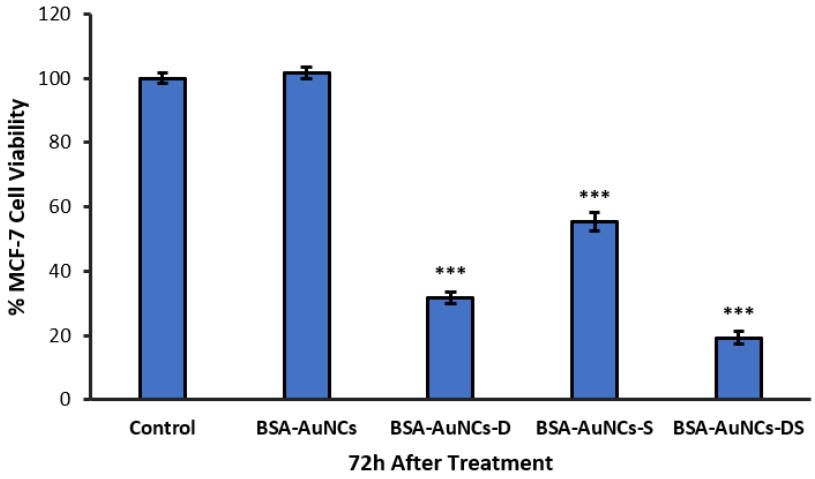

Figure 44. Surviving fraction of MCF-7 cells incubated 24 h with the different BSA-AuNCs formulations and evaluated 48 h after by MTT viability assay. Data correspond to mean ± S.D. values from at least six experiments. Statistical analysis was performed using one-way ANOVA Tukey's test (each group vs. control). ***p-value < 0.001[190].

In addition, the combination therapy (BSA-AuNCs-DS), which showed the highest cytotoxicity in MCF-7 cells at 72 hours after treatment, was also tested in two other cell lines. In this experiment, triple-negative breast cancer (MDA-MB-231)[215] and

pancreatic cancer cells (Panc1)[216] were chosen to assess the potential use of this approach in other cell lines and particularly, a different tumor, such as pancreatic adenocarcinoma. The BSA-AuNCs-DS were incubated in the different cell lines for 24 hours. Then, cells were washed with PBS, and cell viability was measured at 24, 48, and 72 hours after treatment (**Figure 45**).

On the one hand, it is important to note that the BSA-AuNCs were non-toxic in any cell line, as mentioned above, in the case of MCF-7 cells. On the other hand, although the cytotoxic activity in these cells is lower than in MCF-7 (80% cell death at 72 hours after treatment), the obtained results revealing the excellent potential of these nanostructures to reduce the cell viability in the two other cells over time. When the combination therapy was employed, the cell viability in MDA-MB-231 decrease from 10% cell death at 24 hours after treatment to 50% cell death at 72 hours (**Figure 45a**).

Interestingly, similar results were obtained in pancreatic cancer cells (Panc1), where the cell viability decrease from 92% at 24 hours after treatment to 66% at 72 hours (**Figure 45b**).

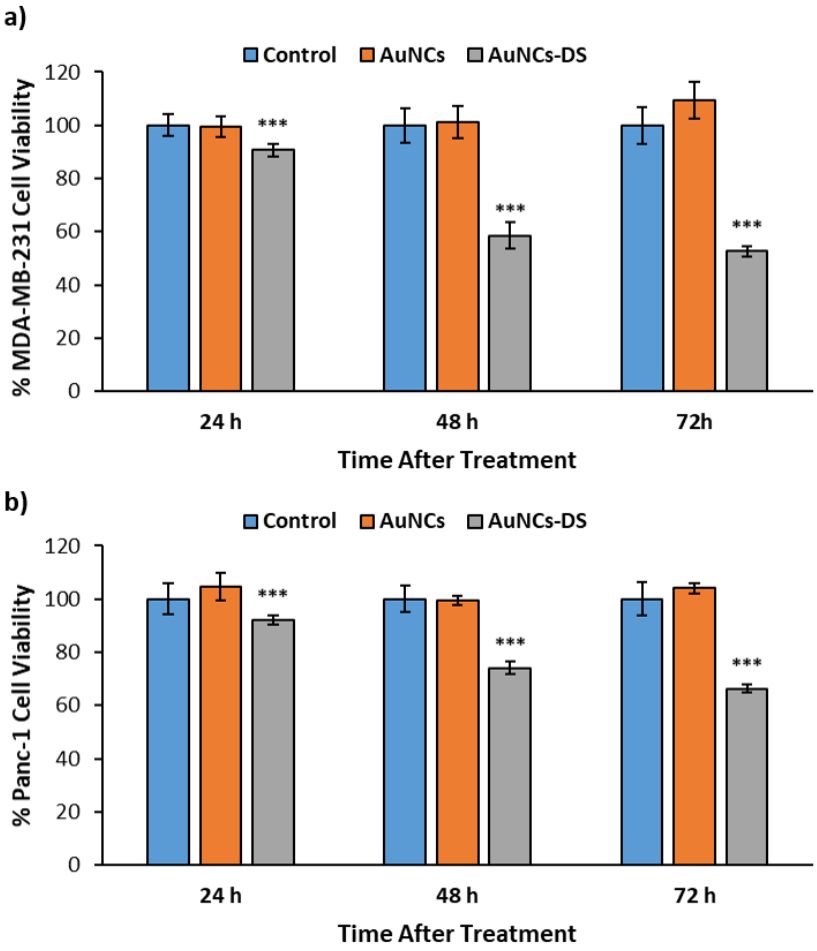

Figure 45. Cell Viability of breast cancer **a)** MDA-MB-231 and **b)** pancreatic cancer Panc1 cells incubated 24 hours with BSA-AuNCs and BSA-AuNCs-DS and evaluated at different times 24, 48 and 72 hours after treatment by resazurin viability assay. Data correspond to mean ± S.D. (n = 4). Statistical analysis was performed using one-way ANOVA Tukey's test (each group vs control). *** p-value < 0.001[190].

It is necessary to mention that the cytotoxicity activity of BSA-AuNCs-DS in the three cells is inferior to free DOX and SN38 (**Figure 46**).

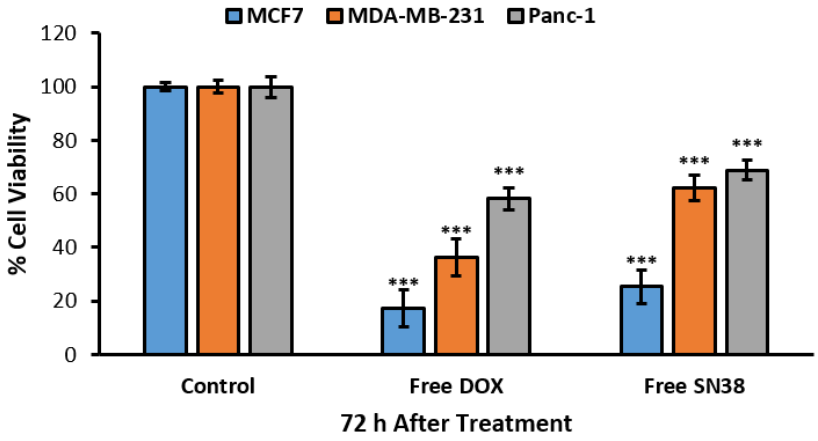

Figure 46. Cell Viability of breast cancer MCF-7 and MDA-MB-231 and pancreatic cancer Panc-1 cells incubated with free DOX and SN38 for 24 hours. Surviving fraction was measured 72 hours after treatment by resazurin viability assay. Data correspond to mean ± S.D. (n = 4). Statistical analysis was performed using one-way ANOVA Tukey's test (each group vs control). ***p-value < 0.001[190].

The cytotoxic activity of the BSA-AuNCs in MCF-7 was confirmed by examining their morphological changes by a neutral red staining assay at 48 hours after treatment with the functionalized nanostructures. Particularly, MCF-7 cells incubated with BSA-AuNCs (**Figure 47b**) showed similar morphology to control cells (**Figure 47a**). On the contrary, samples incubated with BSA-AuNCs-D, or BSA-AuNCs-S and BSA-AuNCs-DS, showed cells with abnormal morphology that present condensed or fragmented apoptotic nuclei (**Figure 47c-e**, respectively).

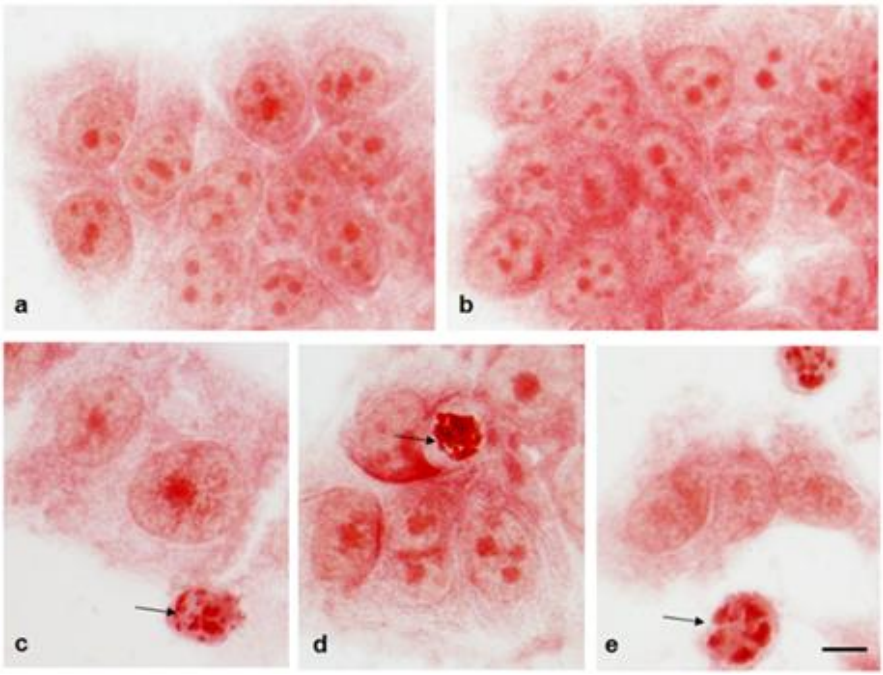

Figure 47. Morphology of MCF-7 cells stained with Neutral Red 48 h after treatment. **a**) Control cells; **b–e**) Cells incubated with BSA-AuNCs, BSA-AuNCs-D, BSA-AuNCs-S, and BSA-AuNCs-DS, respectively. Arrows indicate nuclei with apoptotic nuclear morphology (chromatin condensation and fragmentation). Scale bar: 10 µm[190].

Another complementary experiment to the previous one was the study of cell damage using an optical inverted microscope. In particular, MCF-7 cells were incubated with the different nanostructures using a constant concentration of 2.6 µM of BSA-AuNCs for 24 hours. Then, the cells were washed with PBS and visualized using the mentioned microscope at 48 hours and 9 days after treatment. First, at 48 hours after treatment, the results showed that the cell density observed when BSA-AuNCs-DS was employed (**Figure 48d**) was lower compared to the other two formulations (BSA-AuNCs-D and BSA-AuNCs-S) (**Figure 48b and c**) and the untreated cells (**Figure 48a**). However, the most significant changes were observed 9 days after the treatment, when the cells treated with BSA-AuNCs-DS did not regrow, and the characteristic microcolonies of MCF-7 cells were not detectable (**Figure 48g**). Interestingly, when the cells were incubated with BSA-AuNCs-D (**Figure 48e**) or BSA-AuNCs-S (**Figure 48f**), small microcolonies could be visualized. These results evidenced superior cytotoxic activity of BSA-AuNCs-DS over time, confirming the great advantage of their use in cells.

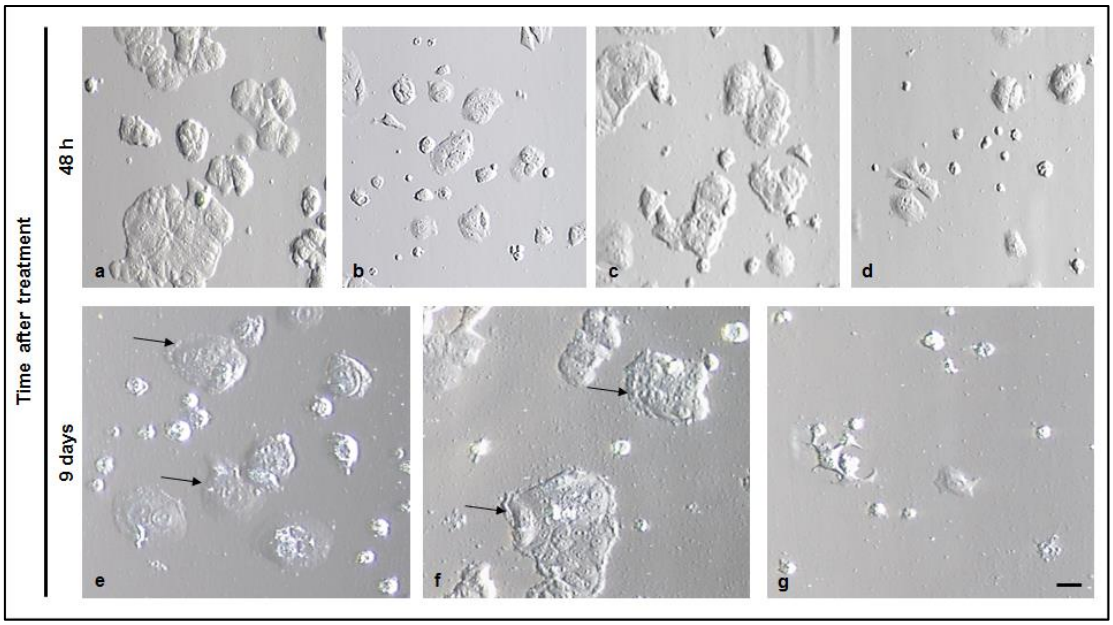

Figure 48. MCF-7 cell density recorded under differential interference contrast (DIC) microscopy 48 hours after treatment in **a)** control (untreated) cells, **b)** BSA-AuNCs-D, **c)** BSA-AuNCs-S and **d)** BSA-AuNCs-DS. Cells 9 days after incubation with **e)** BSA-AuNCs-D, **f)** BSA-AuNCs-S and **g)** BSA-AuNCs-DS. Black arrows indicate the growth of surviving cells, which form new microcolonies. As detected under an inverted microscope, a smaller number of living cells were observed after bifunctional treatment in contrast to monofunctional BSA-AuNCs. Scale bar: 50 µm[190].

Then, ICP-MS and confocal microscopy were performed to confirm that BSA-AuNCs were internalized into MCF-7 cells at different incubation times. For the confocal microscopy experiments, cells were incubated for 3-4 and 24 hours with BSA-AuNCs. At short times (3–4 h after treatment), BSA-AuNCs are clearly detected through its red intrinsic fluorescence inside the cells (**Figure 49a**) and outside the cell membrane (**Figure 49b**). However, at longer times (24 h after treatment), the fluorescence of BSA-AuNCs was reduced, probably due to their degradation inside the cell, although the presence of gold atoms could be detected by ICP-MS (13 pg/cell).

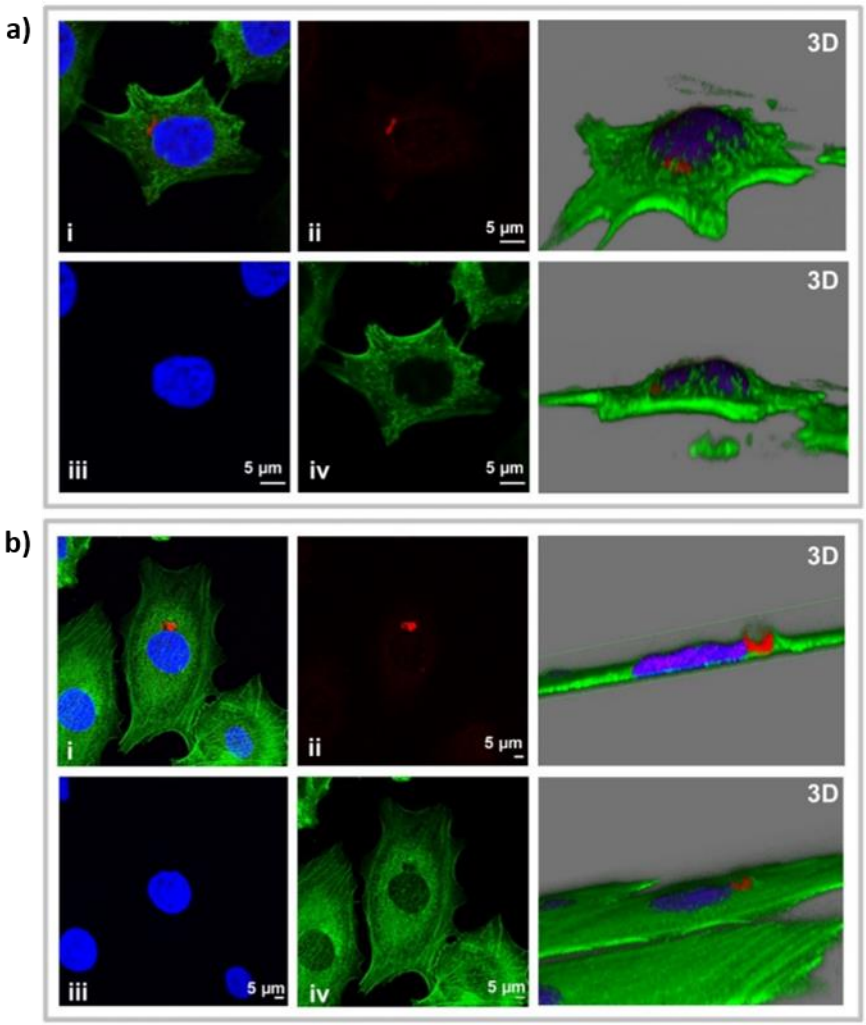

Figure 49. Confocal laser scanning microscope images of BSA-AuNCs localization in MCF-7 cells after 3–4 hours of incubation. Panel **a)** showed an example of BSA-AuNCs cellular internalization while panel **b)** shows BSA-AuNCs layered outside, on top of the cells. The left side of the panel corresponds to 2D images (one section or focal plane) for the merge (**i**), BSA-AuNCs in red (**ii**, Ex.405/Em.680 nm), nucleus with DAPI in blue (**iii**, Ex.358/Em.461) and actin filaments labeled with Phalloidin in green (**iv**, Ex.495/Em.519 nm). The right side shows the 3D reconstructions of those cells[190].

In addition, taking advantage of the fluorescence from DOX and SN38, the uptake of BSA-AuNCs-D and BSA-AuNCs-S, were studied by confocal microscopy in MCF-7 cells at 24 hours after the treatment with the nanostructures. The results showed that most of the fluorescence from DOX (red) co-localized with the fluorescence from SN38 (blue) in the nucleus (**Figure 50**). Thus, both DOX and SN38 can reach the cell nucleus after their release from the BSA-AuNCs inside the cells, leading to the corresponding cytotoxic effect.

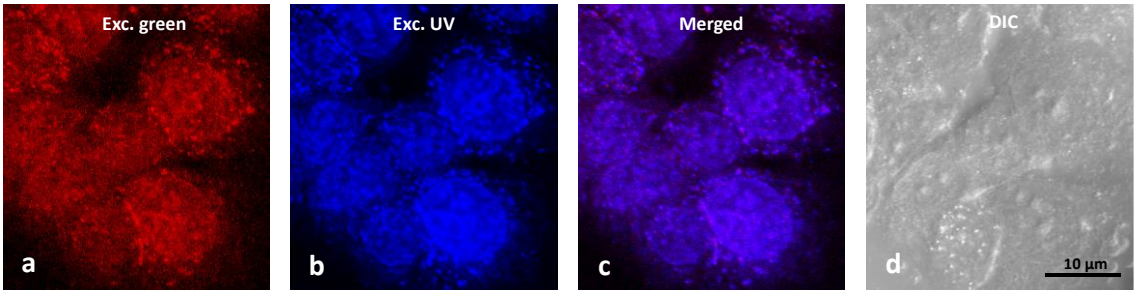

Figure 50. Confocal laser scanning microscope images of subcellular localization of BSA-AuNCs-DS after 24 hours incubation. **a)** DOX internalized are colored red, and **b)** SN38 colored blue. **c)** merged images, and **d)** differential interference contrast (DIC) microscopy are also presented. Scale bar 10 µm[190].

Finally, it is known that DOX and SN38 produce DNA damage and activate the DNA damage response (DDR)[217]. For this reason, we wanted to know if the higher activity of the BSA-AuCNs-DS was due to differences in the induction of DNA damage by the treatment with the nanostructures. In this sense, the phosphorylation of histone H2AX at serine 139 (γ-H2AX) is the most sensitive marker to study DNA damage (double-stranded breaks, DSBs) in cells which have been exposed to ionizing radiation or chemotherapeutic agents. These phosphorylation events are easily detected by specific antibodies to the phosphorylated form of H2AX (γ-H2AX), which has been extensively used as a marker of DSB formation by chemotherapeutics agents[218]. To analyse the DNA damage induced by functionalized BSA-AuNCs, MCF-7 cells were treated with the corresponding nanostructures for 24 hours. Once inside the cells, the drugs must be released and enter the cell nucleus to induce DNA damage, so the detection of the DNA double-strand breaks was performed 48 hours after the treatment by immunofluorescence against γ-H2AX. The fluorescence signal indicative of the DNA damage was detected in both BSA-AuNCs-D and BSA-AuNCs-S. Remarkably the fluorescent intensity in cells treated with the combined chemotherapy was significantly higher. These results, along with the previous ones obtained in the optical microscopy studies, revealed that the superior activity observed in the BSA-AuNCs-DS might be due to an increase in the DNA damage generated by the combination of the two drugs at the nuclei (**Figure 51**).

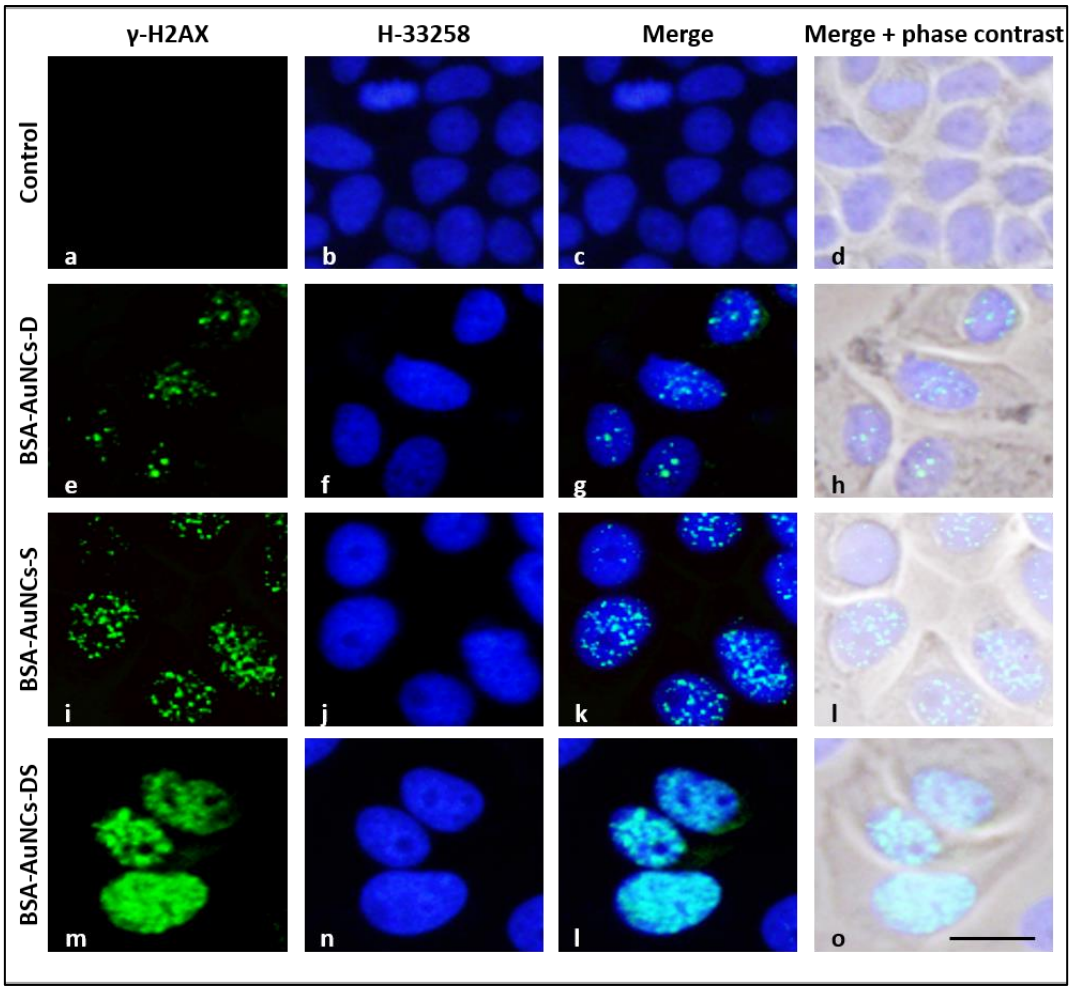

Figure 51. Fluorescence signal of γH2AX (green) in MCF-7 cells was observed at the confocal microscope at 48 hours after incubation with functionalized BSA-AuNCs. Then, cells were fixed and processed for γH2AX immunofluorescence, DNA was counterstained with Hoechst-33258 (blue) and both images were overlapped. **a–d)** control cells; **e–h)** cells treated with BSA-AuNCs-D; **i–l)** cells treated with BSA-AuNCs-S; **m–o)** cells treated with BSA-AuNCs-DS. Scale bar: 7.5 µm[190].

4.2.5. Chemotherapeutic activity of BSA-AuNCs-DS in breast cancer (MCF-7) mammospheres

To further assess the therapeutic potential of BSA-AuNCs, different studies were carried out against breast cancer mammospheres. It is known that isolated mammospheres from MCF-7 cells present characteristics of cancer stem cells (CSCs)[219], and therefore, can better resemble the tumor microenvironment compared with standard 2D cell culture[220].

In this regard, as mentioned above, BSA-AuNCs-DS had demonstrated their efficiency in the generation of DNA damage in MCF-7 cells. Thus, this system might be an excellent candidate to eliminate the CSCs population present in the tumors.

First, the cytotoxic activity of BSA-AuNCs-DS at different concentrations in MCF-7 cells that will derive in mammospheres was assessed to select the best concentration. In this experiment, MCF-7 cells were treated for 7 days with the BSA-AuNCs-DS without changing the medium to resemble de studies in mammospheres (**Figure 52**).

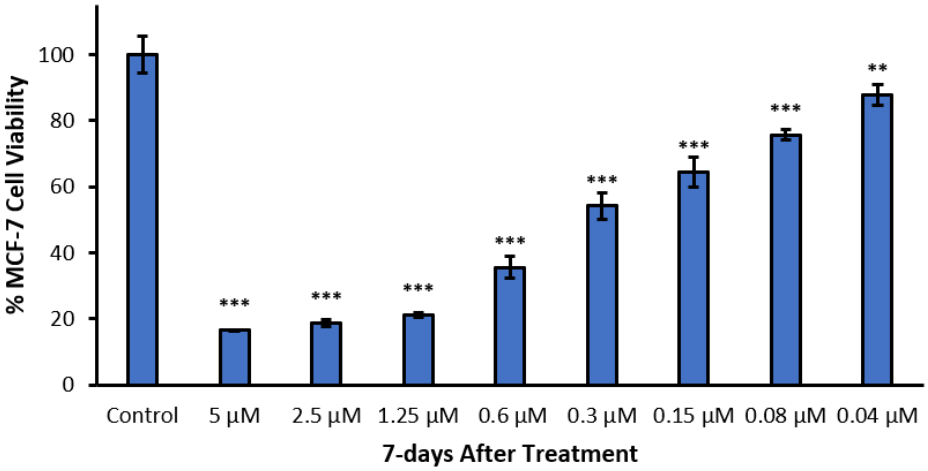

Figure 52. Cell Viability of MCF-7 treated with different concentrations of BSA-AuNCs-DS for 7 days. Data correspond to mean ± S.D. (n = 4). Statistical analysis was performed using one-way ANOVA Tukey's test (each group vs control). **p-value < 0.01, ***p-value < 0.001.

Based on this data, the selected concentrations for the mammosphere experiments were 0.08 µM and 0.6 µM. These concentrations were used in the mammosphere assay model to prevent the complete elimination of the spheres after 7 days of treatment with BSA-AuNCs-DS. The cytotoxic activity was evaluated by analyzing the surviving fraction of the MCF-7 spheres and their size.

The surviving fractions of mammospheres were analyzed by counting the spheres before and after the treatment with BSA-AuNCs-DS at selected concentrations. The results showed a considerable reduction of 24% and 81% in cell viability when treated with 0.08 µM and 0.6 µM, respectively (**Figure 53**).

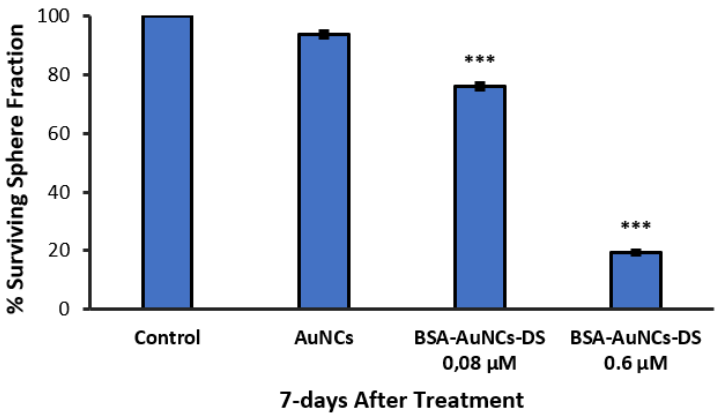

Figure 53. Surviving fraction of mammospheres treated with bi-functionalized BSA-AuNCs for 7 days. Data correspond to the mean ± S.D. values from three experiments. Statistical analysis was performed using one-way ANOVA Tukey's test (each group vs control). ***p-value < 0.001[190].

Finally, a significant variation in the size of the mammospheres was observed after the treatment with 0.08 µM and 0.6 µM of BSA-AuNCs-DS, which are reduced from an average diameter of 465 µm (control) to 176 and 167 µm, respectively (**Figures 54**).

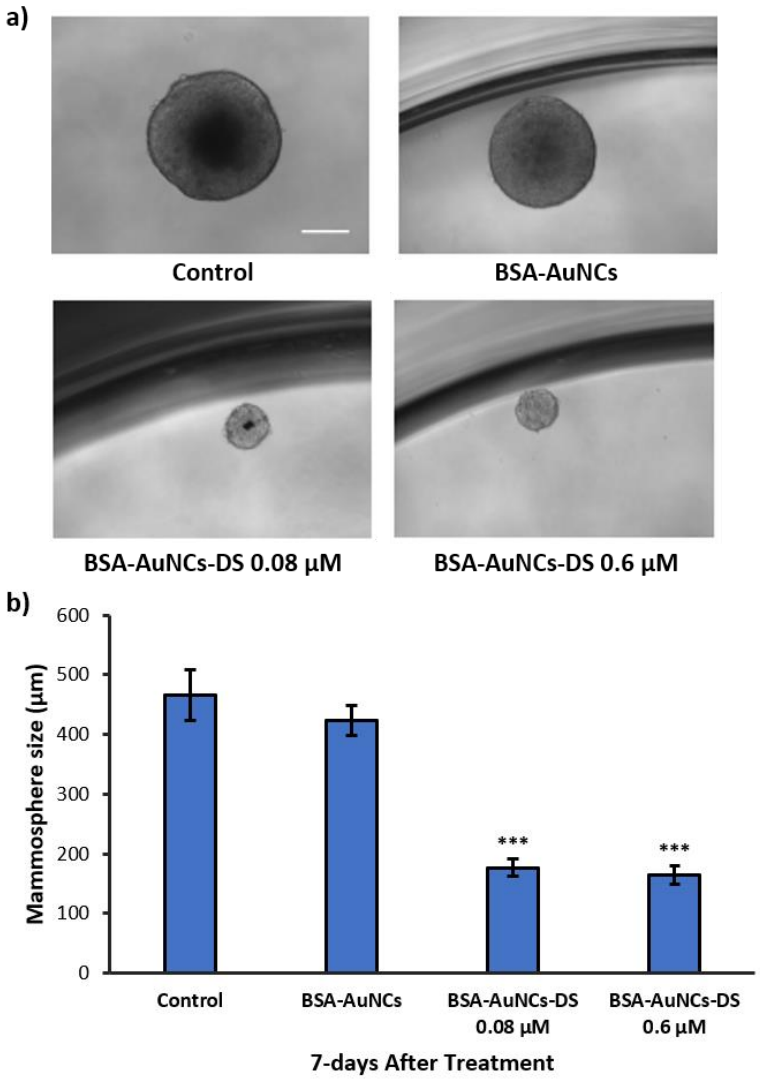

Figure 54. Activity of functionalized BSA-AuNCs in MCF-7 mammospheres. **a)** Microscopy image of mammospheres treated with BSA-AuNCs, BSA-AuNCs-DS 0.08 µM and BSA-AuNCs-DS 0.6 µM. Scale bar 200 µm. **b)** Size of mammospheres treated with BSA-AuNCs-DS at 0.08 µM and 0.6 µM for 7 days. Data correspond to the mean ± S.D. values from ten mammospheres. Statistical analysis was performed using one-way ANOVA Tukey's test (each group vs control). ***p-value < 0.001[190].

4.3. New vehicles based on nanostructures for CRISPR gene-editing system transport

4.3.1. CRISPR/Cas system

Gene editing is a process that implies the modification of DNA sequences in the genome. This process had been employed for the generation of mutant species in the study of diseases, although its use in the clinical field is very limited at the moment[221].

The most used gene editing techniques are based on programmable nucleases composed of sequence-specific DNA-binding domains fused to a nonspecific DNA cleavage domain of a target DNA[222]. These nucleases can be used to modify the genome through the introduction of double-strand breaks (DSBs)[222] at selected regions, which are later repaired by different DNA repair processes, such as the non-homologous end-joining (NHEJ) or the homology-directed repair (HDR). During the NHEJ process, the free ends of the DNA breaks are fused back together, leading to insertions o deletions (indels). On the other hand, HDR needs the presence of a DNA template that is inserted in the cut region[223] (**Figure 55**).

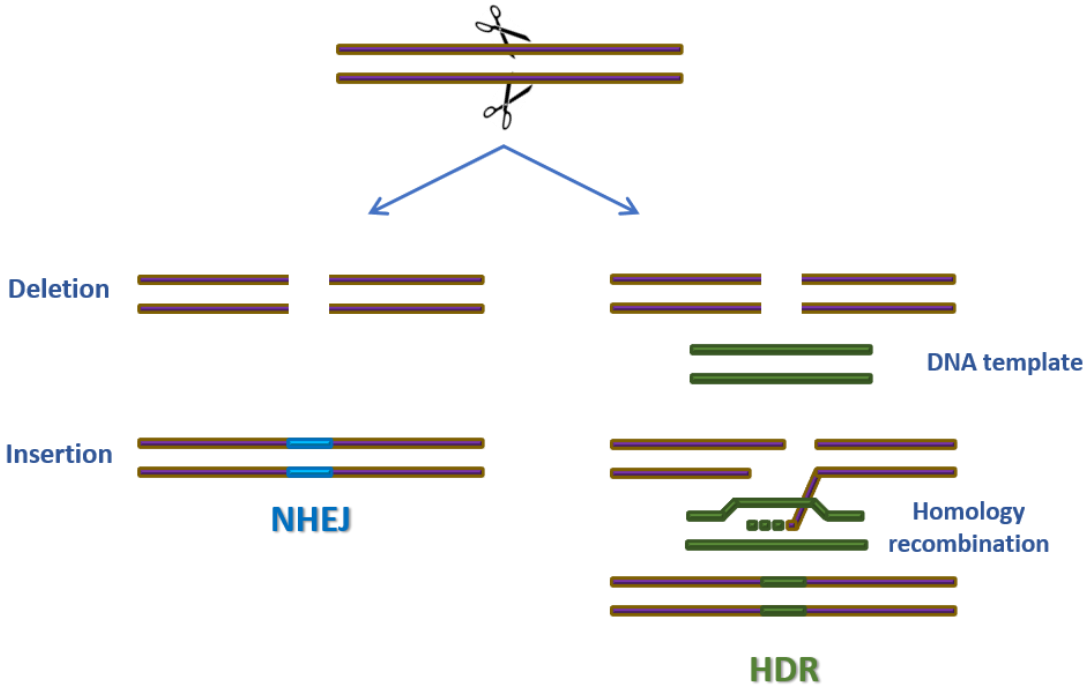

Figure 55. DNA repair mechanism. Double-strands breaks (DSBs) can be repaired by the non-homologous end-joining (NHEJ) or homology-directed repair. The NHEJ is an imprecise repair process that can generate insertions or deletions (indels) of a variable length, while the HDR introduces specific sequences in the cut region.

Among the different gene editing systems based on programmable nucleases are the well-known TAL nucleases (transcription activator-like effector nucleases, TALENs), and zinc fingers (Zinc Nuclease Fingers, ZNFs). TAL nucleases and ZNFs contain domains capable of recognizing and binding to a specific DNA sequence. These nucleases can be modified and recognize a specific DNA sequence, which can be cut by fusing these nucleases to a type IIS restriction enzyme called FokI4[224]. This restriction enzyme is only capable of generating a double-stranded cut in DNA if it is in the form of a dimer[225] (**Figure 56**).

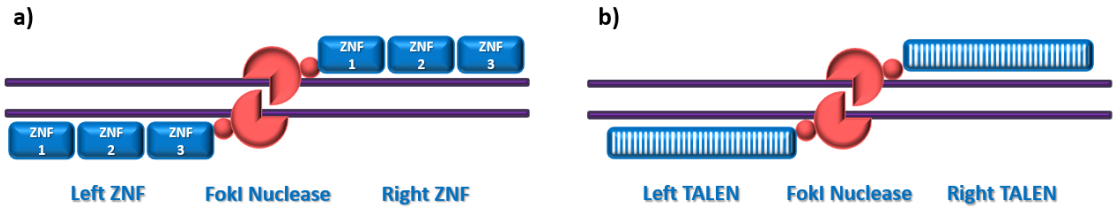

Figure 56. Schematic representation of the **a)** Zinc nuclease Fingers (ZNF) and **b)** TAL nuclease (TALENs).

However, although these systems are very effective, they present a series of drawbacks that make their use more expensive, such as the difficulty of design and synthesis, due to the need for a new DNA-binding domain for each target sequence. Furthermore, these techniques require the modular binding of each of the DNA-binding domains, making the editing process slow[226].

In the last decade, the discovery of the CRISPR system (clustered regularly interspaced short palindromic repeats) associated with Cas9 protein has been a revolution in laboratories of molecular biology due to the high potential it has in gene editing in eukaryotic cells[227,228]. This system allows a better understanding of the gene function in an easy, versatile and specific way through the addition, removal or mutation of genetic material. Compared to other genome editing strategies, such as transcriptional activator-type effector nucleases (TALEN) and zinc finger nucleases (ZFN), CRISPR/Cas9 genome editing is controlled by a single strand of RNA, which provides several advantages that make it a faster and more efficient technology such as easy design, low cost and its possible use in different genes at the same time[227,228].

CRISPR/Cas9 system was discovered in bacteria by Francisco Mojica in the 90's. He found a palindromic structure of approximately 30 base pairs that was repeated serially in the

bacteria genome, and that they were separated by unknown spacer sequences at that moment in microorganism[229,230]. Later, in 2005, Mojica found that these structures protected bacteria from infection caused by bacteriophages or plasmid, and therefore should be involved in their adaptative immune system[231].

There are three mechanisms of CRISPR, of which type II is the most studied. In this mechanism, short fragments of 20 base pairs from foreign DNA (e.g., virus) named "protospacers" are acquired by the bacteria genome between the repeated CRISPR sequences. These repetitions are transcribed to CRISPR RNAs (crRNAs) of approximately 40 nucleotides, which have a variable sequence because they contain a region of the repeated sequence and a protospacer[232]. The crRNAs partially hybridized with a second RNA called trans-activating CRISPR RNA (tracrRNA) of around 90 nucleotides to facilitate the binding of RNAs to Cas9. Then, this complex is processed by the ribonuclease III (RNase III), leading to a shorter hybrid of approximately 85 nucleotides of tracrRNA-crRNA that works as a guide RNA (gRNA). This RNA structure can recognize the sequence of invader complementary DNA and introduce the double-strand break[233–235] (**Figure 57**). In this regard, through the CRISPR mechanism, bacteria can remember and recognize foreign genes and clear virus-host infections.

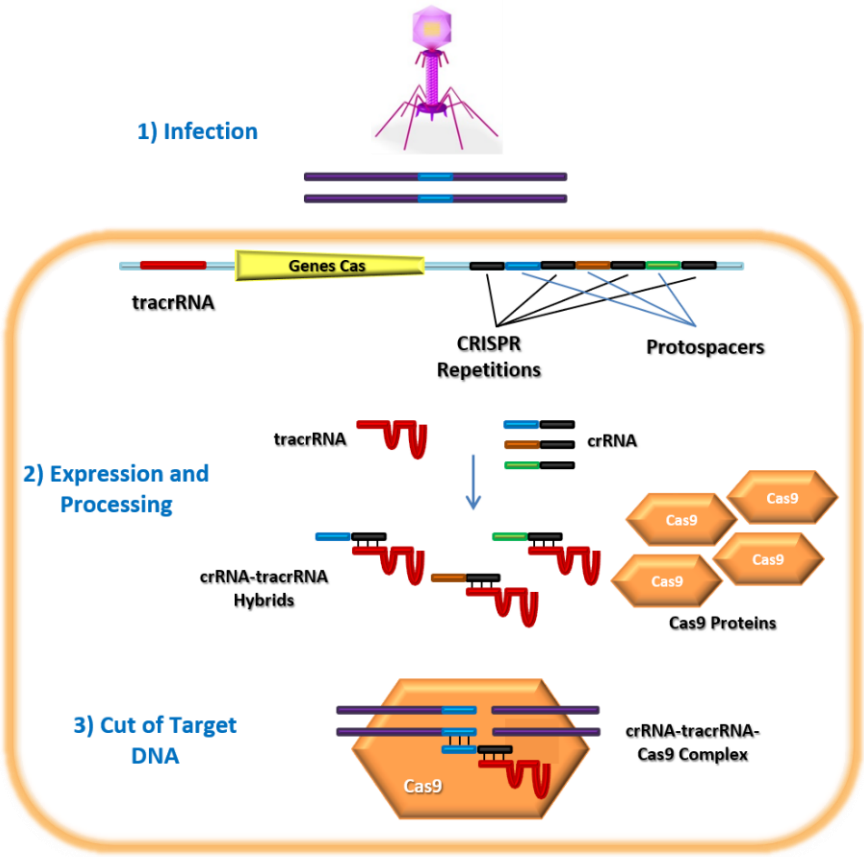

Figure 57. CRISPR/Cas system inserts DNA sequences from pathogens between CRISPR repetitions as protospacers, which will be expressed as crRNA. The processed crRNA hybridizes with the tracrRNA and forms a complex with a Cas9 protein. The resulting complex is able to recognize and cut the invader's DNA.

The Cas9 from *Streptococcus pyogenes* (*S. pyogenes*) contains two nuclease activity domains, RuvC and HNH. These domains can produce double-strands beaks in the invader DNA, only if there is a specific sequence, known as "motif adjacent to the protospacer" (PAM sequence), close to the cutting site, precisely, 3 bases before the PAM sequence[233,236]. It is worth mentioning that this particular sequence is specific to the microorganism that produces the Cas protein, and in the case of *S. pyogenes* is 5'NGG. Complementary PAM sequences from other organisms are the following: 5' NAC, NTG, NTT, NCG and NGG in *S. pyogenes*; 5'NGG in *F. novicida*, 5'NNGRRT in *S. aureus*, 5'-NNNNGATT in *N. meningitidis,* 5'NGGNG in *S. thermophilus*, 5'NNNNACAC in *C. jejuni* and 5'TTTN in *Prevotella and Francisella*[237]. Where "N" can be any nucleotide base and "R" represents a purine such as A or G.

Despite the relevance of these findings associate with this defense mechanism of bacteria, the most relevant milestone of CRISPR technology was reported in 2013, where

it was applied in eukaryotic organisms such as plants, yeasts, and even mammals[238–240]. In these cases, it is required the introduction (or expression) of the Cas9 protein and the gRNA structure to induce the double-strands breaks, since they are not present in eukaryotic cells. The introduction of these elements into cells, and particularly the Cas9 protein, can be achieved in different ways, including as a DNA plasmid, mRNA and pre-complexed Cas protein and gRNA (ribonucleoprotein, RNP). The different approaches present advantages and disadvantages, mainly related to the specificity and length of the expression[241–243]:

- DNA plasmids require their transcription to the mRNA, followed by the translation to the corresponding Cas protein once they reach the cytoplasm. DNA plasmids are very stable and can last few days within cells, which could be useful for long experiments. However, this prolonged expression of the Cas gene may also result in undesired off-target effects. The higher expression levels of expressed Cas protein are detected 24-48 hours after transfection. In addition, because the DNA plasmid needs transcription in the nucleus, the possibility of their random integration into the genome should be considered. This would produce a constant expression of the Cas protein that would lead to the generation of off-target effects and toxicity.
- The Cas mRNA will be translated into protein in the cytoplasm. Then gRNA and Cas protein localize to the nucleus and form the RNP complex. Compared to DNA plasmid, the peak expression is detected 5-7 hours after transfection, and therefore, is more time-efficient. Furthermore, RNA is usually degraded by RNases in the cytoplasm, while plasmid DNA is more stable. For this reason, the shorter duration required for the experiments, prevents the generation of off-target effects.
- The RNP does not require transcription or translation. This format is the most efficient and specific, and its duration in cells is the shortest compared to the previous formats, so that off-target effects are very limited. However, RNP components can be expensive to produce or purchase.

These pros and cons are summarized in **Table 7**.

	DNA	RNA	Protein
Efficiency	Low	Middle	High
Specificity	Low	High	High
Cost	Cheap	Middle	Expensive
Off-target effects	High	Middle	Low

Table 7. Pros and cons of different formats of Cas9 protein delivery.

Recently, it has been discovered a new CRISPR system that uses another type of endonuclease called Cpf1 or Cas12a (CRISPR from *Prevotella* and *Francisella* 1). Compared to the Cas9 protein, this new system has some different characteristics, such as RNase activity, the adjacent T-rich protospacer motif (5'-TTTN-3' PAM) and the generation of sticky ends. Furthermore, maturation of the crRNA does not require the presence of the tracrRNA, resulting in a short guide of approximately 42-44 nucleotides. Finally, this endonuclease has been found to have a low off-target rate, which is an excellent advantage over the Cas9 system[244–246]. The main differences between Cas9 and Cpf1 are summarized in the following table (**Table 8**).

	Cas9	Cpf1
Cleavage activity	DNase activity	DNAse and RNase activity
Guide RNA	crRNA + tracrRNA	crRNA
PAM motif	5'-NGG-3'	5'-TTTN-3'
Cleavage ends	Blunt ends	Sticky ends
Off-target effects	High rate	Low rate

Table 8. Major difference between Cas9 and Cpf1 CRISPR proteins.

Despite all the advantages that the CRISPR/Cas gene editing system offers, it also presents some drawbacks that must be solved before it can be applied as therapy. These limitations are related to the low catalytic efficiency of the Cas protein, the poor stability and durability of the complex, as well as, the need for delivery systems[247]. In addition, the gene-editing process can produce off target-effects, if the specificity of the gRNA is not right, leading to cytotoxicity. In this sense, it has been described that the 10-12 base

pairs of this gRNA (seed region) proximal to the PAM seems to be essential for the CRISPR/Cas specificity and cleavage activity[247,248]. Mismatches in this site lead to a decrease or even complete suppression of the cleavage activity of the target sequence[249].

Another critical factor in the optimization of CRISPR/Cas is the method used to deliver the different components of the system, which could increase the genome-editing efficiency. Various delivery systems have been evaluated, such as viral vectors based on adenovirus[250], physical methods such as electroporation or microinjection[240], peptides[251], and even different kinds of nanostructures[252–256]. Anyhow, none of the methods reported are perfect, and their use will depend on the final application (e.g., disease, cell culture, animal model, target tissue).

Thus, new and complementary approaches are necessary to address the current limitations of the technique. In this sense, albumin nanostructures and carbon nanotubes will be evaluated as nanocarriers for the CRISPR/Cas system due to their good properties as carriers previously described.

4.3.2. Functionalized carbon nanotubes as gene delivery system

4.3.2.1. Design and evaluation of a functional CRISPR/Cas9 plasmid

The first part of this work was focused on the design of two DNA sequences capable of being transcribed into a functional gRNA, a sequence complementary to the EGFP gene (EGFP) and the other non-targeting (NT) as an internal control of the CRISPR system (see Methods, **3.4.1.1.**). In particular, these DNA sequences of 20 base pairs each were cloned into an expression vector capable of expressing a chimeric gRNA and the human codon-optimized Cas9 protein (pSpCas9 (BB)) (**Figure 58a**).

To insert the sequences (EGFP and NT) in the plasmid, two duplexes with specific overhangs were prepared. The sense strands were preceded by 5'- CACC while the antisense strands were preceded by 5'- AAAC. The duplexes were annealed and ligated into the plasmid after the U6 promoter into the gRNA scaffold (**Figure 58b**). Furthermore, a G nucleotide was also added after the sequence 5'- CACC to increase the expression of the U6 promoter, responsible for the transcription of the guide RNA (**Figure 58b**). Cloning of the sequences into pSpCas9 was carried out in a single step using

the restriction enzyme *Fast Digest BbsI* and the DNA ligation enzyme *T7 ligase*. The resulting plasmids containing the sequence complementary to the EGFP gene and a non-targeting sequence were called Cas9-EGFP and Cas9-NT, respectively.

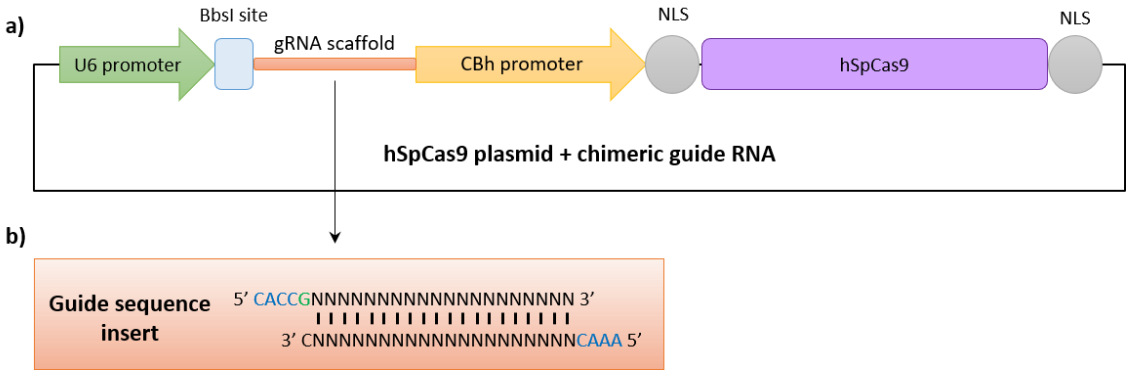

Figure 58. a) Schematic representation of pSpCas9 and **b)** design of DNA duplex (20 base pairs) to clone the guide sequence into the RNA scaffold by adding "CACCG" and "CAAA" at 5' end.

To assess the activity of the resulting plasmids, HEK293 cells were transiently transfected using Lipofectamine 2000 as described in Methods, section **3.4.1.2.2**. In particular, an EGFP reporter plasmid and the CRISPR/Cas9 constructs previously prepared were transfected. After transfection, the cells were evaluated at 72 hours using fluorescence microscopy. The images revealed that the Cas9-NT construct slightly affects the fluorescence of the EGFP, whereas the Cas9-EGFP construct drastically decreases it, even at the lowest concentration (**Figure 59**).

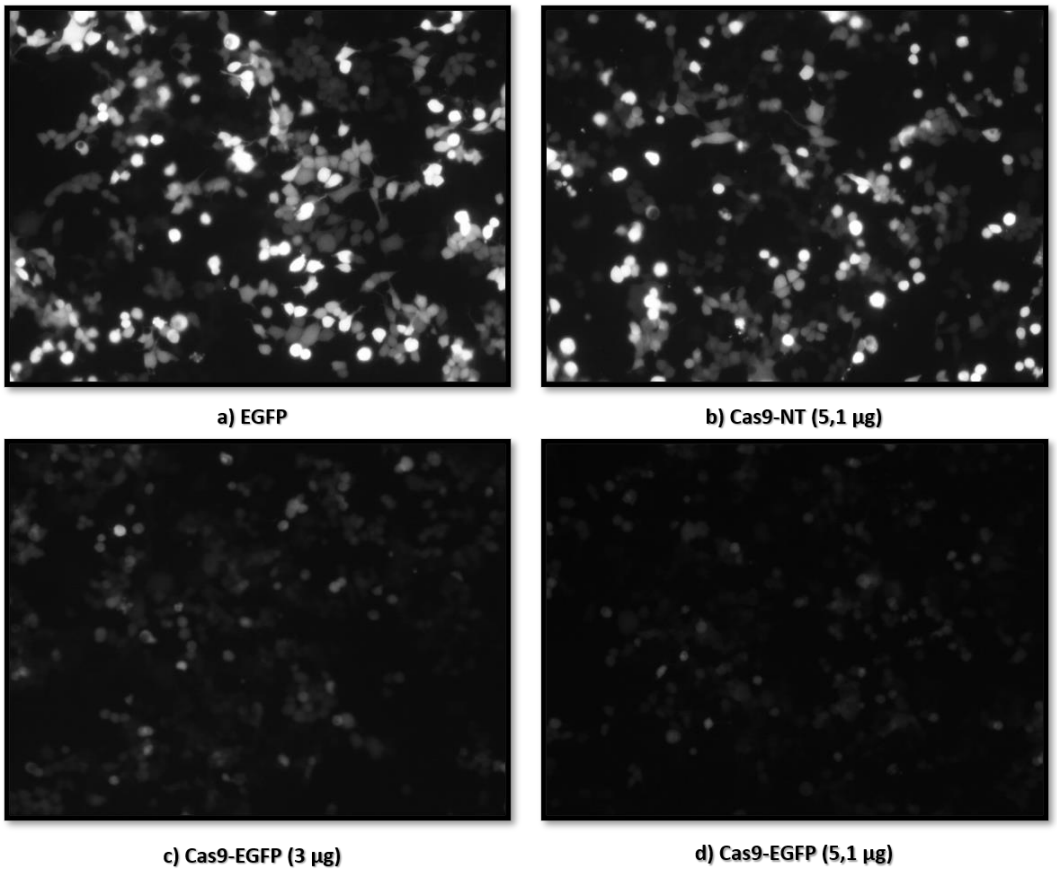

Figure 59. Fluorescence microscopy images of HEK293 cells treated with CRISPR/Cas9. Cells treated with the Cas9-NT construct (**b**) showed little inhibition of EGFP fluorescence compared to the control sample (**a**), whereas with Cas9-EGFP constructs (**c** and **d**) the fluorescence was significantly decreased.

The fluorescence was quantified by flow cytometry, where the EGFP control sample had 73.8% of the living cells expressing EGFP and fluorescence intensity of 237 (A.U.) (**Figure 60a, i**). In the control experiment with the Cas9-NT plasmid, the number of living cells with EGFP expression decreased slightly (71.6%). However, the mean fluorescence intensity was reduced to 123 (A.U.) (**Figure 60a, ii**). Regarding the experiments with Cas9-EGFP systems, both parameters decreased significantly (**Figure 60, iii** and **iv**). Specifically, Cas9-EGFP at the lowest concentration (3 µg) showed 64.9% positive cells and the average fluorescence intensity of 21.5. In contrast, the use of a higher concentration of the Cas9 plasmid (5.1 µg), showed 53.4% of fluorescent live cells and an average fluorescence intensity of 10 (A.U.).

a)

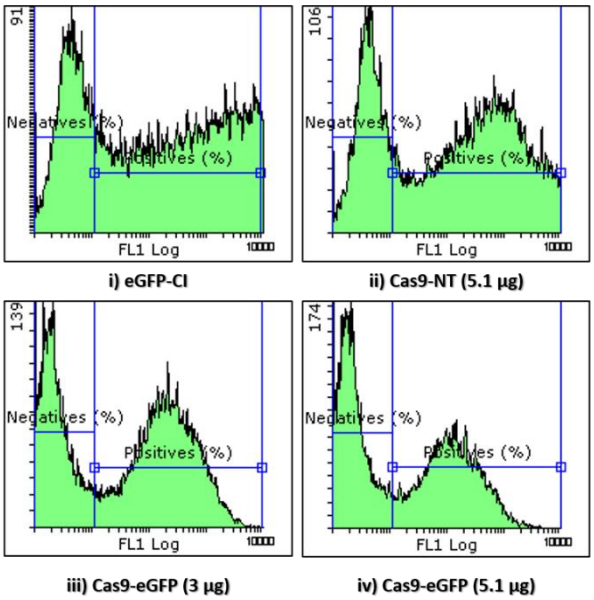

b)

	Positive cells	Intensity (A.U.)
EGFP-CI	73.8 %	237
Cas9-NT (5.1 µg)	71.6 %	123
Cas9-eGFP (3 µg)	64.9 %	21.5
Cas9-eGFP (5.1 µg)	53.4 %	10

Figure 60. a) Flow cytometry histograms of HEK293 cells 72 hours after treatment with the CRISPR/Cas9 constructs. Cas9-NT (**ii**) does not vary the number of positive cells, although the intensity of fluorescence compared to the control (**i**). However, the Cas9-EGFP (**iii, iv**) constructs decrease both the number of positive cells and the intensity of fluorescence. **b)** Fluorescence intensity and % of positive EGFP cells.

4.3.2.2. Functionalized carbon nanotubes (SWNT) as gene delivery system

To use CRISPR/Cas9 constructs for gene editing in eukaryotic cells, a carrier able to transport and release the plasmids into the cells is required. In this sense, carbon nanotubes are characterized by having a high load capacity, intrinsic stability and structural flexibility, which can increase the circulation time, and consequently, the bioavailability of the transported drug molecules[257]. On the other hand, PEI is a polymer formed by repeats of amino groups that can provide multiple positive charges. Thus, it can interact, electrostatically to negatively charged nucleic acids (DNA and RNA), and also with cell membranes, facilitating their internalization in the cell cytoplasm[258].

For these reasons, we proposed the use of single-walled carbon nanotubes (SWNT) covalent modified with the cationic polymer polyethyleneimine (PEI) for plasmid DNA delivery.

4.3.2.2.1. Preparation of complexes of PEI-modified SWNTs and plasmid DNA (PEI-SWNT-pDNA)

The covalent modification of single-walled carbon nanotubes (SWNT) with PEI polymer (PEI-SWNT) was made by Dr. Teresa Naranjo and Dr. Julia Villalva from the group of Prof.

Emilio Pérez at IMDEA Nanociencia. The covalent conjugation was characterized by different techniques: Raman spectroscopy, thermogravimetric analysis (TGA) and zeta potential.

On the one hand, Raman spectroscopy of the SWNTs and PEI-SWNTs were carried out to assess the surface chemistry of SWNTs after their covalent modification with the PEI polymer. In the results obtained by Raman spectroscopy, no significant change was found between the SWNT and PEI-SWNT tubes, demonstrating that after covalent modification, the SWNTs maintain their structural integrity (**Figure 61a**). On the other hand, to study the percentage of PEI covalently bound to the carbon nanotubes, a thermogravimetric analysis was performed. The results obtained in the thermogravimetric analysis showed a weight loss of 50% in the PEI-SWNT, corresponding to the grade of functionalization of the SWNT (**Figure 61b**).

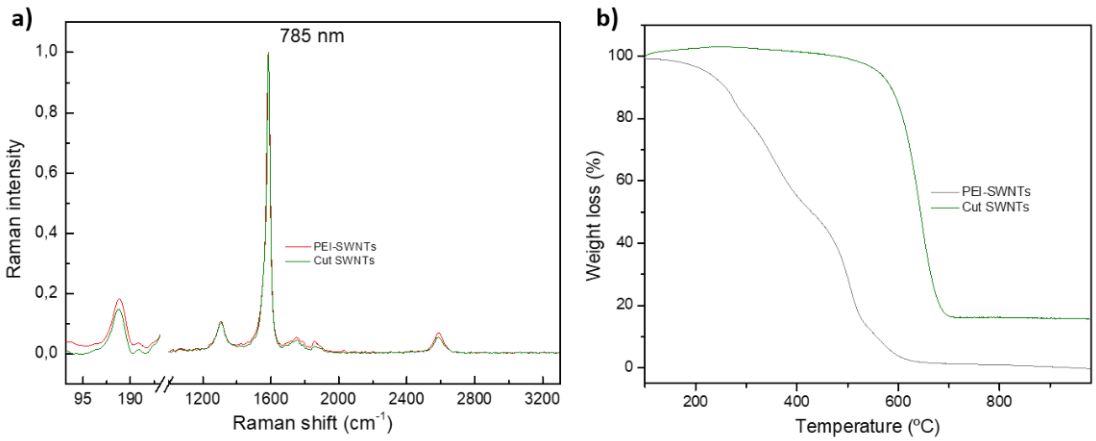

Figure 61. Characterization of PEI-SWNT using (**a**) Raman spectroscopy and (**b**) Thermogravimetric analysis.

Zeta potential measurements of SWNTs showed that the unmodified SWNTs had a negative charge of -30.5 ± 0.794. In contrast, PEI-SWNTs presented +24 ± 3.91, indicating the presence of the cationic polymer in the nanotubes (**Figure 62**).

Then, the formation of the complexes (PEI-SWNT-pDNA) was carried out by incubating 1 µg of the EGFP reporter plasmid with different amounts (1, 5, 10, 15 and 20 µL) of PEI-SWNT in cell culture medium at room temperature for 45 minutes under constant stirring. After incubation with the plasmid, zeta potential measurements were performed again. In this case, the zeta potential measurement showed a negative value

of -26.4 ± 0.850 due to the electrostatic interaction of the negatively charged EGFP plasmid into the surface of the PEI-SWNT (**Figure 62**).

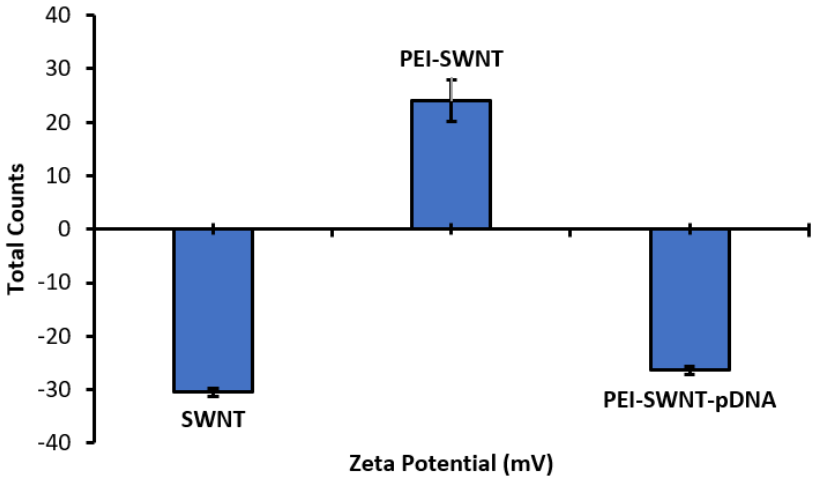

Figure 62. Zeta potential measurements of SWNT, PEI-SWNT and PEI-SWNT-pDNA (n = 3).

Besides, the binding capacity of the EGFP plasmid and PEI-SWNT was studied by a retardation assay on an agarose gel. The plasmid can run on the gel, however, once it is complexed with PEI-SWNT, it is retained in the loading well of the gel. This experiment revealed that at least 20 µL of the PEI-SWNT solution were necessary to bind the total amount of the EGFP plasmid (**Figure 63**).

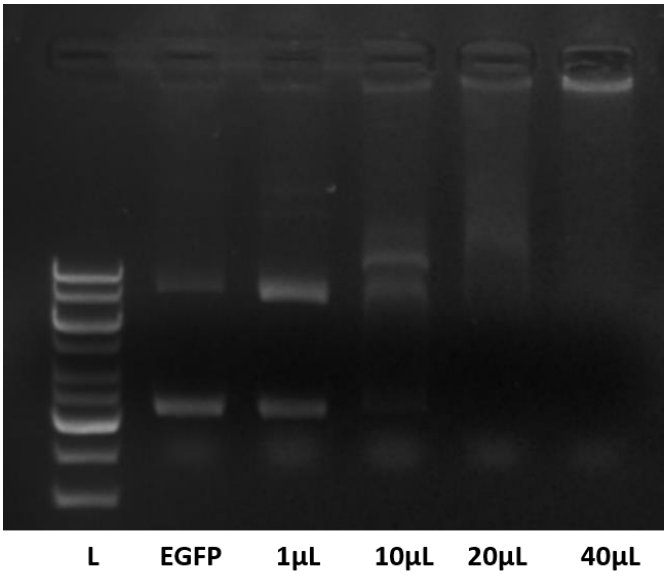

Figure 63. Retardation assay on an agarose gel of the PEI-SWNT-EGFP complex using a constant concentration of 1 µg EGFP plasmid. Naked DNA (1 µg) was used as a control.

4.3.2.2.2. Cellular toxicity of PEI-SWNT-pDNA

The toxicity of the complex in HEK293 cells was assessed by resazurin assay. The complex was incubated for 24 hours in cells at different concentrations. Then, the cells were washed twice with cell culture medium and incubated for 48 hours more (**Figure 64**). In this case, the cells were washed with culture medium instead of PBS, since it caused the aggregation of nanotubes and prevent their correct elimination of the plate-wells. The toxicity results obtained showed that both the PEI-SWNT at the highest concentration and the complexes formed with the EGFP plasmid (PEI-SWNT-EGFP) at none of the concentrations studied decreased cell viability compared to the control of untreated cells. The low toxicity reported, suggests that PEI-SWNTs could be employed in live systems, despite the current safety concerns of SWNT[259].

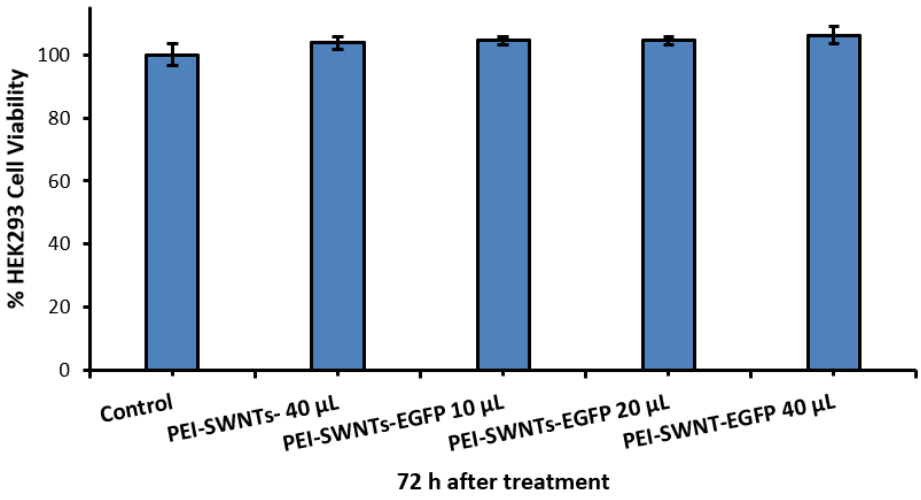

Figure 64. Cell viability assay in HEK293 cells at 48 hours post-incubation with the PEI-SWNT-EGFP complexes at different concentrations studied by resazurin assay. Statistical analysis was performed using one-way ANOVA Tukey's test.

4.3.2.2.3. Gene transfection efficiency of PEI-SWNT-pDNA

To evaluate the transfection efficiency of PEI-SWNT, the EGFP reporter plasmid was used. Thus, 20 and 40 µL of PEI-SWNT were incubated with 1 µg of EGFP plasmid for 45 minutes to form the complex. The resulting complexes were added to HEK293 cells dropwise and incubated for 24 hours. Then, cells were washed with complete culture media to remove the excess of non-internalized PEI-SWNT-pEGFP and incubated for 48 hours more. The fluorescence intensity of the EGFP reporter plasmid was analyzed by fluorescence microscopy every day. The images clearly showed a correlation between

the PEI-SWNT and the fluorescence, where the higher amount of nanotubes used, the higher the fluorescence observed. Furthermore, the fluorescence observed increased over time (**Figure 65**).

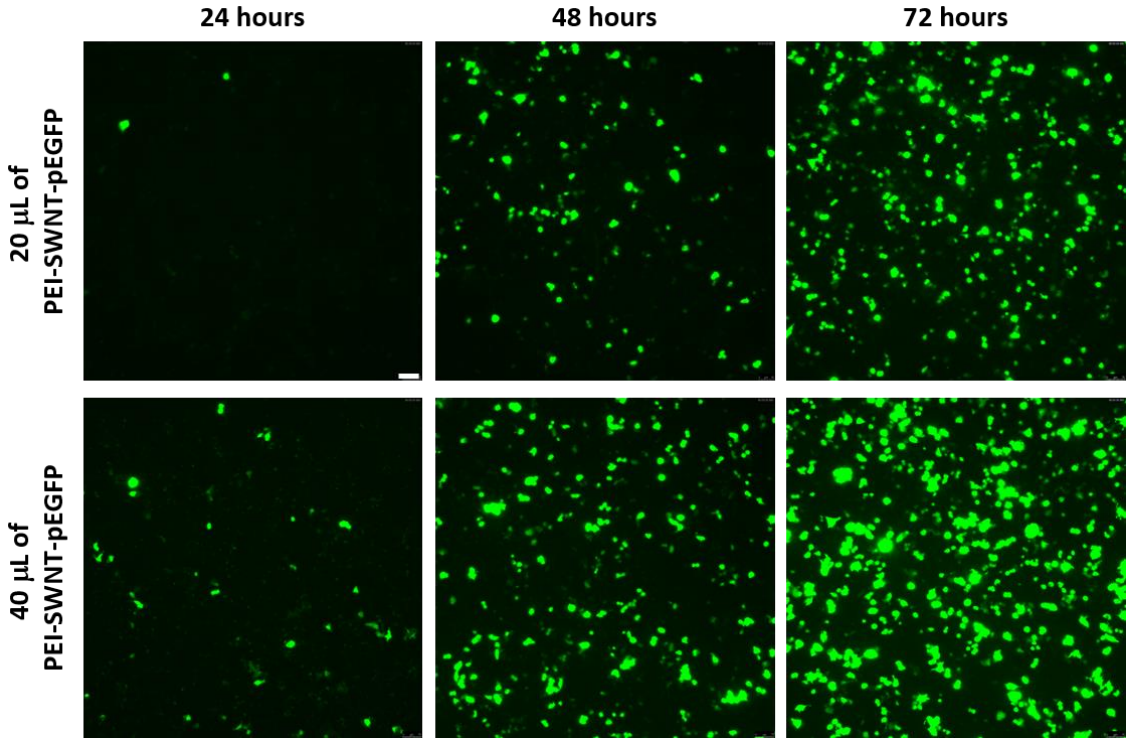

Figure 65. Fluorescence microscopy images of HEK293 cells at different times after treatment showed the high transfection efficiency by the expression of EGFP reporter plasmid using PEI-SWNT. Fluorescence intensity increase both with 20 µL (top) and 40 µL (bottom) of PEI-SWNT-EGFP and with time (24, 48 and 72 hours). Scale bar: 75 µm.

Similarly, two other cell lines were transfected with PEI-SWNT-pDNA. In this case, based on the previous results obtained with HEK293, 20 µL of functionalized SWNTs and 1 µg of EGFP plasmid were employed. The results were analyzed by fluorescence microscopy after 72 hours of treatment. As can be seen in the images, the PEI-SWNT-EGFP complex can internalize in Mel202 and Panc1 cells but with much less efficiency than HEK293 (**Figure 66**).

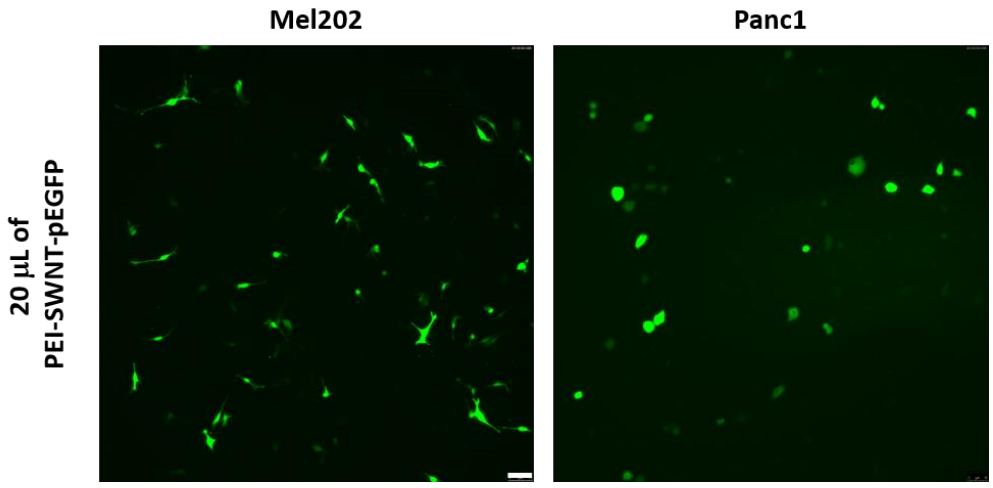

Figure 66. Fluorescence microscopy images of Mel202 and Panc1 cells at 72 hours after treatment showed that the transfection efficiency by the expression of EGFP reporter plasmid using 20 µL PEI-SWNT is low compared to HEK293 cells. Scale bar: 75 µm.

Finally, to investigate whether PEI-SWNT was capable of binding and internalizing the CRISPR/Cas9 plasmid, the complexes were formed as previously described using 20 and 40 µL of the functionalized nanotubes with 1 µg of Cas9-EGFP plasmid, obtaining a new complex called PEI-SWNT-pCas9.

HEK293 cells carrying the EGFP plasmid were treated with 20 and 40 µL of PEI-SWNT-pCas9 for 24 hours. After 72 hours of treatment, the fluorescence of the cells was analyzed by fluorescence microscopy, where three different regions were taken. As a positive control, cells transfected with only EGFP were used (**Figure 67a**). The fluorescence images did not reveal significant differences between the samples treated with 20 and 40 µL of PEI-SWNT-pCas9 complex and the positive control, as it could be seen **Figure 67 b** and **c**, respectively.

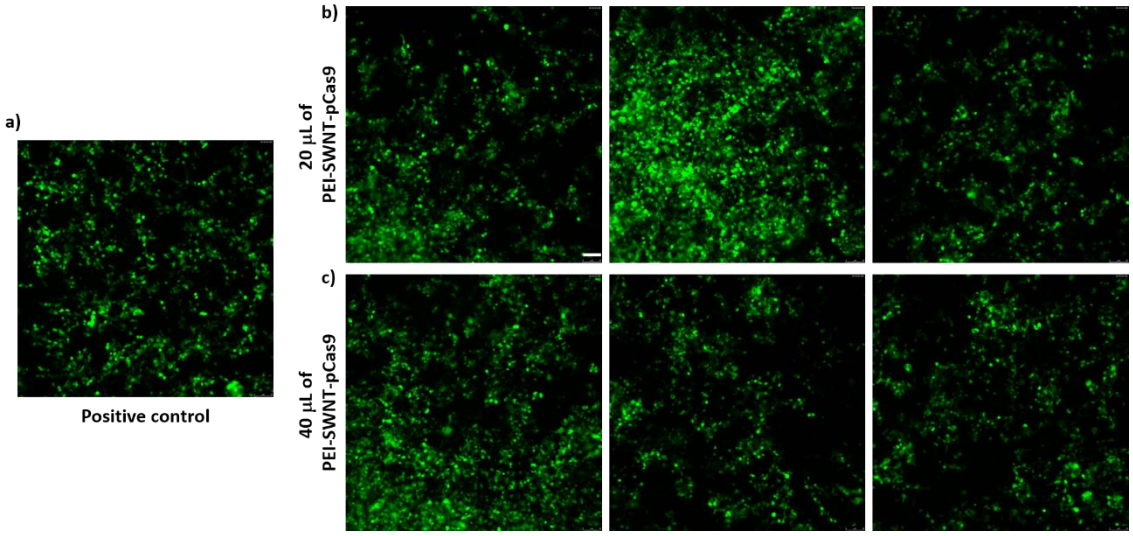

Figure 67. Fluorescence microscopy images of HEK293 cells at 72 hours after transfection with the EFGP plasmid using Lipofectamine 2000 for 6 hours and treated with **b)** 20 µL and **c)** 40 PEI-SWNT-pCas9 complexes for an additional 24 hours. Cells transfected with EGFP plasmid using the commercial reagent Lipofectamine 2000 were used as a positive control **a)**. After treatment with the complexes, no significant difference in fluorescence intensity was observed compared with the positive control. Scale bar: 50 µm.

4.3.3. Albumin-based nanocomplexes for CRISPR-Cpf1 ribonucleoprotein delivery

The main objective of this part of the work was the transport and protection of the ribonucleoprotein of the CRISPR system Cpf1. Protein transport in biological systems is limited by its low stability or by its premature degradation, among others. As previously described, albumin is one of the most abundant proteins in the body and is being widely used as a drug delivery system, as it is biodegradable, non-toxic, and capable of accumulating in tumor tissues. Furthermore, albumin can be covalently modified with therapeutic agents due to the presence of chemical groups on its surface. In this sense, we proposed that the covalent conjugation between BSA and Cpf1 proteins would lead to the formation of BSA-Cpf1 complexes. In these complexes, several BSA molecules would surround a Cpf1 protein, which would allow its protection for a longer time in biological systems and would increase its internalization in cell cultures.

The design and purification of the Cpf1 protein were done by Carmen Escalona from the group of Dr. Begoña Sot at IMDEA Nanociencia.

4.3.3.1. Formation of BSA-Cpf1 complexes

The formation of the BSA-Cpf1 complexes was carried out in three steps as follows (**Figure 68**). First, a solution of BSA in PBS (pH = 7.4) was modified using 20 equivalents of 2-iminothiolane at room temperature for 4 hours, introducing thiol groups on the albumin surface (reaction **1**). Second, 20 equivalents of aldrithiol were added (reaction **2**) to make the thiol groups reactive for the subsequent reaction with the available thiols groups of cysteines present in Cpf1. Finally, the BSA-Cpf1 complexes were prepared at different concentrations of modified BSA (reaction **2**), as follows: 20, 50 and 100 µM of the modified BSA in PBS (pH = 7.4) was incubated with 10 µM of Cpf1 at room temperature for 1 hour and then 4 °C for 16 hours (reaction **3**). Therefore, the resulting complexes were synthesized at a 2:1, 5:1 and 10:1 ratio of BSA:Cpf1. The linker between BSA and Cpf1 presents a disulfide moiety sensitive to high concentrations of a reducing agent such as dithiothreitol (DTT), which promotes the release of proteins under tumor conditions.

In reactions **2** and **3**, the release of pyridinethione (**Figure 68,** orange) occurs from the reaction with aldrithiol. The release of this compound was studied by UV-Vis spectra, revealing a characteristic absorbance spectrum with a maximum at 343 nm, which allows us to know if the reaction has been successful.

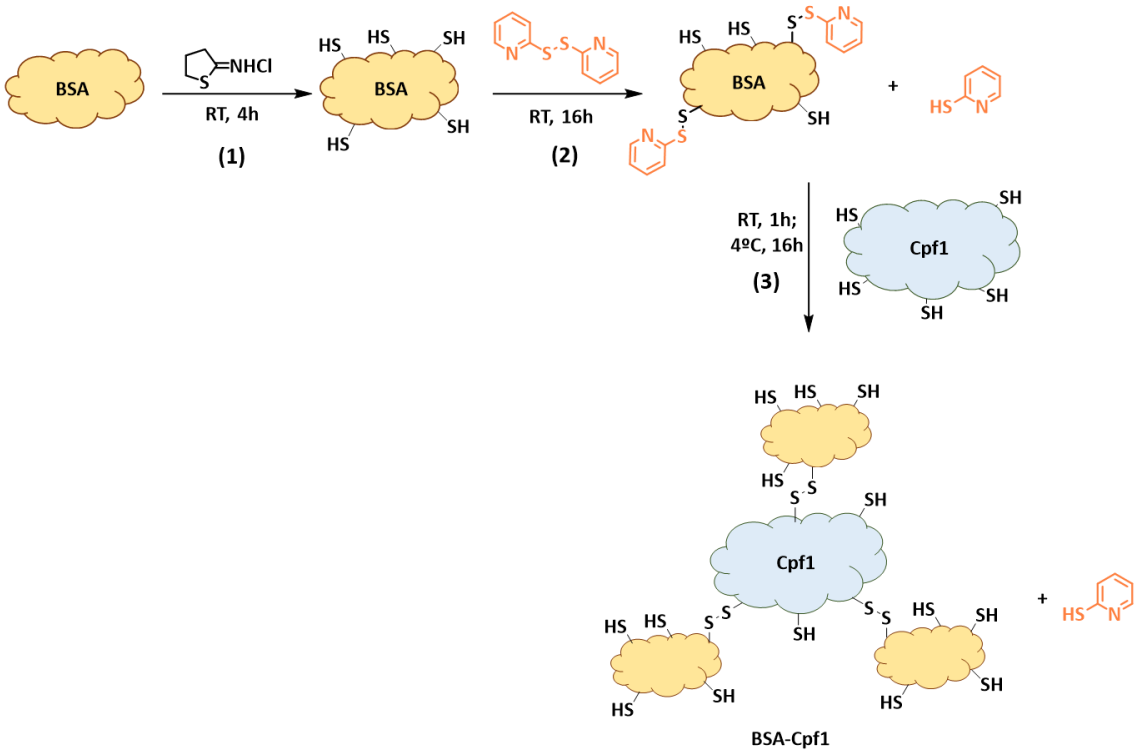

Figure 68. Schematic representation of the synthesis of the BSA-Cpf1 complexes containing a disulfide moiety that promote the release of the proteins in the presence of high concentrations of a reducing agent. In the reaction 2 and 3, pyridinethione (orange) is released.

To confirm the activation of the BSA, the absorbance spectrum of the BSA sample was studied before and after being purified by the NAP-10 size exclusion column. The characteristic UV-Vis spectra of the pyridinethione is only observed before purification, indicating that all the excess of this molecule is retained in the column (**Figure 69**).

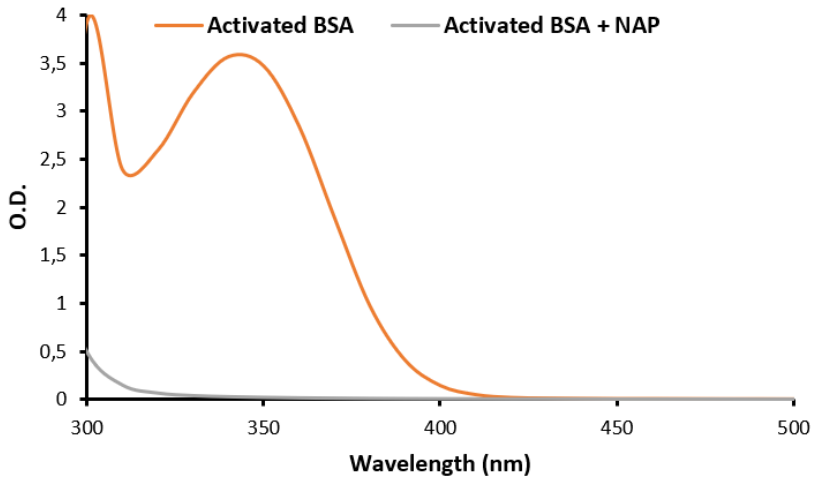

Figure 69. UV-Vis spectrum of activated BSA before (orange) and after (grey) purification revealing the characteristic release profile of the pyridinethione with a maximum peak at 343 nm.

The conjugation of the activated BSA and Cpf1 was also studied by the UV-Vis spectrum of the pyridinethione released. As a control, BSA incubated with Cpf1 was used (BSA Unmod + Cpf1). The results showed two different peaks at 280 and 343 nm, corresponding to the proteins (BSA-Cpf1) and aldrithiol, and pyridinethione, respectively. In the case of unmodified BSA (**Figure 70 a** and **b**), only the peak corresponding to the proteins can be observed, which increases with a higher concentration of BSA. The peak of pyridinethione was not observed in these samples, confirming that there has been no reaction between the two proteins. Remarkably, in the case of BSA activated and incubated with Cpf1, the two peaks at 280 and 343 nm were observed (**Figures 70 c** and **d**). In this sense, we can deduce that the conjugation between Cpf1 and BSA took place due to the presence of the released pyridinethione.

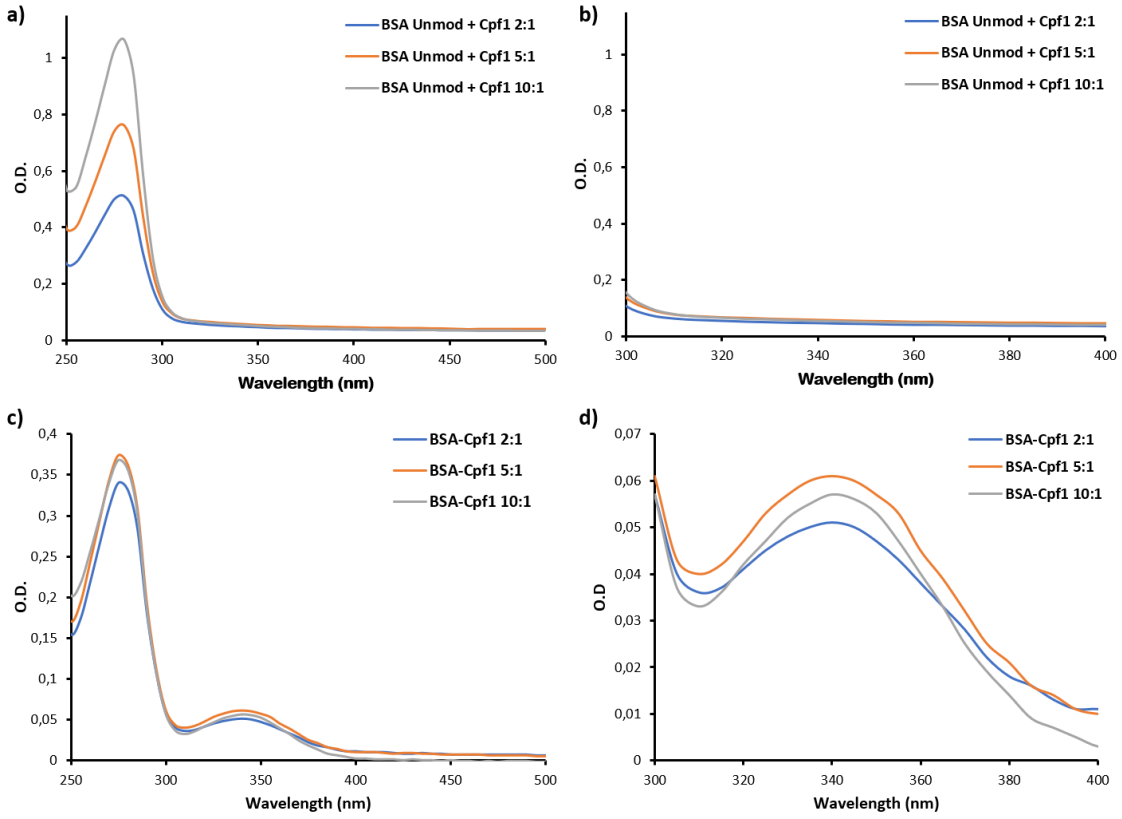

Figure 70. UV-Vis spectrum of the samples of BSA-Cpf1 complexes. **a)** BSA incubated with the Cpf1 and **b)** its amplification from 300 to 400 nm. **c)** BSA-Cpf1 complexes showed the characteristic profile of the pyridinethione released during the conjugation between the two proteins and **d)** its amplification from 300 to 400 nm.

To evaluate the conjugation between the two proteins, the absorbance of pyridinethione was also measured at 343 nm, allowing us to determine the number of BSAs bound to Cpf1, using the Lambert-Beer equation. As a control for this experiment, activated BSA (reaction **2**) was employed. The data obtained suggested that 3-4 BSA were covalently bound to Cpf1. The data was summarized in the following **table 9**.

	Corrected Enpoint at 343 nm	Concentration (µM)
BSA-Cpf1 2:1	0.273	33.8
BSA-Cpf1 5:1	0.338	41.8
BSA-Cpf1 10:1	0.286	35.4

Table 9. Values of absorbance of pyridinethione measured at 343 nm. The calculated concentration was done by Lambert-Beer equation using the extinction coefficient of pyridinethione (8080 L mol^{-1} cm^{-1}).

The size of the resulting products was measured by dynamic light scattering (DLS) in PBS by intensity. In particular, the size of the BSA unmod + Cpf1 and the BSA-Cpf1 complexes at different ratios was studied. On the one hand, two peaks around 10 and 100 nm could be seen in the three BSA unmod + Cpf1 samples. These data suggested that the proteins are free in the solution having a size of approximately 10 nm, but also, form some type of aggregate with a size greater than 100 nm (**Figure 71,** orange line). On the other hand, in the BSA-Cpf1 complexes, it was possible to observe how the 10 nm peak increased in intensity, while the 100 nm peak decreased. These results could indicate less aggregation of proteins that are covalently conjugated to form the BSA-Cpf1 complexes. Specifically, in the 2:1 and 5:1 ratio (BSA:Cpf1), the peaks observed were 24 and 21 nm, respectively (**Figure 71 a** and **b**). However, in the case of the 10:1 ratio, although an increase in size was also detected, it was smaller than expected, with a size of 16 nm (**Figure 71c**).

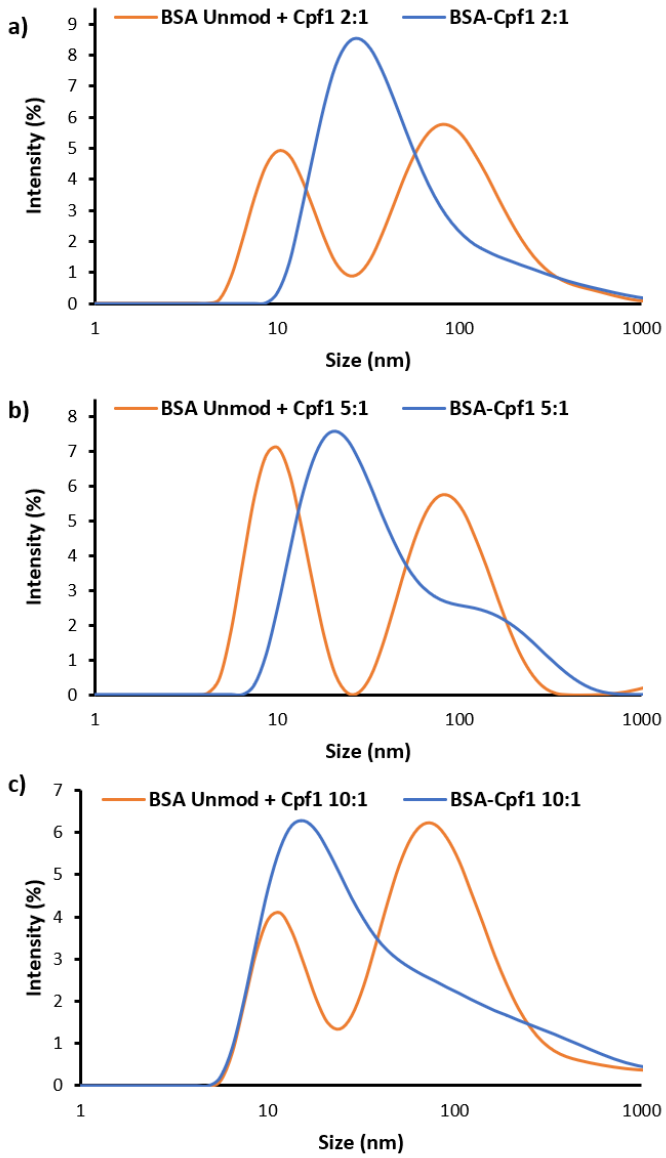

Figure 71. Size of BSA unmodified incubated with Cpf1 and BSA-Cpf1 complexes measured by intensity using dynamic light scattering in PBS (pH = 7.4).

To further assess the formation of the covalently conjugated BSA-Cpf1 complexes, a 10% SDS-PAGE was performed. As mentioned before, the linker between BSA and Cpf1 contains a disulfide moiety that could be cleaved, releasing the two proteins in the presence of high concentrations of DTT (50 mM). In this sense, the samples at different ratios of BSA:Cpf1 (2:1, 5:1, 10:1) were incubated with the loading buffers containing (+) or not (-) DTT and run into the SDS-PAGE. As can be seen in the gels, when the BSA was not modified, two bands corresponding to Cpf1 (top) and BSA (bottom) were observed both in the presence or not of DTT, suggesting that the two proteins were not covalently conjugated (**Figure 72a**). On the contrary, when BSA was activated, in the absence of

DTT, a third band could be seen corresponding to the complexes, which could not run on the gel. However, when DTT was added, this third band disappeared, giving rise to the two bands corresponding to BSA and Cpf1. These results confirmed the covalent binding of the two proteins with a linker sensitive to the reducing environment (**Figure 72b**). Regarding the complexes formed, the 2:1 ratio (BSA:Cpf1) did not show any band corresponding to the molecular weight of BSA and Cpf1, showing that all the BSA is conjugated to form the BSA-Cpf1 complex. However, at higher ratios, 5:1 and 10:1, the BSA band can be observed, which suggests that there was an excess of this protein in these samples.

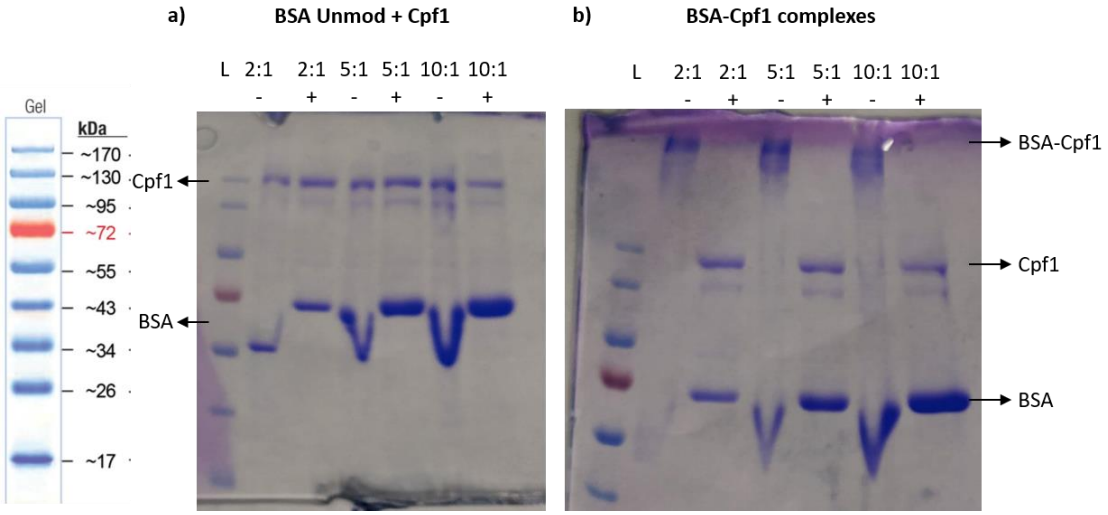

Figure 72. SDS-PAGE of the BSA-Cpf1. **a)** In the gel of unmodified BSA, incubated with the Cpf1 showed two bands corresponding to the separate Cpf1 and BSA. **b)** A third band appears due to the conjugation of activated BSA with the Cpf1 leading to the complex formation. MW: BSA = 66.5 kDa, Cpf1 = 151 kDa.

Next, to determine the release of Cpf1 from BSA, BSA-Cpf1 complexes at different ratios were exposed to increasing concentrations of DTT from 0 to 50 mM for 1 hour at room temperature. After the incubation, the results were analyzed by 10% SDS-PAGE. The results obtained indicate that the release of Cpf1 depends on the concentration of DTT. When a 2:1 (BSA:Cpf1) ratio was used, at least 1mM DTT is required to initiate the release of Cpf1, and above 10 mM all the protein was released. However, when 5:1 and 10:1 (BSA:Cpf1) ratios were used, 10 mM of DTT was required to promote the release of Cpf1. This result suggests that the large excess of BSA in the samples may be forming some type of aggregate with the BSA-Cpf1 complexes or surrounding them, hindering the release of Cpf1 (**Figure 73**).

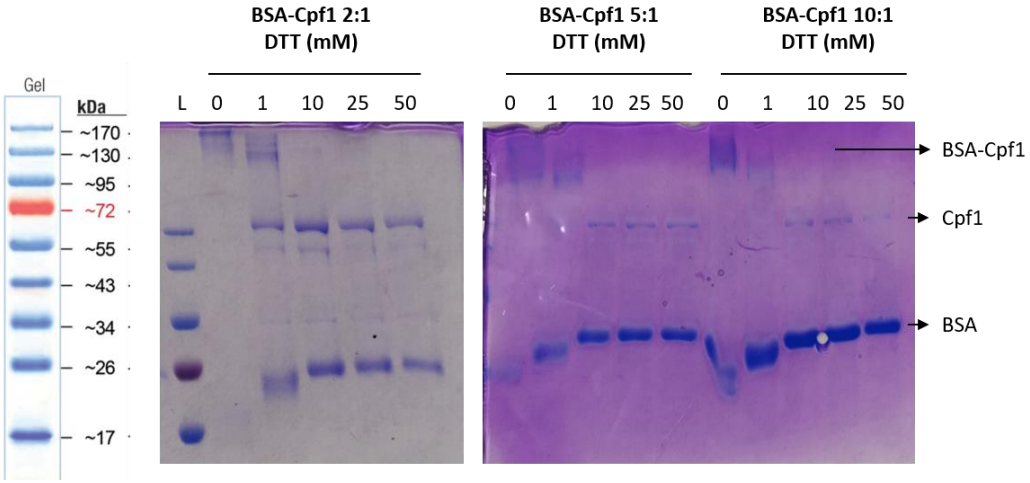

Figure 73. Release profile of Cpf1 from BSA. The BSA-Cpf1 complexes were exposed to a different concentration of DTT (1-50 mM) for 1 hour at room temperature and analyzed by 10% SDS-PAGE. MW: BSA = 66.5 kDa, Cpf1 = 151 kDa.

4.3.3.2. EGFP *in vitro* cleavage

To investigate whether the complexes could edit genes, we compared the ability of BSA-Cpf1(RNP) and Cpf1(RNP) to cleavage *in vitro* an amplicon from a genomic region of the EGFP gene containing the CRISPR target site. In this case, the complexes at different ratios of BSA (2:1, 5:1, 10:1) were formed using Cpf1 bound to the CRISPR sgRNA against EGFP, leading to the desired BSA-Cpf1(RNP) complexes. These complexes were incubated in a buffer containing DTT at 10 mM for 1 hour, and then mixed with the EGFP amplicon for an additional 1 hour. The efficiency of BSA-Cpf1(RNP)-mediated cleavage was analyzed by agarose gel electrophoresis. Cleavage by the BSA-Cpf1(RNP) complex results in another smaller band that can be easily distinguished on an agarose gel. This result revealed that the Cpf1(RNP) released from the complex maintained its activity (**Figure 74**).

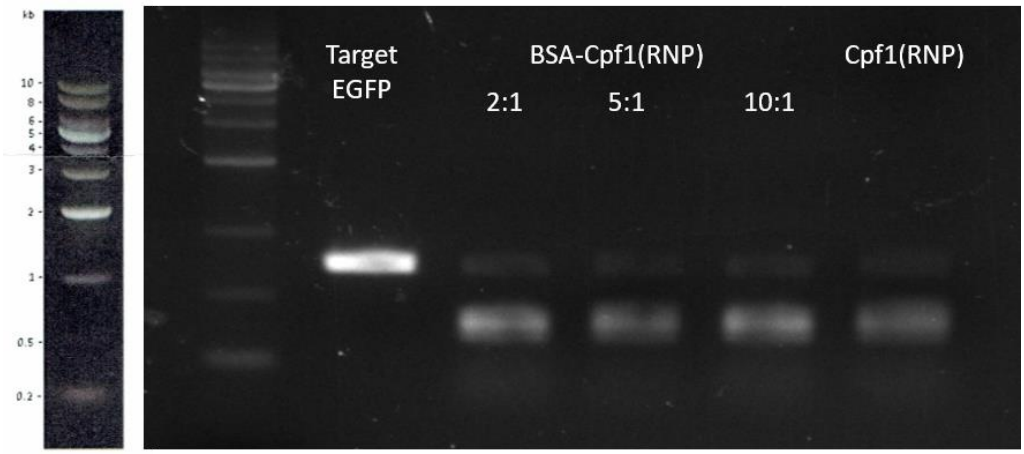

Ready Ladder™, 1 kb DNA Marker resolved on a 1% TAE/Agarose I™ gel

Figure 74. Gel electrophoresis of in vitro DNA cleavage production of EGFP-DNA targeted. As a control, Cpf1(RNP) alone was used.

Discussion

5. DISCUSSION

5.1. Challenges in cancer treatment

Cancer is a very complex disease that affects millions of people every year. In 2018 there were 17 million new cases in the world, and it is estimated that there will be 20 million new cases by 2040, which represents an increase of 62%. According to the World Health Organization (WHO), cancer is the second leading cause of death, accounting for an estimated 9.6 million deaths in 2018[260].

Cancer originates from the uncontrolled proliferation of any type of cell of the body; thus, it could be more than a hundred different types of cancer, which can vary in their behavior and how they respond to treatments[261]. In this regard, there are two major challenges in the fight against cancer: the availability of early detection systems and effective and non-toxic treatments.

Early detection and precise diagnosis are vital to select the most suitable treatment at the beginning of the disease, which significantly increases the survival of the patients. However, some current detection techniques, such as imaging techniques (CT, MRI and PET scans), or protein biomarkers, have low sensitivity and specificity and are not reliable at the early stages of the disease[262,263].

Regarding the therapeutic approaches available, the most widely used for cancer treatment is chemotherapy. However, it involves using cytotoxic drugs that can reach different areas of the body in an unspecified way, leading to undesirable side effects[76]. Furthermore, patients may develop drug resistance during the treatment, resulting in tumor regrowth[264].

For these reasons, more precise therapeutic approaches are being developed, such as targeted therapy, immunotherapy or gene therapy (see Introduction, section **1.4.1.**). Among them, those known as targeted therapies are designed against specific proteins that are mutated or overexpressed in particular types of tumors, such as human epidermal growth factor receptor 2 (HER2), epidermal growth factor receptor (EGFR), vascular endothelial growth factor receptor (VGFR), tyrosine kinase BCR-ABL or CD-20[265,266]. As a result of these approaches, a new type of medicine known as precision oncology has emerged, where genetic information from tumors of patients is used to

prevent, diagnose or treat cancer effectively[267]. For instance, there are genomic alterations in different cancers that can be exploited as predictive biomarkers, such as *HER2*, *BRCA1/BRCA2* or *BRAF*[268]. Interestingly, those can also be used as therapeutic targets. For example, tumors with mutations in the *BRAF V600E* gene, such as in melanoma, are sensitive to Vemurafenib treatment. However, in melanomas with a non-mutated BRAF gene, treatment with Vemurafenib is associated with the development of drug resistance. Therefore, detecting these biomarkers can be critical to determine the appropriate treatment for each patient and predict their prognosis[269].

5.2. Nanoparticles based drug delivery systems for cancer treatment

Despite the enormous potential of targeted therapies, compared to conventional chemotherapeutic drugs, there are still some limitations that make this approach far from ideal. First, despite being design to interact with specific tumoral features, these types of therapies can cause some toxicity in patients. Some of these treatments can cause mild side effects. Vascular endothelial growth factor receptor (VEGFR) kinase inhibitors induce hypertension and epidermal growth factor receptor (EGFR) antibodies cause rash. However, others can produce more severe effects in patients, as in the case of trastuzumab that causes cardiotoxicity[270,271]. Also, the biodistribution and pharmacokinetics of the drugs are not optimum, and, in some cases, the drugs are sensitive to degradation in the bloodstream[126].

For these reasons, in recent years, research has been focused on the development of new nanoparticle-based drug delivery systems[123]. These systems can improve the solubility of drugs and, therefore, improve their stability, level of absorption and bioavailability[272].

There are a wide variety of nanoparticles developed to deliver bioactive molecules for the treatment of cancer (see Introduction, section **1.5.2**). Such systems have been employed mainly for the delivery of chemotherapeutic drugs[273]. But nanoparticles can also be used as transporters of other bioactive molecules such as nucleic acids or proteins. In these latter cases, the use of a nanocarrier is particularly relevant since these biomolecules are more susceptible to degradation and elimination, and their transfection to the target cells is very poor[274,275].

In our group, several strategies to transport nucleic acids and small molecules using nanoparticles have been developed. In particular, gold and magnetic nanoparticles are being used as drug carriers to directly attack different types of cancer cells derive from uveal melanoma or pancreatic cancer, respectively. These nanoparticles have been modified with diverse therapeutics like siRNAs or small molecules using tailored linkers that allow the controlled release of the payloads into the tumoral cells. Additionally, to improve the selectivity of the nanoparticles against tumoral cells, they have also been modified with ligands such as aptamers, peptides or antibodies that recognize overexpressed receptors on the surface of the cancer cells. These modified nanoparticles, resulted in a significant selectivity and decrease in cell viability of tumoral cells[214,276–278].

In this sense, the group is investigating novel approaches for the development of new nanoparticle-based drug delivery systems that may offer different possibilities and advantages for their subsequent application in the treatment of cancer. In particular, in this work, albumin-based nanostructures were selected for the treatment of cancer, and to transport the CRISPR/Cas gene-editing protein. Also, cationic modified single-walled carbon nanotubes (SWNTs) were employed to carry a CRISPR/Cas9 gene-editing plasmid to cells efficiently.

5.3. Albumin-based nanostructures in cancer treatment

During the last decade, the use of albumin as a drug transporter has been extensively investigated due to the excellent safety profile of albumin-based nanoparticles. This is because albumin is highly bioavailable, biodegradable, does not produce toxicity and immunogenicity in the body as an endogenous protein. In addition, albumin-based nanostructures are suitable for passive and active targeting, promoting the selective accumulation in tumors[279].

The great versatility of albumin provides different opportunities to develop various systems based on albumin, including albumin nanoparticles, drug albumin conjugates, and drug derivatives that bind albumin. The binding of drugs to albumin improves their pharmacokinetic properties and increases their circulating half-life. For the development of these nanoformulations, two types of albumin are usually employed:

human serum albumin (HSA) and bovine serum albumin (BSA). These two types of albumin share several characteristics such as high-water solubility, a high circulating life span, similar molecular weight (65-70 kDa), and a very similar number of amino acid residues (585 for HSA and 583 for BSA). The two types of albumin have been widely used to develop nanoparticles, and no significant differences have been observed in their construction[280].

In this thesis, different formulations based on albumin have been used to deliver therapeutic agents for the treatment of cancer efficiently. In particular, BSA-stabilized gold nanoclusters (BSA-AuNCs) and native BSA were used to successfully transport of antitumoral drugs such as AZD8055, DOX and SN38, and CRISPR/Cas gene-editing protein Cpf1 in a simple way.

It is known that albumin has a remarkable ability to bind ligands. There are several binding sites on albumin molecules, located primarily in subdomains IIA and IIIA. This allows albumin to works as a carrier for a variety of different molecules, including small, insoluble molecules like fatty acids, antitumor agents, metal ions, or hormones, among others. Binding modes include hydrophobic and electrostatic interactions, which are mainly reversible, and covalent bonds that can occur reversibly or irreversibly[279,281].

In the case of non-covalent bonds, albumin can bind both endogenous ligands such as fatty acids or bilirubin, and exogenous ones such as penicillin or diazepam. This union influences the pharmacokinetic properties of these molecules, improving their biodistribution and bioavailability[282].

Currently, this approach is used in several clinically approved drugs such as Levemir® (long-acting insulin anabolic), in which insulin is modified with a chain of fatty acid, which has a high affinity to bind to albumin[282]. However, one of the most significant evidence of the success of albumin-based nanostructures has been the development of nanoparticles albumin-bound (nab) technology. This system allows the encapsulation of the hydrophobic drug paclitaxel into the hydrophobic domains of albumin (nab-paclitaxel or Abraxane®), giving rise to structures of about 130 nm. After the systemic administration of the nanostructures, the complex disassembles, resulting in the formation of smaller nanoparticles where some amount of paclitaxel is released. Unlike conventional paclitaxel treatments, these nanoparticles do not require the addition of

cytotoxic solvents such as Cremophor® EL and ethanol, which allow the administration of a higher dosage of drugs [283,284]. Nab-paclitaxel is currently approved for the treatment of different types of tumors, including metastatic breast cancer, non-small cell lung cancer, and metastatic pancreatic cancer[284].

Conversely, covalent binding of drugs to albumin is possible exogenously through chemical conjugation due to the presence of chemical moieties present in their surface (e.g., $-NH_2$, $-CO_2H$, -SH). Another alternative for peptides or proteins is gene fusion, where the gene that encodes for the peptide or protein is fused albumin. Several therapeutics are prepared in this way, such as Albiglutide, a long-acting glucagon-like peptide-1 (GLP-1) receptor agonist composed of a GLP-1 (7-36) dimer fused to recombinant human albumin[285].

In particular, in our case, we proposed the covalent conjugation of the active molecules to BSA. This protein has 59 lysine amine groups, of which approximately 30-35 are sterically available for conjugation. This large number of amine groups allows us to chemically modify albumin efficiently via sulfhydryl activation for its subsequent functionalization with the therapeutic molecules. In contrast to nab-paclitaxel technology, our strategy requires the covalent conjugation of therapeutic agents. This process requires the chemical modification of both the BSA and the actives molecules before use. But it can be used for the controlled release of therapeutic agents thanks to the use of linkers sensitive to stimuli present in the tumor. Thus, the development of these nanostructures will enhance the pharmacokinetics of drugs, improving their half-life and favoring greater internalization in tumor tissues.

5.3.1. BSA-AuNCs as drug delivery systems: AZD8055, doxorubicin (DOX) and SN38

BSA-AuNCs characterization

For the covalent conjugation of the different antitumor drugs, we proposed the use of BSA-AuNCs due to the great advantages reported in previous studies (see Results, chapter **4.1**). These nanostructures are highly fluorescent and stable, exhibit high biocompatibility, and excellent water solubility (**Figure 17**). In addition, its synthesis is easy and reproducible, allowing its scale-up efficiently without losing its properties, which is a great advantage over its possible use in clinical approaches. It is worth

mentioning that, scaling processes is a critical factor in the development of safe and effective nanostructures. Although scaling-up any drug is complex, large-scale production of nanomaterials is even more challenging. In this sense, small variations in the scaling process can result in significantly different nanomaterials, thus reducing their quality and effectiveness[286,287]. Moreover, drug delivery systems have become increasingly complicated, as they often consist of more than one therapeutic agent. For these reasons, the approach described here has great potential due to the ease of implementation. In this regard, we have shown that different antitumor drugs such as AZD8055, DOX and SN38 can be conjugated on the surface of the BSA easily. To do this, in collaboration with the chemists working in the group, the drugs were modified with different types of tailor-made linkers that facilitated their conjugation to the activated BSA in a single step (**Figures 19, 20, 36, 37 and 38**). Remarkably, this strategy not only allows the binding of an active molecule on the surface of the BSA, but also enables the development of multifunctional nanostructures that contain more than one active molecule. This is the case of the BSA-AuNCs functionalized with DOX and SN38, which can be used as a combined therapy to treat breast cancer (**Figure 38**). It is worth mentioning that the delivery of these two drugs in the same nanostructures is not easy due to the differences in hydrophilicity of doxorubicin (hydrophilic) and SN38 (hydrophobic).

Upon conjugation of BSA-AuNCs with the drugs, the formation of larger nanostructures was observed by DLS measurements (**Figures 23 and 40**). In particular, the interaction of hydrophobic drugs such as AZD8055 and SN38 with BSA-AuNCs leads to the self-assembly of hydrophobic BSA domains, achieving the formation of structures up to 10 times larger. Specifically, BSA-AuNCs-AZD present a hydrodynamic size of 141.2 nm (PDI: 0.180), and BSA-AuNCs-S of 117.5 nm (PDI: 0.277). However, the interaction with DOX, a hydrophilic drug, did not produce this remarkable self-assembly of BSA-AuNCs and two populations of nanoparticles with different sizes were obtained. Interestingly, the use of DOX and SN38 in the same nanostructure does not affect the formation of larger nanoparticles with a size of 190.8 nm (PDI: 0.263).

Another strategy employed to measure the size of the BSA-AuNCs-AZD was the use of two different microscopy techniques (**Figures 25 and 42**). In particular, the

nanostructures were measured by SEM and AFM, revealing an average size of 73.29 ± 15.1 and 128.6 ± 10.6 nm, respectively. The size variations obtained are derived from the fact that the techniques are different and measure different properties of the nanostructures. The SEM provides 2D images of the samples, and requires a vacuum environment during the entire imaging process. However, AFM provides 3D images, and does not require any special treatment during the imaging process, as it can work perfectly in ambient air[288]. Anyhow, the resulting nanostructures have the optimum size for their selective accumulation in tumors due to the EPR effect[118]. This effect is based on the hyperpermeability of tumor vessel due to their large intracellular opening (above 10 nm), and the reduction of functional lymphatic vessels. All BSA-AuNCs obtained presented at least 10 nm in diameter, so they cannot leak into normal healthy tissues, but can pass through defective tumor blood vessels and accumulate within their target site. In addition, this functionalized BSA-AuNCs exceeds the renal clearance threshold, which prolongs the half-life of circulating drugs for 19 days[125]. This may be mainly due to the neonatal Fc receptor (FcRn), which protects albumin for intracellular degradation of lysosomes[289], and by the reabsorption by the megalin/cubilin complex in the proximal kidney tube that prevents urinary protein excretion[290].

However, conventional drugs such as DOX, SN38 or AZD8055, are small molecules that have unfavorable pharmacokinetic properties and a nonspecific biodistribution, since they are capable of easily extravasating any blood vessels. As a consequence, these drugs have a short half-life in circulation and can cause side effects in healthy tissues[291]. For example, it has been found that by encapsulating DOX in liposomes, Doxil®, the half-life of the circulating drug increases from 5 to 10 minutes to 2 to 3 days when encapsulated and the amount of drug in the tumor is enhanced in a 4 to 16-fold[292]. Nevertheless, it is worth mentioning, that the therapeutic efficacy of passively targeted nanoparticles is controversial, since clinical results are highly heterogeneous. Despite this, it is essential to note that there are currently many passively targeted nanoparticles in the clinic, such as Doxil®, Abraxane® and Onivyde®, among others[293].

In addition to size, another critical parameter closely related to the toxicity of nanoparticles is their shape. In all cases, the functionalized BSA-AuNCs presented a spherical morphology, as we could verify by SEM and AFM (**Figures 25 and 42**). In this

sense, it has been demonstrated that spherical nanoparticles have lower toxicity compared to other types of nanoparticles, such as cylinder or fiber[294]. What is more, spherical structures are also more likely to internalize through endocytosis at a higher rate than other types of nanoparticles[120,294].

Controlled release from BSA-AuNCs

Nanostructures can be tailor-modified to allow controlled drug release. These are designed to retain the drug during their circulation in the bloodstrem, and release it once the tumor is reached, due to an internal or external stimulus (**Figure 75**)[135,295]. Internal stimuli, are used to improve the specificity of drug action. There are different characteristics between the intracellular and extracellular environment of cancer and normal cells that can be exploited, including low pH, intracellular glutathione levels, or overexpressed enzymes. On the other hand, the external stimuli, such as ultrasound, light or magnetic field (hyperthermia), are applied externally after administration of the nanoparticles. Using these approaches, drug delivery can be better controlled both spatially and temporally, avoiding the premature release of the drugs. In this regard, a recent study from Zhang *et al.*, showed that nanoparticles designed to release their cargo under specific conditions of pH and reductive environment increase the targeting efficiency of tumors[296].

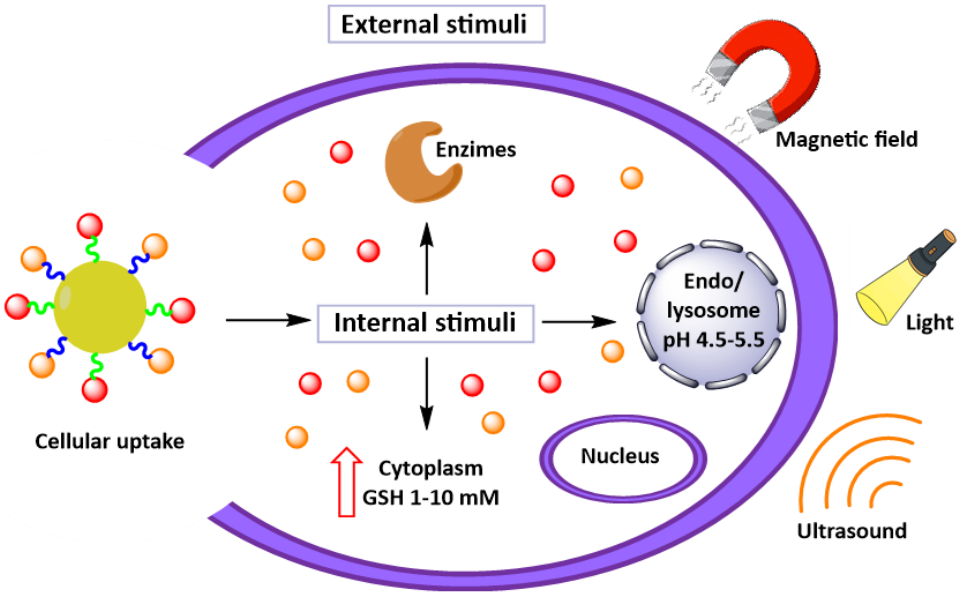

Figure 75. Schematic representation of different internal and external stimuli presents in tumor cells, which are commonly used for stimuli-responsive nanostructures.

For the efficient and controlled release of drugs from BSA-AuNCs, these were modified with linkers sensitive to stimuli present in tumor cells. For these linkers to be effective and functional, they must fulfill two main characteristics. On the one hand, they must keep the drug conjugated into the BSA-AuNCs with a strong bond, so that it is only released into the tumor after exposure to a particular type of stimulus. On the other hand, once the target site is reached, they must release the drug in its most active form without any modification to carry out its function selectively and efficiently.

In this sense, AZD8055 and SN38 were modified using a linker that contains a disulfide moiety that can release the drug inside the cells in the presence of a high concentration of a reducing agent such as glutathione (GSH) or dithiothreitol (DTT). This strategy is being widely exploited for therapeutic purposes, since GSH is overexpressed in the tumor microenvironment, and the concentration increases even more in the cytoplasm of tumoral cells[276]. Particularly, in healthy cells and blood vessels the concentration of GSH can vary between 1 to 20 µM. On the other hand, in tumor cells, this concentration can increase up to 500 times, reaching ranges from 1 to 10 mM. This is because during tumor metabolism, reactive oxygen species such as H_2O_2 are produced, generating cellular damage. For this reason, tumor cells overexpress a variety of enzymes, such as GSH that allow the reduction of H_2O_2 to water[297]. Thus, the different concentrations of this compound between healthy and tumor cells can be exploited to release therapeutics selectively in cancer cells (**Figure 76**).

Conversely, doxorubicin was modified with a linker that contains an imine moiety that releases the drug in acidic conditions. pH variations are another of the most widely used stimuli in the design of nanoparticles for the controlled release of drugs, since they can detect small variations. Tumor cells have lower pH ranges than healthy cells and blood vessels that generally stays at 7.4. The glycolysis rate in solid tumors cells increases, causing a decrease in pH to values below 7 in the extracellular matrix. This can be used as a specific stimulus for the controlled release of drugs that contain pH-sensitive linkers. Also, in different organelles such as endosomes or lysosomes, the pH can decrease, even more, reaching values between 4.5 to 5.5 (**Figure 76**)[298].

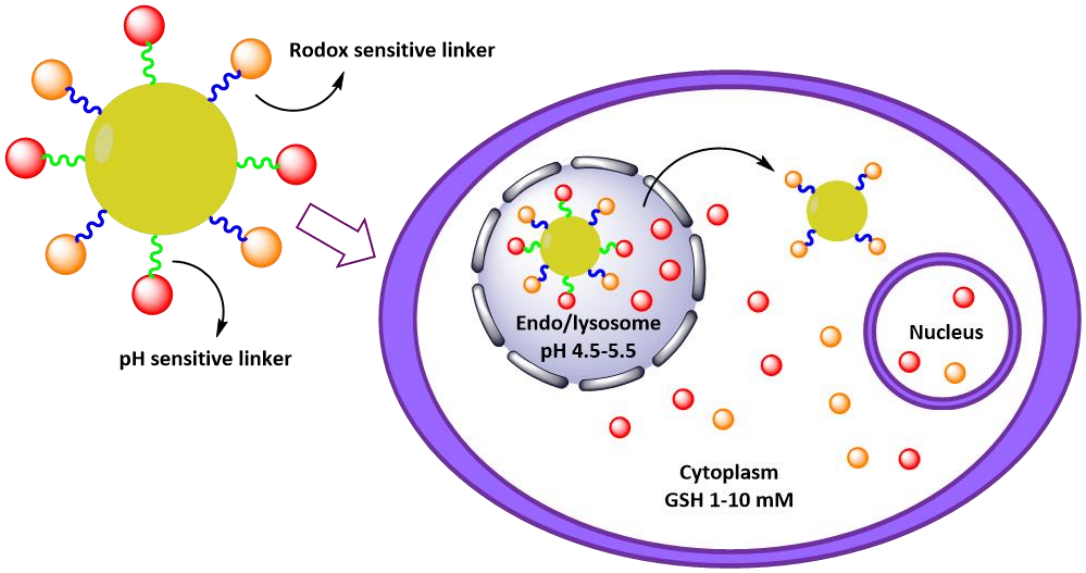

Figure 76. Schematic representation of the albumin nanoparticles functionalized with two drugs modified with linkers sensitive to GSH (blue) and pH (green). Once the nanostructure has reached the tumor, it is incorporated into the endo/lysosomes that are in an acidic environment (pH = 4.5-5.5) and release the pH-sensitive drug. Then, in the cytoplasm of the tumor cells, the drug modified with the GSH-sensitive connector will be released from the nanoparticle due to the higher concentrations of GSH inside the tumor cell (1-10 mM GSH).

Although it has been shown in these formulations that a minimal amount of drug is lost over time under physiological conditions (PBS buffer pH = 7.4), the majority is released over time in a controlled manner after exposure to a high concentration of reducing agent, in the case of SN38 and AZD, and a drop in pH to 5, in the case of DOX (**Figures 26 and 43**). Remarkably, the linkers employed in the modification of drugs allows their release from BSA-AuNCs without any modifications, thus, in its most active form.

For these reasons, controlled release systems based on BSA-AuNCs have great advantages compared to conventional chemotherapy. These systems improve the solubility of drugs, and therefore their stability in biological systems. In addition, they have an optimal size to selectively accumulate in the tumor due to the EPR effect, minimizing the exposure of healthy cells to the cytotoxic effects of antitumor agents. Finally, due to the modification with sensitive linkers to certain stimuli present in the tumor, the drugs will be released in a controlled way only once their target site is reached, avoiding a premature release. Together, these particularities could allow drugs to be administered in lower doses, while maintaining a stable concentration for longer

in the tumor. Therefore, the unwanted side effects derived from conventional chemotherapies could be reduced.

Cellular uptake of BSA-AuNCs

It is known, that albumin can interact with overexpressed cellular receptors that increase its internalization in cancer cells. Unlike conventional medications, albumin is capable of transcytosis through the vascular endothelium (**Figure 77**). This process takes place thanks to the GP-60 receptor (or albondin), present in the vascular endothelium and alveolar epithelium. Albumin binds to GP-60 and accumulates on the cell surface, leading to association with the Caveolin-1 (Cav-1) protein, key in caveola formation in the endocytic pathway. In this way, Cav-1 induces a vesicle's internalization in the endothelial cells that contain the albumin-GP-60 complexes. These complexes travel through the cytoplasm and release material from the vesicle into the tumor interstitium. Then, it has been hypothesized that albumin will bind to the SPARC protein (acidic and cysteine-rich secreted protein), which is overexpressed in tumor cells. This binding could allow the accumulation of therapeutic agents in the tumor interstitium, improving the absorption of albumin by cancer cells. [299,300].

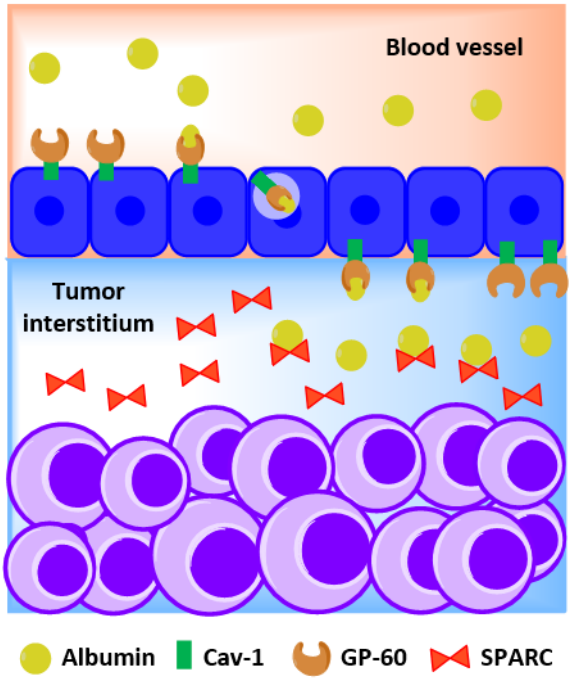

Figure 77. Schematic representation of albumin transcytosis in endothelial cells. Albumin binds to GP-60 receptor, which in turn, is associated with the Cav-1 protein. The complex will lead to the formation of caveola-dependent vesicles, allowing albumin to travel through the cytoplasm of the cells to the interstitium of the tumor. Once there, it will bind to the SPARC protein and accumulate in the tumor area.

In addition, it has been found that while GP-60 binds only to native albumin, GP-18 and GP-30 receptors are capable of binding to modified albumin such as albumin-gold complexes or maleic anhydride-treated albumin. GP-18 and GP-30 are related to the lysosomal degradation of this type of albumin, possibly as a safety mechanism to eliminate old, damaged, or potentially harmful albumin due to modifications such as oxidation, non-enzymatic glycation, and malylation. For this reason, modified albumin is removed more rapidly than native albumin[299,300].

Besides, it is important to note that nanostructures in physiological media can interact with different molecules (opsonization), forming a layer around them called "protein corona". This coating is thought to consist of a hard layer associated with the nanoparticle that contains more than 100 different proteins and a more dynamic soft outer layer. In this sense, the protein corona can dramatically influence the physicochemical properties of nanoparticles, such as size, shape and surface charge[301]. This process can directly affect the cellular uptake and toxicity of nanostructures, which tends to decrease in the presence of this protein layer. This may be because nanoparticles have less affinity for membrane proteins, so interaction with tissues is reduced[302]. In addition, this process can eventually activate an immune response that leads to its subsequent degradation and elimination[303]. Interestingly, albumin-based systems can take advantage of the particle-protein interaction, formulating a pure albumin corona that can reduce the degree of opsonization[304].

The evaluation of the cellular uptake of non-functionalized BSA-AuNCs was carried out by confocal microscopy in breast cancer MCF-7 cells (**Figure 49**) and uveal melanoma Mel202 cells (**Figure 27**). These nanostructures can internalize into the cells in short times between 3 or 4 hours, probably due to interaction with cellular receptors described above. However, at times longer than 24 hours, the BSA-AuNCs were not detected in the cells. This is possibly due to the degradation by proteases that act on the BSA into the cytoplasm.

Remarkably, despite the possible BSA degradation, the drugs are detectable at long times. DOX and SN38 could be visualized under the confocal microscope in the nucleus of MCF7 at 24 hours after treatment with BSA-AuNCs-DS (**Figure 50**). In the case of the AZD8055, it could be detected in Mel202 cells by flow cytometry after the treatment

with BSA-AuNCs-AZD (**Figure 28**). These results evidence the potential of BSA as a drug transporter, since they are biodegradable and non-toxic nanostructures that conjugated with drugs internalize in a very efficient way.

Once inside the cell, the drugs remain stable for a longer time in their active form to carry out their corresponding function. To corroborate the activity of our strategy in biological systems, the functionalized BSA-AuNCs were studied in *in vitro* and *in vivo* models.

Biocompatibility of BSA-AuNCs

For efficient transport of therapeutic agents, nanomaterials have to meet specific requirements. They must be biocompatible to ensure safe drug release and minimize unwanted cytotoxicity. Currently, there is no clear consensus for the evaluation of the biocompatibility of nanoparticles, but it is known that their toxicity is related to their chemical composition and physicochemical properties, including size, shape and surface characteristics, as described in previous sections. For instance, while gold nanoparticles of 1.2 and 1.4 nm core size produce a rapid cell death by apoptosis and necrosis, respectively, those 15 nm core size did not show any toxicity[305].

In our case, to evaluate the toxicity of non-functionalized BSA-AuNCs, cell viability studies using resazurin and MTT assay were carried out. In particular, these nanostructures were tested in the uveal melanoma (Mel202), breast cancer (MCF7, MDA-MB-231) and pancreatic cancer cell lines (**Figures 30, 44 and 45**). Interestingly, the stabilization of the gold atoms with BSA, a biocompatible and biodegradable protein, shows the absence of toxicity of the system in any of the cells studied.

Antitumor activity of BSA-AuNCs-AZD in uveal melanoma cells

In the case of the AuNCs-BSA-AZD, its activity was verified in different uveal melanoma cells harboring GNAQ mutations, since the development of the tumor is attributed to oncogenic mutations in this gene, as described before (see Results, chapter **4.1**.). The wild type GNAQ has a glutamine in position 209 (Q209), which is mutated in the tumor development, particularly that residue is usually replaced by a proline (Q209P) or a leucine (Q209L). In this regard, we selected three types of uveal melanoma cells containing different mutations: Mel202 cells harbor the GNAQ Q209L mutation and

OMM1.3 cells harbor Q209P mutation. However, the Sp6.5 cell line carries a mutation in the BRAF gene (V600E) that is most typical of cutaneous melanoma[306,307]. As a control, non-tumoral keratinocytes (HaCaT cells) were also studied.

In cell viability experiments, we identified that the cells most sensitive to our nanostructures were Mel202 cells that contained the Q209L mutation, compared to OMM1.3 and Sp6.5 that contained another mutation. In the case of the free drug, it also induces a drastic decrease in the viability of these three cell lines, with Mel202 being once again the most sensitive. Remarkably, the BSA-AuNCs-AZD did not produce a significant reduction in cell viability in the HaCaT control cells, whereas the free drug did (**Figure 29**). This fact demonstrates the high selectivity of BSA-AuNCs for tumor cells, possibly due to the presence of receptors that are exclusively overexpressed in tumoral cells, as mentioned above.

On the other hand, the different activity observed between the free AZD8055 and the BSA-AuNCs-AZD in the Mel202 cells could be due to the internalization pathway. Free drugs can diffuse through the membrane directly to the cytoplasm. However, nanostructures have to reach the cell membrane, interact with it, and enter the cell, mainly through endocytosis mechanisms. To investigate the cellular uptake mechanism used for BSA-AuNCs-AZD, two different endocytosis inhibitors were tested to block the entry pathway. In particular, Chlorpromazine, a chemical inhibitor of clathrin-mediated endocytosis, and Filipin III, to inhibit caveolae-mediated endocytosis were employed. The obtained results revealed that the main internalization pathway of BSA-AuNCs-AZD is clathrin-mediated endocytosis (**Figure 31**).

In addition, some studies have demonstrated that the internalization process and the physicochemical properties of nanoparticles can produce free radicals in cells causing oxidative stress, which leads to inflammation and cell destruction[308]. As expected, due to the absence of toxicity of this system in the cells, BSA-AuNCs did not produce any increase in ROS production. Interestingly, the derivative modified with AZD8055 produced a significant increase in ROS production, leading to cell death in the tumoral cells (**Figure 32**).

Finally, we decided to test its potential in *in vivo* models by establishing mouse models by subcutaneous injection of these cells. Free AZD8055 is a hydrophobic drug that does

not allow its intravenous injection in simple aqueous solvent. Therefore, it is necessary to look for new solubilization technologies such as pH modifications or the use of cosolvents, which can lead to failure in drug development and toxicity[309]. Interestingly, the conjugation to the BSA-AuNCs helps in the solubilization of the drug, allowing it to be injected systematically in an efficient way. Furthermore, the results showed that functionalized nanostructures reduce the size of tumors compared to the control and also with the free drug, even at a dose 23 times lower than that used in previous studies (**Figure 33**). This result is in accordance with the fact that nanocarriers can increase the circulation time of the drug (e.g., AZD8055) allowing the use of lower doses without causing substantial damage to other organs (**Figure 34**).

Antitumor activity of BSA-AuNCs-DS in breast cancer cells

Similar results were obtained using BSA-AuNCs-DS for breast cancer treatment luminal-type (see Results, chapter **4.2**).

In previous studies, it has been shown that DOX and SN38 can stabilize the topoisomerase II and I complexes, respectively, during DNA replication and induce DNA double-strand breaks (DSB)[310,311]. This mechanism promotes apoptosis, as can be observed in the formation of apoptotic nuclei in MCF7 cells after the treatment with the nanostructures (**Figure 47**).

Although BSA-AuNCs-D and BSA-AuNCs-S can produce a significant decrease in cell viability, we were able to verify that the combined therapy, BSA-AuNCs-DS, has a more significant antitumor activity than monotherapies in the breast cancer MCF-7 cell line (**Figure 44**). This is because combining the two drugs produces a more substantial number of DNA double-strand breaks than the monotherapies separately (**Figure 51**). This more significant effect of the combined therapy also had a remarkable impact after nine days of incubation, where the cells were not able to regrow (**Figure 48**).

Furthermore, MCF-7 offers the possibility of mammosphere formation, which are groups of 3D spherical cells enriched with cancer stem cells (CSCs). These cells, are small cell populations with self-renewing and high tumorigenic capabilities, which can be responsible for the development of drug resistance, metastases and relapses[312,313].

They are present in different kinds of tumors[314,315], such as glioblastomas[316] or breast cancer[317].

Conventional chemotherapeutics are more effective in treating differentiated tumor cells, but do not eliminate the subpopulation of CSCs, due to their inherent drug resistance and its efficient DNA repair system[318]. For these reasons, one of the great challenges in the treatment of cancer is the development of effective therapies against CSCs in the tumors.

Unlike conventional treatments that are not able to completely eliminate this population of cells, our strategy can reduce the number of mammospheres and their size (**Figures 53 and 54**). This fact, together with the increased antitumor activity over long periods, are keys to possible clinical applications because they could prevent possible tumor relapses in patients.

Additionally, we evaluated the nanoplatform in another basal-type breast cancer cell line (MDA-231) with negative estrogen, progesterone and HER2 receptors. In these cases, the antitumor activity of the combined therapy also significantly decreases the cell viability, although the effect is slightly less than in the case of luminal-type cells (**Figure 45a**). The difference in the sensitivity to the drugs of both cell lines can be due to their biological characteristic along with the distinct clinical prognosis of the tumor types. Although both lines corresponded to the same kind of tumor, MDA-MB-231 cells are included in the triple-negative molecular subtype, while MCF-7 is a luminal type[319].

In addition, to evaluate the potential use of this system in other types of tumors, we decided to study the combined therapy activity in pancreatic cancer cells (**Figure 45b**). Panc1 cell line, is a well-established model for pancreatic ductal adenocarcinoma (PDAC)[216]. This tumor has a poor prognosis, even when diagnosed early, and its survival rate after five years is less than 5%[320]. To the best of our knowledge, this drug combination conjugated to BSA-AuNCs as a potential therapy against pancreatic cancer has never been evaluated. Remarkably, our system also produced a significant reduction in cell viability.

With this experiment, we were able to demonstrate the versatility of BSA-AuNCs-DS, since they are capable of acting on different types of tumor cell lines with different sensitivity to drugs, producing a tremendous therapeutic effect.

As conclusion, albumin-stabilized gold nanoclusters as drug delivery systems can make the drugs more stable and promote the preferable internalization in tumor cells with minimal side effects[321,322]. Compared to conventional treatments, functionalized BSA-AuNCs can increase the treatments' selectivity, prevent the degradation of the drugs, their premature release and improve low bioavailability, thus minimizing side effects[117].

Although BSA-stabilized gold nanoclusters have already been demonstrated to be powerful drug transport vehicles, future projects in the group are focused on developing new multifunctional controlled-release drug platforms that allow the diagnosis and treatment of different types of tumors at the same time.

5.3.2. BSA complex for Cpf1 gene-editing ribonucleoprotein (RNP) transport

This work was carried out in collaboration with Carmen Escalona from the group of Dr. Begoña Sot at IMDEA Nanociencia. It is worth mentioning that this is the first time that our research group explores the nanostructures' functionalization with therapeutic proteins, where the combination of different expertise (e.g., modification and purification of proteins, preparation and modification of nanoparticles) has made it possible to carry out this work.

Protein delivery has many applications, both *in vitro* and *in vivo*, since they can control different signaling pathways related to various diseases such as cancer. However, the main challenges in delivering proteins involve low biological activity, which is due to low stability, poor membrane permeability related to its high molecular weight, immunogenicity, and toxicity. As a result of these drawbacks, proteins have a short plasma half-life, ranging from minutes to several hours. Besides, proteases, rapid metabolism, opsonization and conformational protein changes are other critical factors in the low bioavailability of proteins[323,324].

To overcome these limitations, there are different strategies to improve the bioavailability of proteins, such as alternative delivery routes (e.g., nasal or pulmonary)

or new formulation approaches (spray-freeze drying or lyophilization). Furthermore, in recent years the use of nanomedicine is being widely investigated to improve the pharmacokinetic properties of proteins[325].

In the current work, we demonstrate that albumin can be conjugated covalently with a Cpf1 gene-editing ribonucleoprotein forming BSA-Cpf1(RNP) complexes. In this regard, we hypothesize that native BSA could protect the Cpf1 of the protease degradation and the subsequent elimination, and enhance the effective passage through cell membranes to reach the nucleus.

As mentioned before, BSA has approximately 30-39 lysine amine groups available for chemical modification. Their modification was carried out in two steps to form a linker that contained a disulfide moiety, as previously described (see Results, section **4.3.3.1.**). On the other hand, Cpf1 has between 4 and 6 available cysteines that could simply react with the preactivated BSA (**Figure 68**). The advantage of this new approach is that it allows us to quantify the number of amines that have been modified in BSA and of cysteines in Cpf1 thanks to the pyridinethione released in the two functionalization steps (**Figure 69 and 70**).

According to the data obtained from the pyridinethione, we calculated that approximately 3-4 cysteines were conjugated to the activated BSA. Different ratios of BSA:Cpf1 (2:1, 5:1 and 10:1) were tested with similar results. The final complexes were unable to run on a 10% SDS-PAGE gel due to their larger size. However, after incubating the complex with DTT, Cpf1 was released from BSA, resulting in two independent proteins (**Figure 72**). As we expected, the disulfide moiety of the linker breaks easily in the presence of DTT releasing CPf1 protein.

In this sense, the size of the complexes was measured using the DLS technique (**Figure 71**). The data obtained suggest that the complexes have an approximate size of between 20-30 nm, which is in agreement with the theoretical data, since Cpf1 alone is about 10 nm in size and BSA 7-8 nm. In addition, in the cases where the proteins are not bound, a peak around 100 nm appears. We propose that aggregates formed between the two proteins can be derived. Interestingly, this peak decrease when complexes are formed. TEM measurements of the complexes are ongoing to verify the exact size of these BSA-Cpf1 complexes.

The main idea of this work is that albumin complexes can protect Cpf1(RNP) from premature degradation in biological systems. Also, it could increase its uptake in tumor cells thanks to the ability of albumin to accumulate in cancer tissues due to the overexpression of protein receptors such as SPARC in tumors. In this sense, once the complexes are within the tumor cell, the disulfide covalent bond that forms the complexes could be easily separated due to the large concentration of intracellular GSH. Then, the free protein could internalize in the nucleus and carry out its function as a gene-editing system.

One of the biggest problems with this approach was the need to modify the Cpf1(RNP) protein for covalent binding to albumin, which could result in total or partial loss of its function. To investigate whether the protein modification process could have affected its nuclease activity, we carried out an *in vitro* cleavage activity assay with the EGFP gene. The results obtained demonstrate that the nuclease activity of the protein is not affected, and the Cpf1(RNP) is capable of producing double strand-breaks in the EGFP gene, which is visualized in the gel electrophoresis as two bands of different sizes (**Figure 74**). For this reason, the next step would be to test its activity in cell cultures of tumor cells on a gene of interest such as mutated GNAQ in uveal melanoma tumors or mutated KRAS in pancreatic cancer.

Although this project shows very promising results, it is a work in progress, and therefore much more work in this direction is needed. Deeply characterization of the complexes and cell culture experiments are ongoing.

5.4. Carbon nanotubes in cancer therapy

Carbon nanotubes (CNTs) are allotropic forms of carbon with a cylindrical structure, which means that they are made exclusively of carbon molecules. They can be classified into two categories according to their structure: single-walled carbon nanotubes (SWNT), which consist of a cylindrical carbon layer, or multi-walled carbon nanotubes (MWNT), made of several cylindrical carbon layers[257]. They have unique physicochemical properties such as high aspect ratio, high surface area, high mechanical strength, high electrical and thermal conductivity and ultralight weight.

In the last few years, CNTs have been increasingly studied in the field of nanomedicine due to their inherent properties, such as their high capacity to contain molecules, stability and flexibility, which leads to an increase in the useful circulating half-life of molecules. However, the poor-water solubility prevents its use in almost all biological media. To overcome this limitation, CNTs can be functionalized to be more soluble in aqueous media and serum-stable. The surface modification not only solves the problem related to the solubility but also ensures the biocompatibility and less toxicity of the material itself, avoiding the formation of toxic aggregates[326].

In general, CNTs can be functionalized by both non-covalent or covalent methods with different molecules (**Figure 78**)[327,328].

Covalent functionalization of CNTs is based on the chemical binding of functional groups to their surface, leading to stable and robust chemical bonds (**Figure 78a**). Nanotubes functionalization can be accomplished by oxidation under strong acidic conditions, resulting in the generation of carboxylic acid groups and shortening of CNTs. These groups can improve the biocompatibility of nanotubes and can also be used for covalent functionalization with different molecules. This strategy that generates strong bonds is more suitable for use as a drug delivery vehicle. However, it can affect the properties of the CNTs, as their surface may be damaged.

On the other hand, non-covalent functionalization of CNTs involves the adsorption of different molecules on their surface by Van der Waals or electrostatic interaction (**Figure 78b**). The main advantage of this approach is the preservation of the intrinsic properties of the nanotubes causing minimal damage to their surface. This type of functionalization is not recommended for drug delivery applications.

Using these strategies, the functionalization of CNTs can be achieved by different therapeutic agents such as small molecules drugs or imaging agents, polymers, proteins and genetic material[329].

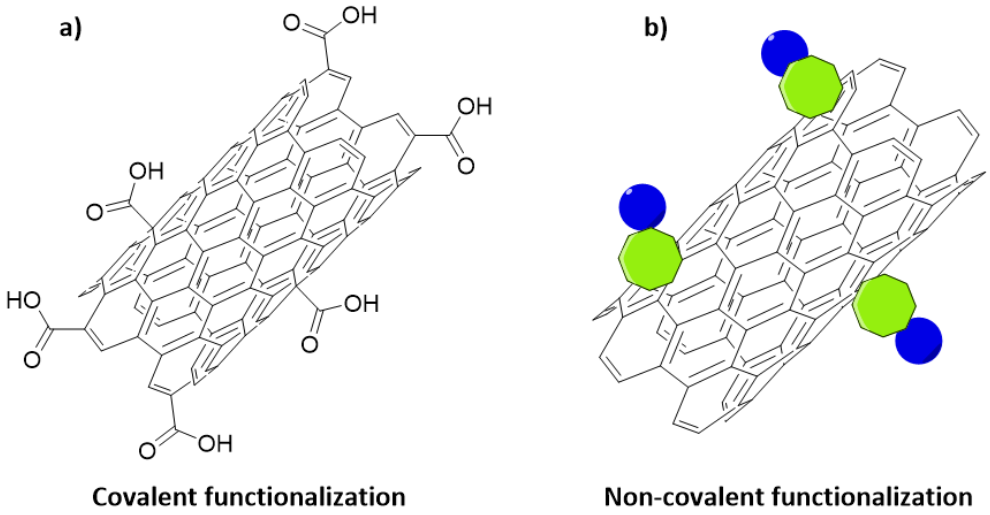

Figure 78. Functionalization methods of carbon nanotubes. **a)** Covalent functionalization consists of the chemical bonding of functional groups to the CNTs wall, leading to stable and robust chemical bonds, for example, through carboxylic acids. **b)** The non-covalent functionalization based on the adsorption of molecules on the surface of the nanotube through electrostatic interaction.

Furthermore, functionalized CNTs can efficiently penetrate biological membranes (by passive diffusion or endocytosis) and accumulate in intracellular compartments[327]. Therefore, their ability to transport therapeutic agents together with their unique physicochemical properties makes these nanomaterials ideal candidates for cancer diagnosis and therapy, since they can be used as imaging agents, drugs and gene delivery systems[330]. For example, as imaging agents, functionalized CNTs have been studied in different types of resonance imaging, including magnetic resonance imaging (MRI) or positron emission tomography (PET) techniques[329].

In this regard, the aim of this work was the study of the ability of functionalized single-wall carbon nanotubes (SWNTs) as a vector for the efficient delivery of a gene-editing CRISPR/Cas9 plasmid. The main objective of the vector is to protect DNA from premature degradation and to reach cells efficiently with minimal toxicity[107].

It is not the first time that PEI functionalized SWNTs have been used to internalize DNA plasmid in cells. For instance, a previous report showed that modified multiwalled carbon nanotubes (MWNTs) could transport a DNA plasmid encoding the β-galactosidase gene. Their surface was modified with two positively charged polymers such as polyethylenimine (PEI), poly(acrylic acid) (PAA) or a mixture of both polymers. The negatively charged DNA plasmid was able to interact electrostatically with modified

MWNTs at different ratios of MWNT:pDNA. This strategy reduced the inherent toxicity of both PEI and PAA polymers, while increasing the gene expression levels of β-galactosidase in human lung epithelial cancer (A549) cells[331]. In addition, Markita Ladry's group, is investigating the use of CNTs to deliver CRISPR/Cas9 components to editing the genome of crop plants[332]. But, remarkably, as far as we know, it is the first time that this system will be used to transport a CRISPR/Cas9 gene-editing plasmid in human cells.

5.4.1. Modified carbon nanotubes (SWNTs) as gene delivery system

In collaboration with Dr. Teresa Naranjo and Dr. Julia Villalva of Dr. Emilio Pérez group at IMDEA Nanociencia, carboxylated SWNTs were chemically modified with the cationic polymer polyethylenimine (PEI) to explore their capacity as a gene delivery system *in vitro*.

PEI is a polymer widely used as a transfection agent due to its high amine content, which gives it a positive charge. Furthermore, it can escape endosomes through the "proton sponge" effect. PEI binds to negative charge DNA through electrostatic interaction, which leads to the formation of PEI:pDNA complexes that can internalize the cell by endocytosis. However, the biological applications of this polymer are affected since it is a non-biodegradable polymer and has high intrinsic cytotoxicity, which limits its efficiency in *in vitro* and *in vivo* studies[258]. There are different forms of commercial PEI available, including linear and branched, but in our case, we used 2 kDa branched PEI. Although it has been seen that longer PEIs have higher transfection efficiency[333], we chose to use the 2 kDa PEI to try to solve the possible derived cellular toxicity.

In this regard, we have verified that our system (PEI-SWNT-pDNA) is not only non-toxic at any of the proposed concentrations (**Figure 64**), but that it is capable of efficiently binding 1 µg of plasmid DNA as observed in the retardation assay (**Figure 63**). This data was crucial for carrying out the following experiments in cell cultures.

To analyze the possible delivery of plasmid DNA to human embryonic kidney (HEK293) cells mediated by SWNTs, the EGFP reporter plasmid was used. It is worth mentioning that for the plasmid DNA to be efficiently expressed in the cells, it is necessary that the

PEI-SWNT-pEGFP successfully internalizes into the cells, release the plasmid and reach the nucleus (**Figure 79**).

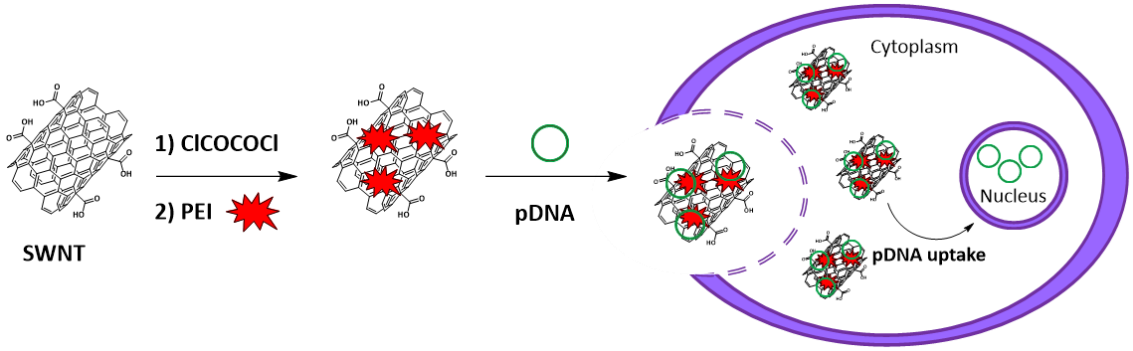

Figure 79. Schematic representation of PEI-modified SWNTs delivery system. Carbon Nanotubes covalently modified with PEI (SWNTs-PEI) allow the electrostatic interaction with DNA plasmids for their efficient delivery in vitro.

The transfection experiments in cells of modified PEI-SWNT-pEGFP complexes are in agreement with the results obtained in the agarose gels in which the correct formation of the complex was observed. Fluorescence images showed a high expression of the EGFP protein, which increases over time from 24 to 72 hours after transfection (**Figure 65**). This means that PEI-modified nanotubes are efficient vectors capable of internalizing in cells and releasing plasmid. The high transfection efficiency could be related to the previously described “proton sponge” capacity of PEI. To test the versatility of this platform, this study was also performed in other cell lines more difficult to transfect, such as uveal melanoma Mel202 cells and pancreatic cancer Panc1 cells (**Figure 66**). However, this system was not as efficient in this type of cells at the same dosage that was tested in HEK293 cells (1 µg of DNA and 20 µL of PEI-SWNTs), and much more work in this direction is needed.

Taking into account these results in HEK293, the ultimate goal of this work was the use of PEI-SWNTs as a transfection vehicle for a plasmid that encodes the CRISPR/Cas9 system. This is one of the most studied strategies in recent years in gene editing, since it allows the modification of genome sequences through the introduction of modifications. In particular, the chosen plasmid (pX330) encodes the human codon-optimized SpCas9 and chimeric guide RNA. In this plasmid, a guide sequence against the EGFP gene was cloned, giving rise to the desired pCas9 plasmid. If cells are edited by the

new plasmid, the generation of the green fluorescent protein will be inhibited, confirming the activity of the system (**Figures 59 and 60**).

In this regard, cells that already expressed the EGFP plasmid were transfected with the PEI-SWNT-pCas9 complexes. However, 72 hours after treatment, no significant decrease in fluorescence was observed (**Figure 67**). This could be mainly due to two main factors. On the one hand, pCas9 may bind to PEI-SWNTs less efficiently, so that it is released prematurely in cell culture medium before its internalization in cells. On the contrary, the release of pCas9 may be slower than what was observed in previous experiments using EGFP plasmid, so the incubation time of the complexes should have been longer.

All fluorescence data from HEK293 cells obtained of transfection of the complex PEI-SWNT-pDNA were attempted to be quantified by flow cytometry analyses. However, in the sample preparation process, the cells died, making their successful quantification impossible.

It is important to mention that this work is still ongoing. The optimization of the system to improve its internalization in different cell lines is necessary to develop an effective gene delivery platform that aims to transport plasmids of CRISPR/Cas9 system.

Conclusions

6. CONCLUSIONS

Cancer is an extremely complex disease that remains a challenge for researchers today. Unfortunately, the incidence of this disease is expected to increase in the following years significantly. For this reason, new tools for early diagnosis and effective therapies with fewer side effects are necessary to tackle this disease.

In recent years, many new approaches, such as those based on targeted therapy or precision oncology, have emerged to overcome the limitations of conventional treatments. These therapies present higher selectivity for tumor cells, minimizing the toxic effects derived from the treatment in healthy tissues. In this sense, nanomedicine can also help to overcome some of the limitations of conventional therapies, due to the unique properties of nanoparticles, as explored in this thesis. In this regard, the main conclusions of this work are the following:

First: Modified BSA can be easily conjugated with different drugs such as doxorubicin, SN38 and AZD8055, leading to the formation of nanoparticles. Also, BSA can be employed to form a complex with the gene-editing protein Cpf1.

Second: BSA-stabilized gold nanoclusters (BSA-AuNCs) are a promising system to deliver drugs.

Third: The use of stimuli-responsive linkers allows for a controlled release of drugs into cells. In addition, they can be employed in the combination of two drugs in the same nanoparticle for combined therapy.

Fourth: BSA-AuNCs-AZD are capable of reducing cell viability in uveal melanoma cells, and even inhibiting tumor growth in animal models.

Fifth: BSA-AuNCs-DS can reduce cell viability in breast cancer cell lines, and in models of cancer stem cells.

Sixth: The conjugation of the Cpf1(RNP) gene-editing protein to BSA does not affect its nuclease activity, leading to loss of function.

Seventh: Drug delivery systems based on PEI-modified SWNT interact with DNA plasmid electrostatically and efficiently internalize in HEK293 cells. However, its use for the transport of the CRISPR/Cas9 system for gene editing must be improved.

References

References

[1] S. Bayda, M. Adeel, T. Tuccinardi, M. Cordani, F. Rizzolio, *Molecules* **2019**, *25*, 112.

[2] P. Mulvaney, *ACS Nano* **2015**, *9*, 2215–2217.

[3] W. G. Kreyling, M. Semmler-Behnke, Q. Chaudhry, *Nano Today* **2010**, *5*, 165–168.

[4] *Nat. Nanotechnol.* **2019**, *14*, 193.

[5] S. A. Mousa, D. J. Bharali, *Cancers (Basel).* **2011**, *3*, 2888–2903.

[6] R. P. Feynman, *There's Plenty of Room at the Bottom*, CRC Press, **1960**.

[7] N. Taniguchi, in *Proc. Int. Conf. Prod. Eng.*, Tokyo, **1974**, pp. 18–23.

[8] The Royal Society, The Royal Academy of Engineering, in *Nanosci. Nanotechnologies Oppor. Uncertainties*, **2004**, p. 116.

[9] F. J. Heiligtag, M. Niederberger, *Mater. Today* **2013**, *16*, 262–271.

[10] P. Sciau, C. Mirguet, C. Roucau, D. Chabanne, M. Schvoerer, *J. Nano Res.* **2009**, *8*, 133–139.

[11] D. Schaming, H. Remita, *Found. Chem.* **2015**, *17*, 187–205.

[12] I. Z. Awan, S. B. Hussain, A. Ul Haq, A. Q. Khan, *Wondrous Nanotechnology*, **2016**.

[13] Reibold M, Paufler P, Levin A.A, Kochmann W, Pätzke N, Meyer D.C, *Nature* **2006**, *444*, 286.

[14] M. Faraday, *Phil. Trans. R. Soc.* **1857**, *147*, 145–181.

[15] G. Mie, *Ann. Phys.* **1908**, *330*, 377–445.

[16] D. R. Boverhof, C. M. Bramante, J. H. Butala, S. F. Clancy, W. M. Lafranconi, J. West, S. C. Gordon, *Regul. Toxicol. Pharmacol.* **2015**, *73*, 137–150.

[17] G. Wang, *Nanotechnology: The New Features*, **2018**.

[18] S. Anu Mary Ealia, M. P. Saravanakumar, *IOP Conf. Ser. Mater. Sci. Eng.* **2017**, *263*, 032019.

[19] E. C. Dreaden, A. M. Alkilany, X. Huang, C. J. Murphy, M. A. El-Sayed, *Chem. Soc. Rev.* **2012**, *41*, 2740–2779.

[20] M. Y. Arfat, S. Zubair, A. Mahmood Dar, M. A. Gatoo, K. Qasim, S. Naseem, *Biomed Res. Int.* **2014**, *2014*, 1–8.

[21] I. Khan, K. Saeed, I. Khan, *Arab. J. Chem.* **2019**, *12*, 908–931.

[22] S. Mohan Bhagyaraj, O. S. Oluwafemi, *Nanotechnology: The Science of the Invisible*, Elsevier Ltd., **2018**.

[23] A. Akbarzadeh, M. Samiei, S. Davaran, *Nanoscale Res. Lett.* **2012**, *7*, 144.

[24] D. Guo, G. Xie, J. Luo, *J. Phys. D. Appl. Phys.* **2014**, *47*, 013001.

[25] S. Navalón, H. García, *Nanomaterials* **2016**, *6*, 4–6.

[26] Khaled Habiba, Vladimir I. Makarov, Brad R. Weiner and, Gerardo Morell, *Fabrication of Nanomaterials by Pulsed Laser Synthesis*, **2014**.

[27] V. Pareek, A. Bhargava, R. Gupta, N. Jain, J. Panwar, *Adv. Sci. Eng. Med.* **2017**, *9*, 527–544.

[28] R. K. Shatrohan Lal, *J. Nanomater. Mol. Nanotechnol.* **2014**, *03*, DOI 10.4172/2324-8777.1000150.

[29] P. Pandey, M. Dahiya, *J. Crit. Rev.* **2016**, *3*, 18–26.

[30] M. Nasrollahzadeh, Z. Issaabadi, M. Sajjadi, S. M. Sajadi, M. Atarod, in *Interface Sci. Technol.*, Elsevier Ltd., **2019**, pp. 29–80.

[31] J. Jeevanandam, A. Barhoum, Y. S. Chan, A. Dufresne, M. K. Danquah, *Beilstein J. Nanotechnol.* **2018**, *9*, 1050–1074.

[32] R. Ghosh Chaudhuri, S. Paria, *Chem. Rev.* **2012**, *112*, 2373–2433.

[33] C. Cha, S. R. Shin, N. Annabi, M. R. Dokmeci, A. Khademhosseini, *ACS Nano* **2013**, *7*, 2891–2897.

[34] M. Gómez Garzón, *Repert. Med. y cirugía* **2019**, *28*, 5–11.

[35] C. Fruijtier-Pölloth, *Toxicology* **2012**, *294*, 61–79.

[36] F. Paladini, M. Pollini, *Materials (Basel).* **2019**, *12*, 2540.

[37] S.S. Manaktala, K. M. Singh, *J. Electr. Electron. Eng.* **2016**, *1*, 63–69.

[38] E. Serrano, G. Rus, J. García-Martínez, *Renew. Sustain. Energy Rev.* **2009**, *13*, 2373–2384.

[39] M. S. A. Abdel-Mottaleb, J. A. Byrne, D. Chakarov, *Int. J. Photoenergy* **2011**, *2011*, 1–2.

[40] J. Lu, Z. Chen, Z. Ma, F. Pan, L. A. Curtiss, K. Amine, *Nat. Nanotechnol.* **2016**, *11*, 1031–1038.

[41] Magy M. Kandil, *The Role of Nanotechnology in Electronic Properties of Materials*, **2016**.

[42] S. C. B. Gopinath, T. Lakshmipriya, M. K. Md Arshad, M. N. A. Uda, Y. Al-Douri, *Nanoelectronics in Biosensing Applications*, Elsevier Inc., **2019**.

[43] D. S. Grewal, *Res. Dev. Mater. Sci.* **2018**, *8*, 925–930.

[44] D. Goldhaber-Gordon, M. S. Montemerlo, J. C. Love, G. J. Opiteck, J. C. Ellenbogen, *Proc. IEEE* **1997**, *85*, 521–540.

[45] G. Ali Mansoori, T. R. Bastami, A. Ahmadpour, Z. Eshaghi, **2008**, pp. 439–493.

[46] K. Pathakoti, M. Manubolu, H.-M. Hwang, in *Handb. Nanomater. Ind. Appl.*, Elsevier, **2018**, pp. 894–907.

[47] C. Fruijtier-Pölloth, *Arch. Toxicol.* **2016**, *90*, 2885–2916.

[48] T. Singh, S. Shukla, P. Kumar, V. Wahla, V. K. Bajpai, *Front. Microbiol.* **2017**, *8*, 1–7.

[49] X. He, H. Deng, H. min Hwang, *J. Food Drug Anal.* **2019**, *27*, 1–21.

[50] L. Rashidi, K. Khosravi-Darani, *Crit. Rev. Food Sci. Nutr.* **2011**, *51*, 723–730.

[51] S. Raj, S. Jose, U. S. Sumod, M. Sabitha, *J. Pharm. Bioallied Sci.* **2012**, *4*, 186–193.

[52] A. P. S. Sawhney, B. Condon, K. V. Singh, S. S. Pang, G. li, D. Hui, *Text. Res. J.* **2008**, *78*, 731–739.

[53] R. Mahmud, F. Nabi, *IOSR J. Polym. Text. Eng.* **2017**, *04*, 01–06.

[54] T. Harifi, M. Montazer, *J. Ind. Text.* **2017**, *46*, 1147–1169.

[55] “Cancer: Overview, causes, treatments, and types,” can be found under https://www.medicalnewstoday.com/articles/323648#what-is-cancer, **n.d.**

[56] “What is Cancer? | Common Forms and Oncology Treatment Options | CTCA,” can be found under https://www.cancercenter.com/what-is-cancer, **n.d.**

[57] “What Is Cancer? - National Cancer Institute,” can be found under https://www.cancer.gov/about-cancer/understanding/what-is-cancer, **n.d.**

[58] World Health Organization, **2020**, 2.

[59] “Cancer - Our World in Data,” can be found under https://ourworldindata.org/cancer, **n.d.**

[60] “Cancer,” can be found under https://www.who.int/health-topics/cancer#tab=tab_1, **n.d.**

[61] World Health Organization, **2020**, 2.

[62] K. Zhu, Q. Liu, Y. Zhou, C. Tao, Z. Zhao, J. Sun, H. Xu, *BMC Genomics* **2015**, *16*, S8.

[63] et al Lodish H, Berk A, Zipursky SL, in *Mol. Cell Biol.*, **2000**.

[64] G. M. Cooper, in *Cell A Mol. Approach.*, Sunderland (MA), **2000**.

[65] A. J. Levine, W. Hu, Z. Feng, in *Mol. Basis Cancer*, Elsevier, **2008**, pp. 31–38.

[66] A. Sidow, N. Spies, *Trends Genet.* **2015**, *31*, 208–214.

[67] G. M. Wahl, B. T. Spike, *npj Breast Cancer* **2017**, *3*, 14.

[68] D. Hanahan, R. A. Weinberg, *Cell* **2000**, *100*, 57–70.

[69] D. Hanahan, R. A. Weinberg, *Cell* **2011**, *144*, 646–674.

[70] Y. A. Fouad, C. Aanei, *Am. J. Cancer Res.* **2017**, *7*, 1016–1036.

[71] S. Chakraborty, T. Rahman, *Ecancermedicalscience* **2012**, *6*, ed16.

[72] "How Surgery Is Used for Cancer," can be found under https://www.cancer.org/treatment/treatments-and-side-effects/treatment-types/surgery/how-surgery-is-used-for-cancer.html, **n.d.**

[73] "Cancer Treatments | CancerQuest," can be found under https://www.cancerquest.org/patients/treatments, **n.d.**

[74] R. Baskar, K. A. Lee, R. Yeo, K. W. Yeoh, *Int. J. Med. Sci.* **2012**, *9*, 193–199.

[75] "How Radiation Therapy Is Used to Treat Cancer," can be found under https://www.cancer.org/treatment/treatments-and-side-effects/treatment-types/radiation/basics.html, **n.d.**

[76] "Chemotherapy for Cancer: How It Works, Chemo Side Effects & FAQs," can be found under https://www.webmd.com/cancer/chemotherapy-what-to-expect#1, **n.d.**

[77] Y. A. Luqmani, *Med. Princ. Pract.* **2005**, *14*, 35–48.

[78] Y. Qu, B. Dou, H. Tan, Y. Feng, N. Wang, D. Wang, *Mol. Cancer* **2019**, *18*, 1–16.

[79] M. Dean, T. Fojo, S. Bates, *Nat. Rev. Cancer* **2005**, *5*, 275–284.

[80] J.-P. Gillet, M. M. Gottesman, in *Business* (Ed.: J. Zhou), Humana Press, Totowa, NJ, **2010**, pp. 47–76.

[81] B. Mansoori, A. Mohammadi, S. Davudian, S. Shirjang, B. Baradaran, *Adv. Pharm. Bull.* **2017**, *7*, 339–348.

[82] T. Ozben, *FEBS Lett.* **2006**, *580*, 2903–2909.

[83] D. A. Yardley, *Int. J. Breast Cancer* **2013**, *2013*, 1–15.

[84] E. Scholar, in *XPharm Compr. Pharmacol. Ref.*, Elsevier, **2007**, pp. 1–4.

[85] R. J. Van Vuuren, M. H. Visagie, A. E. Theron, A. M. Joubert, *Cancer Chemother. Pharmacol.* **2015**, *76*, 1101–1112.

[86] V. V. Padma, *BioMedicine* **2015**, *5*, 19.

[87] "How Targeted Therapies Are Used to Treat Cancer," can be found under https://www.cancer.org/treatment/treatments-and-side-effects/treatment-types/targeted-therapy/what-is.html, **n.d.**

[88] D. E. Gerber, *Am. Fam. Physician* **2008**, *77*, 311–319.

[89] D. D. Rosa, G. Ismael, L. D. Lago, A. Awada, *Cancer Treat. Rev.* **2008**, *34*, 61–80.

[90] N. Diamantis, U. Banerji, *Br. J. Cancer* **2016**, *114*, 362–367.

[91] H. Akbulut, M. Ocal, G. Sonugur, in *Gene Ther. - Princ. Challenges*, InTech, **2015**, pp. 159–165.

[92] D. Singh, S. Chaudhary, R. Kumar, P. Sirohi, K. Mehla, A. Sirohi, S. Kumar, P. Chand, P. K. Singh, in *RNA Interf.*, InTech, **2016**.

[93] T. Zhan, N. Rindtorff, J. Betge, M. P. Ebert, M. Boutros, *Semin. Cancer Biol.* **2019**, *55*, 106–119.

[94] T. Wirth, S. Ylä-Herttuala, *Biomedicines* **2014**, *2*, 149–162.

[95] M. H. Amer, *Mol. Cell. Ther.* **2014**, *2*, 27.

[96] J. Li, H. Liang, J. Liu, Z. Wang, *Int. J. Pharm.* **2018**, *546*, 215–225.

[97] S. J. Oiseth, M. S. Aziz, *J. Cancer Metastasis Treat.* **2017**, *3*, 250.

[98] "Immune Checkpoint Inhibitors - National Cancer Institute," can be found under https://www.cancer.gov/about-cancer/treatment/types/immunotherapy/checkpoint-inhibitors, **n.d.**

[99] C. Graham, R. Hewitson, A. Pagliuca, R. Benjamin, *Clin. Med. J. R. Coll. Physicians London* **2018**, *18*, 324–328.

[100] "T-cell Transfer Therapy - Immunotherapy - National Cancer Institute," can be found under https://www.cancer.gov/about-cancer/treatment/types/immunotherapy/t-cell-transfer-therapy, **n.d.**

[101] "Monoclonal Antibodies and Their Side Effects," can be found under https://www.cancer.org/treatment/treatments-and-side-effects/treatment-types/immunotherapy/monoclonal-antibodies.html, **n.d.**

[102] L. M. Weiner, M. V Dhodapkar, S. Ferrone, *Lancet* **2009**, *373*, 1033–1040.

[103] "Immunotherapy for Cancer - National Cancer Institute," can be found under https://www.cancer.gov/about-cancer/treatment/types/immunotherapy#what-is-the-current-research-in-immunotherapy, **n.d.**

[104] A. Schroeder, D. A. Heller, M. M. Winslow, J. E. Dahlman, G. W. Pratt, R. Langer, T. Jacks, D. G. Anderson, *Nat. Rev. Cancer* **2012**, *12*, 39–50.

[105] N. Ahmed, H. Fessi, A. Elaissari, *Drug Discov. Today* **2012**, *17*, 928–934.

[106] "Nanotechnology Cancer Therapy and Treatment - National Cancer Institute," can be found under https://www.cancer.gov/nano/cancer-nanotechnology/treatment, **n.d.**

[107] M. K. R. Ii, W. Vermerris, **2017**, 1–19.

[108] R. Sinha, G. J. Kim, S. Nie, D. M. Shin, *Mol. Cancer Ther.* **2006**, *5*, 1909–1917.

[109] K. Park, *J. Control. Release* **2014**, *190*, 3–8.

[110] A. E. Vladár, V.-D. Hodoroaba, in *Micro Nano Technol.* (Eds.: V.-D. Hodoroaba, W.E.S. Unger, A.G.B.T.-C. of N. Shard), Elsevier, **2020**, pp. 7–27.

[111] B. Kwiecińska, S. Pusz, B. J. Valentine, *Int. J. Coal Geol.* **2019**, *211*, 103203.

[112] W. D. Pyrz, D. J. Buttrey, *Langmuir* **2008**, *24*, 11350–11360.

[113] P. Klapetek, M. Valtr, D. Nečas, O. Salyk, P. Dzik, *Nanoscale Res. Lett.* **2011**, *6*, 1–9.

[114] A. Rao, M. Schoenenberger, E. Gnecco, T. Glatzel, E. Meyer, D. Brändlin, L. Scandella, *J. Phys. Conf. Ser.* **2007**, *61*, 971–976.

[115] J. Stetefeld, S. A. McKenna, T. R. Patel, *Biophys. Rev.* **2016**, *8*, 409–427.

[116] S. A. A. Rizvi, A. M. Saleh, *Saudi Pharm. J.* **2018**, *26*, 64–70.

[117] D. Lombardo, M. A. Kiselev, M. T. Caccamo, *J. Nanomater.* **2019**, *2019*, 1–26.

[118] T. Stylianopoulos, *Ther. Deliv.* **2013**, *4*, 421–423.

[119] J. Fang, H. Nakamura, H. Maeda, *Adv. Drug Deliv. Rev.* **2011**, *63*, 136–151.

[120] A. Sukhanova, S. Bozrova, P. Sokolov, M. Berestovoy, A. Karaulov, I. Nabiev, *Nanoscale Res. Lett.* **2018**, *13*, DOI 10.1186/s11671-018-2457-x.

[121] N. P. Truong, M. R. Whittaker, C. W. Mak, T. P. Davis, *Expert Opin. Drug Deliv.* **2015**, *12*, 129–142.

[122] P. Foroozandeh, A. A. Aziz, *Nanoscale Res. Lett.* **2018**, *13*, DOI 10.1186/s11671-018-2728-6.

[123] H. Wen, H. Jung, X. Li, *AAPS J.* **2015**, *17*, 1327–1340.

[124] S. M. Dizaj, Z. Vazifehasl, S. Salatin, K. Adibkia, Y. Javadzadeh, *Res. Pharm. Sci.* **2015**, *10*, 95–108.

[125] M. Longmire, P. L. Choyke, H. Kobayashi, *Nanomedicine* **2008**, *3*, 703–717.

[126] J. Wolfram, M. Ferrari, *Nano Today* **2019**, *25*, 85–98.

[127] S. Y. Fam, C. F. Chee, C. Y. Yong, K. L. Ho, A. R. Mariatulqabtiah, W. S. Tan, *Nanomaterials* **2020**, *10*, 787.

[128] R. BAZAK, M. HOURI, S. EL ACHY, W. HUSSEIN, T. REFAAT, *Mol. Clin. Oncol.* **2014**, *2*, 904–908.

[129] A. Angelopoulou, A. Kolokithas-Ntoukas, C. Fytas, K. Avgoustakis, *ACS Omega* **2019**, *4*, 22214–22227.

[130] F. Fay, C. J. Scott, *Immunotherapy* **2011**, *3*, 381–394.

[131] A. Latorre, C. Posch, Y. Garcimartín, A. Celli, M. Sanlorenzo, I. Vujic, J. Ma, M. Zekhtser, K. Rappersberger, S. Ortiz-Urda, et al., *Nanoscale* **2014**, *6*, 7436–42.

[132] A. Parodi, J. Miao, S. M. Soond, M. Rudzińska, A. A. Zamyatnin, *Biomolecules* **2019**, *9*, 218.

[133] F. Hossain, P. R. Andreana, *Pharmaceuticals* **2019**, *12*, 84.

[134] M. Z. El-Readi, M. A. Althubiti, *J. Nanomater.* **2019**, *2019*, 1–13.

[135] A. Raza, T. Rasheed, F. Nabeel, U. Hayat, M. Bilal, H. Iqbal, *Molecules* **2019**, *24*, 1117.

[136] M. A. Obeid, R. J. Tate, A. B. Mullen, V. A. Ferro, in *Lipid Nanocarriers Drug Target.*, Elsevier, **2018**, pp. 313–359.

[137] B. García-Pinel, C. Porras-Alcalá, A. Ortega-Rodríguez, F. Sarabia, J. Prados, C. Melguizo, J. M. López-Romero, *Nanomaterials* **2019**, *9*, 638.

[138] Y. Zhu, C. Liu, Z. Pang, *Biomolecules* **2019**, *9*, 790.

[139] A. Sharma, A. K. Goyal, G. Rath, *J. Drug Target.* **2018**, *26*, 617–632.

[140] S. Ji, C. Liu, B. Zhang, F. Yang, J. Xu, J. Long, C. Jin, D. Fu, Q. Ni, X. Yu, *Biochim. Biophys.*

Acta - Rev. Cancer **2010**, *1806*, 29–35.

[141] K. Kostarelos, L. Lacerda, G. Pastorin, W. Wu, S. Wieckowski, J. Luangsivilay, S. Godefroy, D. Pantarotto, J.-P. Briand, S. Muller, et al., *Nat. Nanotechnol.* **2007**, *2*, 108–113.

[142] K. H. Son, J. H. Hong, J. W. Lee, *Int. J. Nanomedicine* **2016**, *Volume 11*, 5163–5185.

[143] J. Chattopadhyay, F. de Jesus Cortez, S. Chakraborty, N. K. H. Slater, W. E. Billups, *Chem. Mater.* **2006**, *18*, 5864–5868.

[144] D. Verma, N. Gulati, S. Kaul, S. Mukherjee, U. Nagaich, *J. Pharm.* **2018**, *2018*, 1–18.

[145] A. Jain, S. K. Singh, S. K. Arya, S. C. Kundu, S. Kapoor, *ACS Biomater. Sci. Eng.* **2018**, *4*, 3939–3961.

[146] W. Lohcharoenkal, L. Wang, Y. C. Chen, Y. Rojanasakul, *Biomed Res. Int.* **2014**, *2014*, 1–12.

[147] S. Hossen, M. K. Hossain, M. K. Basher, M. N. H. Mia, M. T. Rahman, M. J. Uddin, *J. Adv. Res.* **2019**, *15*, 1–18.

[148] J. M. Metselaar, T. Lammers, *Drug Deliv. Transl. Res.* **2020**, *10*, 721–725.

[149] B. Fadeel, *Front. Toxicol.* **2019**, *1*, 1–4.

[150] M. M. Roberto, C. A. Christofoletti, in *Nanomater. - Toxicity, Hum. Heal. Environ.*, IntechOpen, **2020**.

[151] P. Jain, R. S. Pawar, R. S. Pandey, J. Madan, S. Pawar, P. K. Lakshmi, M. S. Sudheesh, *Biotechnol. Adv.* **2017**, *35*, 889–904.

[152] R. Paliwal, R. J. Babu, S. Palakurthi, *AAPS PharmSciTech* **2014**, *15*, 1527–1534.

[153] P. N. Navya, A. Kaphle, S. P. Srinivas, S. K. Bhargava, V. M. Rotello, H. K. Daima, *Nano Converg.* **2019**, *6*, 23.

[154] L. Young, J. Sung, G. Stacey, J. R. Masters, *Nat. Protoc.* **2010**, *5*, 929–934.

[155] G. Sittampalam, N. Coussens, M. Arkin, D. Auld, C. Austin, B. Bejcek, M. Glicksman, J. Inglese, P. Iversen, J. Mcgee, et al., *Assay Guid. Man.* **2016**, 305–336.

[156] M. Lapeyre, J. Leprince, M. Massonneau, H. Oulyadi, *Chem. - A Eur. J.* **2006**, *12*, 3655–3671.

[157] R. E. Juárez-Hernández, P. A. Miller, M. J. Miller, *ACS Med. Chem. Lett.* **2012**, *3*, 799–803.

[158] D. Willner, P. A. Trail, S. J. Hofstead, H. D. King, S. J. Lasch, G. R. Braslawsky, R. S.

Greenfield, T. Kaneko, R. A. Firestone, *Bioconjug. Chem.* **1993**, *4*, 521–527.

[159] B. A. Krantz, N. Dave, K. M. Komatsubara, B. P. Marr, R. D. Carvajal, *Clin. Ophthalmol.* **2017**, *11*, 279–289.

[160] S. Kaliki, C. L. Shields, *Eye* **2017**, *31*, 241–257.

[161] P. Rutkowski, P. J. Wysocki, A. Nasierowska-Guttmejer, A. Jeziorski, W. M. Wysocki, E. Kalinka-Warzocha, T. Świtaj, K. Kozak, G. Kamińska-Winciorek, A. M. Czarnecka, et al., *Noncutaneous Melanoma*, Codon Publications, **2018**.

[162] "Tratamiento del melanoma ocular uveal (PDQ®)–Versión para profesionales de salud - Instituto Nacional del Cáncer," can be found under https://www.cancer.gov/espanol/tipos/ojo/pro/tratamiento-melanoma-ocular-pdq, **n.d.**

[163] E. E. Nichols, A. Richmond, A. B. Daniels, *Semin. Ophthalmol.* **2016**, *31*, 304–309.

[164] D. Lorenzo, J. M. Piulats, M. Ochoa, L. Arias, C. Gutiérrez, J. Català, E. Cobos, P. Garcia-Bru, B. Dias, N. Padrón-Pérez, et al., *Jpn. J. Ophthalmol.* **2019**, *63*, 197–209.

[165] E. Szalai, J. R. Wells, L. Ward, H. E. Grossniklaus, *Ophthalmology* **2018**, *125*, 203–209.

[166] B. Álvarez-Rodríguez, A. Latorre, C. Posch, Á. Somoza, *Med. Res. Rev.* **2017**, *37*, 1350–1372.

[167] M. Patel, E. Smyth, P. B. Chapman, J. D. Wolchok, G. K. Schwartz, D. H. Abramson, R. D. Carvajal, *Clin. Cancer Res.* **2011**, *17*, 2087–2100.

[168] C. D. Van Raamsdonk, K. G. Griewank, M. B. Crosby, M. C. Garrido, S. Vemula, T. Wiesner, A. C. Obenauf, W. Wackernagel, G. Green, N. Bouvier, et al., *N. Engl. J. Med.* **2010**, *363*, 2191–2199.

[169] C. Posch, A. Latorre, M. B. Crosby, A. Celli, A. Latorre, I. Vujic, M. Sanlorenzo, G. A. Green, J. Weier, M. Zekhtser, et al., *Biomed. Microdevices* **2015**, *17*, DOI 10.1007/s10544-014-9908-7.

[170] J. Yang, D. K. Manson, B. P. Marr, R. D. Carvajal, *Ther. Adv. Med. Oncol.* **2018**, *10*, 175883401875717.

[171] A. L. Ho, E. Musi, G. Ambrosini, J. S. Nair, S. Deraje Vasudeva, E. de Stanchina, G. K. Schwartz, *PLoS One* **2012**, *7*, e40439.

[172] A. Naing, C. Aghajanian, E. Raymond, D. Olmos, G. Schwartz, E. Oelmann, L. Grinsted, W.

Burke, R. Taylor, S. Kaye, et al., *Br. J. Cancer* **2012**, *107*, 1093–1099.

[173] C. M. Chresta, B. R. Davies, I. Hickson, T. Harding, S. Cosulich, S. E. Critchlow, J. P. Vincent, R. Ellston, D. Jones, P. Sini, et al., *Cancer Res.* **2010**, *70*, 288–298.

[174] D. Decaudin, E. Frisch Dit Leitz, F. Nemati, M. Tarin, A. Naguez, M. Zerara, B. Marande, R. Vivet-Noguer, E. Halilovic, C. Fabre, et al., *Eur. J. Cancer* **2020**, *126*, 93–103.

[175] J. I. Fletcher, M. Haber, M. J. Henderson, M. D. Norris, *Nat. Rev. Cancer* **2010**, *10*, 147–156.

[176] G. Housman, S. Byler, S. Heerboth, K. Lapinska, M. Longacre, N. Snyder, S. Sarkar, *Cancers (Basel).* **2014**, *6*, 1769–1792.

[177] L. Shang, S. Dong, G. U. Nienhaus, *Nano Today* **2011**, *6*, 401–418.

[178] J. Xie, Y. Zheng, J. Y. Ying, *J. Am. Chem. Soc.* **2009**, *131*, 888–889.

[179] L. Y. Chen, C. W. Wang, Z. Yuan, H. T. Chang, *Anal. Chem.* **2015**, *87*, 216–229.

[180] Z. Luo, K. Zheng, J. Xie, *Chem. Commun.* **2014**, *50*, 5143–5155.

[181] M. E. Davis, Z. Chen, D. M. Shin, *Nat. Rev. Drug Discov.* **2008**, *7*, 771–782.

[182] B. Elsadek, F. Kratz, *J. Control. Release* **2012**, *157*, 4–28.

[183] X. Wu, X. He, K. Wang, C. Xie, B. Zhou, Z. Qing, *Nanoscale* **2010**, *2*, 2244.

[184] N. Kaur, R. N. Aditya, A. Singh, T.-R. Kuo, *Nanoscale Res. Lett.* **2018**, *13*, 302.

[185] M. Matulionyte, D. Dapkute, L. Budenaite, G. Jarockyte, R. Rotomskis, *Int. J. Mol. Sci.* **2017**, *18*, 1–17.

[186] D. Ding, X. Tang, X. Cao, J. Wu, A. Yuan, Q. Qiao, J. Pan, Y. Hu, *AAPS PharmSciTech* **2014**, *15*, 213–222.

[187] H. Lian, J. Wu, Y. Hu, H. Guo, *Int. J. Nanomedicine* **2017**, *Volume 12*, 7777–7787.

[188] R. Mo, Z. Gu, *Biochem. Pharmacol.* **2016**, *19*, 274–283.

[189] W. Zhang, J. Ye, Y. Zhang, Q. Li, X. Dong, H. Jiang, X. Wang, *RSC Adv.* **2015**, *5*, 63821–63826.

[190] Latorre, Latorre, Castellanos, Diaz, Lazaro-Carrillo, Aguado, Lecea, Romero-Pérez, Calero, Sanchez-Puelles, et al., *Cancers (Basel).* **2019**, *11*, 969.

[191] J. Rejman, A. Bragonzi, M. Conese, *Mol. Ther.* **2005**, *12*, 468–474.

[192] Y. Mo, M. E. Barnett, D. Takemoto, H. Davidson, U. B. Kompella, *Mol. Vis.* **2007**, *13*, 746–

757.

[193] A. Manke, L. Wang, Y. Rojanasakul, *Biomed Res. Int.* **2013**, *2013*, 1–15.

[194] X. Wang, M. G. Roper, *Anal. Methods* **2014**, *6*, 3019–3024.

[195] "WHO | Breast cancer," can be found under https://www.who.int/cancer/prevention/diagnosis-screening/breast-cancer/en/, **n.d.**

[196] G. N. Sharma, R. Dave, J. Sanadya, P. Sharma, K. K. Sharma, *J. Adv. Pharm. Technol. Res.* **2010**, *1*, 109–126.

[197] B. Weigelt, F. C. Geyer, J. S. Reis-Filho, *Mol. Oncol.* **2010**, *4*, 192–208.

[198] R. M. Tamimi, H. J. Baer, J. Marotti, M. Galan, L. Galaburda, Y. Fu, A. C. Deitz, J. L. Connolly, S. J. Schnitt, G. A. Colditz, et al., *Breast Cancer Res.* **2008**, *10*, 1–9.

[199] B. Kondov, Z. Milenkovikj, G. Kondov, G. Petrushevska, N. Basheska, M. Bogdanovska-Todorovska, N. Tolevska, L. Ivkovski, *Open Access Maced. J. Med. Sci.* **2018**, *6*, 961–967.

[200] S. M. Fragomeni, A. Sciallis, J. S. Jeruss, *Surg. Oncol. Clin. N. Am.* **2018**, *27*, 95–120.

[201] F. K. Al-thoubaity, *Ann. Med. Surg.* **2020**, *49*, 44–48.

[202] "Targeted Therapy for Breast Cancer," can be found under https://www.cancer.org/cancer/breast-cancer/treatment/targeted-therapy-for-breast-cancer.html, **n.d.**

[203] "Breast Cancer: Types of Treatment | Cancer.Net," can be found under https://www.cancer.net/cancer-types/breast-cancer/types-treatment, **n.d.**

[204] D. Wu, M. Si, H. Y. Xue, H. L. Wong, *Int. J. Nanomedicine* **2017**, *12*, 5879–5892.

[205] F. A. Fisusi, E. O. Akala, *Pharm. Nanotechnol.* **2019**, *7*, 3–23.

[206] C. F. Thorn, C. Oshiro, S. Marsh, T. Hernandez-Boussard, H. McLeod, T. E. Klein, R. B. Altman, *Pharmacogenet. Genomics* **2011**, *21*, 440–446.

[207] A. G. Patel, S. H. Kaufmann, *Elife* **2012**, *1*, 2011–2013.

[208] O. Tacar, P. Sriamornsak, C. R. Dass, *J. Pharm. Pharmacol.* **2013**, *65*, 157–170.

[209] D. K. Maurya, R. Ayuzawa, C. Doi, D. Troyer, M. Tamura, *J. Environ. Pathol. Toxicol. Oncol.* **2011**, *30*, 1–10.

[210] C. Wu, Y. Zhang, D. Yang, J. Zhang, J. Ma, D. Cheng, J. Chen, L. Deng, *Int. J. Nanomedicine* **2019**, *14*, 75–85.

[211] K. M. Camacho, S. Kumar, S. Menegatti, D. R. Vogus, A. C. Anselmo, S. Mitragotri, *J. Control. Release* **2015**, *210*, 198–207.

[212] M. C. Llinàs, G. Martínez-Edo, A. Cascante, I. Porcar, S. Borrós, D. Sánchez-García, *Drug Deliv.* **2018**, *25*, 1137–1146.

[213] F. Kratz, A. Warnecke, K. Scheuermann, C. Stockmar, J. Schwab, P. Lazar, P. Drückes, N. Esser, J. Drevs, D. Rognan, et al., *J. Med. Chem.* **2002**, *45*, 5523–5533.

[214] A. Latorre, P. Couleaud, A. Aires, A. L. Cortajarena, Á. Somoza, *Eur. J. Med. Chem.* **2014**, *82*, 355–362.

[215] K. J. Chavez, S. V. Garimella, S. Lipkowitz, *Breast Dis.* **2011**, *32*, 35–48.

[216] E. L. Deer, J. González-Hernández, J. D. Coursen, J. E. Shea, J. Ngatia, C. L. Scaife, M. A. Firpo, S. J. Mulvihill, *Pancreas* **2010**, *39*, 425–435.

[217] S. Matt, T. G. Hofmann, *Cell. Mol. Life Sci.* **2016**, *73*, 2829–2850.

[218] A. Sharma, K. Singh, A. Almasan, in *Life Sci.*, **2012**, pp. 613–626.

[219] S. Yousefnia, K. Ghaedi, F. Seyed Forootan, M. H. Nasr Esfahani, *Tumor Biol.* **2019**, *41*, 1–14.

[220] Z. F. Bielecka, K. Maliszewska-Olejniczak, I. J. Safir, C. Szczylik, A. M. Czarnecka, *Biol. Rev.* **2017**, *92*, 1505–1520.

[221] D. B. T. Cox, R. J. Platt, F. Zhang, *Nat. Med.* **2015**, *21*, 121–131.

[222] T. Gaj, C. A. Gersbach, C. F. Barbas, *Trends Biotechnol.* **2013**, *31*, 397–405.

[223] C. Wyman, R. Kanaar, *Annu. Rev. Genet.* **2006**, *40*, 363–383.

[224] D. Carroll, *Genetics* **2011**, *188*, 773–782.

[225] Y. Zhang, *Adv. Genet. Eng.* **2014**, *03*, 1–2.

[226] R. M. Walsh, K. Hochedlinger, *Proc. Natl. Acad. Sci. U. S. A.* **2013**, *110*, 15514–5.

[227] L. Cong, F. A. Ran, D. Cox, S. Lin, R. Barretto, N. Habib, P. D. Hsu, X. Wu, W. Jiang, L. A. Marraffini, et al., *Science (80-.).* **2013**, *339*, 819–823.

[228] H. Wang, H. Yang, C. S. Shivalila, M. M. Dawlaty, A. W. Cheng, F. Zhang, R. Jaenisch, *Cell* **2013**, *153*, 910–918.

[229] F. J. Mojica, G. Juez, F. Rodríguez-Valera, *Mol. Microbiol.* **1993**, *9*, 613–621.

[230] F. J. M. Mojica, C. Ferrer, G. Juez, F. Rodríguez-Valera, *Mol. Microbiol.* **1995**, *17*, 85–93.

[231] F. J. M. Mojica, C. Díez-Villaseñor, J. García-Martínez, E. Soria, *J. Mol. Evol.* **2005**, *60*, 174–182.

[232] R. Barrangou, C. Fremaux, H. Deveau, M. Richards, Patrick Boyaval, S. Moineau, D. Romero, P. Horvath, *Science (80-.).* **2007**, *315*, 1709–1712.

[233] M. Jinek, K. Chylinski, I. Fonfara, M. Hauer, J. A. Doudna, E. Charpentier, *Science (80-.).* **2012**, *337*, 816–821.

[234] E. Deltcheva, K. Chylinski, C. M. Sharma, K. Gonzales, Y. Chao, Z. A. Pirzada, M. R. Eckert, J. Vogel, E. Charpentier, *Nature* **2011**, *471*, 602–607.

[235] P. D. Hsu, D. A. Scott, J. A. Weinstein, F. A. Ran, S. Konermann, V. Agarwala, Y. Li, E. J. Fine, X. Wu, O. Shalem, et al., *Nat. Biotechnol.* **2013**, *31*, 827–832.

[236] H. Nishimasu, F. A. Ran, P. D. Hsu, S. Konermann, S. I. Shehata, N. Dohmae, R. Ishitani, F. Zhang, O. Nureki, *Cell* **2014**, *156*, 935–949.

[237] H. Manghwar, K. Lindsey, X. Zhang, S. Jin, *Trends Plant Sci.* **2019**, *24*, 1102–1125.

[238] K. Xie, Y. Yang, *Mol. Plant* **2013**, *6*, 1975–1983.

[239] J. E. Dicarlo, J. E. Norville, P. Mali, X. Rios, J. Aach, G. M. Church, *Nucleic Acids Res.* **2013**, *41*, 4336–4343.

[240] W. Qin, S. L. Dion, P. M. Kutny, Y. Zhang, A. W. Cheng, N. L. Jillette, A. Malhotra, A. M. Geurts, Y.-G. Chen, H. Wang, *Genetics* **2015**, *200*, 423–30.

[241] S. W. Cho, S. Kim, J. M. Kim, J.-S. Kim, *Nat. Biotechnol.* **2013**, *31*, 230–2.

[242] P. Mali, L. Yang, K. M. Esvelt, J. Aach, M. Guell, J. E. DiCarlo, J. E. Norville, G. M. Church, *Science (80-.).* **2013**, *339*, 823–826.

[243] A. K. Fajrial, Q. Q. He, N. I. Wirusanti, J. E. Slansky, X. Ding, *Theranostics* **2020**, *10*, 5532–5549.

[244] F. Safari, K. Zare, M. Negahdaripour, M. Barekati-Mowahed, Y. Ghasemi, *Cell Biosci.* **2019**, *9*, 1–21.

[245] T. Li, L. Zhu, B. Xiao, Z. Gong, Q. Liao, J. Guo, *CRISPR-Cpf1-Mediated Genome Editing and Gene Regulation in Human Cells*, Elsevier Inc, **2019**.

[246] X. Zhang, L. Xu, R. Fan, Q. Gao, Y. Song, X. Lyu, J. Ren, Y. Song, *Cell Discov.* **2018**, *4*, DOI 10.1038/s41421-018-0035-0.

[247] X.-H. Zhang, L. Y. Tee, X.-G. Wang, Q.-S. Huang, S.-H. Yang, *Mol. Ther. Acids* **2015**, *4*, e264.

[248] X. Wu, A. J. Kriz, P. A. Sharp, *Quant Biol* **2014**, *2*, 59–70.

[249] X. Wu, A. J. Kriz, P. A. Sharp, *Quant. Biol.* **2014**, *2*, 59–70.

[250] E. Senís, C. Fatouros, S. Große, E. Wiedtke, D. Niopek, A.-K. Mueller, K. Börner, D. Grimm, *Biotechnol. J.* **2014**, *9*, 1402–1412.

[251] F. Le Dily, D. Baù, A. Pohl, G. P. Vicent, F. Serra, D. Soronellas, G. Castellano, R. H. G. Wright, C. Ballare, G. Filion, et al., *Genes Dev.* **2014**, *28*, 2151–2162.

[252] J. A. Zuris, D. B. Thompson, Y. Shu, J. P. Guilinger, J. L. Bessen, J. H. Hu, M. L. Maeder, J. K. Joung, Z.-Y. Chen, D. R. Liu, *Nat. Biotechnol.* **2014**, *33*, 73–80.

[253] W. Sun, W. Ji, J. M. Hall, Q. Hu, C. Wang, C. L. Beisel, Z. Gu, *Angew. Chemie - Int. Ed.* **2015**, *54*, 12029–12033.

[254] L. Li, L. Song, X. Liu, X. Yang, X. Li, T. He, N. Wang, S. Yang, C. Yu, T. Yin, et al., *ACS Nano* **2017**, *11*, 95–111.

[255] R. Mout, M. Ray, G. Yesilbag Tonga, Y. W. Lee, T. Tay, K. Sasaki, V. M. Rotello, *ACS Nano* **2017**, *11*, 2452–2458.

[256] H. Peng, C. Le, J. Wu, X. F. Li, H. Zhang, X. C. Le, *ACS Nano* **2020**, DOI 10.1021/acsnano.9b05276.

[257] S. K. S. Kushwaha, S. Ghoshal, A. K. Rai, S. Singh, *Brazilian J. Pharm. Sci.* **2013**, *49*, 629–643.

[258] S. Taranejoo, J. Liu, P. Verma, K. Hourigan, *J. Appl. Polym. Sci.* **2015**, *132*, n/a-n/a.

[259] D. Mohanta, S. Patnaik, S. Sood, N. Das, *J. Pharm. Anal.* **2019**, *9*, 293–300.

[260] "Cancer," can be found under https://www.who.int/news-room/fact-sheets/detail/cancer, **n.d.**

[261] G. M. Cooper, in *Cell A Mol. Approach.* (Ed.: 2nd Edition), **2000**.

[262] R. Cagan, P. Meyer, *DMM Dis. Model. Mech.* **2017**, *10*, 349–352.

[263] J. D. Schiffman, P. G. Fisher, P. Gibbs, *Am. Soc. Clin. Oncol. Educ. B.* **2015**, 57–65.

[264] C. Pucci, C. Martinelli, G. Ciofani, *Ecancermedicalscience* **2019**, *13*, 1–26.

[265] A. Angelucci, *Cancers (Basel).* **2019**, *11*, 1–4.

[266] L. Yan, N. Rosen, C. Arteaga, *Chin. J. Cancer* **2011**, *30*, 1–4.

[267] "What is Precision Oncology and Personalized Cancer Treatment," can be found under

https://www.ctoam.com/precision-oncology/, **n.d.**

[268] J. Remon, R. Dienstmann, *ESMO Open* **2018**, *3*, 1–7.

[269] A. M. Bailey, Y. Mao, J. Zeng, V. Holla, A. Johnson, L. Brusco, K. Chen, J. Mendelsohn, M. J. Routbort, G. B. Mills, et al., *Discov. Med.* **2014**, *17*, 101–114.

[270] G. Riccio, C. Coppola, G. Piscopo, I. Capasso, C. Maurea, E. Esposito, C. De Lorenzo, N. Maurea, *Hum. Vaccines Immunother.* **2016**, *12*, 1124–1131.

[271] S. Liu, R. Kurzrock, *Cancer Treat. Rev.* **2014**, *40*, 883–891.

[272] A.-R. Coltescu, M. Butnariu, I. Sarac, *Biomed. Pharmacol. J.* **2020**, *13*, 577–583.

[273] S. Jain, M. Edwards, L. Spencer, *Regul. Rapp.* **2016**, *13*, 4–8.

[274] K. A. Jinturkar, A. Misra, in *Challenges Deliv. Ther. Genomics Proteomics*, Elsevier, **2011**, pp. 45–82.

[275] B. Thapa, R. Narain, in *Polym. Nanomater. Gene Ther.*, Elsevier, **2016**, pp. 1–27.

[276] A. Latorre, C. Posch, Y. Garcimartín, A. Celli, M. Sanlorenzo, I. Vujic, J. Ma, M. Zekhtser, K. Rappersberger, S. Ortiz-Urda, et al., *Nanoscale* **2014**, *6*, 7436–7442.

[277] A. Latorre, A. Somoza, *Curr. Top. Med. Chem.* **2014**, *14*, 2662–2671.

[278] A. Aires, S. M. Ocampo, B. M. Simões, M. Josefa Rodríguez, J. F. Cadenas, P. Couleaud, K. Spence, A. Latorre, R. Miranda, Á. Somoza, et al., *Nanotechnology* **2016**, *27*, 065103.

[279] U. Bairagi, P. Mittal, B. Mishra, *Austin Ther.* **2015**, *2*, 1021.

[280] F. F. An, X. H. Zhang, *Theranostics* **2017**, *7*, 3667–3689.

[281] G. J. Quinlan, G. S. Martin, T. W. Evans, *Hepatology* **2005**, *41*, 1211–1219.

[282] J. C. Philips, A. Scheen, *Vasc. Health Risk Manag.* **2006**, *2*, 277–283.

[283] I. Cucinotto, L. Fiorillo, S. Gualtieri, M. Arbitrio, D. Ciliberto, N. Staropoli, A. Grimaldi, A. Luce, P. Tassone, M. Caraglia, et al., *J. Drug Deliv.* **2013**, *2013*, 1–10.

[284] N. Desai, in *Albumin Med.*, Springer Singapore, Singapore, **2016**, pp. 101–119.

[285] Z. Liu, X. Chen, *Chem. Soc. Rev.* **2016**, *45*, 1432–1456.

[286] S. Soares, J. Sousa, A. Pais, C. Vitorino, *Front. Chem.* **2018**, *6*, 1–15.

[287] F. Dormont, M. Rouquette, C. Mahatsekake, F. Gobeaux, A. Peramo, R. Brusini, S. Calet, F. Testard, S. Lepetre-Mouelhi, D. Desmaële, et al., *J. Control. Release* **2019**, *307*, 302–314.

[288] P. Russell, D. Batchelor, A. I. Facility, P. E. Russell, *Microsc. Anal.* **2001**, 9–12.

[289] J. Nilsen, M. Bern, K. M. K. Sand, A. Grevys, B. Dalhus, I. Sandlie, J. T. Andersen, *Sci. Rep.* **2018**, *8*, 1–12.

[290] R. Nielsen, E. I. Christensen, H. Birn, *Kidney Int.* **2016**, *89*, 58–67.

[291] S. K. Golombek, J.-N. May, B. Theek, L. Appold, N. Drude, F. Kiessling, T. Lammers, *Adv. Drug Deliv. Rev.* **2018**, *130*, 17–38.

[292] A. Gabizon, R. Catane, B. Uziely, B. Kaufman, T. Safra, R. Cohen, F. Martin, A. Huang, Y. Barenholz, *Cancer Res.* **1994**, *54*, 987–992.

[293] D. Rosenblum, N. Joshi, W. Tao, J. M. Karp, D. Peer, *Nat. Commun.* **2018**, *9*, 1410.

[294] Y. W. Huang, M. Cambre, H. J. Lee, *Int. J. Mol. Sci.* **2017**, *18*, DOI 10.3390/ijms18122702.

[295] A. Jhaveri, P. Deshpande, V. Torchilin, *J. Control. Release* **2014**, *190*, 352–370.

[296] L. Zhang, Y. Qin, Z. Zhang, F. Fan, C. Huang, L. Lu, H. Wang, X. Jin, H. Zhao, D. Kong, et al., *Acta Biomater.* **2018**, *75*, 371–385.

[297] D. Liu, F. Yang, F. Xiong, N. Gu, *Theranostics* **2016**, *6*, 1306–1323.

[298] N. Deirram, C. Zhang, S. S. Kermaniyan, A. P. R. Johnston, G. K. Such, *Macromol. Rapid Commun.* **2019**, *40*, 1–23.

[299] M. T. Larsen, M. Kuhlmann, M. L. Hvam, K. A. Howard, *Mol. Cell. Ther.* **2016**, DOI 10.1186/s40591-016-0048-8.

[300] E. N. Hoogenboezem, C. L. Duvall, *Adv. Drug Deliv. Rev.* **2018**, *130*, 73–89.

[301] M. Hadjidemetriou, K. Kostarelos, *Nat. Nanotechnol.* **2017**, *12*, 288–290.

[302] J. Wolfram, M. Zhu, Y. Yang, J. Shen, E. Gentile, D. Paolino, M. Fresta, G. Nie, C. Chen, H. Shen, et al., *Curr. Drug Targets* **2015**, *16*, 1671–1681.

[303] S. Naahidi, M. Jafari, F. Edalat, K. Raymond, A. Khademhosseini, P. Chen, *J. Control. Release* **2013**, *166*, 182–194.

[304] Y. L. Tan, H. K. Ho, *Drug Discov. Today* **2018**, *23*, 1108–1114.

[305] Y. Pan, S. Neuss, A. Leifert, M. Fischler, F. Wen, U. Simon, G. Schmid, W. Brandau, W. Jahnen-Dechent, *Small* **2007**, *3*, 1941–1949.

[306] M. J. de Lange, L. Razzaq, M. Versluis, S. Verlinde, M. Dogrusöz, S. Böhringer, M. Marinkovic, G. P. M. Luyten, R. J. W. de Keizer, F. R. de Gruijl, et al., *PLoS One* **2015**, *10*,

e0138002.

[307] M. J. Jager, J. A. B. Magner, B. R. Ksander, S. R. Dubovy, *Trans. Am. Ophthalmol. Soc.* **2016**, *114*, T5.

[308] E. Biazar, Majdi, M. Zafari, M. Avar, S. Aminifard, D. Zaeifi, Ai, Jafarpour, Montazeri, Gh, *Int. J. Nanomedicine* **2011**, 1117.

[309] S. Kalepu, V. Nekkanti, *Acta Pharm. Sin. B* **2015**, *5*, 442–453.

[310] L. Pfitzer, C. Moser, F. Gegenfurtner, A. Arner, F. Foerster, C. Atzberger, T. Zisis, R. Kubisch-Dohmen, J. Busse, R. Smith, et al., *Cell Death Dis.* **2019**, *10*, 302.

[311] C. Gongora, N. Vezzio-Vie, S. Tuduri, V. Denis, A. Causse, C. Auzanneau, G. Collod-Beroud, A. Coquelle, P. Pasero, P. Pourquier, et al., *Mol. Cancer* **2011**, *10*, 64.

[312] H. S. Choi, D.-A. Kim, H. Chung, I. H. Park, B. H. Kim, E.-S. Oh, D.-H. Kang, *Cancer Cell Int.* **2017**, *17*, 25.

[313] M. Liu, S. Shen, D. Wen, M. Li, T. Li, X. Chen, Z. Gu, R. Mo, *Nano Lett.* **2018**, *18*, 2294–2303.

[314] E. Batlle, H. Clevers, *Nat. Med.* **2017**, *23*, 1124–1134.

[315] F. Papaccio, F. Paino, T. Regad, G. Papaccio, V. Desiderio, V. Tirino, *Stem Cells Transl. Med.* **2017**, *6*, 2115–2125.

[316] A. Bradshaw, A. Wickremsekera, S. T. Tan, L. Peng, P. F. Davis, T. Itinteang, *Front. Surg.* **2016**, *3*, 1–15.

[317] A. Bozorgi, M. Khazaei, M. R. Khazaei, *J. Breast Cancer* **2015**, *18*, 303.

[318] M. Maugeri-Sacca, M. Bartucci, R. De Maria, *Mol. Cancer Ther.* **2012**, *11*, 1627–1636.

[319] X. Dai, H. Cheng, Z. Bai, J. Li, *J. Cancer* **2017**, *8*, 3131–3141.

[320] C. G. Willett, B. G. Czito, J. C. Bendell, D. P. Ryan, *J. Clin. Oncol.* **2005**, *23*, 4538–4544.

[321] N. Singh, A. Joshi, A. P. Toor, G. Verma, *Drug Delivery: Advancements and Challenges*, **2017**.

[322] B. S. Pattni, V. P. Torchilin, *Targeted Drug Delivery : Concepts and Design*, **2015**.

[323] B. J. Bruno, G. D. Miller, C. S. Lim, *Ther. Deliv.* **2013**, *4*, 1443–1467.

[324] Y. W. Lee, D. C. Luther, J. A. Kretzmann, A. Burden, T. Jeon, S. Zhai, V. M. Rotello, *Theranostics* **2019**, *9*, 3280–3292.

[325] T. Feridooni, A. Hotchkiss, R. U. Agu, in *Smart Drug Deliv. Syst.*, InTech, **2016**.

[326] A. Sanginario, B. Miccoli, D. Demarchi, *Biosensors* **2017**, *7*, 1–23.

[327] A. Seifalian, *Int. J. Nanomedicine* **2011**, 2963.

[328] P. M. Costa, M. Bourgognon, J. T. W. Wang, K. T. Al-Jamal, *J. Control. Release* **2016**, *241*, 200–219.

[329] H. Hong, T. Gao, W. Cai, *Nano Today* **2009**, *4*, 252–261.

[330] Z. Chen, A. Zhang, X. Wang, J. Zhu, Y. Fan, H. Yu, Z. Yang, *J. Nanomater.* **2017**, *2017*, 1–13.

[331] A. Nunes, N. Amsharov, C. Guo, J. Van Den Bossche, P. Santhosh, T. K. Karachalios, S. F. Nitodas, M. Burghard, K. Kostarelos, K. T. Al-Jamal, *Small* **2010**, *6*, 2281–2291.

[332] G. S. Demirer, H. Zhang, J. L. Matos, N. S. Goh, F. J. Cunningham, Y. Sung, R. Chang, A. J. Aditham, L. Chio, M. J. Cho, et al., *Nat. Nanotechnol.* **2019**, *14*, 456–464.

[333] J. W. Wiseman, C. A. Goddard, D. McLelland, W. H. Colledge, *Gene Ther.* **2003**, *10*, 1654–1662.